UNIVERSITY OF SOUTHAMPTON

FACULTY OF ENGINEERING AND THE ENVIRONMENT

Institute of Sound and Vibration Research

PREDICTION OF SUPERSONIC FAN NOISE GENERATED BY TURBOFAN AIRCRAFT ENGINES

by

Oluwaseun Emmanuel Adetifa

Thesis for the degree of Doctor of Philosophy

December 2015

UNIVERSITY OF SOUTHAMPTON

ABSTRACT

FACULTY OF ENGINEERING AND THE ENVIRONMENT
Institute of Sound and Vibration Research

Doctor of Philosophy

PREDICTION OF SUPERSONIC FAN NOISE GENERATED BY TURBOFAN AIRCRAFT ENGINES

by Oluwaseun Emmanuel Adetifa

Prediction of Supersonic Fan Noise Generated by Turbofan Aircraft Engines was focussed on improving the capability of predicting supersonic fan noise from modern high-bypass-ratio turbofan aero-engines. The shift from single core jet engines to high-bypass-ratio turbofan engines brought about a reduction in the overall aircraft engine noise principally by reducing the jet-broadband noise. However, this new design meant the size of the fan of a high-bypass-ratio turbofan engine, over subsequent years, has increased in diameter. This increase allowed for the speed of the tips of the fan blades to reach and exceed the speed of sound.

At high power engine operation conditions, especially at take-off conditions, the noise levels observed from such engines is very high. A major component of this noise is the supersonic fan noise which is also referred to as buzz-saw noise. Shocks are produced at the fan blade tips at this high power engine operation condition. These shocks propagate upstream, against the inflow, following a helical path dictated by the rotation of the fan. The pressure field produced at the tip of the fan is represented as a series of shock waves and expansion waves. As this pressure field advances, it interacts with the incoming flow and acoustic treatment in the intake duct.

The shocks in the pressure field are all unique and are of different amplitudes. This is because the fan blades, although manufactured to tight tolerances, are not perfectly alike. Also, the arrangement of these fan blades on the fan hub will also lead to unavoidable differences among the fan blades. These minute differences are reflected in the amplitudes of the shocks, making each shock slightly different from the others. Shocks in the pressure field propagate with respect to the magnitude of their pressure amplitude. Therefore, the shocks travel at different speeds. In the course of propagation, faster shocks catch up with slower ones, and they merge into a single shock, even as the shocks' amplitudes are attenuated. The difference in speeds and the interactions among the shocks ensure a transfer of energy among the harmonics of the pressure field. This process is nonlinear; the work in this thesis is focussed on modelling the nonlinear propagation of the shocks pressure pattern.

These interactions greatly enhance the lower frequency harmonics of the pressure field shifting the dominance from the blade passage frequency and its harmonics. Further upstream, the dominance of the low frequency harmonics is unmistakable. Subsequently the pressure field is radiated from the aircraft intake duct. The resultant radiated pressure field is that which is perceived by an observer in the far-field. The models presented in this thesis capture the main features of this nonlinear propagation and radiation of the pressure field generated at the fan blade tips, and generates predictions for supersonic fan noise levels in the intake duct and in the far-field.

A time domain model named SPRID (Sawtooth Propagation in Rigid Intake Ducts) developed is presented. This model predicts the supersonic fan noise levels in ducts without any acoustic treatment, and has been validated against a benchmark frequency domain nonlinear propagation model (FDNS), and also measured data from a model-scale fan rig test provided by Rolls-Royce PLC. The need to incorporate the effect of acoustic liners in the modelling led to the development of a new model which employs the combined time-frequency domain approach. In this model, the nonlinear propagation of the pressure field is simulated in the time domain, while the acoustic liner effects are implemented in the frequency domain. This model also has been validated with measured data.

The combined time-frequency domain prediction method was improved to incorporate more complex features of supersonic fan noise propagation. Features such as the change in duct radius along the duct axis and the consequent change in mean flow speeds, and boundary layer effects on the liner absorption have been included in a more advanced model. The advanced nonlinear model is a more representative model of real aircraft intake duct. Also, a theoretical radiation model (GX-Munt) was utilized to predict supersonic fan noise in the far-field. In this thesis, a whole study of supersonic fan noise, starting from source generation at the fan plane up to the radiation to the far-field is presented. The thesis includes an extensive literature review, research on the generation of a source sawtooth for propagation utilizing measured data, and development of equations for nonlinear propagation in axisymmetric intake ducts. Results of the parametric studies using the advanced nonlinear propagation model reliably show all the effects of nonlinear distortion of the shock waves, variation in intake geometry, flow speeds, and variations in the acoustic liner absorption as a consequence of changes in boundary-layer thickness. Comparisons made against measured data, from model-scale fan rig tests conducted by Rolls-Royce PLC, show good and reasonable agreement. The advanced nonlinear propagation model achieves improved prediction capability for supersonic fan noise.

Contents

Declaration of Authorship xxi

Acknowledgements xxiii

Abbreviations xxv

1 Introduction 1
- 1.1 Aircraft Noise . . . 1
  - 1.1.1 Aircraft Noise Sources . . . 2
    - 1.1.1.1 Engine Noise . . . 2
    - 1.1.1.2 Airframe Noise . . . 4
  - 1.1.2 Aircraft Noise Prediction . . . 4
- 1.2 Research objectives and original contributions . . . 5
- 1.3 Project and Report Overview . . . 7

2 Supersonic Fan Noise 9
- 2.1 'Buzz-saw' Noise . . . 9
  - 2.1.1 Source and Mechanism of Generation . . . 10
  - 2.1.2 Propagation and Interaction of Supersonic Fan Tones . . . 15
  - 2.1.3 Buzz Tones Peculiarities and Complexities in Propagation . . . 17
- 2.2 Summary . . . 20

3 Theories and Models for Buzz-saw Noise Prediction 21
- 3.1 Duct Acoustics . . . 21
  - 3.1.1 Waves in Ducts with Rigid Walls . . . 21
    - 3.1.1.1 Cylindrical Duct with No Flow . . . 22
    - 3.1.1.2 Cylindrical Duct with Uniform Flow . . . 24
    - 3.1.1.3 Annular Duct . . . 25
  - 3.1.2 Waves in Ducts with Lined Walls . . . 27
    - 3.1.2.1 Lined Cylindrical Duct . . . 27
    - 3.1.2.2 Lined Annular Duct . . . 28
- 3.2 Nonlinear Propagation . . . 29
  - 3.2.1 Analytical and Numerical Models . . . 34
    - 3.2.1.1 Analytical Models and Benchmarks . . . 34
- 3.3 Summary . . . 38

4 Source Sawtooth Pressure Waveform Modelling 39
- 4.1 Background . . . 39

4.1.1 Waveform Phase Investigations . . . 44
4.2 Generating Waveforms that match the measured data at the start position 47
4.2.1 Extrapolation Method . . . 48
4.2.2 Optimization Method . . . 52
4.2.2.1 Scaling Method . . . 55
4.3 Applying the Methods to Spectrum from Smooth Sawtooth Waveforms . 57
4.4 Discussions . . . 59
4.4.1 Methods, Results and Comparisons . . . 59
4.4.2 Predictions against measurement . . . 60
4.5 Summary . . . 61

5 Nonlinear Propagation of Buzz-saw Noise 63
5.1 Modes in a Duct . . . 63
5.1.1 Duct-Code Validation . . . 63
5.2 1D Nonlinear Wave Propagation . . . 67
5.2.1 Sawtooth Profiles . . . 67
5.3 Propagation Code Validation . . . 68
5.3.1 Comparisons with measured data . . . 71
5.4 Summary . . . 72

6 Time-Frequency Domain Supersonic Fan Noise Propagation 75
6.1 Background . . . 75
6.2 The Propagation Model . . . 76
6.2.1 Nonlinear Distortion in the Time Domain . . . 76
6.2.1.1 The Grid . . . 76
6.2.1.2 Nonlinear Propagation . . . 77
6.2.2 Absorption in the Frequency Domain . . . 82
6.2.3 Model Overview . . . 82
6.3 Results and Validations . . . 83
6.3.1 Convergence Studies and Comparison with Benchmarks . . . 83
6.3.1.1 Grid Resolution and First-phase testing . . . 84
6.3.1.2 Evaluating Propagation Distance before Application of Absorption . . . 86
6.3.2 Validation of Nonlinear Propagation . . . 89
6.3.3 Simulation Results . . . 89
6.4 Summary . . . 91

7 Validation of Aircraft Intakes Time-Frequency Domain Nonlinear Propagation Code 95
7.1 Information on measured data . . . 95
7.2 Waveform near the fan . . . 96
7.2.1 Measured against averaged-centred sawtooth . . . 97
7.2.1.1 Making use of frequency spectrum of measured data . . . 98
7.2.1.2 Correction for variations over each revolution . . . 99
7.2.1.3 Measurements in Rigid Duct . . . 100
7.2.1.4 Measurements in Lined Duct . . . 100
7.2.2 Spatial representation of measured data . . . 100
7.3 Comparisons: Measurement against prediction . . . 104

7.3.1 Rigid Duct-wall Configuration . . . 105
7.3.2 Lined Duct-wall Configuration . . . 107
7.4 Comparisons against FDNS . . . 115
7.5 Summary . . . 115

8 Radiation of Supersonic Fan Noise from Aircraft Intakes 119
8.1 Far-Field Radiation . . . 119
8.1.1 Principal angle of radiation . . . 120
8.2 Radiation Model . . . 123
8.2.1 Using in-duct pressure with unit amplitude directivity . . . 128
8.3 Far-field measurements . . . 128
8.4 Radiation results and comparisons . . . 131
8.4.1 Radiation from rigid intake duct . . . 135
8.4.2 Radiation from lined intake duct . . . 139
8.4.2.1 Incoherent sum of higher radial orders . . . 140
8.4.2.2 Inclusion of almost cut on radial orders . . . 146
8.5 Geometry and flow effects on radiation . . . 150
8.6 Summary . . . 152

9 Development of Irregular Sawtooth Propagation Equations for Axisymmetric Ducts with Axially Non-uniform flows 159
9.1 Analytical equations for propagation in axisymmetric rigid ducts . . . 159
9.1.1 Basic derivation for regular sawtooth propagation in a rigid duct . 160
9.1.2 Propagation of a regular sawtooth in a rigid duct with varying duct geometry . . . 162
9.1.3 Propagation of irregular sawtooth in a rigid duct . . . 163
9.1.4 Propagation of irregular sawtooth in a rigid duct with varying duct radius . . . 165
9.2 Analytical equations for propagation in axisymmetric lined ducts . . . 167
9.2.1 Propagation of regular sawtooth in a lined duct . . . 167
9.2.2 Propagation of regular sawtooth in a lined duct with varying geometry . . . 167
9.2.3 A Note on Analytical Equations and Acoustic Liners . . . 168
9.3 Summary . . . 168

10 Axisymmetric Ducts with Varying Radius and Effects of Nonlinear Propagation 169
10.1 Duct Geometry . . . 169
10.2 Real Flows and the Boundary Layer . . . 171
10.2.1 Nozzle flow approximation . . . 171
10.2.2 Non-uniform flow . . . 172
10.3 Acoustic Liner . . . 173
10.4 Geometry effects . . . 173
10.4.1 Converging ducts . . . 174
10.4.2 Diverging ducts . . . 177
10.4.3 A Note on Converging and Diverging Ducts . . . 180
10.4.4 Converging-Diverging and Diverging-Converging Ducts . . . 180
10.5 Propagation effects . . . 184

10.5.1 Significance of Geometry and Flow effects . . . 184
10.5.1.1 Time of Flight and Equivalent Cylindrical Ducts . . . 185
10.5.2 Rigid duct with varying radius and its equivalent cylindrical duct . 185
10.5.3 Lined duct with varying radius and its equivalent cylindrical duct 187
10.6 Summary . . . 189

11 Advanced Supersonic Fan Noise Model 191
11.1 Overview of the Advanced Model . . . 191
11.2 Axisymmetric Ducts . . . 192
11.3 Intake flow simulation . . . 193
11.3.1 Acoustic Liner effects . . . 198
11.4 Results from Advanced Model . . . 201
11.4.1 Results for rigid wall ducts . . . 202
11.4.2 Results for lined wall ducts . . . 204
11.4.2.1 Lined cylindrical duct . . . 204
11.4.2.2 Lined FTG duct . . . 207
11.4.2.3 Lined STG duct . . . 209
11.4.3 Comparison of results: IR1 versus IR2 . . . 211
11.4.4 Results in the flow speed-up region . . . 219
11.5 Axial variation of liner absorption . . . 221
11.6 Comparison with measurements . . . 223
11.6.1 Comparison against Rigid wall measurements . . . 224
11.6.2 Comparison against Lined wall measurements . . . 225
11.7 Summary . . . 227

12 Conclusions 229

A Flow chart: Combined Time-Frequency Domain Model 235

B Experimental Measurements at axial stations 239

C Duct wall pressure plots 243

References 249

List of Figures

1.1 Helical path: shock propagation in a cylindrical duct . . . 3

2.1 Shock and Expansion waves at supersonic fan blade tips . . . 11

3.1 Cylindrical duct . . . 22
3.2 Cross section of an annular duct . . . 25
3.3 Acoustically lined annular duct . . . 27
3.4 An illustration of shock amplitude attenuation . . . 31
3.5 For large T values, attenuation becomes independent of initial shock strength . . . 32
3.6 An illustration of two shocks merging . . . 33

4.1 Regular sawtooth (a)waveform (b) its frequency spectrum and (c) phases angles . . . 41
4.2 Buzzsaw-like sawtooth (a) pressure waveform (b) its frequency spectrum and (c) phases angles . . . 41
4.3 Phase angle order example 1: (a) Pressure waveform (b) its frequency spectrum and (c) phases angles . . . 42
4.4 Phase angle order example 2: (a) Pressure waveform (b) its frequency spectrum and (c) phases angles . . . 42
4.5 Phase angle order example 3: (a) Pressure waveform (b) its frequency spectrum and (c) phases angles . . . 43
4.6 Phase angle order example 4: (a) Pressure waveform (b) its frequency spectrum and (c) phases angles . . . 43
4.7 BPF tone attenuation of measured data against those of 100 waveforms generated from measured data and random phases [Key: * Measured data; — 100 predictions; - - average of predictions] . . . 45
4.8 The resulting sawtooth and spectrum . . . 46
4.9 Attenuation of BPF tone. [Key: * Measured data; — 100 predictions; - - average of predictions] . . . 46
4.10 Plot of extrapolated spectrum against measured spectrum . . . 48
4.11 A section of the pressure profile showing Gibb's phenomenon observed . . . 50
4.12 Flow chart showing the main stages of extrapolation method code . . . 50
4.13 Extrapolation Method: average sawtooth waveform and spectrum, and measured spectrum . . . 51
4.14 Extrapolation method: attenuation of BPF tone [Key: * Measured data; — 100 predictions; - - average of predictions] . . . 52
4.15 Flow chart showing the main stages of optimization method code . . . 53

4.16 Optimization method: Predicted sawtooth waveform and spectrum, and measured spectrum . . . 54
4.17 Optimization method: Attenuation of BPF tone . . . 54
4.18 Flow chart showing the main stages of scaling method code . . . 55
4.19 Scaling Method: Average sawtooth waveform and spectrum, and measured spectrum . . . 56
4.20 Scaling Method: Attenuation of BPF tone . . . 57
4.21 Extrapolation Method: Sawtooth waveform and spectrum comparison for constructed sawtooth and prediction . . . 58
4.22 Optimization Method: Sawtooth waveform and spectrum comparison for constructed sawtooth and prediction . . . 58
4.23 Scaling Method: Sawtooth waveform and spectrum comparison for constructed sawtooth and prediction . . . 59

5.1 (a) Axial wavenumbers for a lined cylindrical duct (b) Axial wavenumbers for a lined annular duct, for case 1 at BPF (1400Hz) for azimuthal mode m = 20 . . . 64
5.2 (a) Axial wavenumbers for a rigid cylindrical duct (b) Axial wavenumbers for a lined annular duct, for case 2 at BPF(2200Hz) for azimuthal mode m = 20 . . . 65
5.3 (a) Axial wavenumbers for a rigid annular duct (b) Axial wavenumbers for a lined annular duct, for case 3 at BPF(2600Hz) for azimuthal mode m = 20 . . . 65
5.4 (a) Axial wavenumbers for a lined cylindrical duct (b) Axial wavenumbers for a lined annular duct, for case 2 at BPF(2200Hz) for azimuthal mode m = 40 . . . 65
5.5 (a) Axial wavenumbers for a rigid annular duct (b) Axial wavenumbers for a lined annular duct, for case 3 at BPF(2200Hz) for azimuthal mode m = 40 . . . 66
5.6 Regular sawtooth profile . . . 67
5.7 Irregular sawtooth profile . . . 68
5.8 Attenuation of BPF tone for regular sawtooth . . . 69
5.9 Initial frequency spectra for irregular sawtooth 1 . . . 69
5.10 Frequency spectra 0.5m away from start point for irregular sawtooth 1 . . . 70
5.11 Frequency spectra 1m away from start point for irregular sawtooth 1 . . . 70
5.12 Illustration of the AneCom modular fan rig: measurement locations and lined region . . . 71
5.13 Prediction against measurement at (a) fan-case (b) axial distance 0.1m [Note: Prediction is the average of 100 simulations and calculating the mean value of the SPL] . . . 72
5.14 Prediction against measurement at (a) axial distance 0.12m (b) axial distance 0.15m [Note: Prediction is the average of 100 simulations and calculating the mean value of the SPL] . . . 73
5.15 Prediction against measurement at (a) axial distance 0.19m (b) axial distance 0.25m [Note: Prediction is the average of 100 simulations and calculating the mean value of the SPL] . . . 73

6.1 Illustration of the one dimensional finite difference grid . . . 77
6.2 Helical path of waveform along the intake duct axial direction . . . 78

6.3 Resampling of points on waveform back to the base grid 80
6.4 Illustration of the reduction in amplitude due to resampling waveform back to the grid 80
6.5 Resolution of a multivalued part of the waveform 81
6.6 The main steps in the nonlinear distortion process 81
6.7 Illustration of the main elements in the model 83
6.8 Percentage error for propagation of regular sawtooth in rigid duct for various grid resolutions compared to analytical results 85
6.9 Relative percentage error (on logarithm scale) for propagation of regular sawtooth in rigid duct for various grid resolutions compared to analytical results 86
6.10 Shock amplitude attenuation for FFT and IFFT performed at various intervals for rigid intake duct 87
6.11 Sound level attenuation for FFT and IFFT performed at various intervals for a rigid intake duct 87
6.12 Shock amplitude attenuation for FFT and IFFT performed at various intervals with constant absorption in a lined duct compared to analytical results 88
6.13 Sound level attenuation for FFT and IFFT performed at various intervals with constant absorption in a lined duct compared to analytical results . . 89
6.14 Comparison between results of Benchmark SPRID and the NP-SWIND model at $z = 0.5D$ 90
6.15 Pressure waveform and its frequency spectrum at the start of propagation $z = 0$ 91
6.16 Waviness of expansion waves commences as acoustic liner absorption is being applied 91
6.17 Pressure waveform and its frequency spectrum at $z = 0.1D$ using absorption k_{z_i} only 92
6.18 Pressure waveform and its frequency spectrum at $z = 0.2D$ using absorption k_{z_i} only [- - - line indicates the minimum of the vertical scale of the figure showing spectrum at $z = 0$] 92
6.19 Pressure waveform and its frequency spectrum at $z = 0.3D$ using absorption k_{z_i} only [- - - line indicates the minimum of the vertical scale of the figure showing spectrum at $z = 0$] 93
6.20 Pressure waveform and its frequency spectrum at $z = 0.1D$ using whole axial wavenumber; absorption and K_{z_i} and phase K_{z_r} 93
6.21 Pressure waveform and its frequency spectrum at $z = 0.2D$ using whole axial wavenumber; absorption and K_{z_i} and phase K_{z_r} [- - - line indicates the minimum of the vertical scale of the figure showing spectrum at $z = 0$] 94

7.1 Illustration of the model-scale fan rig and measurement stations 96
7.2 Measurement near the fan at distance $0.05r_d$ 97
7.3 Comparison of measurement and idealized sawtooth at distance $0.05r_d$ . . 98
7.4 Spatial representation of measurement (a) near the fan (b) at $0.35r_d$ (c) at $0.483r_d$ (d) at $0.616r_d$ (e) at $0.75r_d$ [Note: pressure P normalized by measured ambient pressure P_M] 101
7.5 Spatial representation of measurement (a) near the fan at distance $0.05r_d$ (b) at $0.35r_d$ (c) at $0.483r_d$ (d) at $0.616r_d$ (e) at $0.75r_d$ [Note: pressure P normalized by measured ambient pressure P_M] 103

7.6 Waviness of the expansion waves for the lined duct . . . 104
7.7 Measurement against prediction: Fan case station . . . 105
7.8 Measurement against prediction: axial station 1 . . . 106
7.9 Measurement against prediction: axial station 4 . . . 107
7.10 Measurement against prediction: axial station 7 . . . 108
7.11 Measurement against prediction: axial station 10 . . . 108
7.12 Measurement (*) against prediction (—) in rigid-wall intake: BPF harmonics attenuation (a) BPF (b) 2BPF (c) 3BPF (d) 4BPF . . . 109
7.13 Liner decay rates . . . 109
7.14 Measurement against prediction: axial station 1 . . . 111
7.15 Measurement against prediction: axial station 1 . . . 111
7.16 Measurement against prediction: axial station 4 . . . 112
7.17 Measurement against prediction: axial station 7 . . . 113
7.18 Measurement against prediction: axial station 10 . . . 113
7.19 Measurement (*) against prediction (—) in lined-wall intake: BPF harmonics attenuation (a) BPF (b) 2BPF (c) 3BPF (d) 4BPF . . . 114
7.20 Measurement (*) against prediction (—) for both rigid and lined-wall intake: BPF tone attenuation . . . 114
7.21 FDNS results against prediction: initial source waveform . . . 115
7.22 FDNS results against prediction for rigid walled duct at distance 0.5m . . . 116
7.23 FDNS results against prediction for lined walled duct at distance 0.5m . . . 116

8.1 Intake duct approximation for radiation . . . 120
8.2 Effect of external flow on radiation angle . . . 122
8.3 Unit amplitude far-field directivities for EO 20 (—) and E0 40 (- -) . . . 129
8.4 Unit amplitude far-field directivities for EO 60 (—) and E0 80 (- -) . . . 129
8.5 Measured far-field directivity at 70, 80 and 90 % engine operation: rigid duct (a) BPF (b) 2BPF (c) 3BPF (d) 4BPF . . . 130
8.6 Measured SPL-EO spectrum at 70, 80 and 90 % engine operation for a rigid duct at polar angle (a) 30^o (b) 60^o . . . 131
8.7 Measured SPL-EO spectrum at 70, 80 and 90 % engine operation for a rigid duct at polar angle (a) 90^o (b) 120^o . . . 132
8.8 Measured far-field directivity at 70, 80 and 90 % engine operation: lined duct (a) BPF (b) 2BPF (c) 3BPF (d) 4BPF . . . 132
8.9 Measured SPL-EO spectrum at 70, 80 and 90 % engine operation for a lined duct at polar angle (a) 30^o (b) 60^o . . . 133
8.10 Measured SPL-EO spectrum at 70, 80 and 90 % engine operation for a lined duct at polar angle (a) 90^o (b) 120^o . . . 133
8.11 Rigid against lined measured directivities at 90% engine operation (a) BPF (b) 2BPF (c) 3BPF (d) 4BPF . . . 134
8.12 Rigid against lined measured SPL-EO spectrum at 90% engine operation for polar angle (a) 30^o (b) 60^o . . . 134
8.13 Rigid against lined measured SPL-EO spectrum at 90% engine operation for polar angle (a) 90^o (b) 120^o . . . 135
8.14 Far-field directivity: measurements against prediction: rigid duct (a) BPF (b) 2BPF (c) 3BPF (d) 4BPF . . . 136
8.15 Measured against predicted SPL-EO spectrum for rigid intake duct at polar angle (a) 30^o (b) 60^o . . . 137

8.16 Measured against predicted SPL-EO spectrum for rigid intake duct at polar angle (a) 90^o (b) 120^o . . . 137
8.17 Measured against predicted SPL-EO spectrum for rigid intake duct at polar angle (a) 55^o (b) 75^o . . . 138
8.18 Far-field directivity: measurements against predictions: lined duct (a) BPF (b) 2BPF (c) 3BPF (d) 4BPF . . . 138
8.19 Measured against predicted SPL-EO spectrum for lined intake duct at polar angle (a) 30^o (b) 60^o . . . 139
8.20 Measured against predicted SPL-EO spectrum for lined intake duct at polar angle (a) 90^o (b) 120^o. [NOTE: the green line marks the lower limit of the vertical axis in previous plots] . . . 140
8.21 Measured against predicted SPL-EO spectrum for lined intake duct at polar angle (a) 55^o (b) 75^o . . . 141
8.22 Unit amplitude directivities (a) EO 37 (b) EO 38 (c) EO 39 (d) 2BPF . . 141
8.23 Unit amplitude directivities (a) EO 67 (b) EO 68 (c) EO 69 (d) EO 70 . . 142
8.24 Measurement against prediction (a) EO 37 rigid (a) EO 37 lined (a) EO 67 rigid (a) EO 67 lined . . . 144
8.25 Far-field directivities of measurements against predictions: rigid duct (a) BPF (b) 2BPF (c) 3BPF (d) 4BPF [Prediction: single radial order; Prediction(Mod): all cut-on radial orders assuming equal power per mode] . . 146
8.26 Measured against predicted (with all cut-on radial orders) SPL-EO spectrum for rigid intake duct at polar angle (a) 30^o (b) 60^o [Error bars show the range of prediction for variation of power among all cut-on radial orders] 147
8.27 Measured against predicted (with all cut-on radial orders) SPL-EO spectrum for rigid intake duct at polar angle (a) 90^o (b) 120^o [Error bars show the range of prediction for variation of power among all cut-on radial orders] 148
8.28 Measured against predicted (with all cut-on radial orders) SPL-EO spectrum for rigid intake duct at polar angle (a) 55^o (b) 75^o [Error bars show the range of prediction for variation of power among all cut-on radial orders] 149
8.29 Far-field directivities of measurements against predictions: lined duct (a) BPF (b) 2BPF (c) 3BPF (d) 4BPF [Prediction: single radial order; Prediction(Mod): all cut-on radial orders assuming equal power per mode] . . 150
8.30 Measured against predicted (with all cut-on radial orders) SPL-EO spectrum for lined intake duct at polar angle (a) 30^o (b) 60^o [Error bars show the range of prediction for variation of power among all cut-on radial orders] 151
8.31 Measured against predicted (with all cut-on radial orders) SPL-EO spectrum for lined intake duct at polar angle (a) 90^o (b) 120^o [Error bars show the range of prediction for variation of power among all cut-on radial orders] 152
8.32 Far-field directivities with all cut-on radial orders: measurements against prediction(*): rigid duct (a) BPF (b) 2BPF (c) 3BPF (d) 4BPF [Prediction: single radial order. Prediction(*): prediction using pressure amplitudes from measured data with predicted unit amplitude directivities.] . . 153
8.33 Measured against prediction(*) SPL-EO spectrum for rigid intake duct at polar angle (a) 30^o (b) 60^o [Prediction: single radial order. Prediction(*): prediction using pressure amplitudes from measured data with predicted unit amplitude directivities.] . . . 153

8.34 Measured against prediction(*) SPL-EO spectrum for rigid intake duct at polar angle (a) 90^o (b) 120^o [Prediction: single radial order. Prediction(*): prediction using pressure amplitudes from measured data with predicted unit amplitude directivities.] . . . 154
8.35 Measured against prediction(*) SPL-EO spectrum for rigid intake duct at polar angle (a) 55^o (b) 75^o [Prediction: single radial order. Prediction(*): prediction using pressure amplitudes from measured data with predicted unit amplitude directivities.] . . . 154
8.36 Far-field directivities with all cut-on radial orders: measurements against prediction(*): lined duct (a) BPF (b)2BPF (c) 3BPF (d) 4BPF [Prediction: single radial order. Prediction(*): prediction using pressure amplitudes from measured data with predicted unit amplitude directivities.] . . 155
8.37 Measured against prediction(*) SPL-EO spectrum for lined intake duct at polar angle (a) 30^o (b) 60^o [Prediction: single radial order. Prediction(*): prediction using pressure amplitudes from measured data with predicted unit amplitude directivities.] . . . 155
8.38 Measured against prediction(*) SPL-EO spectrum for lined intake duct at polar angle (a) 90^o (b) 120^o [Prediction: single radial order. Prediction(*): prediction using pressure amplitudes from measured data with predicted unit amplitude directivities. NOTE: the green line marks the lower limit of the vertical axis in previous plots] . . . 156
8.39 Measured against prediction(*) SPL-EO spectrum for lined intake duct at polar angle (a) 55^o (b) 75^o [Prediction: single radial order. Prediction(*): prediction using pressure amplitudes from measured data with predicted unit amplitude directivities.] . . . 156
8.40 Illustration of flow in and around (a) cylindrical duct (b) Axisymmetric duct . . . 157

9.1 Distortion of waveform . . . 161
9.2 Resolution of waveform by removal of distorted multi-valued regions . . . 162
9.3 Illustration for upper half of a single shock wave . . . 163
9.4 Illustration for lower half of a single shock wave . . . 163
9.5 Illustration of converging duct using nozzle analogy . . . 165

10.1 Ducts with varying cross-section: (a) Cylindrical (b) Converging (c) Diverging (d) Converging-Diverging (e) Diverging-Converging . . . 170
10.2 Nozzle flow . . . 172
10.3 Variation of duct radius compared to constant area duct . . . 174
10.4 Difference in attenuation of rigid converging duct compared to rigid constant area duct . . . 175
10.5 Axial Mach number for the converging ducts . . . 175
10.6 Time of flight for various converging ducts . . . 176
10.7 Cylindrical duct with variations in BPF tone attenuation . . . 177
10.8 Difference in BPF tone attenuation of lined converging duct compared to lined constant area duct . . . 177
10.9 Difference in attenuation of the BPF tone for lined converging ducts with variations in throat contraction compared to a rigid constant area duct . . . 178
10.10Difference in BPF tone attenuation of diverging duct compared to constant area duct . . . 178

10.11Time of flight for various diverging ducts . . . 178
10.12Mach number variations for various diverging ducts . . . 179
10.13Difference in BPF tone attenuation of lined diverging duct compared to lined constant area duct . . . 179
10.14Converging-diverging ducts (a) radius variation (b) time of flight variation 180
10.15Mach number variations for various converging-diverging ducts . . . 180
10.16Regular sawtooth BPF tone attenuation in a rigid Converging-Diverging ducts with variations in throat contraction . . . 181
10.17Regular sawtooth BPF tone attenuation in a lined Converging-Diverging ducts with variations in throat contraction . . . 182
10.18Diverging-converging ducts (a) radius variation (b) time of flight variation 182
10.19Mach number variations for various diverging ducts . . . 183
10.20Regular sawtooth BPF tone attenuation in a rigid Diverging-Converging ducts with variations in throat contraction . . . 183
10.21Regular sawtooth BPF tone attenuation in a lined Converging ducts with variations in throat contraction . . . 184
10.22Equivalent cylindrical duct for (a) converging ducts (b) diverging ducts . 185
10.23Trend line for equivalent length of cylindrical duct for converging ducts . 185
10.24Evaluating the time of flight over small axial steps dz . . . 186
10.25Equivalent cylindrical duct for (a) converging ducts (b) diverging ducts . 187
10.26Trend line for equivalent length of cylindrical duct for converging ducts . 188
10.27Equivalent cylindrical duct (- - -) for converging ducts (——) . . . 188
10.28Equivalent cylindrical duct (- - -) for diverging ducts (——) . . . 188
10.29Equivalent cylindrical duct (- - -) for converging-diverging ducts (——) . . 189
10.30Equivalent cylindrical duct (- - -) for diverging-converging ducts (——) . . 189

11.1 Illustration of structure of the advanced supersonic fan noise model . . . 192
11.2 Static-test and flight-test Intakes Ducts . . . 193
11.3 Flow simulation for an axisymmetric flight test duct: compressible flow domain . . . 194
11.4 Flow simulation mesh for FTG . . . 195
11.5 Flow simulation mesh for FTG: intake region . . . 195
11.6 Flow simulation mesh for FTG: duct lip elements . . . 196
11.7 Mean flow in FTG duct . . . 196
11.8 Mean flow in FTG: intake region . . . 197
11.9 Mean flow distribution in STG: intake region [not to scale] . . . 197
11.10Static-test and flight-test Intakes Ducts . . . 198
11.11Acoustic liner optimized to attenuate BPF (EO20) tone . . . 200
11.12Acoustic liner optimized to attenuate half-BPF (EO10) tone . . . 200
11.13Acoustic liner optimized to attenuate BPF (EO20) tone absorption for different boundary layer thicknesses . . . 201
11.14Comparisons of regular sawtooth BPF tone attenuation in rigid wall ducts 202
11.15Comparisons of IR1 BPF tone attenuation in rigid wall ducts . . . 203
11.16Comparisons of IR2 BPF tone attenuation in rigid wall ducts . . . 203
11.17IR1 BPF tone attenuation in lined wall cylindrical duct: BPF-optimized liner . . . 204
11.18IR1 BPF tone attenuation in lined wall cylindrical duct: half-BPF optimized liner . . . 205

11.19IR2 BPF tone attenuation in lined wall cylindrical duct: BPF-optimized liner . . . 205
11.20IR2 BPF tone attenuation in lined wall cylindrical duct: half-BPF optimized liner . . . 206
11.21IR1 BPF tone attenuation in lined wall FTG: BPF-optimized liner . . . 206
11.22IR2 BPF tone attenuation in lined wall FTG: BPF-optimized liner . . . 207
11.23IR1 BPF tone attenuation in lined wall FTG: half-BPF-optimized liner . 208
11.24IR2 BPF tone attenuation in lined wall FTG: half-BPF-optimized liner . 208
11.25IR1 BPF tone attenuation in lined wall STG: BPF-optimized liner . . . 209
11.26IR2 BPF tone attenuation in lined wall STG: BPF-optimized liner . . . 209
11.27IR1 BPF tone attenuation in lined wall STG: half-BPF-optimized liner . . 210
11.28IR2 BPF tone attenuation in lined wall STG: half-BPF-optimized liner . . 210
11.29Initial waveforms (a) IR1 (b) IR2 and initial spectrum (c) IR1 (d) IR2 . . 211
11.30Simulation for rigid wall FTG: station I waveform (a) IR1 (b) IR2 and spectrum (c) IR1 (d) IR2 . . . 212
11.31Simulation for rigid wall FTG: station II waveform (a) IR1 (b) IR2 and spectrum (c) IR1 (d) IR2 . . . 212
11.32Simulation for rigid wall FTG: station III waveform (a) IR1 (b) IR2 and spectrum (c) IR1 (d) IR2 . . . 213
11.33Simulation for lined wall FTG: station I waveform (a) IR1 (b) IR2 and spectrum (c) IR1 (d) IR2 . . . 214
11.34Simulation for lined wall FTG: station II waveform (a) IR1 (b) IR2 and spectrum (c) IR1 (d) IR2 . . . 214
11.35Simulation for lined wall FTG: station III waveform (a) IR1 (b) IR2 and spectrum (c) IR1 (d) IR2 . . . 215
11.36Simulation for rigid wall STG: station I waveform (a) IR1 (b) IR2 and spectrum (c) IR1 (d) IR2 . . . 216
11.37Simulation for rigid wall STG: station II waveform (a) IR1 (b) IR2 and spectrum (c) IR1 (d) IR2 . . . 216
11.38Simulation for rigid wall STG: station III waveform (a) IR1 (b) IR2 and spectrum (c) IR1 (d) IR2 . . . 217
11.39Simulation for lined wall STG: station I waveform (a) IR1 (b) IR2 and spectrum (c) IR1 (d) IR2 . . . 217
11.40Simulation for lined wall STG: station II waveform (a) IR1 (b) IR2 and spectrum (c) IR1 (d) IR2 . . . 218
11.41Simulation for lined wall STG: station III waveform (a) IR1 (b) IR2 and spectrum (c) IR1 (d) IR2 . . . 218
11.42IR1 and IR2 BPF tone attenuation for rigid STG duct . . . 219
11.43IR1 BPF tone attenuation for STG: Lined Duct: BL 0% to 10% of the radius . . . 220
11.44IR2 BPF tone attenuation for STG: Lined Duct: BL 0% to 10% of the radius . . . 220
11.45Simulation for rigid wall FTG at the point of highest flow speed: waveform (a) IR1 (b) IR2 and spectrum (c) IR1 (d) IR2 . . . 221
11.46Simulation for rigid wall FTG at the duct lip: waveform (a) IR1 (b) IR2 and spectrum (c) IR1 (d) IR2 . . . 222

11.47 Acoustic liner decay rates in the FTG for different boundary-layer thicknesses, based on a SDOF cavity liner. Acoustic liner optimized for the BPF tone attenuation . . . 223
11.48 Acoustic liner decay rates in the STG for different boundary-layer thicknesses, based on a SDOF cavity liner. Acoustic liner optimized for the BPF tone attenuation . . . 223
11.49 Rigid Duct: Measurements against prediction . . . 224
11.50 Rigid-wall duct: measurements against prediction at the first axial station 224
11.51 Rigid-wall duct: measured spectrum against prediction at the last axial station . . . 225
11.52 Lined-wall duct: measurements against prediction . . . 225
11.53 Lined-wall duct: measurements against prediction at the first axial station 226
11.54 Lined-wall duct: measured spectrum against prediction at the last axial station . . . 227
11.55 Lined-wall duct: measured spectrum against prediction with liner decay rates of 8% boundary-layer thickness at the last axial station . . . 227

B.1 Rigid-walled intake measurements: (a) near the fan (b) at $0.35r_d$ (c) at $0.483r_d$ (d) at $0.616r_d$ (e) at $0.75r_d$ . . . 240
B.2 Lined-walled intake measurements: (a) near the fan (b) at $0.35r_d$ (c) at $0.483r_d$ (d) at $0.616r_d$ (e) at $0.75r_d$ . . . 241

C.1 Pressure field adjacent to the wall for regular sawtooth propagation in a cylindrical duct (a) side view (b) fan plane . . . 243
C.2 Three-dimensional view of pressure field adjacent to the wall for regular sawtooth propagation in a cylindrical duct . . . 244
C.3 Three-dimensional view of pressure field adjacent to the wall for irregular sawtooth propagation in a rigid cylindrical duct . . . 244
C.4 Pressure field adjacent to the wall for irregular sawtooth propagation in a rigid cylindrical duct: side view . . . 245
C.5 Pressure field adjacent to the wall for irregular sawtooth propagation in a rigid cylindrical duct: fan 2D cascade . . . 245
C.6 Three-dimensional view of pressure field adjacent to the wall for irregular sawtooth propagation in a lined cylindrical duct . . . 246
C.7 Pressure field adjacent to the wall for irregular sawtooth propagation in a lined cylindrical duct: side view . . . 246
C.8 Pressure field adjacent to the wall for irregular sawtooth propagation in a lined cylindrical duct: fan 2D cascade . . . 247

List of Tables

4.1 Sawtooth profiles for phase angle investigations 44

5.1 Engine Properties 64

10.1 Equivalent Cylindrical duct for various converging ducts 186

11.1 Liner parameters for acoustic liner model 199
11.2 Information quantities for propagation at fan plane 202

Declaration of Authorship

I, Oluwaseun Emmanuel Adetifa , declare that the thesis entitled *PREDICTION OF SUPERSONIC FAN NOISE GENERATED BY TURBOFAN AIRCRAFT ENGINES* and the work presented in the thesis are both my own, and have been generated by me as the result of my own original research. I confirm that:

- this work was done wholly or mainly while in candidature for a research degree at this University;
- where any part of this thesis has previously been submitted for a degree or any other qualification at this University or any other institution, this has been clearly stated;
- where I have consulted the published work of others, this is always clearly attributed;
- where I have quoted from the work of others, the source is always given. With the exception of such quotations, this thesis is entirely my own work;
- I have acknowledged all main sources of help;
- where the thesis is based on work done by myself jointly with others, I have made clear exactly what was done by others and what I have contributed myself;
- parts of this work have been published as:

  O.E. Adetifa, A. McAlpine, and G. Gabard. *Modelling the nonlinear sound propagation and radiation of supersonic fan tones*, 20th AIAA/CEAS Aeroacoustics Conference, AIAA 2014-2945, 16 - 20 June 2014.

Signed:.....

Date:.....

Acknowledgements

I sincerely appreciate and acknowledge the Engineering and Physical Science Research Council (EPSRC) and Rolls-Royce PLC who gave me the opportunity to do useful research I had always hoped for by funding my PhD studies through the Dorothy Hodgkin Postgraduate Award (DHPA). My thanks also goes to the Rolls-Royce University Technical Centre, Institute of Sound and Vibrations Research and the University of Southampton for the space and resources, useful training and development and experience through various opportunities and activities.

Through out this project, I received immense support, guidance, sound instructions from my supervisor Dr. Alan McAlpine. Thank you very much. I am also grateful to Dr. Gwenael Gabard for his support, advice and directions throughout the project as well. The encouragement, suggestions and instructions from my supervisors, Dr. McAlpine and Dr. Gabard made sure the success of this project. I gained so much academically and personally during your tutelage and supervision.

My thanks also goes to my parents, Ven. and Mrs. S.P.K. Adetifa for the constant encouragement, prayers and words of advice. Thanks also goes to my Adeyinka for her understanding and support especially in the latter parts of this work. And to all who made life enjoyable and gave encouragement in the Rolls-Royce University Technical Centre, Institute of Sound and Vibrations Research; I am very grateful to you all. The thanksgiving is not complete without expressing my sincere thanks to God Almighty for strength, wisdom and wellbeing to do this work.

Oluwaseun E. Adetifa
July, 2015

Abbreviations

BPF	Blade Passage Frequency
CAA	Computational Aeroacoustics
COMSOL	Commercial Multi-physics software for simulations
CFD	Computational Fluid Dynamics
EO	Engine Order
EPNL	Effective Perceived Noise Level
FDNS	Frequency Domain Numerical Simulation Model
FFT	Fast Fourier Transform
FTG	Flight Test Geometry
GX-Munt	Code for Radiation from Semi-infinite Ducts (based on Weiner-Hopf Technique)
IFFT	Inverse Fast Fourier Transform
ISVR	Institute of Sound and Vibration Research University of Southampton
FORTRAN	Commercial Software for Numerical calculations
HBR	High bypass ratio
MATLAB	Commercial Software for Numerical calculations and Simulations
NP-SWIND	Nonlinear Propagation of Sawtooth Waveform in INtake Ducts (Time-Frequency Domain Model)
STG	Static-Test Geometry
SPL	Sound Pressure Level
SPRID	Sawtooth Propagation in Rigid Intake Ducts

Chapter 1

Introduction

The development of robust noise prediction models for noise generated by high-bypass-ratio turbofan aircraft engines is important in the efforts to reduce noise emisssions associated with the civil aviation and meeting set targets for aircraft noise reduction [1]. Increased awareness of the negative impact of aviation noise has led, over the years, to increased control and careful regulation of the civil aerospace sector, with stringent rules and procedures set for aircraft and aircraft engine manufacturers [1], and airline operators [2, 3].

Introduction of the high-bypass-ratio (HBR) turbofan aircraft engine to civil aviation brought about significant reduction in the noise emitted by aircraft engines as a result of the reduction of jet noise produced by these engines [4, 5]. However, a high-bypass-ratio turbofan engine generally incorporates a larger fan for the initial low pressure compression stage making the noise generated by the fan a major noise source [4–6]. The significance of the noise produced by the fan of a high-bypass-ratio turbofan engine is even more pronounced when the tip of the fan rotates at supersonic speed while the engine operates at high power at sideline (aircraft take-off) conditions. At supersonic fan tip speeds, the fan produces high amplitudes tones (multiple-pure-tones or 'buzz-saw' noise) which occur at integer multiples of the frequency of the rotating shaft of the engine. Therefore, in order to meet stringent noise regulations set in certification procedures [2, 3], and to reduce the buzz-saw noise, reliable prediction models can be very useful tool to determine the contribution of buzz-saw noise on the overall Effective Perceived Noise Level (EPNL) for different aircraft engines.

1.1 Aircraft Noise

Significant progress in the analysis of aircraft noise followed the work on aerodynamically generated sound by Sir James Lighthill in 1952 [7]. A major step reduction in aircraft

effective perceived noise was achieved by the change from turbojet to high-bypass-ratio (HBR) turbofan engines and installation of acoustic treatment[4]. Various levels of reduction in overall aircraft noise have since been achieved from the 1980s to date.

Noise is generated from a number of sources on and around an aircraft, and the noise levels vary with flight and operation conditions. The noise sources are influenced by environmental conditions that are, to a large extent, uncontrollable and unpredictable, and are directly traceable to interaction of air with various parts of the aircraft body (the airframe) and the aircraft engine. Interactions of air flow with the discontinuities in the structure of the aircraft, and the operation of the aircraft engine, generates pressure fluctuations that propagate to an observer within the aircraft cabin or on the ground [6, 8]. The overall noise produced and perceived is generally referred to as aircraft noise.

1.1.1 Aircraft Noise Sources

It is common to classify aircraft noise sources into two categories; namely, airframe noise and engine noise. These are briefly discussed.

1.1.1.1 Engine Noise

The interaction of rotating blades of the fan of an aircraft engine with air flow generates fan noise. Fan noise is not limited to this case as it also involves the noise produced by interactions of fans and stator vanes, blades of counter rotating fans and the non-uniform flow [4]. Fan noise is particularly prominent at some engine operation conditions, notably, when the relative speed of the rotating fan and the approaching flow becomes supersonic and shock waves are formed. The noise generated by this interaction propagates away from the fan through the oncoming flow in a helical path (illustration in figure 1.1). Perceived noise at these supersonic fan-tip speeds is mainly tonal 'buzz-saw' noise (also referred to as multiple-pure-tones (MPT) or combination tone noise), and is generated at harmonics of the frequency of the rotating shaft to which the fan is coupled [4, 9–11].

When fan-tip speeds are subsonic, some of fan tones produced are found to decay rapidly during transmission for a fan in a duct. These tones are generally a result of the interaction between the fan of the aircraft engine and the stator or guide vanes that are installed to direct the flow. They are referred to accordingly as rotor-stator interaction tones. At the leading edge of the fan, the interaction of atmospheric turbulence, flow distortions[4, 9, 10] and, in ducted fans, duct boundary layer turbulence are noise (mainly broadband) sources. Whilst for the trailing edge, there is interaction between the rotor blades' turbulent wakes and other downstream structures causing noise generation[6].

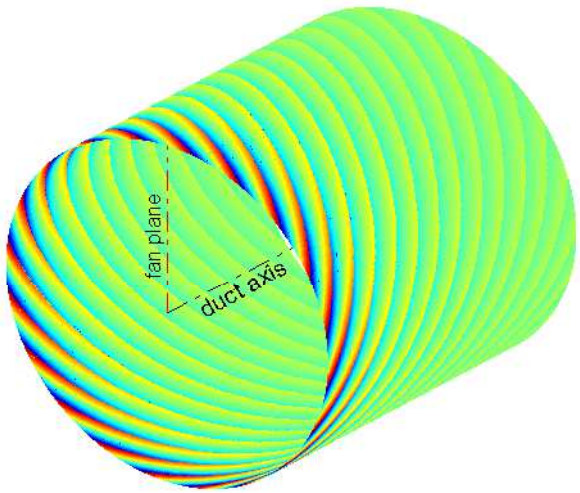

Figure 1.1: Helical path: shock propagation in a cylindrical duct

Fan single-frequency tones were classified in reference[5] as a direct consequence of changes in blade motion relative to an observer (loading noise), effects of supersonic blade tip speeds, a combination of non-uniform flow and periodic unsteady loadings on blades, blade-wake interaction with other structures, and effects of flow displacement as blades cut through air flow to produce pulses relative to an observer (thickness noise). The broadband content is present as a result of random pressure fluctuations over a range of frequencies due to the blade wakes, turbulent flow in the approach stream and turbulence in the boundary layers.

Jet noise is produced by the exhaust gas jet of an aircraft engine as the intense release of the exhaust into the surrounding air behind the aircraft engine induces high levels of turbulence. In HBR engines, this complex process involves the exhaust jet from the combustion within the core of the engine, and the exhaust from the bypass duct around the core of the engine. These two exhaust flows are most times at different speeds. The interaction of these high speed exhaust flows and their mixing with atmospheric air is responsible for the production of the noise . The greater the bypass flow, the lesser the jet exhaust and, consequently, lesser noise is produced by their interaction/mixing and vice versa [5, 6, 12]. Jet noise scales with exhaust jet velocity [7].

The noise generated at the combustion stage of an operating aircraft engine is linked to various processes; injection of fuel, mixing of fuel and air, burning of the fuel, and mixing of the combustion gases and air. The turbulence levels required to achieve the mixing processes in a very short time span are very high. Due to the turbulence of the

mixing, noise is generated and propagated through to the turbine and finally out from the exhaust nozzles[4, 5]. It is not easy to trace the direct source of combustion noise but identified sources include turbulent mixing of combustion elements, high temperature of the combustion, and the interaction of fluctuations in combustion gas temperature with components downstream of the combustion chamber[5].

Compressor noise is similar to the fan noise and the characteristics are alike. There are two components of the noise: tonal and broadband components. The broadband components are due to flow turbulence generating pressure fluctuations at the blade, the propagation of this away from the blade in the form of wakes, and the subsequent interaction of the wakes with other structures (especially the stator vanes) in the core of the aircraft engine. The compressor has several rotating and stationary stages through which the flow passes[6]. This is the same for turbine noise. The tonal component of the compressor noise is mainly related to the disturbance to the flow by the rotating elements of the compression stage. The production of tones in this stage of the aircraft engine is very complex owing to the multistage arrangement of the combination of the compressor rotors and stators. The interaction of the wake and the field of pressure within the separation between the rotating and stationary elements is the key source of tones especially in the subsonic phase[5]. The smaller the separation of the compression phases, the stronger the tones expected.

1.1.1.2 Airframe Noise

Airframe noise is the noise generated by the components of an aircraft that are not directly involved in the propulsion of the aircraft. These include the high lift devices, fuselage, landing gear, wings, flaps and slats, and other stationary or movable surfaces. The airframe noise forms a particularly significant part of the overall perceived noise during the landing approach of an aircraft because it is during this time that the landing gear and high-lift devices are deployed [5]. The airframe also generates noise at significant levels during the take off of an aircraft the same way it does while the aircraft is in its landing phase [5, 8], though there is the possibility of different levels of noise generated during these flight phases as environmental conditions and flight speed play a large part in the generation of noise by the airframe. These airframe noise sources produce noise in a number of ways and through particular interactions. The action of air flow on the components of the landing gear gives rise to a complex multi-scale vortex [4] due to the unsteady force due to the airflow applied directly on these components.

1.1.2 Aircraft Noise Prediction

The complexity of aircraft noise can not be overemphasized as the aircraft operates in different atmospheric and operation conditions. Owing to the varied sources of noise and

mechanisms of production, and the costs of model or full-scale tests and experiments, aircraft noise prediction models are highly useful to aircraft and aircraft engine manufacturers. These are developed to identify noise sources, and to determine expected levels of noise from these sources by modeling the mechanisms of noise generation. Prediction models range from simple to complex, part to full-scale simulations, analytic or semi-analytical (that are sometimes based on previous experiments, measurements and observations) to exclusive numerical models [13–15].

Noise prediction is particularly useful in the aircraft engine design phase and can be used to judge various noise reduction strategies; tip-speeds reduction, reduction of load on each blade by increase in the number of blades, change in the geometry and arrangement of fan blades, levels of irritation of 'reduced' noise to an observer, blade row variation for control of blade-wake interaction, control of acoustic energy by pushing tones out of the audible range[5, 15], generation of 'cut-off' (non-propagating) modes, acoustic liner effects (in the intake ducts and bypass ducts) and frequency targeted noise attenuation, exhaust nozzle chevrons performance among others [15]. These have also been useful for the determination of aerodynamic properties and interactions of an aircraft airframe, landing gear and have led to some novel designs and configurations[16].

1.2 Research objectives and original contributions

In this project, the focus has been on developing and validating methods for the prediction of the noise generated at supersonic fan tip rotation speeds by the ducted fan in a high-bypass-ratio turbofan engine. The aims of the project were to:
(a) Develop a new nonlinear propagation model for more realistic mean flows and use analytical or numerical methods to generate a suitable radiation model.
(b) Couple together both models (propagation and radiation) in order to develop a more holistic prediction methodology for supersonic fan noise.
(c) Validate the new prediction methods using rig or engine test data provided by Rolls-Royce plc.
The underlying challenge in the project was the complexity of the prediction of supersonic fan noise due to the complexity of modelling the nonlinear acoustic propagation, as well as modelling sound absorption by acoustic liners, modelling a complete fan blade set, calculations at high frequencies, and, modelling more realistic mean flows.

Prior to the commencement of this project, analytic models for the nonlinear propagation of regular sawtooth waveforms in rigid and lined cylindrical intakes have be presented in the works of McAlpine *et al*[17, 18], which further developed original work by Morfey and Fisher [19, 20]. Also, a simulation method forthe nonlinear propagation of 'buzz-saw' noise in the frequency domain, referred to as Frequency Domain Nonlinear Simulation (FDNS), has been presented by McAlpine[18, 21] and validated [21]. In accordance with

the key aims of this project, various improvements to the prediction capability connected to the nonlinear propagation and radiation of 'buzz-saw' noise have been carried out.

The key achievements and original contributions of this thesis are

I Development of new codes for time-domain shock-tracking methods. These methods simulate the propagation of a one-dimensional sawtooth pressure waveform. This is representative of the rotor-locked pressure field generated by a supersonic ducted fan. This type of time-domain approach can be used to predict supersonic fan tone noise levels at axial stations along the intake duct wall, for an idealized cylindrical rigid intake.

II Time-Frequency domain nonlinear propagation model for prediction of supersonic fan tones in both rigid and acoustically-lined cylindrical ducts. An extension of I above with the addition of absorption of sound by acoustic liners, calculated in the frequency domain. Validation of Time domain model and Time-Frequency domain model with real data acquired by Rolls-Royce from rig-scale fan tests. Evaluation of the one-dimensional sawtooth representation of the rotor-locked pressure field for reliable predictions of supersonic fan tone noise.

III Generation of realistic one-dimensional sawtooth waveforms from measured data to form source inputs for shock-tracking based nonlinear propagation models.

IV Prediction of supersonic fan tone radiation from aircraft intakes using a theoretical model based on radiation of sound from a semi-infinite cylindrical duct. Investigation of far-field predictions against measured data using existing radiation model 'GXMunt' [22] coupled to in-duct shock-tracking nonlinear propagation method.

V Development of an advanced nonlinear propagation model for supersonic fan tone noise prediction in axisymmetric ducts with varying radius incorporating geometry variation effects, acoustic liner effects, realistic mean flow effects, and boundary layer effects on liner absorption. Development of equations for propagation of an irregular sawtooth in rigid-walled axisymmetric ducts where the radius and flow varies axially. Extension of equations for nonlinear propagation of regular sawtooth in rigid walled axisymmetric ducts with varying radius [23] to lined wall with fixed absorption for all BPF harmonics. Analysis and parametric studies on nonlinear propagation in various axisymmetric ducts and a study on effects variation of radius, flow speed and liner decay rates in the axial direction on supersonic fan tone noise predictions.

1.3 Project and Report Overview

Various steps have been taken in order to achieve the key aims of this project. A thorough literature review was carried out on 'buzz-saw' noise building on a foundation of a general appreciation of aircraft noise and existing prediction capabilities. Significant progress was made in the prediction of nonlinear propagation of the pressure waveform from the fan plane to the point of radiation from the intake duct and radiation to far-field.

The thesis, which consist of 11 chapters, is presented in a way to reflect the chronological steps in the methodology in particular to show the gradual improvements made in the advancement of the prediction model for supersonic fan noise. A broad literature review on 'buzz-saw' noise or multiple pure tones is presented in chapter 2 with a focus on the mechanism of generation. Chapter 3 presents the theories and models for prediction which had been developed before the commencement of this project.

Generation of a source sawtooth to utilize for propagation simulation is presented in chapter 4. Modes in ducts and the time-domain nonlinear propagation results are explained in chapter 5. The time-frequency domain model for 'buzz-saw' noise and the validation of results are in chapters 6 and 7 respectively. Chapter 8 contains the far-field radiation results preceded by a brief overview of the radiation model.

The incorporation of advanced features (variation in duct radius, real mean flow and variable liner absorption and boundary layer effects) in the prediction model commenced by the development of equations for various rigid and lined axisymmetric duct cases (chapter 9) and a study on the effects of the features to be added (chapter 10). The results for model axisymmetric ducts, and comparisons with measured data, are presented in chapter 11, followed by conclusions drawn from the study.

Chapter 2

Supersonic Fan Noise

2.1 'Buzz-saw' Noise

Prior to the introduction of the high-bypass-ratio turbofan engine there was little concern about noise generated by the fan of aircraft engines. The introduction of the high-bypass-ratio engines meant an increase in the size of the fan, the single stage compressor, of an aircraft engine[9–11, 19, 24–28]. Basically, the major reduction in aircraft noise by the introduction of the high bypass ratio turbofan engine was in jet noise. This increase in size/diameter of the engine translated to an increase in distance between the tip of the fan blades to the center of the fan hub resulting in an increase in the relative speed of the tip of the fan blades for the same rotational frequency. This meant that fan blade tips could achieve speeds in excess of the speed of sound leading to another class of aircraft noise. This noise generated by aircraft fans at supersonic fan tip speeds are multiple pure tones referred to as combination tones or 'buzz-saw' noise (due to its similarity to the noise of a chain saw)[9–11, 19, 20, 24–30].

Aircraft fan noise is normally classified into two main parts - tonal noise and broadband noise. Tonal noise from the fan of an aircraft engine was, before the identification of buzz-saw noise, mainly as a result of the interaction of rotor wakes on stator vanes known as rotor-stator interaction tones [27], or rotor-rotor interaction tones in the turbine stage. These tones are discrete tones[9, 11], and are generally classified as sum or difference tones[29], at integer sums or differences of the blade passing frequencies of the rotors[27, 29]. Broadband noise, on the other hand, was a result of turbulence in the free stream and boundary layers, and vortex shedding into the blade wake caused by random fluctuations in the lift forces on the blades[9, 20]. Both the discrete tones and the buzz-saw noise are periodic[9–11, 20, 24–27]. Buzz-saw noise contains much more tones than the discrete tones of interaction noise (of multistage compressors), with a large part occurring at frequencies less than the blade-passing frequency, BPF (a product of the rotating shaft frequency and the number of blades)[9–11].

Multiple pure tones generated at these rotating shaft frequency harmonics comprise of pressure patterns which spiral upstream through the duct and are eventually radiated out of the duct. The radiated tones are those perceived by an observer far away from the aircraft engine[9, 10, 19, 25, 28]. Buzz-saw noise is arguably less annoying to an observer when compared to the irritation of noise generated exclusively at blade passing frequency[27]. This is a conclusion drawn from psychoacoustic tests carried out and explained in reference [27]. Buzz-saw noise tones are low frequency tones, sometimes at frequencies of about 100Hz, in contrast to tones at subsonic speeds which can be at several thousand Hertz[30].

History shows that buzz-saw noise was first reported in the earlier 1960s as aircraft engines were being modified and fan tip speeds increased. The increase in the number and change in geometry (especially span length) of blades meant that the characteristics of former aircraft engines were changed, and hence new characteristics were revealed[27].The decay of the rotor-locked pressure field generated by fan blades at subsonic tip-speeds is rapid, and this decay is found to be complete at a distance not far away from the leading edge of the fan. A single stage compressor such as a high-bypass ratio turbofan engine's fan can therefore mainly generate tonal noise that can be propagated to an observer in the far-field only when the relative speed at the fan tip is supersonic[9, 11, 19, 24–26].

At supersonic speeds, the acoustic theory that governs the production of fan noise is nonlinear as a linear theory will be unable to define the mechanism of the noise because of the shock waves formed and the very high sound pressure levels generated inside the inlet duct[20, 27].

2.1.1 Source and Mechanism of Generation

In the event that the relative speed between the approaching flow and blade tips becomes supersonic, shock waves are formed at the blade tips. These shocks are bow[10, 26] or curved[11] shocks that occur at the tip of the fan blades, and are detached from the leading edge to varying degrees, depending on the geometry of the fan blade tip. The ideal case will be such that the shock waves are all similar in all their physical characteristics. This ideal is only possible if the fan has blades that are perfectly identical and are spaced and oriented exactly the same way. It will then be possible to represent the shock waves with a single shock wave repeated a number of times equal to the number of blades. The multiple pure tones expected in this case will be present only at the blade passing frequency and its harmonics due to the similarity of the fan blades [9–11, 20, 24–26]. In the real world, even though the manufacture of fan blades and the assembly of the fan are done to very small tolerances, fan blades are not identical. Neither are their blade-to-blade spacing or stagger angles absolutely the same.

Also, various changes occur in individual blades during and after they have been put into operation[9, 19]. These very minute differences or changes in blade and fan geometry make it impossible for any two shock waves formed at the fan blade tip to be exactly alike. The implication of the uniqueness of each blade and blade-to-blade characteristic is that the multiple pure tones produced will no longer be expected only at the blade passing frequency[10, 11, 24, 25]. The shock wave pattern, at the fan blade tips, is unique for one full revolution of the fan and repeats for each full revolution[9, 11, 20, 24, 28]. Each shock is unique and behaves uniquely and is believed to travel away from the leading edge at its own unique speed different from those of others[10]. No two fans (or compressors) are exactly the same even when manufactured under the same conditions. This implies that there is a unique multiple tone distribution for every fan or compressor. An interesting behaviour is that the multiple tones do not necessarily occur at the blade passing frequency but are present at any harmonic of the rotating shaft frequency[11, 25].

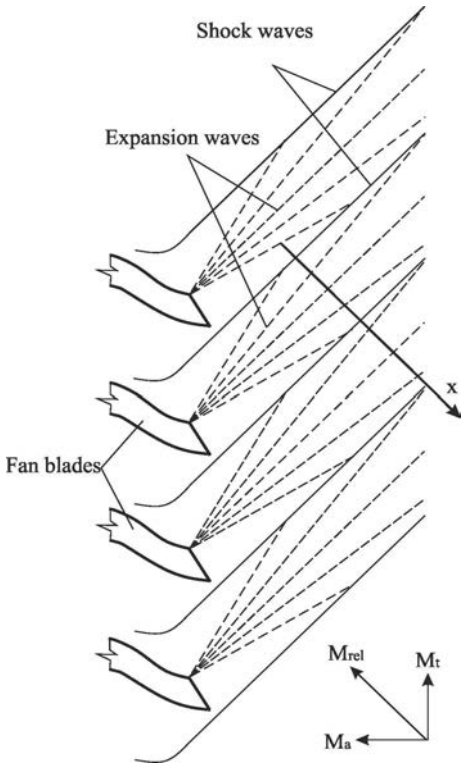

Figure 2.1: Shock and Expansion waves at supersonic fan blade tips

Very close to the fan, the profile of the variation of pressure has a sharp sudden rise at the point of shock formation (where the blade cuts into the incoming flow) and is followed by a region of approximately linear pressure reduction. This profile is repeated for the subsequent shocks but with their own unique magnitudes for different quantities[10]. The fan profile very close to the fan will have slightly varying amplitudes and almost equal spacings. This seemingly uniform profile changes considerably as it propagates upstream inside the inlet duct[25]. In the attempt to describe the generation of multiple pure tones, researchers have made use of simplified approaches in their explanations.

A number of assumptions are commonly made by buzz-saw noise researchers and they carefully point out how, or how not, their assumptions affect the analyses and the conclusions they make from their analyses.

A common simplification is the reduction of the number of dimensions considered in the investigation. For example, a one-dimensional acoustic theory for the shock has been employed [11] and the three dimensional phenomenon at the blades reduces to the two-dimensional planar case [9, 19, 24] as in Figure 2.1. Exploring the buzz-saw phenomenon in three dimensions makes both theoretical and experimental studies complicated due to the addition of the radial variations for the blades and the flow [27]. Other assumptions that are employed are directly connected to the blade geometry. The blades are sometimes taken to be perfectly alike and with equal spacing. This assumption is used many times as the basis for the actual case where the blades have unique geometry and are irregularly spaced. Another noteworthy assumption is that the mean flow is uniform along the axial direction. Also assumed, as explained in references [19, 26], is that the shock waves are not detached from the leading edge and the expansion fans(waves) are centered at a particular point on each blade. Viscous and heat conduction effects and boundary-layer effects (near the fan blade tip) are also mostly considered negligible [26]. The backing for these assumptions by researchers has been observed levels of agreement when the theoretical results are compared with experimental results. For example, in reference [28], while investigating the effect of the length of the inlet duct on multiple pure tone noise levels, it was proposed that the assumption that the shocks were attached may have caused a discrepancy between the theoretical predictions and experimental measurements.

The general belief of most researchers [9–11, 19, 20, 24–31] is that the origin of the noise can be traced to the non-uniformities and irregularities in the blades and their arrangement. These imperfections are responsible for the definition of the pressure field generated at the fan which is eventually propagated to the far-field. A number of experiments were carried out by researchers [9, 24, 27] to investigate the characteristics of buzz-saw noise and to validate the theoretical postulations on the mechanism of generation of buzz-saw noise. These experiments include those used to check the effect of blade non-uniformities on the generation of multiple pure tones [19], investigation of the effect of various relative speeds, and those particularly carried out to generate plots in the explanation of the nature of the noise [9].

A very notable conclusion of the experiments on the effect of relative speeds is that at subsonic relative flow speeds, the observed pressure fluctuations decay very quickly and are already negligible at distances near the fan blades [9, 10]. This is not the case at supersonic relative tip speeds, in which case the shocks waves are able to propagate upstream against the incoming flow, resulting in sound radiation of ‘buzz-saw’ noise to the far-field. The appearances of the combination tones at frequencies of the order of the rotating shaft frequency is due to the redistribution of acoustic energy by the

propagation of imperfections, of the fan and its blades, 'encoded' into the field at the point of its formation [9]. The propagated irregularities are in the form of differences in amplitudes and intervals and are the observable unique characteristic of a shock wave pressure profile[25].

Shock waves formed at the fan blade tips are weak aerodynamically but have very high intensities when examined from the acoustical perspective with sound pressure levels in the neighbourhood of 170dB [11].

The effect of the blade shape, and the shape of the entrance region between adjacent blades, on the formation of shock waves and the sound level was investigated in reference [10] and predicted in reference [25]. They concluded that very near the fan, one can expect the shock strength to be halved whenever the blade's radius of curvature is doubled, and a fixed level of decay will take double the distance it would otherwise have taken, but the effect described is not evident in the strength of the shock at upstream distances far from the fan. The bluntness to blade-spacing ratio was found not to have a significant effect on the shock strength far away upstream from the fan. The effect of the leading edge of the blade on the shock strength formed was also examined in reference [10]. A very small and sharp leading edge results in a weak shock that is displaced backwards of its position and has insufficient expansion, while a leading edge with a curvature too large or square is expected to produce a strong shock displaced forward, quickly impinging on the expansion fans of the preceding shock wave thus having similitude of a blade that is misaligned to a significant degree [10].

For a fan operating at supersonic tip speed, the main source of irregularities are the blade spacings, blade contours and blade stagger angles. The individual effect of these three key geometrical factors on the production of multiple pure tones has been investigated [24, 26]. Out of the three, the most significant factor causing the significant increase in the generation of multiple pure tones is the blade stagger (the angle between the duct axis and relative velocity at the leading edge of the fan blade) [11, 24, 26, 28, 31]. The blade stagger's importance on the generation of 'buzz-saw' noise can be seen from its direct influence on the incidence angle of the blade on the incoming flow. This directly dictates the position and detachment of the shock, and consequently, the strength of the shock and distance or time taken by the shock to interact with adjacent expansion waves.

The experimental work done by Kantola et al [24] showed arguably that the effect of blade spacing on the generation of 'buzz-saw' noise is much less significant contrary to the argument in reference [25] which sees the blade spacing as key to the production of combination tones. Intervals between shock waves, not particularly the blade spacing, are critical to the determination of the expected power spectrum of the shock-wave system and this outweighs the effect of shock strength [27]. Blade contour irregularities have not been deeply investigated due to the complexity in the measurements of these

irregularities. The contribution of blade contour to the production of multiple tone fields has, mostly, been factored out in experiments [24, 26], by the use of short length blades in order to justify the assumption of negligible differences in blade contours.

The theoretical investigation of buzz-saw noise is complex as it involves understanding the nature of the shocks formed at the fan blade tip and relies mainly on the methods of finite-amplitude wave theory[27]. The confinement of the shock-wave pattern in the duct makes non-linear characteristics to be retained over significant distances, and pressure amplitudes consequently remain high as well [20].

A number of researchers [9–11, 19, 20, 24–27, 30] affirm that blade-to-blade irregularities ensure sound power is transferred into harmonics of the rotating shaft frequency from blade passing frequency. In reference [27], measurement of the power level of the tone at the blade-passing frequency was at the initial stage about 20dB greater than power levels at any of the rotating-shaft frequency, but as the propagation proceeded, the variations in shock strength and spacing became more evident, as stronger shock waves overtake weaker ones, and, hence, multiple pure tones were generated. This continues until a point where the shocks have decayed so much that there is no more transfer of power among the tones.

This understanding of the generation of the tones at these frequencies is challenged in reference [32]. The argument was that the non-uniformities, especially blade stagger angle variation, are not directly responsible for the generation of buzz-saw noise. The shock strength was suggested to be determined by the amount of shock detachment from the fan blade tip and the flow spillage, occurring behind the detached shock, from one entrance region to the next. The pressure gradient across the flow, at the point where the shock is detached, is said to be responsible for the spillage which as a result changes the inclination of the shock wave [32].

The interesting point to note is that just like in previous research studies [9–11, 19, 25, 27, 28], the amount by which the shock at the tip is detached is due to the blade geometry and the flow conditions, and all these factors contribute to the shock strength. To consider shock detachment and flow spillage without an account of the blades irregularities and flow conditions will be inappropriate. Reference [32] does not in any way play down the importance of the blade stagger in determining the shock strength but stresses that the noise profile is always already established very near to the fan plane (where the tone at blade-passing frequency is still very dominant). The blade-passing frequency decays very rapidly (loses dominance), while the multiple pure tones decay more slowly (become dominant), and are more and more evident as the axial distance increases away from the fan plane.

A three-dimensional look at buzz-saw generation and propagation may be beneficial to an in-depth understanding of the noise observed [11]. It is pointed out in reference [9] that three-dimensional effects can not be neglected at certain high Mach numbers and

supersonic flow conditions. This is because a large part of each fan blade span will have gone supersonic and will contribute significantly in the production of the pressure field that is propagated. Correct mapping of the overall noise levels will require the consideration of the supersonic conditions of the fan blade span as well. Reference [27] counters the above argument categorically. It is pointed out that experimental results reveal that the study of buzz-saw noise done on a two-dimensional basis (ignoring radial complications) is sufficient as no essential feature is lost in the analysis [27, 28].

2.1.2 Propagation and Interaction of Supersonic Fan Tones

Shock waves initiated at the leading edge of the blades of a fan operating at relative tip-speeds higher than the speed of sound are locked to each blade and spin around the duct with the blades. Therefore, they are said to be 'rotor-locked'. The wave fronts thereby form a helical shape as they advance upstream of the duct traveling through the incoming flow. The angle of the helical shape or pattern formed is a function of the magnitude of the relative blade-tip speed [9, 28]. Propagating shock waves work against the flow and are retarded by the flow to varying degrees depending on the flow conditions and the speed of propagation of the shocks. As the waves advance away from the fan the retardation offered by the flow ensures the gradual decay of the waves [9].

The strength of the shock waves plays a major part influencing 'buzz-saw' noise observed at different locations in the propagated field [9]. Analysis shows that, except for points close to the fan, the region of expansion of the shock waves determine the noise level rather than the initial shock strength [9, 11]. The angle subtended between two adjacent waves, which depends on the Mach angle, curvature of the waves, the level to which the shock is detached from the leading edge and spacing between the shocks, influences the noise levels observed at particular locations. The flow behind a detached shock is initially subsonic but builds up speed to become supersonic. When it becomes supersonic, its interaction with the bulk of the expansion fans generates a raised level in the observed noise [9].

In a series of shock waves, the expansion waves occurring just after a particular shock are expected to impinge on the subsequent shock wave [19] at a distance not far away from the fan/rotor plane [27]. These interactions of the expansion fans and the shocks bring about a change in the rate of decay of the shocks. The decay rate change, at the point of interaction of the expansion fans and shock waves, is actually observed as an increase in the decay rate of the shock with increasing axial distance. The point at which the expansion fans and the shock waves meet marks the origin of the amplification of the irregularities in the shock pattern [11], which are themselves a consequence of the non-uniformities in the blade geometry and arrangement [11, 26, 27]. The increase in the irregularities as the wave propagates is an internal feature of propagation of shock waves modelled by the theory of nonlinear waves.

As the shock waves formed at each fan blade leading edge travel through the duct, interactions occur with other shock waves, with the incoming flow, and in-duct acoustic treatment, leading to the evolution of the waves prior to radiation from the inlet duct. The shocks at the fan blade tips all spin around the duct locked to the fan blades. At some distance not too far away from the fan leading edge plane, expansion fans of a shock interact with the adjacent shock. Prior to this interaction the shock waves decay at a rate proportional to the inverse of the distance away from the fan. As the interaction begins, the rate of decay of the shock is altered making it proportional to the inverse of the square root of the distance [9, 10, 24, 26, 27]. This change in the decay is the combination of the effect of the flow coming through the inlet of the duct and interaction with the expansion fans/waves of the preceding shock.

As distance increases away from the fan plane, the spacing between shock waves increase or decrease as the shock waves decay. Irregularities that are present in the shock pattern are amplified and the spectrum increasingly shows multiple pure tones [27]. Stronger shocks overtake adjacent weaker shocks making the separation distance change and the number of shocks reduce as the distance from the fan increases [10, 11, 27]. When two shocks merge, the velocity ahead of the shock is the lesser of those of the two shocks while the velocity behind the shock formed is the greater of the velocities of the shocks [11]. Far away from the fan plane, the shock system would have evolved and will be very different from its original form observed near the fan plane. The degree of non-uniformities in the fan blades is a strong and major influence on the shock system evident in the far-field [11, 25, 28]. In the profile of the shock system as it propagates away from the fan, the overall pressure amplitude decreases [9, 10, 19] but the amplitude ratio of strong to weak shocks present in the profile increases [11, 25]. The random shock system formed is the foundation of the acoustic field of multiple tones. The more irregular and random the shock wave system, the stronger the overall strength of the field and the less the level of decay. A major determinant of the evolution of the shock wave system is the velocity of the flow. It basically controls the advancement of the shock system along the axial distance. The faster the flow the greater the retardation offered to the shock waves pushing them more closely together and vise versa. Attenuation of a unique shock wave pattern is less than that of the even spaced uniform shock waves over the same distance [10].

The influence of the length of the intake duct on the propagation of multiple pure tones is very important. The fact that it takes a particular shock wave system some time over an axial distance to evolve means that the length of the duct influences the exit wave system radiated from the inlet of the duct. Kantola et al [28] argue that the noise level for the multiple tones generated reach a peak faster in a short intake duct. This was said to be based on the experimental investigation carried out on the influence of the inlet duct on the multiple pure tones measured.

Larger axial distances are needed for small measures of non-uniformities to develop to an appreciable level [20]. Effects of the intake duct are not limited to investigation of the intake duct length, but also on the non-uniformities in the duct. The character of a uniform intake duct as an ideal situation for proper propagation of the shock wave is recommended [20]. Most research works on buzz-saw noise have taken the flow approaching the fan to be uniform. This is considered a fair assumption as the intake duct guide vanes and struts (used in intake ducts) in early aircraft engines [27] are no more used in modern high-bypass ratio turbofan engines. Therefore, inflow is relatively uniform (neglecting areas in the boundary layer close to the duct wall).

The effect is similar to a decrease in blade spacing if axial mean flow gradient is increased. More energy is dissipated with increase in the mean axial flow gradient [31]. Since in a real world aircraft engine, particularly the high-bypass-ratio turbofan engine, the inlet duct does not have a constant cross-section from the inlet to the fan plane, the non-uniformities in the cross-section (though not large) are expected to have an effect on the propagation of the shock waves generated at the fan blade tips. The main effect of cross-section changes is to change the axial flow velocity which may result in lower or higher rates of retardation and decay of propagated waves, and consequently on the sound radiation from the intake duct [30].

The ability of the sound exiting the nacelle of an aircraft engine, which is a duct, to propagate in three-dimensions make non-linear effects less important to a significant level. This is because the strength of the shock patterns at the end of the duct dictates the magnitude of sound power expected to be radiated from the duct. The strength of the shocks at the exit of the duct are dependent on the pressure field and the transmission coefficient at that point [19]. Noise levels at the exit of the duct are most likely to be low enough to assume linear propagation in their forward radiation.

2.1.3 Buzz Tones Peculiarities and Complexities in Propagation

Buzz-saw tones are periodic with a pressure pattern repeated over each complete cycle [33–36]. The non-uniformities in the shock wave pattern which are evidence of the non-uniformities of the fan blades have a pressure profile that can be estimated through numerical methods [33]. These methods are not without various assumptions to reduce the complexity in computation, and adjustments that make them comparable to experimental results. Therefore, it is common to observe under-predictions or over-predictions of various tones. In order to entirely represent and predict the propagation of shock waves as it concerns the production of multiple pure tones, it is necessary to consider changes in the axial flow velocity, three-dimensional sonic effects and the effect of the duct wall in eliminating certain modes from propagating [33]. In addition to these, considering the effects in the radial direction together with the other two dimensions will give a three dimensional view in the methods of analysis of ‘buzz-saw’ tones, and this is

very important to getting the theoretical results close to the experimental measurements [35].

The contribution of the shock waves produced at the fan blade tips to the generation of 'buzz-saw' tones is undeniable, although there has been some arguments debating the degree of influence the shock waves have on the production of the tones. These arguments include the suggestion that what is most important is the detachment of the shock from the leading edge of the fan blades, and the amount of spillage behind these shocks. Another argument in reference [34] suggests that looking only at the shock waves as generators of the multiple pure tones is an inadequate explanation of the mechanism of generation of 'buzz-saw' tones. The emphasis was put on the interaction between various harmonics of the rotating shaft frequency.

It is argued that since the multiple pure tones advance (tracing a helical path) through a duct, hence the name spinning modes, there are strong interactions taking place as the modes move towards the entrance of the duct. The strength of an interaction is proportional to the closeness of the axial wave number of the propagating wave to the closest cut-off wave number. The closer the wave number to the cut-off wave number, the stronger the interaction expected [34]. These interactions transfer energy from the high-amplitude blade-passing frequency to harmonics (with lower amplitudes), reducing the amplitude of the blade passing-frequency while increasing those of the harmonics. It is important to see that this argument focusses more on what ensues after the shocks have been formed at the blade tip, and shifts focus to the acoustic field as the wave-form propagates in the duct. These interactions are regarded as responsible for the appreciable increase in buzz-saw noise levels observed between Mach numbers 1.2 and 1.3, rapid decay of the tone at blade passing frequency and the reduction in the ability of liners, installed on the duct wall close to the fan, to have significant attenuation of multiple pure tones as predicted by some liner optimization techniques [34].

The points mentioned above attributed to strong inter-harmonic interactions are those which the weak-shock theory does not account for [34]. It is clearly observable that the foundation on which the suggestion of inter-harmonic interactions as the generator of multiple pure tones [34] is based on the fact that multiple pure tones are observed at subsonic tip speed conditions when shocks are absent [34, 35]. This argument is analogous to the interaction and merging of shock waves propagating from fan-blade tips amplifying the non-uniformity of the pressure profile, particularly for buzz-saw tones at harmonics lower than blade passing frequency at supersonic tip speeds. The focus is on strong interactions between harmonics of spinning modes as opposed to 'weak' interactions between shocks.

As mentioned above, the observance of multiple pure tones at subsonic relative tip speeds [34, 35] has brought about a concern on the classification for buzz-saw tones. Buzz-saw tones are generally regarded as those multiple pure tones observed when relative speeds

of fan-blade tips go supersonic, and they are most significantly evident at harmonics of the rotating shaft frequency. This is not the case in reference [35] as buzz-saw tones were classified into three types; tones due to inflow distortions impinging on a fan, tones at supersonic tip speeds, and, rotor-stator interaction tones. With reference to the argument in reference [34], Vaidya [35] stated that multiple tones observed at subsonic fan tip speeds are mostly overshadowed by broadband noise, and that the acoustic liners placed on the duct wall tend to attenuate these tones very easily, whereas they only tend to reduce the nonlinear interactions in the case of buzz-saw tones.

Contrary to the arguments in reference [35], although most other studies have acknowledged the existence of tones through the three mechanisms used in the classification, these tones are named differently. The tones at subsonic relative blade tip speeds due to flow non-uniformities are overshadowed by broadband noise as even reference [34] confirms. The second kind of tones observed at supersonic fan-blade tip speeds are those generally considered as buzz-saw tones. And finally, the third kind, tones generated by rotor-stator interaction are referred to as interaction tones, and are further classified as sum or difference tones. This shows that Buzz-saw tones are considered clearly as very specific type of tones and should not be confused with other tones.

An interesting point made in reference [35] is that apart from shock waves formed at supersonic fan-blade tips, an initially sinusoidal wave with high enough amplitude can change into a shock in the presence of high levels of distortions as the wave propagates. This does not in anyway affect the viability of nonlinear acoustic theory in explaining the characteristics of the wave system as long as the shocks can still be assumed to be 'weak' [35].

The renewed interest in the study of buzz-saw noise over the last twenty years, after a significant period of studies in the 1970s, is perhaps attributable to the fact that aircraft engines are getting bigger and greater fan-tip speeds are achievable [36]. The propagation of buzz-saw tones has been modeled in various ways. These were stepwise advancement with increasing computational complexity towards a more realistic theoretical representation of the real-world situation. First, a system of regular shock waves in the form of a sawtooth profile was considered. Following this the irregular sawtooth profile which is a representation of the real-world case was also considered. Also regarding duct walls, the hard wall with perfect reflection of the waves was studied first before the soft-wall (lined wall) case was looked into. The regular sawtooth and hardwall cases form an ideal test case for comparison, and a foundation on which the more realistic models can be built. For example, the hard-wall case allows for analysis in the time domain. The inclusion of a soft-wall meant that the problem could be far more easily tackled in the frequency domain since the impedance of an acoustic liner will be frequency dependent [36]. Both methods simulate nonlinear propagation of shock waves and have been compared with experimental results. The ability to consider various cases enables useful comparison of results. This includes determining the effect of liners, length of ducts, diameter of

ducts, and nonlinear propagation, as opposed to linear propagation, without the need to construct elaborate and expensive experiments.

It is useful to point out that owing to increase in computational power available there is increasing investigation of the propagation of buzz-saw noise using Computational Fluid Dynamics CFD or Computational Aeroacoustics CAA methodology or a combination of both. A number of studies [37–40] have demonstrated this prediction capability. In order to minimize computational cost, various simplifications such as characterizing the whole blade set by a few blades and unwrapping the fan blades into a two dimensional cascade without representation of the intake duct. As computational power increases and with development of new methodologies, the feasibility of using CFD and CAA methods to simulate the whole system; fan and propagation in the intake and the onward radiation will increase.

The nonlinear nature of the propagation of shocks in the intake duct of an aero-engine, and the presence of various in-flow interactions, all contribute to the behaviour of buzz-saw noise. This is founded mainly on the redistribution of energy among harmonics of rotating shaft frequency by the nonlinear propagation [17, 18, 21, 41, 42]. The theories and models for buzz-saw noise prediction will now be examined.

2.2 Summary

Literature review on buzz-saw noise has been presented with a focus on the description of the mechanism of generation, features of nonlinear propagation, complexity of prediction and theoretical and experimental observations from various studies.

Chapter 3

Theories and Models for Buzz-saw Noise Prediction

3.1 Duct Acoustics

In order to develop a code to evaluate the acoustic modes in a duct, a number of different boundary conditions are applied to the wave equation for particular duct configurations. These boundary conditions ensure the right solution is obtained for that particular duct type. Evaluation of the modes is a convenient approach to analyze sound fields in a duct. A number of limitations exist when trying to mimic real-world conditions in a duct, but with the adoption of a set of reasonable assumptions, a reliable mathematical model can be solved to obtain the duct modes. The solution obtained is essentially a solution to the wave equation for that particular duct configuration. A brief overview of the important steps and solutions for the cylindrical and annular duct configurations are discussed.

3.1.1 Waves in Ducts with Rigid Walls

The linear wave equation is the starting point to look at acoustic modes in a duct. This equation allows for the generation of particular solutions using appropriate conditions for the types of ducts that are of interest.

The wave equation, in terms of pressure, is written as

$$\frac{\partial^2 p}{\partial t^2} - c^2 \nabla^2 p = 0, \tag{3.1}$$

where ∇^2 is the Laplacian operator.

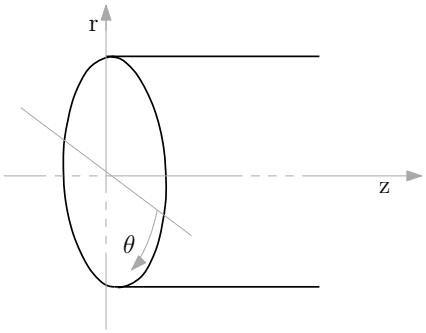

Figure 3.1: Cylindrical duct

3.1.1.1 Cylindrical Duct with No Flow

As this work focusses on cylindrical and annular ducts, the pressure is expressed in cylindrical coordinates in three-dimensions as shown in (Figure 3.1).

The three-dimensional wave equation in cylindrical polar coordinates is

$$\frac{\partial^2 p}{\partial t^2} - c^2 \left(\frac{\partial^2 p}{\partial r^2} + \frac{1}{r}\frac{\partial p}{\partial r} + \frac{1}{r^2}\frac{\partial^2 p}{\partial \theta^2} + \frac{\partial^2 p}{\partial z^2} \right) = 0. \tag{3.2}$$

The expected solution for equation (3.2) is of the form;

$$p(r, \theta, z, t) = R(r)\,\Theta(\theta)\,Z(z)\,T(t). \tag{3.3}$$

Substituting (3.3) into (3.2), and after a number of mathematical manipulations, a system of equations in terms of $R(r)$, $\Theta(\theta)$, $Z(z)$ and $T(t)$ are obtained:

$$\begin{aligned} T'' - A\,c^2\,T &= 0, \\ Z'' + BZ &= 0, \\ \Theta'' + E\Theta &= 0, \\ R'' + \frac{1}{\kappa r}R' + \big(1 - \frac{E}{\kappa r}\big)R &= 0, \end{aligned}$$

where $'$ denotes differentiation with respect to the function's argument and $A = k^2$, $B = k_z^2$, $E = m^2$ and κ are constants.

Applying Boundary Conditions

Boundary conditions are necessary for the solution of the wave equation for a particular duct geometry. The duct is assumed to be infinitely long in the axial direction. Therefore, the boundary conditions for the cylindrical duct (Figure 3.1) are:
In the direction of θ:
A periodic condition exists. $\Theta(\theta) = \Theta(\theta + 2\pi n)$; $n = 0, 1, 2, ...$ At any azimuthal point in the duct, the same values are expected after every period 2π.
In the direction of r:
The radius, r, varies from 0 to a. Hence, the boundary conditions are:

$$p = \text{finite at } r = 0 \text{ and } \frac{\partial p}{\partial r} = 0 \text{ at } r = a.$$

At the centre of the cross section of the duct, a measurable finite value of the pressure exists. This explains the first condition. The differential equations in T, Z, Θ and R are solved by assuming solutions of particular forms. For differential equations in $T(t)$, $Z(z)$ and $\Theta(\theta)$, a solution of an exponential form is assumed, whereas for $R(r)$, the differential equation is Bessel's differential equation. The solution is a sum of Bessel functions of the first and second kinds. These solutions (in general forms) to the differential equations are:

$$T(t) = C_1\, e^{i\omega t} \tag{3.4}$$
$$Z(z) = C_2\, e^{\pm ik_z z} \tag{3.5}$$
$$\Theta(\theta) = C_3\, e^{\pm im\theta} \tag{3.6}$$
$$R(\kappa r) = C_4\, J_m(\kappa r) + C_5\, Y_m(\kappa r) \tag{3.7}$$

where, C_1, C_2, C_3, C_4 and C_5 are constants. J_m and Y_m are Bessel Functions of the first and second kind respectively, evaluated at specific m values. Also $\omega(= kc)$ is the angular frequency.

It is important to note here that k is the free-space wave number. Wavenumbers k_z and κ are the components of the wavenumber in the direction of the duct axis and duct radius and are known as axial wavenumber and radial wavenumber respectively.

These wavenumbers are related by the dispersion relation:

$$k^2 = \kappa^2 + k_z^2 \tag{3.8}$$

as derived from the solution of equations (3.5)-(3.7). Now applying the boundary conditions to (3.6) and (3.7), we have

for θ: $\Theta(\theta) = C_3\, e^{\pm im\theta}$

where, m $(m = 0, 1, 2, ...)$ is the azimuthal mode for a periodical $\Theta(\theta)$.

for r: In order for the condition at $r = 0$ to be satisfied and due to the fact that the Bessel function of the second kind Y_m blows up (becomes infinite) at this point, the constant C_5 in (3.7) must be put to zero. Hence, equation (3.7) is reduced to $R(\kappa r) = C_4\, J_m(\kappa r)$. Applying the second boundary condition points out the fact that there exist an infinite number of values (in the radial direction) of κ for every azimuthal mode number m that satisfies the boundary condition $(J'_m(\kappa_{mn} a) = 0)$. Hence, κ is written as κ_{mn} $\forall$ m $(m = \pm 0, 1, 2, ...)$ and n $(n = 1, 2, 3, ...)$. Also, k_z becomes $k_{z_{mn}}$ as there exists a k_z for every κ (equation (3.8)). Hence, we have

$$R(\kappa r) = C_{4_m}\, J_m(\kappa_{mn} r). \tag{3.9}$$

Substituting (3.4), (3.6), (3.5) and (3.9) into (3.3), we obtain the expression for the pressure of a cylindrical duct

$$p(r, \theta, z, t) = \sum_{m=0}^{\infty} \sum_{n=1}^{\infty} C_{4_{mn}}\, J_m(\kappa_{mn} r)\; C_{3_m}\, e^{\pm im\theta}\; C_{2_{mn}}\, e^{\pm ik_{z_{mn}} z}\; C_1\, e^{i\omega t}.$$

Bringing all the constants together as P_{mn} and rearranging yields;

$$p(r, \theta, z, t) = \sum_{m=-\infty}^{\infty} \sum_{n=1}^{\infty} P^{\pm}_{mn}\, J_m(\kappa_{mn} r)\; e^{i(\omega t - m\theta - k^{\pm}_{z_{mn}} z)}. \tag{3.10}$$

Superscript $\pm$ indicates the positive and negative directions. Equation (3.10) represents the total pressure field for all modes in a cylindrical duct.

3.1.1.2 Cylindrical Duct with Uniform Flow

Equation (3.2) does not include the effect of flow in the duct. To include the presence of uniform flow in the duct, we employ the convective time derivative

$$\frac{D}{Dt} = \frac{\partial}{\partial t} + U\, \frac{\partial}{\partial z}, \tag{3.11}$$

in place of $\partial/\partial t$ in the wave equation (equation (3.2)) . Using (3.11) in (3.2) gives

$$\left(\frac{\partial^2 p}{\partial t^2} + 2U\, \frac{\partial p}{\partial z \partial t} + U^2\, \frac{\partial^2 p}{\partial z^2}\right) - c^2 \left(\frac{\partial^2 p}{\partial r^2} + \frac{1}{r}\frac{\partial p}{\partial r} + \frac{1}{r^2}\frac{\partial^2 p}{\partial \theta^2} + \frac{\partial^2 p}{\partial z^2}\right) = 0 \tag{3.12}$$

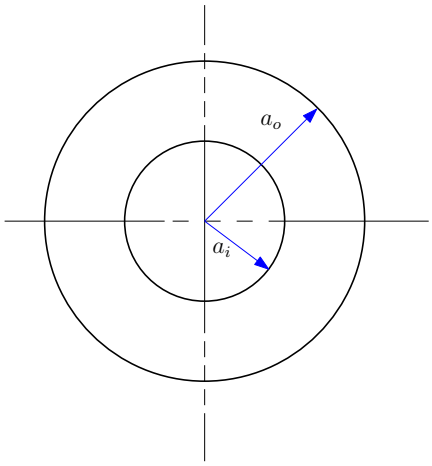

Figure 3.2: Cross section of an annular duct

Taking (3.12) through a similar process as (3.2), we obtain the same final expression for the pressure in a cylindrical duct with uniform flow U. The important difference between the no-flow and uniform flow cases is the dispersion relation which relates the wave number k, axial wave number k_z and the radial wave number κ. For this case with a uniform flow, the dispersion relation is [43, 44],

$$k_z = \frac{-k}{(1-M^2)}\left[M \pm \sqrt{1-(1-M^2)\frac{\kappa^2}{k^2}}\right]. \tag{3.13}$$

The dispersion relations (3.8) and (3.13) give the characteristics of the wave in the duct for each flow condition.

3.1.1.3 Annular Duct

The main difference between the cylindrical duct and the annular duct is the presence of an inner surface which means that, as seen in (Figure 3.2), the radius now varies from a non-zero value, a_i, at the inner wall to a_o at the outer wall. This situation changes the boundary conditions to;

$$\frac{\partial p}{\partial r} = 0 \ ; r = a_i \ \text{ and } \ \frac{\partial p}{\partial r} = 0 \ ; r = a_o,$$

where a_i and a_o are the inner and outer radii respectively.

The equations related to the axial and azimuthal directions are unchanged from those obtained for the cylindrical duct. However, in the radial direction, the new set of boundary conditions are applied to (3.7). This yields two equations.

$$D_{1_{mn}}\, J'_m(\kappa_{mn} a_i) + D_{2_{mn}}\, Y'_m(\kappa_{mn} a_i) = 0,$$

$$D_{1_{mn}}\, J'_m(\kappa_{mn} a_o) + D_{2_{mn}}\, Y'_m(\kappa_{mn} a_o) = 0,$$

where J'_m and Y'_m are the first derivatives of the Bessel functions of the first and second kind respectively.
Dividing through by $D_{1_{mn}}$ and setting $D_{mn} = D_{1_{mn}}/D_{2_{mn}}$ gives:

$$J'_m(\kappa_{mn} a_i) + D_{mn}\, Y'_m(\kappa_{mn} a_i) = 0 \tag{3.14}$$

$$J'_m(\kappa_{mn} a_o) + D_{mn}\, Y'_m(\kappa_{mn} a_o) = 0 \tag{3.15}$$

which can be also expressed as;

$$\begin{bmatrix} J'_m(\kappa_{mn} a_o) & Y'_m(\kappa_{mn} a_o) \\ J'_m(\kappa_{mn} a_i) & Y'_m(\kappa_{mn} a_i) \end{bmatrix} \begin{bmatrix} 1 \\ D_{mn} \end{bmatrix} = \begin{bmatrix} 0 \\ 0 \end{bmatrix}.$$

Solutions exist only when the determinant of the 2x2 matrix is zero[45]. That is when

$$J'_m(\kappa_{mn} a_o)\, Y'_m(\kappa_{mn} a_i) - J'_m(\kappa_{mn} a_i)\, Y'_m(\kappa_{mn} a_o) = 0. \tag{3.16}$$

Equation (3.16) represents an eigenvalue problem. Trial values of κ are used in (3.16) for fixed values for m to obtain n solutions (eigenvalues) κ_{mn} that satisfy the equation. The trial values are taken through iterations using a numerical method (in this case, the *Newton-Raphson Method* to obtain the solutions). An eigenvalue κ_{mn} can then be used in either (3.14) or (3.15) to obtain D_{mn} as

$$D_{mn} = \frac{-J'_m(\kappa_{mn} a_o)}{Y'_m(\kappa_{mn} a_o)} = \frac{-J'_m(\kappa_{mn} a_i)}{Y'_m(\kappa_{mn} a_i)}.$$

The axial wavenumbers $k_{z_{mn}}$ can be calculated from κ_{mn} using equations (3.8) or (3.13) depending on the flow condition in the duct.

The pressure field in an annular duct can therefore be expressed as;

$$p(r, \theta, z, t) = \sum_{m=-\infty}^{\infty} \sum_{n=1}^{\infty} P^{\pm}_{mn} \Big(J_m(\kappa_{mn} r) + D_{mn}\, Y_m(\kappa_{mn} r) \Big)\, e^{i(\omega t - m\theta - k^{\pm}_{z_{mn}} z)}. \tag{3.17}$$

3.1.2 Waves in Ducts with Lined Walls

Consider two ducts, a cylindrical duct and an annular duct, geometrically similar to the ones discussed above but with lined walls (or soft walls or acoustically absorbent walls). Unlike a rigid wall, which possesses an infinite impedance (zero admittance), an acoustically-lined wall has a finite value impedance (and admittance). The dimensionless admittance is defined as β and dimensionless impedance as $\mathcal{Z}$. These two are related as;

$$\beta = \frac{1}{\mathcal{Z}}$$

where, the impedance $\mathcal{Z} = \mathbf{z}/\rho c$; ρ is the density of the flow medium and c is the speed of sound in the medium, and $\mathcal{Z} = R_s + iX_s$. R_s is the specific acoustic resistance and X_s is the specific acoustic reactance (depends on the properties of the liner).

The condition of the wall influences the boundary conditions just as the geometry of the duct also has a part to play in the determination of the boundary conditions. The boundary condition evaluated at the wall is expressed in terms of the wave numbers and the admittance of the wall as[46]

$$\frac{\partial p}{\partial r} = \pm i\beta \frac{(k - k_z M)^2}{k} p \tag{3.18}$$

The '+' in the RHS of the equation is used when the outer cylinder is lined while '–' is for a lined inner hub as shown in Figure 3.3.

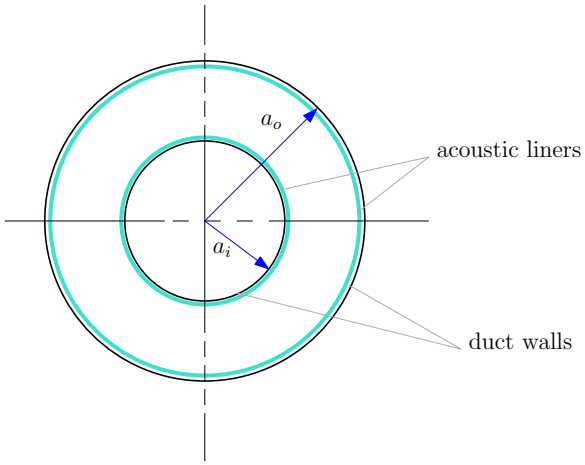

Figure 3.3: Acoustically lined annular duct

3.1.2.1 Lined Cylindrical Duct

The pressure field in a lined cylindrical duct is expressed as (3.10). The boundary condition at $r = 0$ is the same as for the rigid wall case. However, at the lined wall,

equation (3.18) (with the negative sign) is used as the boundary condition.

Applying the boundary conditions at r = 0 and at the lined wall r = a, yields

$$\kappa_{mn} J'_m(\kappa_{mn} a) + i\beta \frac{(k - k_{z_{mn}} M)^2}{k} J_m(\kappa_{mn} a) = 0. \tag{3.19}$$

This characteristic equation (equation (3.19) together with the dispersion relation (3.13)) is solved by using trial values through the *Newton-Raphson Method* to obtain the eigenvalues (axial wave numbers $k_{z_{mn}}$) that satisfy equation (3.19).

3.1.2.2 Lined Annular Duct

In the case of a lined annular duct, the component of the pressure in the radial direction, $R(\kappa_{mn} r)$, is as expressed in (3.7). The boundary conditions for this case (Figure 4) are:
At $r = a_i$

$$\frac{\partial p}{\partial r} = +i\beta \frac{(k - k_{z_{mn}} M)^2}{k} p, \tag{3.20}$$

and at $r = a_o$

$$\frac{\partial p}{\partial r} = -i\beta \frac{(k - k_{z_{mn}} M)^2}{k} p. \tag{3.21}$$

Applying these boundary conditions in the radial direction gives two equations

$$\begin{bmatrix} J'_m(\kappa_{mn} a_i) - \aleph_i J_m(\kappa_{mn} a_i) & Y'_m(\kappa_{mn} a_i) - \aleph_i Y_m(\kappa_{mn} a_i) \\ J'_m(\kappa_{mn} a_o) + \aleph_o J_m(\kappa_{mn} a_o) & Y'_m(\kappa_{mn} a_o) + \aleph_o Y_m(\kappa_{mn} a_o) \end{bmatrix} \begin{bmatrix} 1 \\ \Gamma_{mn} \end{bmatrix} = \begin{bmatrix} 0 \\ 0 \end{bmatrix},$$

where $\aleph_{i,o} = -i\beta_{i,o} \frac{(k - k_{z_{mn}} M)^2}{\kappa_{mn} k}$, and

$$\Gamma_{mn} = \frac{-J'_m(\kappa_{mn} a_i) - \aleph_i J_m(\kappa_{mn} a_i)}{Y'_m(\kappa_{mn} a_i) - \aleph_i Y_m(\kappa_{mn} a_i)} = \frac{-J'_m(\kappa_{mn} a_o) - \aleph_o J_m(\kappa_{mn} a_o)}{Y'_m(\kappa_{mn} a_o) - \aleph_o Y_m(\kappa_{mn} a_o)}.$$

This is used to obtain the characteristic equation to the lined annular duct

$$\begin{aligned} &\left(J'_m(\kappa_{mn} a_i) + \aleph_i J_m(\kappa_{mn} a_i)\right) \left(Y'_m(\kappa_{mn} a_o) - \aleph_o Y_m(\kappa_{mn} a_o)\right) \\ &\quad - \left(J'_m(\kappa_{mn} a_o) - \aleph_o J_m(\kappa_{mn} a_o)\right) \left(Y'_m(\kappa_{mn} a_i) + \aleph_i Y_m(\kappa_{mn} a_i)\right) = 0 \end{aligned} \tag{3.22}$$

Equation (3.22) is solved iteratively using the *Newton-Raphson Method* to obtain values of axial wavenumbers, $k_{z_{mn}}$, that satisfy the equation. A trial value , a complex number with real and imaginary parts close to zero, is employed to start the iterations. Say, equation (3.22) is represented by ℶ, and its derivative obtain by finite difference is ℶ'. The axial wavenumbers $k_{z_{mn}}$ are obtained by minimizing the error

$$\text{error} = |\frac{k_{z(i+1)} - k_{z(i)}}{k_{z(i)}}| \tag{3.23}$$

where successive iteration are obtained as

$$k_{z(i+1)} = k_{z(i)} - \frac{\beth(k_{z(i)})}{\beth(k_{z(i)})'}. \tag{3.24}$$

This process is carried out for each $k_{z_{mn}}$ and guess values are progressively chosen using a predefined complex number grid of equal-spaced real and imaginary parts.

3.2 Nonlinear Propagation

Knowledge of nonlinear propagation of shocks, which is the basis of understanding of the development and behaviour of buzz-saw noise, is essential to the prediction and control of buzz-saw noise. Ability to predict the propagation of shock waves to a significant level of accuracy will possibly mean that appreciable control of buzz-saw noise is achievable. The control of buzz-saw noise is particularly desirable for engine operating conditions during aircraft take-off and climb conditions[17, 41] when buzz-saw (fan) noise is the most significant contributor to the overall aircraft noise.

In order to understand non-linear propagation of shock waves, a model of the shocks pressure signature can be made and taken through a series of steps that approximate the real-life situations that occur in the inlet duct[21]. Before this, it is beneficial to look at the region close to the tips of the blades of the fan. This is shown, as also seen in references[17, 18], in two dimensions in Figure 2.1 with x as the direction to which the shock front advances.

M_{rel}, M_a and M_t are the relative, axial and tangential Mach numbers respectively. They are related by the expression, $M_{rel}^2 = M_a^2 + M_t^2$ where, $M_{rel} > 1$ is supersonic operating condition. The propagation model of the shock wave system in Figure 2.1, is based on the weak shock theory with an assumption that there are no dissipative effects of viscosity and heat transfer, and that there are no obstructions to the flow (i.e. uniform flow). Although, in reality, the flow is not uniform. Flow distortions are present and are capable of leading to the production of other sources of noise as well. The representation of the waveform in the x-direction is like a sawtooth[18]. The sawtooth is a series of expansion and shock waves combining to form the pressure profile. The number of shocks present is initially equal to the number of blades in the fan. The expansion waves facilitate the turning of the flow to the suction surface of the blades. Owing to the fact that all the blades in the aero-engine fan will not be aligned perfectly alike, the expected sawtooth waveform will be irregular, with shock waves having varying amplitudes and spacings within the entire sawtooth profile.

If all the blades were exactly alike and perfectly aligned, a regular sawtooth profile will result with all shocks equal in amplitude and equally spaced. When a regular wave is propagated inside the inlet, the attenuation is expected to be uniform for all the shocks, and the energy distribution in the harmonics of the rotating shaft frequency will be similar in profile to the waveform observed at the fan plane. The frequency spectrum of a regular sawtooth waveform is comprised of the harmonics of blade passing frequency. For a regular sawtooth with shock spacing of λ, the time (in seconds) for the wave to spiral to a distance z in the axial direction can be defined as t. The dimensionless 'time of flight', T, for the spiralling wave is [17, 18],

$$T = \frac{c_0 t}{\lambda} = \frac{zK}{D}, \tag{3.25}$$

where c_0 is the speed of sound, B is the number of blades of the fan, D is the duct diameter (in meters) and

$$K = \frac{B}{\pi} \frac{M_{rel}^4}{\sqrt{M_{rel}^2 - 1}} \left[M_a \sqrt{M_{rel}^2 - 1} - M_t \right]^{-2}. \tag{3.26}$$

Every point on the shock moves at the same onward speed, v_s[1],

$$v_s = c_0 + \frac{\gamma + 1}{2\rho_0 c_0} p_m \tag{3.27}$$

where p_m is the acoustic pressure (deviation from the mean in-duct static pressure) value at the mid-point of each shock (this is the same value for all shocks in a regular sawtooth waveform), and γ is the ratio of specific heat capacity at constant pressure to specific heat capacity at constant volume. While the points on the expansion waves progress at a speed, v_e,

$$v_e(p) = c_0 + \frac{\gamma + 1}{2\rho_0 c_0} p \tag{3.28}$$

where p is the acoustic pressure at each point on the expansion wave.

Throughout the finite time for which the waveform propagates in the inlet duct, the amplitude of the waveform decays with time. The decay or attenuation is nonlinear in nature and can be expressed in terms of the dimensionless time of flight T[17, 18], for a regular sawtooth waveform, as

$$p_s(T) = \frac{p_s(0)}{1 + \left(\frac{\gamma+1}{2\gamma}\right) Ts}, \tag{3.29}$$

where p_s is the amplitude of the shock ($p_s(0)$ is the initial amplitude of the shock at time T = 0) and shock strength s is the ratio of $p_s(0)$ and the ambient pressure, P_0.

The attenuation of a single shock (regular sawtooth) is illustrated in Figure 3.4 (a-d). The initial waveform is shown in Figure 3.4(a). All points on the shock advance

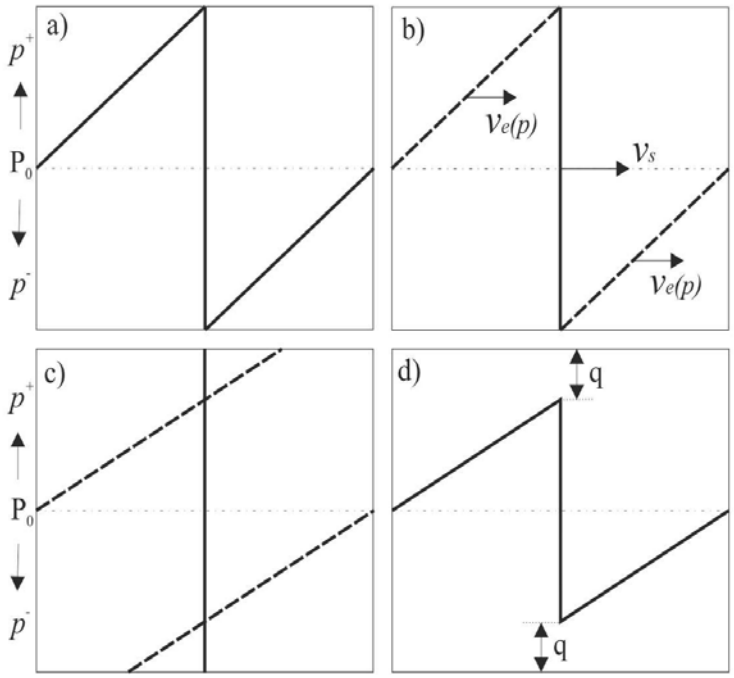

Figure 3.4: An illustration of shock amplitude attenuation

at speed v_s (equation (3.27)) while points on both expansion waves travel at different speeds $v_e(p)$ with respect to the acoustic pressure at each point (Figure 3.4(b)). The shock and expansion waves can be examined separately (- - - - expansion waves and ——— shock) and propagated for some time, t, as seen in Figure 3.4(c). At some points pressure values from both expansion waves exist but since pressure is not multi-valued, the illustration in Figure 3.4(c) is not feasible. On coupling back the waves and the shock (Figure 3.4(d), the amplitude of the shock is observed to have reduced by $2q$ (using equation (3.29), within a time interval T_1 to T_2, $q = \frac{1}{2}[p_s(T_1) - p_s(T_2)]$).

An important characteristic to note is that at a time, T, when $Ts \gg 1$ equation (3.29) reduces[17] to

$$p_s(T) \approx \left[\frac{2\gamma P_0}{\gamma + 1}\right]\frac{1}{T}. \tag{3.30}$$

This implies that at some distance from the inception of the sawtooth waveform at the fan-tip, the attenuation becomes independent of the initial shock strength. Two sawtooth waveforms with different initial shock amplitudes may be indistinguishable in amplitude after some time as illustrated in Figure 3.5. Figure 3.5 shows the plots of pressure amplitude against the time of flight (T) for two regular sawtooth profiles of different initial shock amplitudes (strengths) as they are propagated. From point a (in Figure 3.5), the pressure amplitudes have converged to the same value. If the pressure amplitude at a is known, tracking back to the initial amplitude would be impossible

(without any other information) because any number of initial amplitudes could have resulted in the same value after a large time of flight, due to nonlinear propagation.This is an important characteristic to be kept in mind when nonlinear propagation is being investigated.

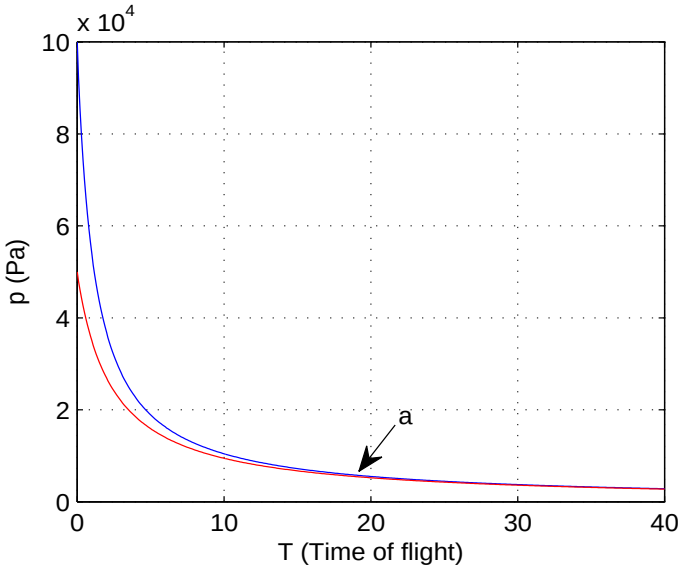

Figure 3.5: For large T values, attenuation becomes independent of initial shock strength

As the waveform advances, the waveform observed at any upstream station will be very different from that which was observed at the fan plane. The dominance of the BPF and its harmonics may be lost as energy will have been distributed to other harmonics of the rotation shaft frequency. Variations in shock amplitudes, and consequently the mid-point shock pressures, implies that some shocks travel faster than others, and there is a possibility of shocks catching up with other shocks as the waveform propagates. When a shock catches up with a shock in front of it, the two shocks merge into a single shock[17, 18]. Figure 3.6 (a-d) show an example of two shocks merging. The first of the two shocks has a higher mid-point pressure. Since the speed of propagation of the shock is dependent on the mid-point pressure, the first shock travels faster than the second. Define x_1 and x_2 as the values at pos_1 and pos_2 respectively. At a time, t_m (merging time), when $v_{s_1}t_m + x_1 = v_{s_2}t_m + x_2$ the two shocks will merge and continue to travel at speed v_s. Note that the amplitude of the shocks continue to be attenuated as the waves propagates.

The number of shocks which was initially equal to the number of fan blades will now be less. This gives an impression that the wave observed after some point far away from the fan plane may look totally unrelated to the initial sawtooth waveform. It is pointed out by McAlpine and Fisher[17] that the energy redistribution occurs for both the regular and irregular sawtooth waveforms, but the difference is that the energy is distributed

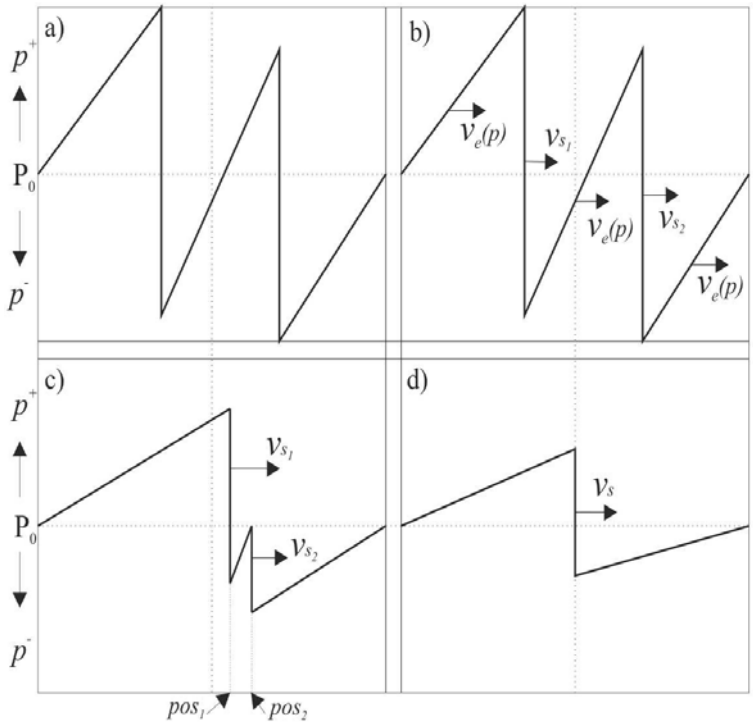

Figure 3.6: An illustration of two shocks merging

among the BPF and its harmonics in the regular sawtooth, but among all the harmonics of the rotation shaft frequency in the irregular sawtooth.

The sawtooth waveform can be decomposed into a Fourier series. The complex Fourier series (valid for both regular and irregular sawtooth waveforms) is expressed as

$$F(X,T) = \sum_{m=-\infty}^{\infty} C_m(T)\ e^{imX}, \tag{3.31}$$

where $X = 2\pi x/B\lambda$ (x is the direction of propagation of the shock front). For a regular sawtooth with B (number of fan blades) shocks, the complex coefficient of the Fourier series C_m is

$$C_m = \frac{ip_s}{2\pi\alpha}\ cos\ \alpha\pi \tag{3.32}$$

for $\alpha = m/B$ ($\forall\ m \in \mathbb{Z}$). The expansion of equation (3.32) gives the amplitudes of each BPF harmonic.

3.2.1 Analytical and Numerical Models

3.2.1.1 Analytical Models and Benchmarks

In [17], two sawtooth propagation models (Time Domain Numerical Solution TDNS and Frequency Domain Numerical Solution FDNS) were discussed using weak shock theory as the basis to model the propagation of the sawtooth waveform. The TDNS model propagates a specified sawtooth wave profile over a defined time interval and was presented as a viable model for the investigation of the propagation of sawtooth waveforms. The FDNS model was formulated as a result of the need to incorporate the effects of liner absorption for lined ducts and the 'cut-off' phenomenon[18] in hard-wall ducts, which is not possible using the time domain approach, owing to the dependence of liner attenuation on the frequency. The TDNS model, as well as modeling the propagation of a regular sawtooth, can model the propagation of an irregular sawtooth as well. Its downside is only the difficulty in incorporating duct wall conditions to the model.

The FDNS model allows for the incorporation of dissipation, due to nonlinear propagation of the sawtooth, by the transformation of the non-dimensional Burgers equation to the frequency domain. This takes the FDNS model to the same state as the TDNS model. A linear attenuation term is then added to the Burgers equation used in the FDNS model to model the effect of sound absorption provided by acoustic liners. These models were both validated against measured data and yielded plausible results.

The effect of lined ducts on sawtooth propagation was the focus in reference[18]. The speed of the flow into the duct and the consequent frequency and mode number of the sound produced affect the overall performance of the acoustic lining in the duct. An improvement in the FDNS model[17] was presented in reference[18] which enabled the number of harmonics used in the Fourier series to be significantly reduced. It is important to point out that only the rotor-alone pressure field was examined in these models. The contribution of sound/noise from flow distortions and in-duct interactions were assumed to be very small[18].

The dominant tones predicted by the model for the hard-wall case are those at the harmonics of the rotation shaft frequency (buzz-saw noise). For acoustic liners optimized for the attenuation of buzz-saw noise, at transonic fan tip speeds at which the buzzsaw noise is not yet dominant, the BPF harmonics are predicted to be dominant.

The model of propagation presented by Uellenberg[41] is similar to and based on the theory used by McAlpine and Fisher[17, 18]. This model (referred to as the modified Hawkings' Method) was used to propagate the unsteady pressure measurements from an engine test. The results of the propagation model were compared with results from measurement for various conditions. It was found that the waveform evolves rapidly with buzz-saw tones appearing very quickly as propagation progresses. The production

of buzz-saw tones was said to reach a peak within a particular range of axial distance from the fan plane and, after this point, independence of the attenuation of tones from the initial shock strength was observed[41].

The generation of buzz-saw noise, although possible through other interactions of the pressure field with flow distortions, is predominantly as a result of the rotor-alone pressure field. It is this same rotor-alone pressure field that interacts with flow distortions and may in the process produce buzz-saw-like tones. This distinction is important to clearly define the two modes of generation due to the same rotor-alone pressure field's involvement in both. At high frequencies, the efficiency of nonlinear propagation process is higher and the dissipation increases as energy is moved from lower to higher frequencies[21]. This process of energy transfer is called Nonlinear Attenuation.

The presence of acoustic liners in the duct bring in an additional effect to the propagation as the liners are installed to attenuate fan noise. The absorption offered by the liners are frequency-dependent and, therefore, different tones will be attenuated at different rates. Various flow issues (unsteadiness, turbulence and flow boundaries) affect the performance of acoustic liners. Also, the engine operation conditions can influence the choice, tuning and use of acoustic liners. A reliable prediction model of the buzz-saw noise produced in the inlet duct of a turbofan aircraft engine must factor in the effects of the acoustic liner(s), as well as the effects of variations in the pressure field produced by the fan (since every blade has a unique signature).

All the models discussed in this section are propagation models, and they all require an input defining the initial sawtooth waveform at (or very close to) the fan plane. As seen in [41], this initial waveform was extracted from measured data taken at a point in the duct very close to the fan blade tips. Experimental measurements from a model fan rig with a number of microphones installed at various axial positions within the inlet duct was the source of experimental results[21]. This experiment was conducted for hard-wall and lined cases which allowed for the comparison between the results of the two duct wall conditions. The acoustic liner was arranged in such a way that it had two sections with different characteristics in order to achieve different attenuations. In the case of the hard-wall the propagation was carried out directly, but for the lined wall case, propagation included the acoustic liner absorption.

From the results, it was inferred that the variations in stagger angle of the fan blades directly affected the amplitude of the tones[21]. In the comparisons between the predicted and the measured frequency spectra for the rigid wall case, there was a reasonable level of agreement especially at frequencies at which dominant tones occurred. An absorption term was included in the predictions to account for the cut-off of the lower-order modes. This is to enable a more reliable prediction of modes at the rotation shaft frequency and its first few harmonics. For the duct with acoustic liners, the prediction model employed the decay rates of the least attenuated modes to evaluate the results. For this

lined duct case, the prediction and measurements did not agree as well compared with the rigid duct case. The first five harmonics of the rotation shaft frequency seem to be well predicted for all the fan speeds considered.

Agreement of the FDNS predicted results and measured data dropped off and was significantly less than the measured values from about the fifth harmonic of the rotation shaft frequency and the blade passing frequency. Over-prediction by the FDNS is observed in the plots for the higher harmonics especially from about 2×BPF to 4×BPF. This over-prediction lessened with increasing fan speed, so the prediction of the harmonics of the rotating shaft less than the BPF seemed to improve as well at higher fan speeds. Experimental results in reference[21] pointed out the fact that tones at lower-harmonics of the rotation shaft frequency – low frequency buzz-saw tones – may well be attenuated to some degree by the acoustic liners but these liners may have much less effect on the high-frequency buzz-saw noise away from their optimum. Since liners are optimized for particular frequency ranges, as the fan speed increases, more modes become cut-on thereby increasing the number of modes that will be less well attenuated by the liner[21].

An understanding of the interactions and processes occurring at the boundary layer interface between the incoming flow and the duct wall or the acoustic liner allows for the addition of the shear flow effect to the FDNS model employed in the prediction of buzz-saw noise. It is stated clearly that the boundary layer can act to shield the acoustic liners thereby affecting their performance. This is what is referred to as boundary-layer shielding[42]. The in-duct flow was still taken as uniform flow away from the wall or the acoustic liner, but near the wall a boundary-layer shear profile is present[42].

The presence of a boundary layer is expected to cause a refractive effect on the sound. Upstream sound waves will be refracted away from the surface of the acoustic liner thereby reducing the level of attenuation that the acoustic liner will have otherwise offered. The decay rates of modes are expected to be less than those calculated for a uniform flow because of the presence of the boundary layer[42]. At high frequencies the acoustic liners could be completely shielded, that is, the sound may be totally refracted away from the acoustic liner making the liner surface seem in effect a rigid wall.

The FDNS model was also the foundation of investigations in shock wave propagation in reference [47]. Although this was a study of propagation in a hard wall, the study was able to incorporate a non-dissipative form of the Burgers equation and methods of dispersion and modal attenuation. This was in the attempt to include the effect of the shock occurring over a fraction of the length of the blade span and not only at the tip in the model. Arguments in [47] point out the need for a three-dimensional model in the prediction of propagation of the shocks due to the extension of the shock over a significant section of the blade span. This will mean the inclusion of radial variations in the shock modelling. It may be extremely tedious and difficult to include all these effects but as numerical simulation capabilities improve this may become more realizable.

Fernando et al[47] attempted, in their subsequent work[48], to take into consideration the interactions of modes in nonlinear propagation of waves with changing amplitudes of the modes. This was expected to generate nonlinear interactions among higher-order modes. An understanding of these interactions is useful in order to properly predict the nonlinear propagation of waves in two or three-dimensions. The recent attempt at a uniform flow three-dimensional nonlinear propagation semi-analytical model [49] gives a rudimentary insight into the scale of complexity of such endeavour. Fernando et al pointed out that the assumptions in references[21] and [42] that the pressure field is a superposition of only the first radial order due to the shock being only at the fan blade tip can be questioned, due to the fact that the shocks actually extend over a fraction of the radial length of the fan blades. The argument is that radial modes other than the first radial mode may also occur due to the significant radial range of the shock. However, the higher radial orders may be 'cut-off'

To completely add the contributions of various sources of Buzz-saw noise will mean an addition of results from models predicting the contribution of other sources or the incorporation of the effect of these other sources into the existing rotor-alone pressure field model. The latter may further complicate the FDNS propagation model. In reference [50], perturbation in the non-uniform steady pressure near the fan in a circumferential direction was found to significantly increase the fan noise especially as the fan operating speed was increased. This also allowed for buzz-saw-like noise to be observed at transonic (very high subsonic) fan blade tip speeds. Perturbation of the pressure pattern increases the likelihood of changes in the strengths of the shocks in the azimuthal direction, and also influence the merging of the shocks since the shock amplitudes have been altered[50].

It is indeed more pressing to accurately predict the rotor-alone contribution to the overall buzz-saw noise as the rotor-alone pressure field is overwhelmingly the main source of buzz-saw noise. The comparisons between measurements and predictions [21, 41, 42, 47, 51–53] give insight into the areas of the propagation model that need improvement. Agreement between the results of the prediction model and the measurements dropped off as distance increased away from the fan[51]. This slight disagreement was clearly a phase angle difference as the predicted and measured amplitude remained in the same order for all the stations of measurement considered. The differences were ascribed to the fact that the model fan used in experiments did not have a straight inlet duct as assumed in the prediction model[51]. The achievements of one-dimensional modelling of the nonlinear propagation of the fan-blade tip shock system in form of a sawtooth waveform using 'weak' shock theory is significant, and one that can be taken forward, enhanced and improved upon.

3.3 Summary

The foundational theory for nonlinear propagation and corresponding duct acoustic theory are presented. Analytical equations and equations for nonlinear propagation are also presented for wave propagation in ducts and for nonlinear propagation of sawtooth waveforms in cylindrical intakes. Features of existing nonlinear propagation models, simplifications applied to complex features of rotor-locked pressure field and their prediction capabilities are discussed in this chapter. These are much less computationally expensive models when compared to full computational fluid dynamics modelling, using Navier-Stokes equations, which can also be used to capture the propagation of shocks in full intake simulations.

Chapter 4

Source Sawtooth Pressure Waveform Modelling

4.1 Background

The prediction of the propagation of shock waves generated at the fan tip rotating at supersonic speeds is important to the control of buzz-saw noise. In order to correctly validate any prediction model, results of such models are to be compared against measured data. This is a direct method of judging how closely the prediction model approximates the real life situation.

Simulating the nonlinear propagation of the pressure field generated at or close to the fan plane of an inlet duct in the time domain requires the specification of the characteristic pressure waveform. This waveform is basically a system of shock and expansion waves at the fan plane or at a specified start point near the fan plane. The start point is generally just forward of the fan, that is, the location of the pressure transducer installed closest to the fan. Knowledge of the pressure waveform at this axial position allows for the upstream propagation of the pressure field inside the inlet of the duct to be simulated. A comparison is therefore possible between measured data and results of the prediction model at various axial positions in the duct.

However, at the time of this study, only the measured SPL values were provided by Rolls-Royce for comparisons with predictions. Therefore it was necessary to generate a realistic source waveform, for input to the propagation model, utilising the measured SPL data acquired close to the fan. Owing to the absence of phase information in the available measured data (sound pressure level spectrum over a range of engine order frequencies), the production of suitable pressure waveforms for a time-domain-based prediction model is not straight-forward. The availability of phase information allows for the construction of a representative waveform which is unique to the characteristics

of the particular fan which produced the pressure field. Without the phase information, it is only possible to obtain a waveform which will give a satisfactory sound pressure level spectrum matched as close as possible to the measured spectrum.

Past research work on buzzsaw noise with comparisons between measurements and prediction [17, 18, 21] have made use of random phases together with the measured sound pressure levels to generate the complex amplitudes of the Fourier series representing the starting waveform. It is important to note that measured data are generally in the range up to four times the blade passing frequency (BPF). This is basically a limit dictated by the resolution achievable for high frequencies by the measurement systems used.

The allocation of random phases to the measured data is justified by repeating the random allocation a number of times, typically around a hundred times, and subsequently averaging results from a set of simulations. This helps to smooth out biases or errors that may have been generated by an outright use of a single set of random phases. This method was used in the FDNS propagation model which is a frequency domain nonlinear propagation code[17]. Recently, Thisse [54] proposed the use of actuators and sensors mounted on the fan to capture blade-to-blade differences at the fan plane in order to determine an approximate start waveform. This method is only useful when access to the actual fan is possible but focus is kept in this thesis on existing experimental data or for cases where only sound pressure level measurements are available as is commonly the case.

For a model in the time-domain, using the same method of random phase allocation with the measured data close to fan, in order to produce an initial waveform to be propagated, did not work as well as it seems to have done in the frequency-domain model. This is attributable to the need of an actual time series of shocks and expansion waves for the propagation in the time domain. In the time domain, employing random phases across the measured spectrum showed that the BPF and its harmonics for the starting waveform were all under-predicted when the spectrum of the waveform is compared with measured spectrum. The under-prediction of the initial waveform is expected to affect the propagation to other axial positions making the sound pressure levels predicted at these position to be under-predicted as well. In summary, the lower values at the BPF and its harmonics imply that the pressure field at the start point is not sufficiently represented and very good agreement can not be expected between predictions and measured data.

The regular sawtooth waveform with 20 shocks shown in figure 4.1(a) has tones at BPF and its harmonics (figure 4.1(b)) and its phase angles alternate for these tones between $-\pi/2$ and $\pi/2$ (figure 4.1(c)).

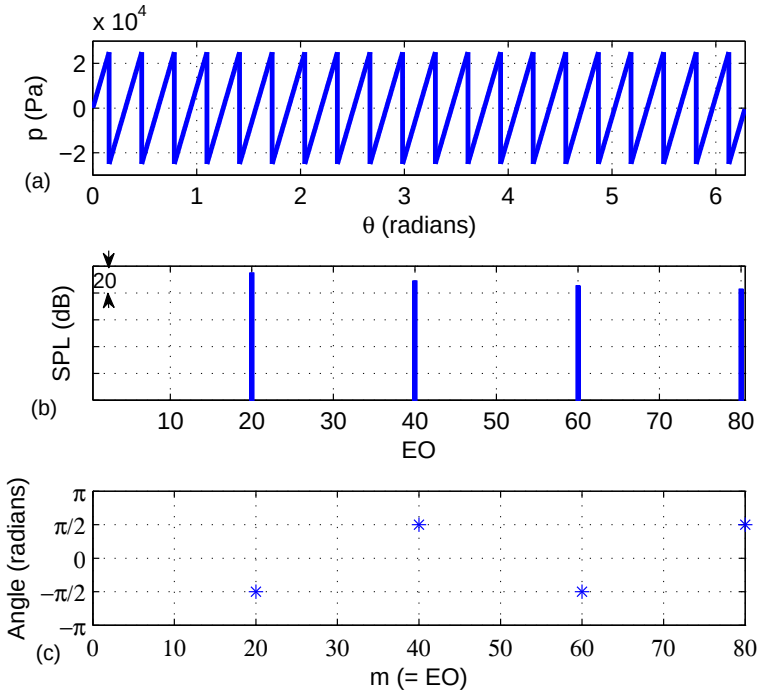

Figure 4.1: Regular sawtooth (a)waveform (b) its frequency spectrum and (c) phases angles

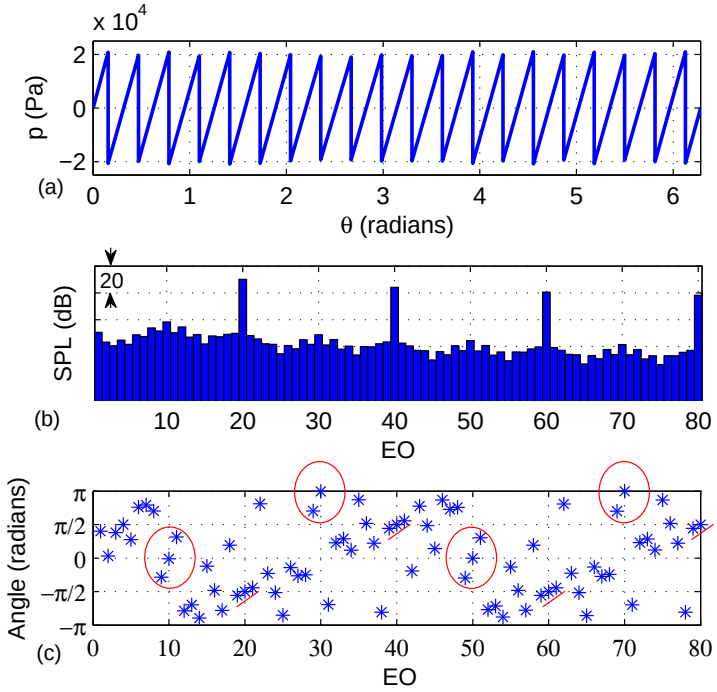

Figure 4.2: Buzzsaw-like sawtooth (a) pressure waveform (b) its frequency spectrum and (c) phases angles

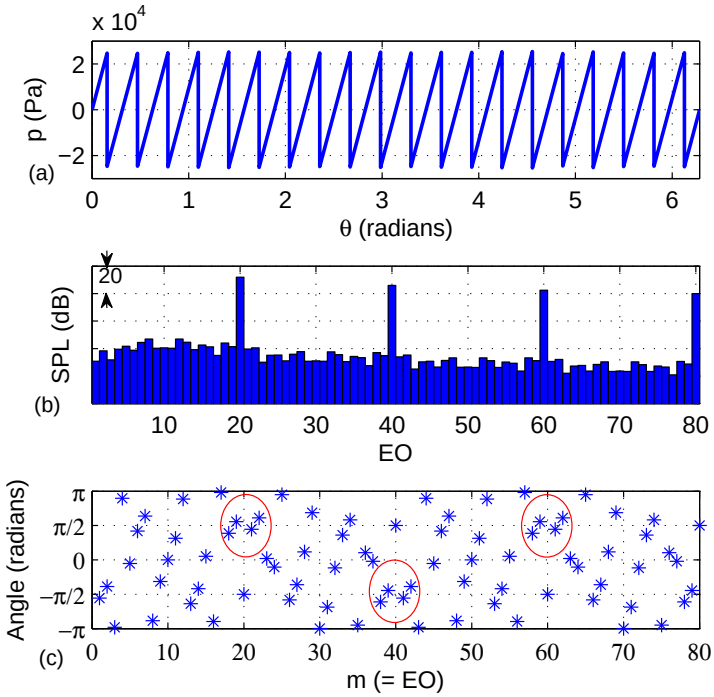

Figure 4.3: Phase angle order example 1: (a) Pressure waveform (b) its frequency spectrum and (c) phases angles

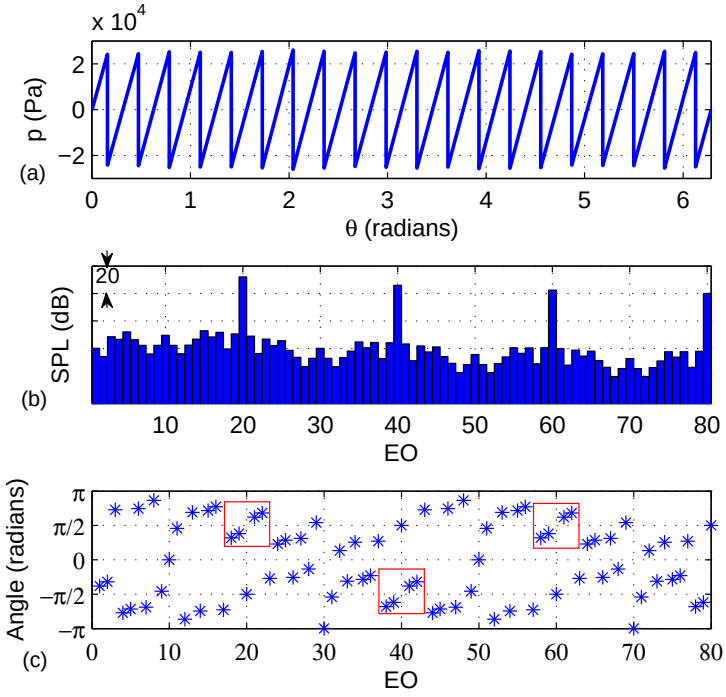

Figure 4.4: Phase angle order example 2: (a) Pressure waveform (b) its frequency spectrum and (c) phases angles

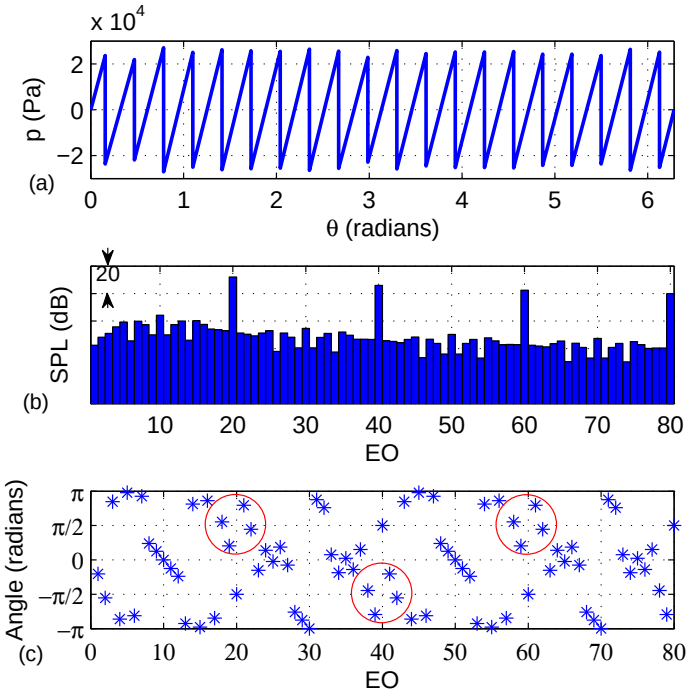

Figure 4.5: Phase angle order example 3: (a) Pressure waveform (b) its frequency spectrum and (c) phases angles

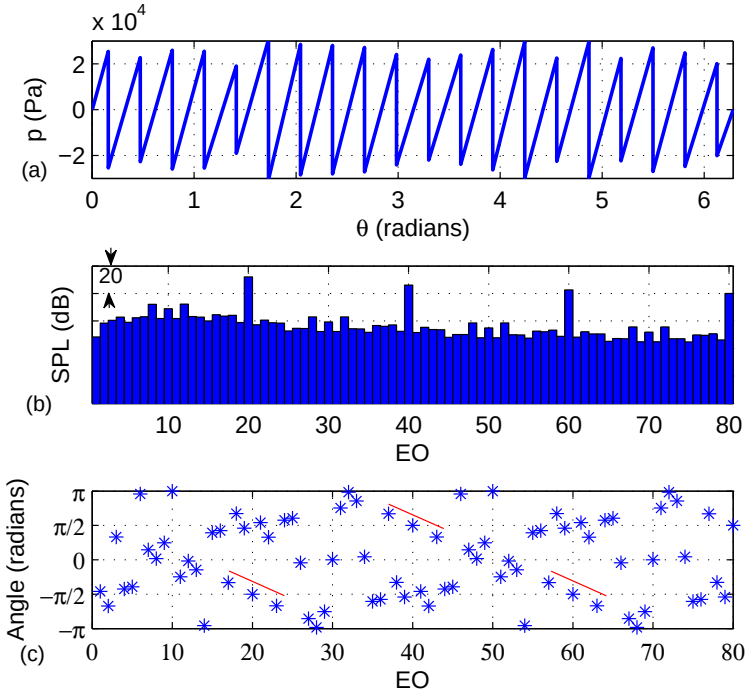

Figure 4.6: Phase angle order example 4: (a) Pressure waveform (b) its frequency spectrum and (c) phases angles

4.1.1 Waveform Phase Investigations

The inability of the use of entirely random phases together with measured data to generate a suitable starting pressure waveform led to the investigation of the characteristics of the phases of waveforms that are representative of real-life measured examples. Various sawtooth pressure waveforms with frequency spectrum similar to measured buzz-saw spectrum were investigated. Their phase angles were plotted out to see whether there were any patterns or correlations among the phases.

Table 4.1: Sawtooth profiles for phase angle investigations

	Deviation from average shock amplitude (%)	Deviation from mean shock spacing (%)	Deviation from mid-point pressure (%)
Waveform 1	1	1	0
Waveform 2	2	1	1
Waveform 3	5	1	0
Waveform 4	10	1	1

Figure 4.2(a)-(c) shows an example of the pressure waveform, its SPL-frequency spectrum and plot of phase angles. From figure 4.2(c) it can easily be observed that the phases are not random but are to a very notable extent in a pattern. Every pressure waveform investigated was seen to have a unique pattern to the distribution of its phases. To further appreciate distribution of phase patterns in the spectrum, using the areas marked in red in figures 4.3-4.5, the repeated pattern can be more easily spotted. In Figure 4.6, the phase pattern is very obvious. Figures 4.3-4.6 are in order of increasing perturbation (Table 4.1) of the sawtooth pressure profile (see figures 4.3(a),4.4(a),4.5(a) and 4.6(a)) and the increased perturbation is evident in their respective spectrum (figures 4.3(b),4.4(b),4.5(b) and 4.6(b)) in the increase in the sound level of the inter-BPF harmonics. Despite the increase in perturbation levels in the sawtooth, the phases still come out in their patterns.

A notable observation is that the patterns appear to be repeated over every harmonic of BPF but are shifted by π radians after every BPF harmonic. Another interesting characteristic observed is that the pattern up to BPF, which is then repeated, appears as a single pattern up to $\frac{1}{2}$BPF. This pattern is rotated 180 degrees anticlockwise about the $\frac{1}{2}$BPF value for other tones up to BPF i.e. for phase up to B (number of fan blades), phase(m) = - phase(B-m); where m = 1,2,...,B-1. This observation strengthens the notion that the phases are not random. This insight into the pattern of the phase angles allows that if random phases are allocated to tonal amplitudes, then it is sufficient to allocate the random phases up to BPF and thereafter employ the π phase shift for subsequent BPF harmonic ranges. This can be expressed as

$$\xi_m = \xi_{(\bar{n}B+m)} + \left|\sin\left(\bar{n}\frac{\pi}{2}\right)\right|\pi \tag{4.1}$$

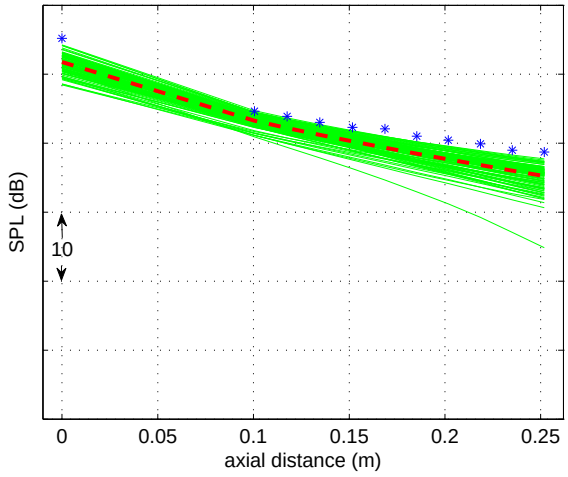

Figure 4.7: BPF tone attenuation of measured data against those of 100 waveforms generated from measured data and random phases [Key: * Measured data; — 100 predictions; - - average of predictions]

where ξ are pahse angles, m equals the engine order and $\bar{n}B$ equals the engine order of the $\bar{n}$th BPF harmonic. This allows for reduction of the use of random phases over the whole measured spectrum to just random phases up to the BPF tone.

Further investigation by perturbation of shock amplitude, shock mid point pressure and shock spacing of a regular sawtooth waveform show that although every waveform has a unique pattern for the distribution of its phase angles, the phase angles for $\frac{1}{2}$BPF and BPF tones do not change significantly from their values in a regular sawtooth waveform. From figure 4.2(c), the phase angle for the $\frac{1}{2}$BPF and BPF tones are $\pi/2$ apart and this is maintained for all their harmonics and are approximately equal to the value they would have been if the pressure waveform was regular. The observation just discussed suggests that the number of random phases needed to be allocated can be further reduced.

It can be inferred then that random phase angles can be allocated up to engine order $\frac{1}{2}$BPF-1 only. Then using the ordering of the phases discussed, the phase angles for engine order $\frac{1}{2}$BPF+1 up to BPF-1, are given by

$$\xi_m \equiv -\xi_{(B-m)} \quad \text{for} \quad m = \frac{1}{2}B + 1, \cdots, B - 1. \tag{4.2}$$

The measured data used in this study are those obtained from fan model-scale rig test programme conducted by Rolls-Royce plc. Data was acquired while the test engine was running 90% of maximum rating. At this engine speed the fan blades tip speed is just supersonic ensuring the presence of the shock at the tips and the viability of the data for this study.

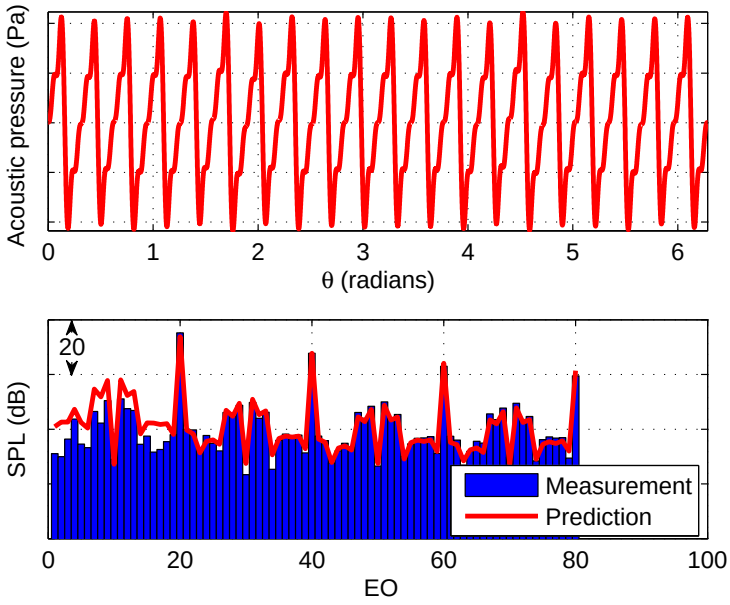

Figure 4.8: The resulting sawtooth and spectrum

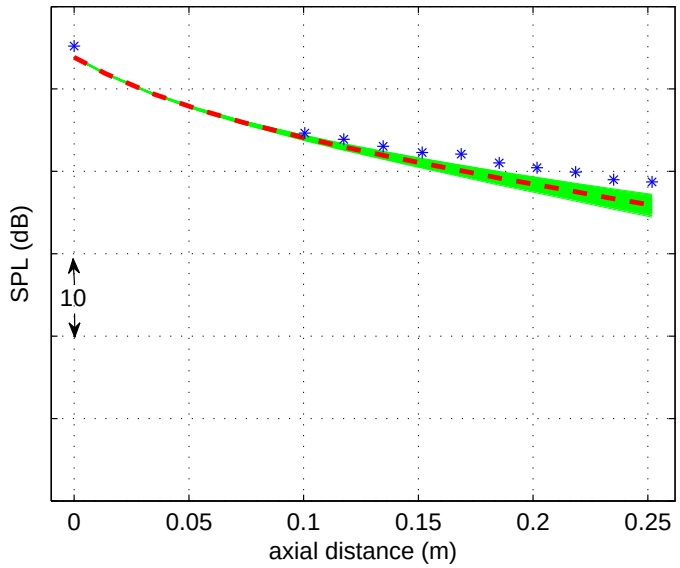

Figure 4.9: Attenuation of BPF tone. [Key: * Measured data; — 100 predictions; - - average of predictions]

If sawtooth waveforms are constructed from measured data using random phases up to BPF and propagated over an axial distance 0.25m, figure 4.7 shows the BPF tone attenuation obtained for the nonlinear propagation of these sawtooth waveforms. In the figure, 100 waveforms constructed from 100 different sets of random phases (for tones up to BPF) are propagated in a hard wall duct. For all the waveforms, the BPF tone at the start is under-predicted and are spread over a 7dB range. Deviations are observed through the various axial stations, where measurements were taken, and even larger overall deviations are seen at the position of the last axial measurement as a result of the deviations at the starting point.

We consider the same measured data in figures 4.8 and 4.9 but with random phases allocated up to $\frac{1}{2}$BPF-1 as explained above. Figure 4.8(a) shows the average waveform for 100 waveforms propagated while figure 4.8(b) shows the average spectrum for the waveforms against the measure data. Here, it is clear that the reduction of number of random phases has allowed the values at the start point to approximately be the same although still under-predicted when compared with measured data (Figure 4.9). The effect of the various phases can still be seen in the propagation which has about 3dB deviation for the 100 waveforms at the end of propagation.

There is a considerable improvement just by the reduction of the number of random phases employed in the reconstruction of the waveform with basis on the knowledge that the phases are not entirely random but in particular repeated patterns. Comparing figures 4.7 and 4.9, the BPF tone is better predicted in the latter and so also the average line of BPF attenuation (blue lines) is better in the latter as well. Note, the vertical axes ranges are different in the two figures.

In both approaches to phase allocation, the level of the BPF tone at the start point is less than the actual BPF tone level measured and this difference affected the predictions at other axial stations as well. The aim of the methods discussed in the next section is to ensure that the starting levels for the prediction and measurement are as close as possible.

4.2 Generating Waveforms that match the measured data at the start position

In order to match the tone levels of the measured spectrum at the start position (near the fan plane), three methods have been employed - Extrapolation Method, Optimization Method and BPF Scaling method. These methods are aimed at obtaining a suitable pressure sawtooth that will produce a SPL-frequency spectrum that closely matches data measured near the fan.

It is important to note that the sawtooth pressure waveform is only a representation of the physical phenomenon, and does not include all the features of actual in-duct pressure waveforms. The assumption of a one-dimension shock wave system which exists at the tip of the fan blades is an approximation which reduces the complexity of the analysis. The expansion waves are assumed to be linear from shock to shock in the one-dimensional approximation. Owing to this simplification, the results from these methods were not expected to match the measured data exactly, but the methods are aimed to match the measured data sufficiently as close as possible.

4.2.1 Extrapolation Method

The ability to reconstruct a sawtooth waveform near the fan plane using measurements of the SPL-frequency spectrum depends to some extent on the number of harmonics which were measured. In the measured data, up to four times BPF harmonics is available. Studies have shown that reconstruction with this frequency range yields sawtooth waveforms that have SPL-frequency spectrum with tones, most especially the BPF and its harmonics, underestimated. This is because the values available up to 4×BPF are not sufficient to reconstruct a suitable waveform. In fact, the shock amplitudes in the waveform are, to a significant extent, undervalued because of the lack of higher frequency values in the spectrum.

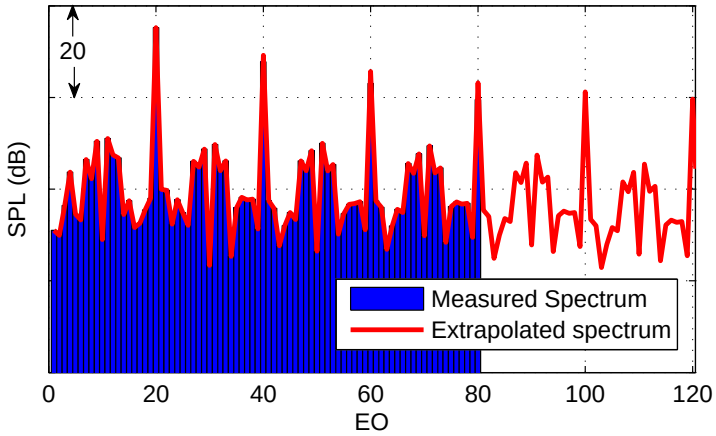

Figure 4.10: Plot of extrapolated spectrum against measured spectrum

As shown in Figure 4.10, the 1st step in this method entails the extension of the measured SPL-Frequency Spectrum to a sufficient range by creating higher frequency values which will then allow for the generation of suitable sawtooth waveform for the pressure field.

Procedure of extrapolation

The extrapolation of the measured SPL-frequency spectrum was carried out using information available from the measured spectrum. It is important to note here that, for the fan with 20 blades considered here, the number of harmonics of the BPF needed to generate a pressure waveform which does not underestimate the BPF tones was first investigated. This was done by using computer generated sawtooth waveforms, decomposing the sawtooth waveforms to the frequency components and reconstructing back the waveform using increasing number of BPF harmonics. The gradual increase of the number of harmonics of BPF used in the reconstruction allowed for the identification of the number of harmonics needed before a waveform with similar shock amplitude levels are obtained.

During this investigation it was discovered that a spectrum with a range of at least 6 BPF harmonics is required to get a sawtooth with closely matching shock amplitude levels.

It should be noted that the sawtooth profiles obtained with the reconstruction look noticeably different from the original sawtooth even when a sufficient range is used. This is because a particular frequency spectrum can be generated by a number of different sawtooth profiles especially when random phase angles are used. A closer look at the waveforms shows that similarities exist still between the profiles. This can only be seen when individual shocks in the reconstructed sawtooth are compared with shocks in the original sawtooth. In the ideal case, the shocks in the reconstructed sawtooth will be the same shocks as in the original sawtooth but have their order rearranged.

When the range of frequencies employed for the reconstruction of the sawtooth is further increased, the shock amplitude levels exceed the levels in the original sawtooth. This observation is due to the Gibb's phenomenon which occurs at the junction between the expansion waves and the shock waves. Figure 4.11, a section of the pressure profile, shows the observed Gibb's phenomenon in that part of the waveform.

The reconstruction routine code in MATLAB® was written to reconstruct the sawtooth waveform smoothly by using the maximum and minimum values just at the shocks. The presence of the overshoots of the Gibb's phenomenon therefore, cause over-estimation of pressure amplitudes across each shock in the sawtooth waveforms. These overshoots, which have been widely studied for various wave types in signal processing, are relative to the number of terms used in the reconstruction. Hence, a correction of the overshoot can be applied with respect to the number of BPF harmonics used in the construction to correct to the right shock amplitude levels.

Given that measured data (frequency spectrum) is commonly available up to around 4 times BPF, extrapolation of the spectrum is employed in this study to get the required range of frequencies for reconstruction of a suitable waveform. Extrapolation can be

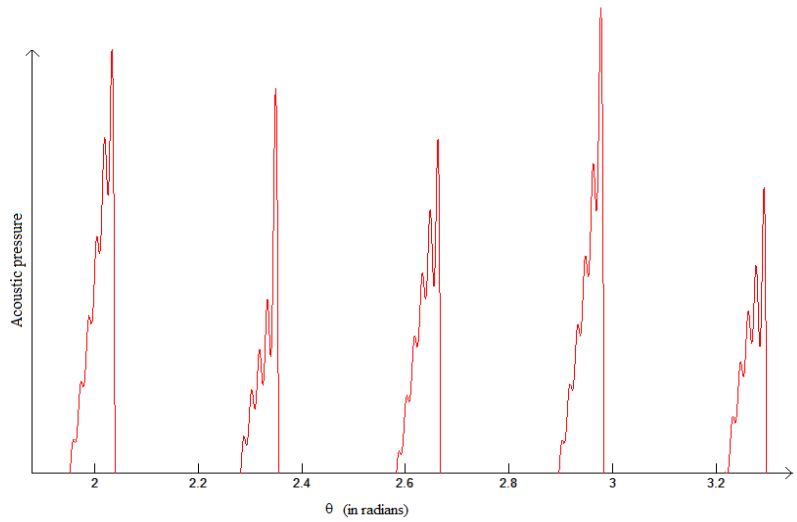

Figure 4.11: A section of the pressure profile showing Gibb's phenomenon observed

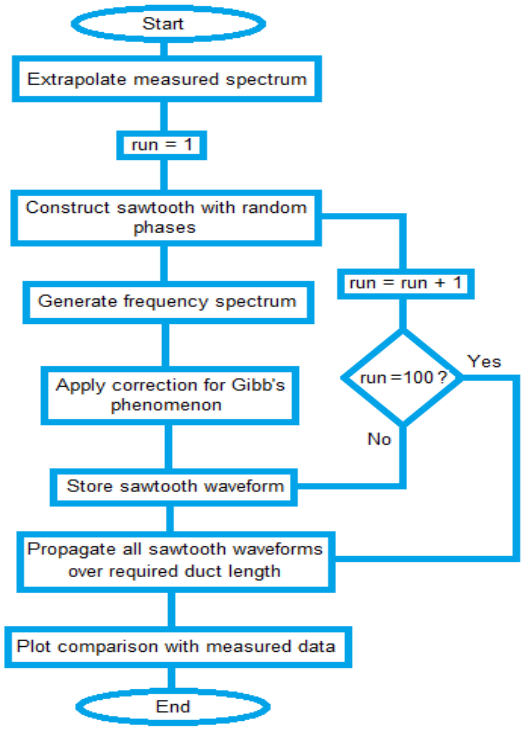

Figure 4.12: Flow chart showing the main stages of extrapolation method code

done up to any multiple of the BPF since the Gibb's phenomenon can be corrected, but it is better to limit the extrapolation to the minimum required number of modes as the extrapolated part of the spectrum is a projection of what may have been measured at higher frequencies, and, hence, it is useful to limit the extent of extrapolation to avoid marring the measured spectrum.

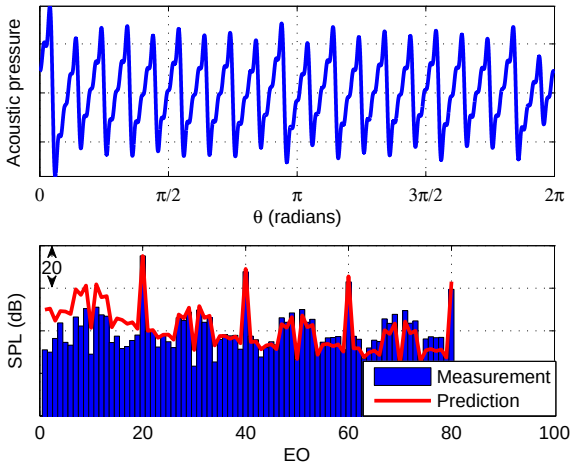

Figure 4.13: Extrapolation Method: average sawtooth waveform and spectrum, and measured spectrum

Here, the extrapolation is done up to 6×BPF making sure to keep the length of the extrapolation less than (in this case half of) that of the originally measured spectrum. Prior investigations with measured data analysis on irregular sawtooth waveforms were carried out to compare extrapolated spectra to original spectra. This enabled the evaluation of the extrapolation routine to be assessed to see how close the extrapolation values are to actual values.

Extrapolation is achieved by assuming that BPF harmonics in the spectrum decay in a similar manner to a regular sawtooth with the same level at BPF. This assumption is supported by the fact that the frequency spectrum to be extrapolated was measured at a position close to the fan, a position where non-uniformities in the sawtooth waveform are at their minimum. Also, the tones between the BPF harmonics are assumed to decrease by the same amount over every BPF harmonic. Figure 4.12 shows all the main steps of the extrapolation method. The measured spectrum is fed in as an input file and results output are shown in figures 4.13 and 4.14.

In figure 4.13, the top plot is that of average of 100 waveforms obtained after the extrapolation method has been implemented. The bottom plot shows an average of the frequency spectrum of the 100 waveforms compared against the measured data. In this figure, it can be observed that most of the tones less than the BPF are overpredicted. The opposite happens at the other end of the spectrum where the tones are underpredicted.

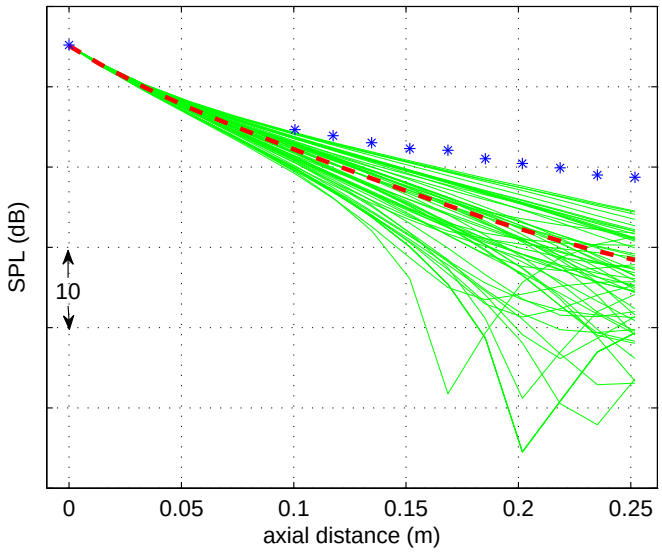

Figure 4.14: Extrapolation method: attenuation of BPF tone [Key: * Measured data; — 100 predictions; - - average of predictions]

However, the BPF tone is matched, but harmonics of the BPF tone are slightly over-predicted as well. The attenuation of the BPF tone, for the 100 waveforms, over the propagation distance in the duct can be seen in figure 4.14.

As required, the extrapolation method ensures that the starting BPF tone level matches the measured BPF tone level. Every waveform generated through the extrapolation method had a BPF tone matching the measured data. On propagating these waveforms, it is observed from figure 4.14 that the over-predicted levels of lower frequency tones, less than the BPF tone, causes more rapid attenuation of the BPF tone as energy is transferred more rapidly from the BPF tone. Also, the unique characteristic of the waveforms, traceable to the random phases from which they were generated, and the interactions between the shock waves directly affected the energy transfer among various frequencies. At the end of propagation, over 20dB difference is observed for the BPF tone for the 100 waveforms propagated. This large deviation is reflected in the average line which is equal to measured data at the start but 10dB lower at the end of propagation.

In summary, the extrapolation method allows the starting BPF tone levels to be matched but the structure of any waveform generated through this method (the phases and the order of the shocks) determines how closely results compare with measured data.

4.2.2 Optimization Method

The optimization method is a direct attempt at matching the levels in the measured SPL-frequency spectrum without need of extension or extrapolation of the measured

data. It entails using a base sawtooth and changing various parameters until a suitable sawtooth which generates an SPL-frequency spectrum which is as close as possible to that of the measured spectrum. This is second approach considered in order to match the levels in the SPL-frequency spectrum measured near the fan plane.

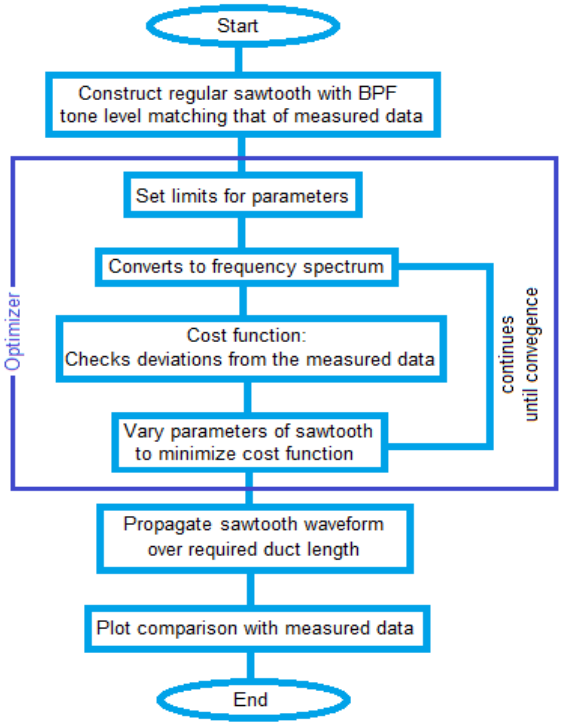

Figure 4.15: Flow chart showing the main stages of optimization method code

Procedure of optimization

Optimization is carried out by using the base regular sawtooth as the start point. This regular sawtooth is constructed to have the same BPF tone level as the measured data. The shock amplitudes are equal, shock mid-point pressures are set to the ambient pressure and spacing between the shocks are also kept regular. This forms a convenient platform from where the optimization routine can be launched. The optimization code was written to carry out various steps aimed at constructing a sawtooth waveform that will generate a frequency spectrum which will closely approximate the measured data as laid out in figure 4.15. Figure 4.15 shows the main steps in the code written for the optimization method. At the start of the method, the measured spectrum is utilized as an input and a regular sawtooth waveform is constructed. Other steps are carried out and the output is an irregular sawtooth representative of the measured data.

Using the 'fmincon' function in MATLAB, the shock amplitudes (the highest and lowest pressure values across each shock) and shock spacing are set as variables with realistic

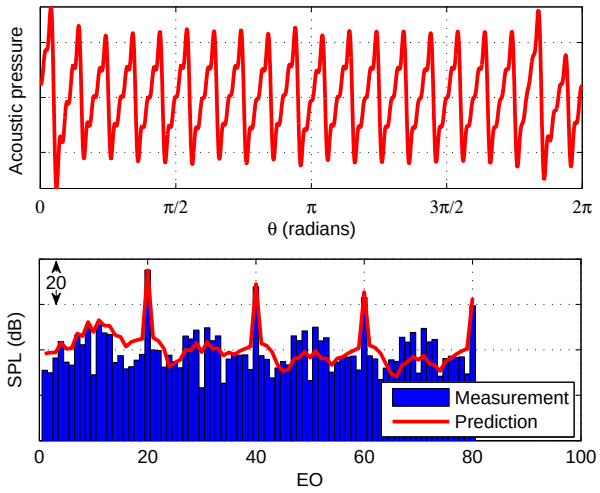

Figure 4.16: Optimization method: Predicted sawtooth waveform and spectrum, and measured spectrum

upper and lower bounds. The function optimizes these shock parameters by generating a frequency spectrum for each iteration and trying to minimize the difference between the tones in the spectrum and the measured data. The minimization is controlled by a cost function that evaluates the deviations of tones in the two spectra at individual frequencies. As a built in function in MATLAB, 'fmincon' runs many iterations using the parameters within their user defined preset boundaries until some form of convergence is reached. This is the region labelled as the optimizer in Figure 4.15.

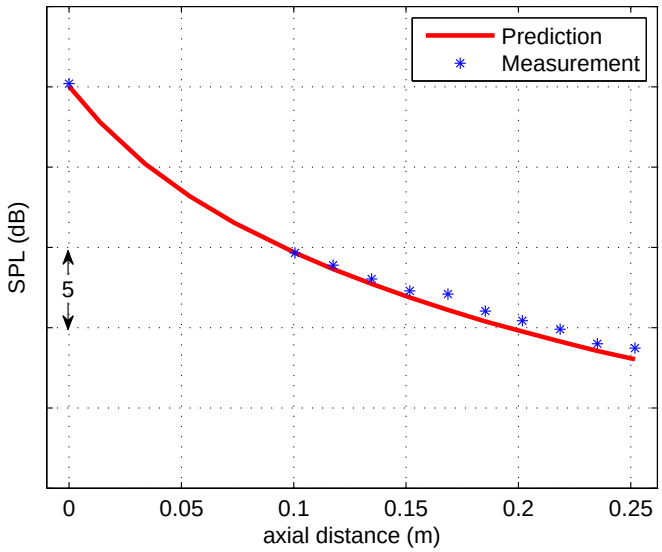

Figure 4.17: Optimization method: Attenuation of BPF tone

It is important to mention that the default number of iterations per parameter for the

function 'fmincon' is 100. The function stops and outputs a result to whatever degree of convergence has been achieved after the default number of iterations. It may be useful in some other studies to increase this number by specifying a higher number of iterations but the results presented here are for the default number of iterations as increasing the number of iterations in this case did not give very significant improvements to the results. This is discussed in the discussion section.

Figure 4.16 shows an example of the result of the optimization method. The top plot shows a representation of the sawtooth pressure waveform predicted to represent the measured data. The bottom plot in figure 4.16 is the spectrum generated from this sawtooth against the measured spectrum. It was observed that the general level of the predicted spectrum was close to that of the measured spectrum up to BPF (and a few tones after the BPF) but after this point, the inter-BPF-harmonic tones are under-predicted and this under-prediction increases as the frequency increases. On propagating this predicted sawtooth over an axial distance of 0.25m, the comparison of the BPF attenuation between the predictions and measurements is shown in figure 4.17. Although there exists some significant difference in the inter-BPF harmonics tones, the prediction of the BPF tone attenuation along the axial direction is in very good agreement with measured data owing to the inclination of the method to resolving the dominant tones. The resultant waveform from the optimization method can be said to be a better representation of the pressure field that produced the measured data.

4.2.2.1 Scaling Method

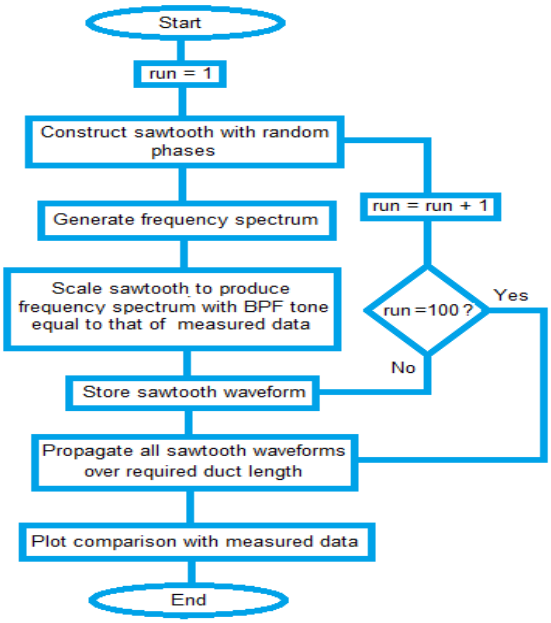

Figure 4.18: Flow chart showing the main stages of scaling method code

This method was conceived following the observation that the otherwise under-predicted levels, obtained when the measured data is used to generate a sawtooth and then decomposed to its frequency content (as shown in figure 4.9), can be scaled up to match the BPF level in the measured data. Scaling still involves the construction of the sawtooth with random phases up to $\frac{1}{2}$BPF-1 but with an added step where the sawtooth is scaled up until its frequency spectrum has a BPF tone level which exactly matches the level of the BPF tone of the measured SPL-frequency spectrum. The procedure of the scaling method is shown in Figure 4.18. It should be noted that in the scaling method, the measured spectrum is not extrapolated or modified in any way.

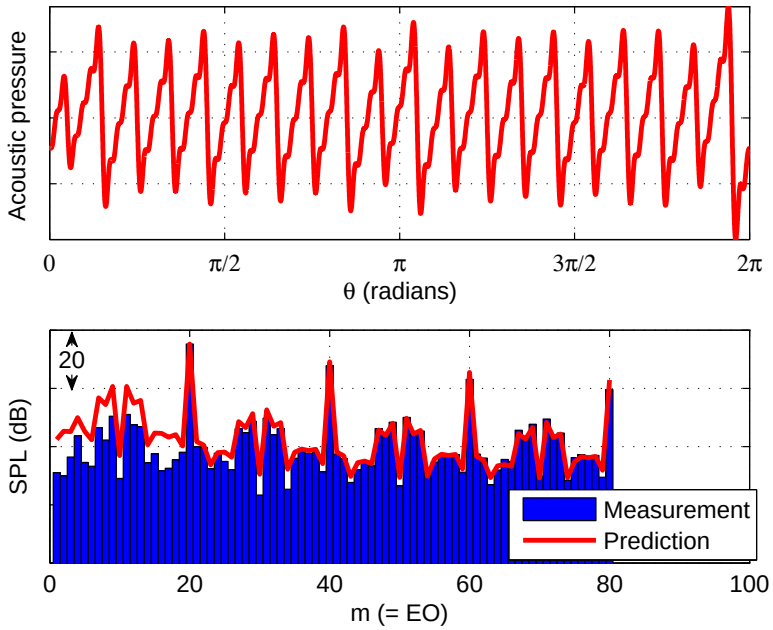

Figure 4.19: Scaling Method: Average sawtooth waveform and spectrum, and measured spectrum

Figure 4.19(a) shows a sawtooth waveform which is an average of 100 sawtooth waveforms generated from measured data and scaled to match the BPF tone level. From comparison between the averaged spectrum against the measured spectrum (figures 4.19(b)), the low frequencies are still over-predicted. Attenuation of the BPF tone for 100 sawtooth waveforms generated are shown in figure 4.20 and their average against BPF tone attenuation values of measured data.

The scaling routine, as shown in the scaling procedure diagram, ensures that the sawtooth constructed is scaled with respect to the amplitude of each shock wave in order to maintain the shock midpoint pressures of the shocks in the sawtooth before it was scaled. The shock spacings are not scaled, neither are there any phases shift incorporated in the scaling. Some effects of these choices are discussed in the next section.

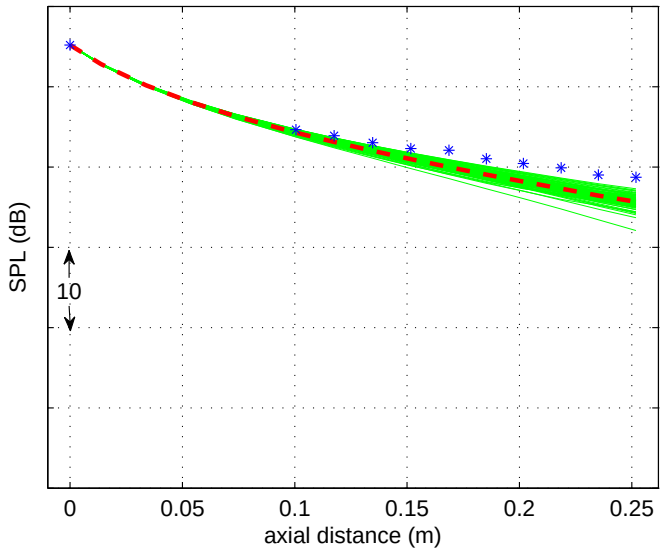

Figure 4.20: Scaling Method: Attenuation of BPF tone

4.3 Applying the Methods to Spectrum from Smooth Sawtooth Waveforms

The extrapolation, optimization and scaling methods were initially used with the spectrum obtained from a smooth sawtooth waveform. This allowed for a check on the outputs of the methods before implementing them on the measured data. A sawtooth waveform with 20 shocks (from 20 blades similar to experimental set up from which measured data was acquired) was constructed by perturbing shock amplitude, shock spacing and mid point pressures of a regular sawtooth. The sawtooth was decomposed to its frequency content up to 4×BPF (the same frequency range available in measured data). The methods were then applied to this frequency spectrum to regenerate a sawtooth waveform. Figures 4.21-4.23 show the results (comparison between sawtooth waveforms and spectra) from each method and from the random irregular sawtooth waveform.

It is notable that for all three methods (figures 4.21-4.23), better agreement is achieved when these results are compared to those when the methods were used with measured data (Figures 4.13, 4.16 and 4.19). This is because the frequency spectrum input into these methods was generated from an ideal smooth sawtooth waveform making better prediction possible for the all three methods used.

All three methods come quite close to matching the initial sawtooth waveform used to generate the input frequency spectrum (in figures 4.21(a), 4.22(a) and 4.23(a)) and the level of the matching is visible in the comparison between the spectra in figures 4.21(b), 4.22(b) and 4.23(b).

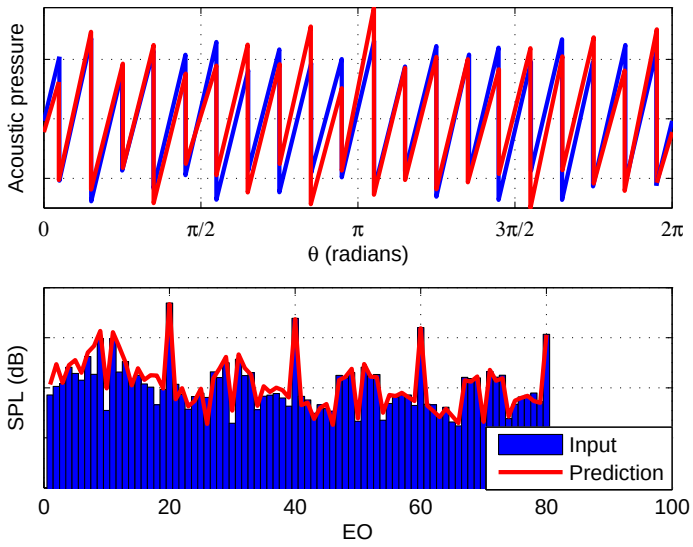

Figure 4.21: Extrapolation Method: Sawtooth waveform and spectrum comparison for constructed sawtooth and prediction

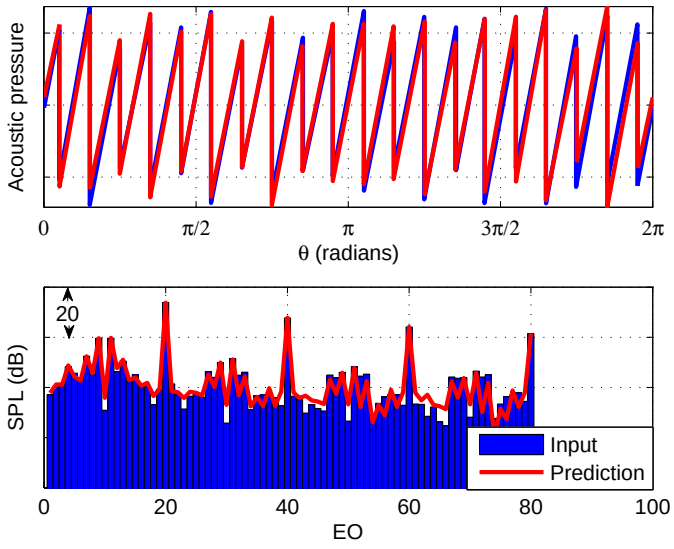

Figure 4.22: Optimization Method: Sawtooth waveform and spectrum comparison for constructed sawtooth and prediction

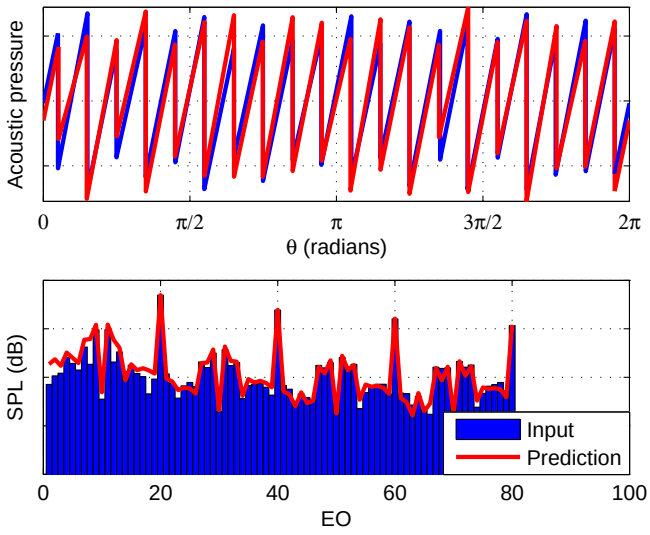

Figure 4.23: Scaling Method: Sawtooth waveform and spectrum comparison for constructed sawtooth and prediction

4.4 Discussions

The three methods that have been employed to obtain sawtooth waveforms that are representative of the measured data have generated somewhat different results.

4.4.1 Methods, Results and Comparisons

Results from the extrapolation method (Figures 4.13 and 4.14) show that extrapolation of the measured data and the use of this extrapolated frequency spectrum actually corrects the under-prediction otherwise observed when only the measured data is used. It is clear in figure 4.13 that although the BPF tone level is matched, the extrapolation raised the levels of all the tones lower than BPF. The sound pressure levels of tones higher in frequency than the BPF are closely matched up to about 3×BPF after which point the tones are slightly under-predicted. Higher BPF harmonics are slightly under-predicted as well.

Figure 4.14 sheds some light on the implications of the over-prediction of the sound level of the low frequency tones less than the BPF. These Engine orders are major tones in the nonlinearity of the propagation of the pressure waveform. The higher these tones are the greater the nonlinear character of the propagation and consequently, the greater the level of attenuation observed over the propagation distance. This is evident in figure 4.14 as it is observed that for the 100 sawtooth waveforms, although they all have the BPF tone matching the measured data taken close to the fan, the attenuation of the BPF tone is well over-predicted up to about 10dB at the axial position of the last measurement.

Only a few had similar levels to the measured data at the first axial measurement after the start point.

The optimization method, by the virtue of the steps involved, was expected to give the most suitable results because it was developed to match the measured frequency spectrum tone-by-tone. The resulting sawtooth waveform and its frequency spectrum, as seen in figure 4.16, indicates that the optimization closely matched the measured data up to about the BPF but increasingly under-predicts the higher frequency tones.

As mentioned earlier, the gradual reduction in tone levels from low frequency to high frequency evident in predictions is not present in measurements. The close matching of the low frequency tones up to BPF ensured the appropriate levels of nonlinearity and prevented the over-prediction of the attentuation of the BPF tone. As a result, very good agreement between measurement and predictions of the attenuation of the BPF are observed in figure 4.17.

Scaling the sawtooth waveform until the BPF tone level in the measured data is matched also resulted in the increase in the sound pressure levels of low frequency tones (figure 4.19) causing a greater level of nonlinear interactions as the waveform was propagated. Attenuation of the BPF tone is shown in figure 4.20 for the propagation of 100 sawtooth waveforms with an average trend line which has at most about 3dB difference from the measured data at the last axial measurement. It is of note that the scaling method generates a spectrum that are in very good agreement with the measured spectrum except at frequencies lower than BPF.

On the whole, it appears the extrapolation and the scaling both over-predict the lower frequencies. The over-prediction observed in the extrapolation method is slightly higher and therefore causes greater over-prediction of the attenuation of the BPF tone. The optimization method, on the other hand, more closely approximates the lower frequencies and hence, has the best agreement (of the three methods) with the measured data in the attenuation of the BPF tone.

4.4.2 Predictions against measurement

A few notes have to be made about the measured data. There is a gradual reduction in the level from one BPF harmonic to the next, but the levels of tones lower than the BPF and those of their harmonics are nearly equal with only about 0.5dB difference between subsequent harmonics. The reduction in sound level observable for the BPF harmonics, which is expected over the whole spectrum as well (as derived in theoretical analysis), is therefore not present in measured data. This is believed to be mainly due to the fact that the sawtooth representation can not exactly or fully describe the phenomenon in real life cases, and it is therefore difficult to find any sawtooth waveform that will produce the same frequency spectrum as the measured data. The sawtooth

waveform always generates a spectrum with reduced tone levels at high frequencies both over the BPF harmonics and the inter-BPF-harmonic tones. But since, as evident in the measured data presented in this study, the inter-BPF-harmonic tones seem to show almost no reduction in sound levels at all at high frequencies, hence the conclusion that there may be no smooth sawtooth waveform idealization for the real-life case. Images from experiments [27] show that the expansion waves between shock are curved and not straight lines as in the idealized sawtooth waveform. There are other flow effects, boundary layer effects and duct geometry effects that may further alter the pressure pattern observed in real-life situations. Also, the shocks may extend along the span of the fan blades, that is, they may not only occur at the fan blade tips. This radial shock span is not captured in this one dimensional idealization which limits the shocks to the tips of the fan blades.

4.5 Summary

Various methods have been used to obtain representative sawtooth waveforms using measured data and employing random phases to reconstruct the waveform. It appears that the unavailability of the phase information and the fact that the real-life pressure waveform is not a smooth sawtooth prevents the exact matching of the measured spectrum. When compared with measured data, the extrapolation and scaling methods over-predict the low frequency tones while the optimization under-predicts the high frequencies. The BPF attenuation is best predicted by the optimization method followed by the scaling method and then the extrapolation method. It is important to note that all these methods, produce good agreement if the spectrum to be matched had been produced from an ideally smooth sawtooth waveform as shown.

Chapter 5

Nonlinear Propagation of Buzz-saw Noise

This chapter aims to show the implementation of the theories discussed in chapter 3. There are two part covered in this chapter; the duct acoustics code and the nonlinear propagation of a sawtooth in a rigid intake duct in the time domain.

5.1 Modes in a Duct

A code to evaluate the modes in both cylindrical and annular ducts for both rigid and lined wall conditions was written and validated. The code is based on the theory of duct acoustics as explained in section 3.1.

5.1.1 Duct-Code Validation

The procedure to obtain the axial wave-numbers k_z for the duct modes (described in the sections above) was coded in MATLAB®. This code is referred to as, *duct-code*. The results obtained by this code were compared to the the results from a validated code (which will be referred to as *AMCode*[55] for reference) written in FORTRAN® by Dr. A. McAlpine[1]. The results from the two codes were plotted together to check that the results were the same for various realistic test cases similar to conditions in the inlet duct of an aircraft at take-off, cruise and landing engine operation conditions.

For the validation, the fixed properties considered are; Number of fan blades = 20, Duct radius = 0.5m, Sound speed = 340ms^{-1} and Mean air density = 1.2kgm^{-3}.

[1]Author's research supervisor at the ISVR, University of Southampton, UK.

Values for the three cases corresponding to aircraft take-off, cruise and landing engine operation conditions are shown in Table 5.1.

Table 5.1: Engine Properties

Operation condition	Case 1 (landing)	Case 2 (cruise)	Case 3 (take-off)
Axial flow speed (ms^{-1})	80	140	170
Shaft rotation frequency (Hz)	70	110	130
Blade passing frequency (Hz)	1400	2200	2600
Face sheet resistance, R	2.5	3.0	3.5
Mass reactance, m_r (m)	0.01	0.01	0.01
Liner depth, h (m)	0.02	0.02	0.02

The liner impedance model equation is given as $Z = R + i[k\, m_r - cot(kh)]$.

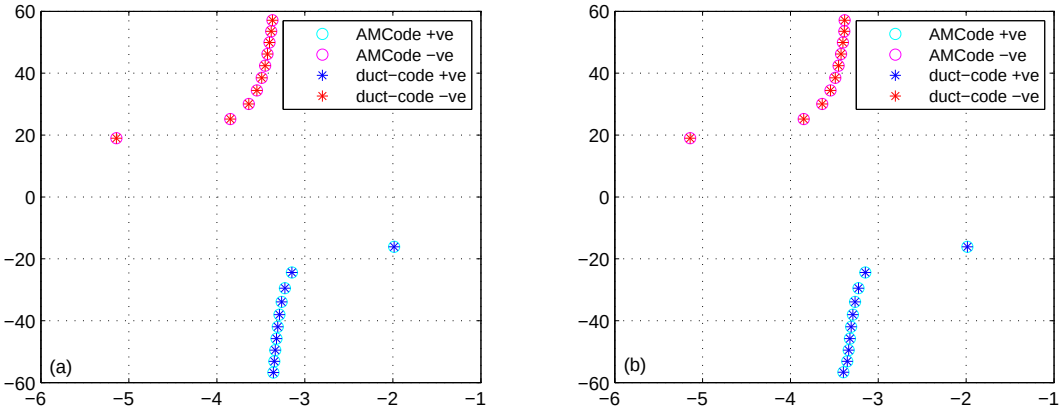

Figure 5.1: (a) Axial wavenumbers for a lined cylindrical duct (b) Axial wavenumbers for a lined annular duct, for case 1 at BPF (1400Hz) for azimuthal mode m = 20

For each case, the code was run for both the rigid and lined wall conditions for the cylindrical and annular duct arrangements. The axial wavenumbers multiplied by the external duct radius (to obtain dimensionless axial wavenumbers) were plotted for the *duct-code* together with the results of the *AMCode* for the cases in Table 5.1. A number of the plots for various cases were selected to show the correlation of the results generated by the two codes. The plots are complex value plots of the imaginary part (vertical axis) against the real part (horizontal axis) of the dimensionless axial wavenumber.

In high bypass ratio aero-engines, the part of the inlet duct not far away from the fan can be considered as an annular duct because of the presence of the spinner. As distance from the fan increases and the radius of the spinner decreases the duct can be represented as a cylindrical duct. A large part of the inlet duct is lined and there are very small areas (in comparison to the duct surface area) that are not acoustically lined.

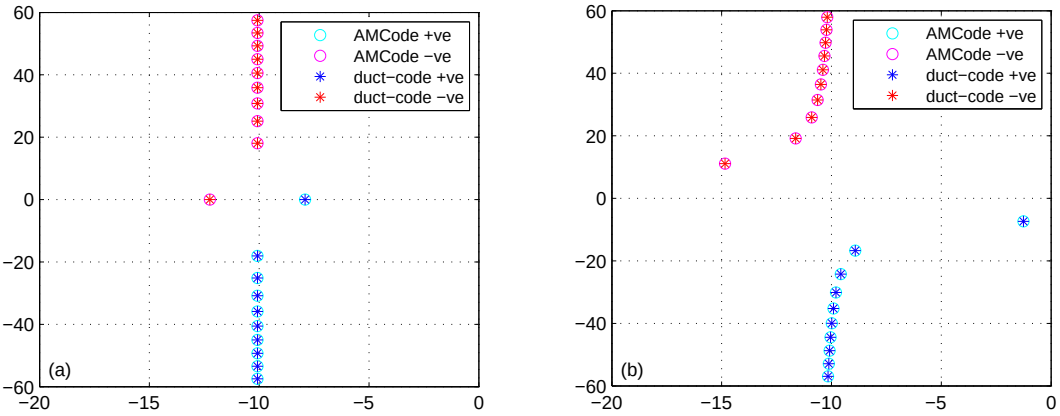

Figure 5.2: (a) Axial wavenumbers for a rigid cylindrical duct (b) Axial wavenumbers for a lined annular duct, for case 2 at BPF(2200Hz) for azimuthal mode m = 20

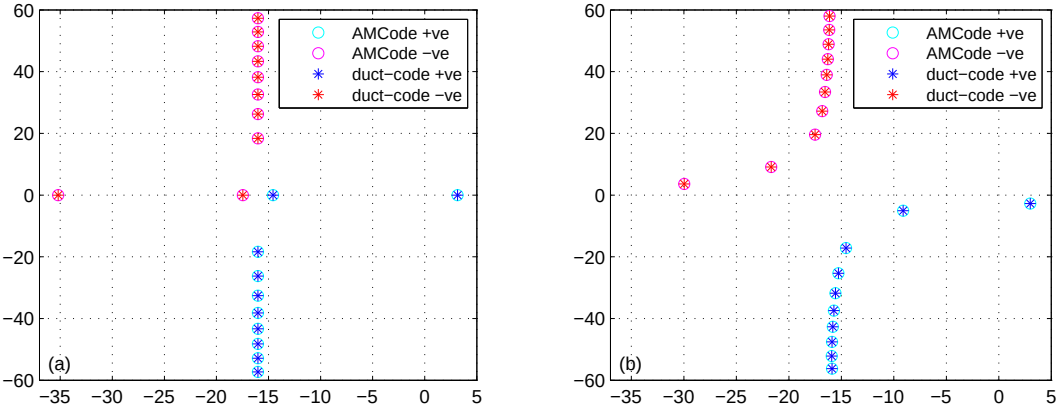

Figure 5.3: (a) Axial wavenumbers for a rigid annular duct (b) Axial wavenumbers for a lined annular duct, for case 3 at BPF(2600Hz) for azimuthal mode m = 20

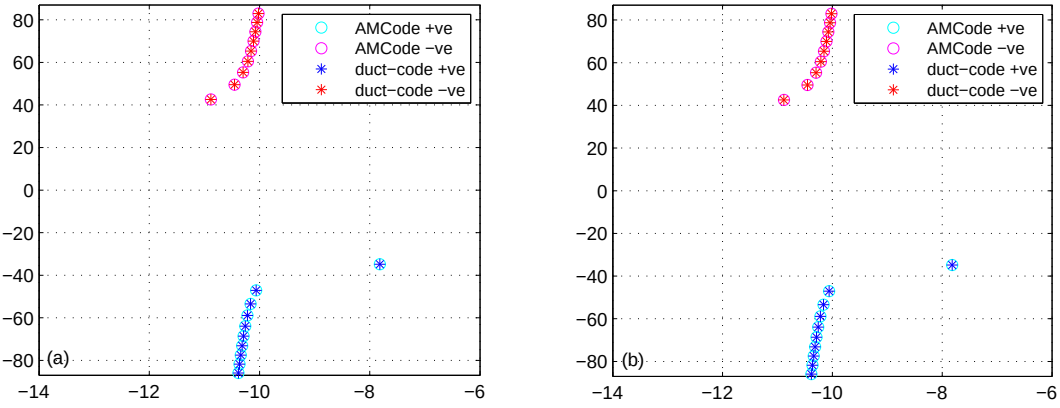

Figure 5.4: (a) Axial wavenumbers for a lined cylindrical duct (b) Axial wavenumbers for a lined annular duct, for case 2 at BPF(2200Hz) for azimuthal mode m = 40

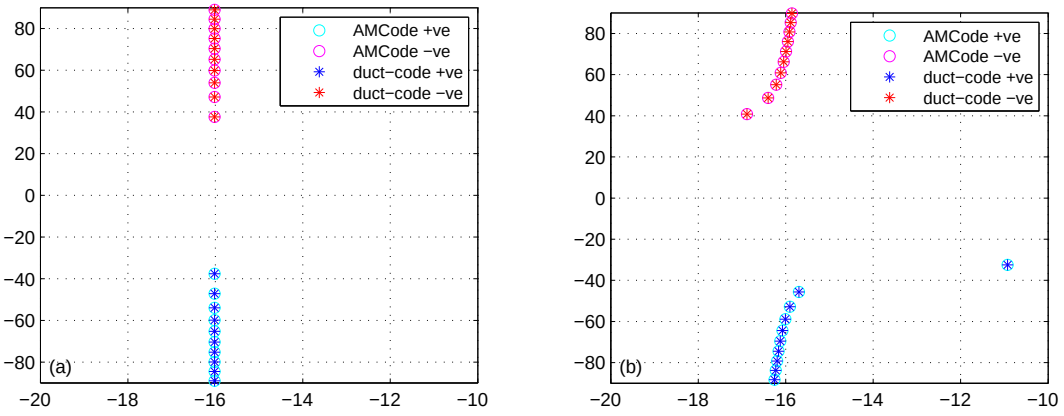

Figure 5.5: (a) Axial wavenumbers for a rigid annular duct (b) Axial wavenumbers for a lined annular duct, for case 3 at BPF(2200Hz) for azimuthal mode m = 40

For the duct configurations considered for cases 1-3 (in Table 5.1), it can be seen from Figures 5.1 - 5.5 that the results for both the rigid and lined wall conditions for cylindrical and annular ducts are exactly the same for both the *AMCode* and *duct-code*. It is important to note that the number of values plotted for *duct-code* were more than those plotted for *AMCode*. This is the reason for the points in the plots without matching values from the *AMCode*. These results validate the new *duct-code*.

The consistency of the results of *duct-code* with those of *AMCode* is shown in various operation conditions – Figure 5.1, for the acoustical lined cylindrical and annular ducts at BPF of 1400Hz and at higher BPFs (2200Hz and 2400Hz), Figure 5.2 and Figure 5.3 respectively. All these results were generated for azimuthal mode, $m = 20$, which is the same as the number of blades of the ducted fan. Figures 5.4 and 5.5 are plots of values for azimuthal mode $m = 40$ for different wall conditions for cases 2 and 3.

The evolution of modes in a duct can be appreciated through a close look at the differences in Figures 5.1 - 5.5 for the operation and wall conditions considered. At the slowest speed considered (Case 1), there is very little difference between the plots for the lined cylindrical duct and annular cylindrical duct (Figure 5.1). All modes have very high imaginary parts and are not very significant as they quickly decay in the duct. A similar situation is observed in Figure 5.4 for a higher BPF and azimuthal mode number.

Figures 5.2 and 5.3 show the effect of acoustic liners in a duct. In Figure 5.2(a), a mode is 'cut-on' (i.e. it has no imaginary part) in the rigid cylindrical duct. Also, in Figure 5.3 (a), there are two 'cut-on' modes in the rigid annular duct. These modes are not much attenuated and will be radiated from the duct. When acoustic liners are introduced (see Figures 5.2(b) and Figures 5.3(b)), the modes are seen now to have shifted away from the zero-value horizontal line and they now have imaginary parts, i.e. they will decay to varying degrees as they propagate in the duct.

Another noteworthy event observable in Figure 5.5 is that, especially at high rotational frequencies, the acoustic liner can have significant effect on modes that already have significant attenuation (imaginary parts). In this figure, the first mode in the rigid annular duct, Figure 5.5(a), has its real part increased significantly when the duct walls are lined (Figure 5.5 (b)).

5.2 1D Nonlinear Wave Propagation

The pressure profile generated at the tip of the blades of a fan (rotating at supersonic relative tip speeds) of an aero-engine is characterized by a system of shocks and expansion waves. This system of shock and expansion waves for a complete revolution is visualized as a set of N waves (sawtooth) within which the number of shocks equals the number of blades of the rotating fan. A propagation model can be developed to propagate the sawtooth from the fan plane to the entrance of the inlet duct. This enables the investigation of the evolution of the sawtooth profile. The propagated sawtooth can be visualized at any specified point within the duct using the model.

Moreover, the decay of the pressure amplitude of the shocks within the sawtooth profile can be tracked and the sound pressure level amplitude spectrum for a range of frequencies of interest can be generated at any specified location within the inlet duct. A one-dimensional propagation model is considered, based on the assumption that the shock waves generated at the fan blade tips do not vary in the radial direction i.e. they only occur at the tip of the blades. The propagation of this rotor-alone pressure profile is essential to understanding and control of buzz-saw noise.

5.2.1 Sawtooth Profiles

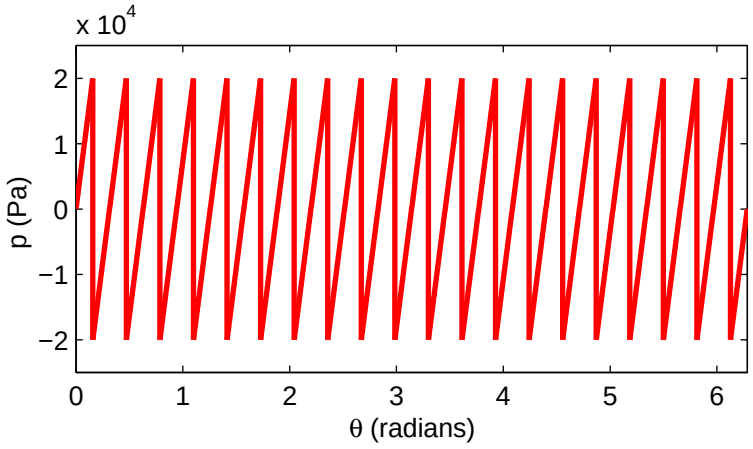

Figure 5.6: Regular sawtooth profile

To propagate the sawtooth profile of a system of shock and expansion waves, a nonlinear propagation theory is employed owing to the high amplitudes of the pressures. The weak-shock theory (discussed in section 3.2) is used in the modeling of the propagation of N-wave profiles. The system of shock and expansion waves observed in Figure 2.1 can

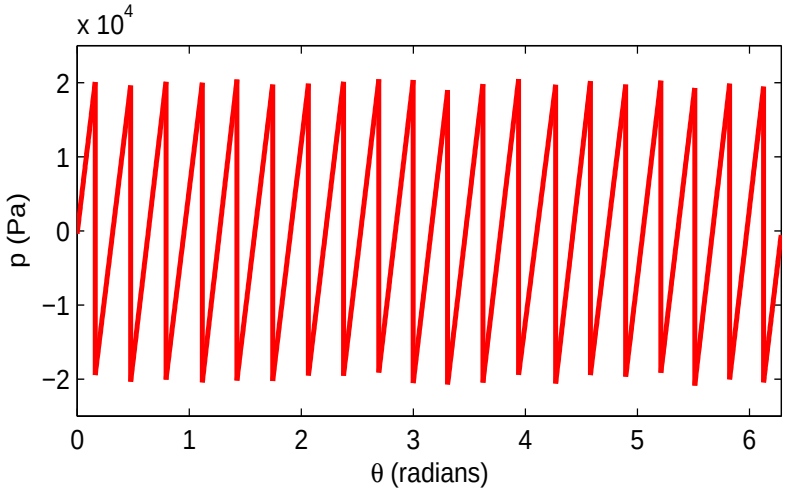

Figure 5.7: Irregular sawtooth profile

be shown in a representative and characteristic sawtooth. Figure 5.6 shows a sawtooth waveform for a fan with 20 blades. This regular profile represents a situation in which there are no blade-to-blade differences; all blades are exactly alike and arranged perfectly alike. On the other hand, a situation in which there exist differences among the blades, an irregular sawtooth profile like the one shown in Figure 5.7 is generated as the pressure profile.

5.3 Propagation Code Validation

In the investigation of the propagation of buzz-saw noise and to compare predictions with measured data, a one-dimensional sawtooth propagation time domain code was written in MATLAB®. For easy identification, this code will be referred to as 'SPRID' (Sawtooth Propagation in Rigid Intake Duct) . SPRID was generated based of the non-linear wave theory of propagation of shock waves as explained in section 3.2. The SPRID code can produce outputs showing the waveform at various specified axial stations in the inlet duct, and the SPL frequency spectrum at these stations. In the propagation, SPRID also incorporates the cross-over and merging of shocks as explained in the physics of the propagation of shocks. To authenticate the results of this code, results generated were compared with the results obtained from an existing-validated[17, 18] frequency domain code[56] (discussed in section 3.2.1.1), for the same examples already used in section 5.1.1 and particularly for case 3 in Table 5.1.

The stations specified for the outputs were spaced at every 10cm for 1m from the fan plane, i.e. a total of 10 axial stations forward of the fan plane.

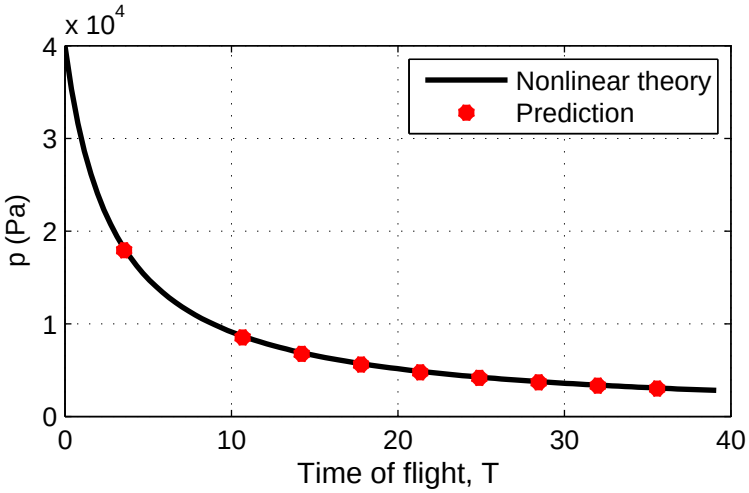

Figure 5.8: Attenuation of BPF tone for regular sawtooth

The initial sawtooth profiles used in this analysis were generated from a code written to generate random sawtooth waves. One regular and three irregular sawtooth profiles were generated, and their nonlinear propagation was computed using both codes.

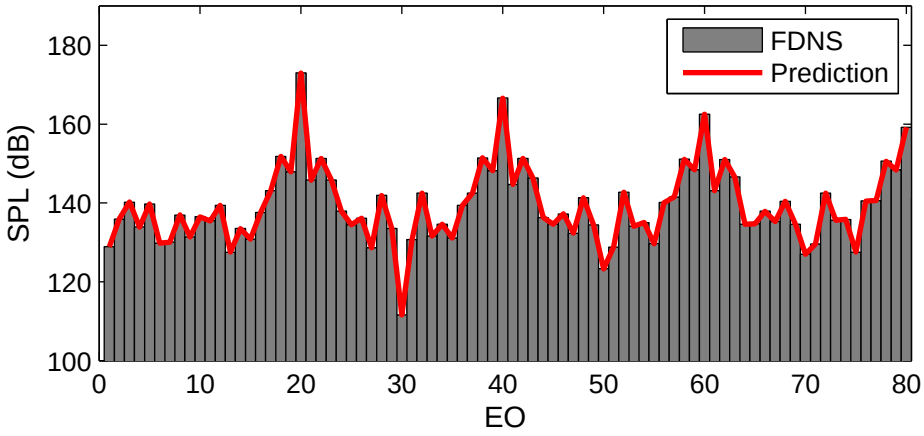

Figure 5.9: Initial frequency spectra for irregular sawtooth 1

The regular sawtooth (with average shock amplitude of 40000 Pa) is shown in figure 5.6, and the first of the three irregular sawtooth profiles is shown in figure 5.7. This irregular sawtooth profile was generated from the regular sawtooth by variations of 1 and 2 percents in shock amplitude and shock spacing respectively. For the propagation of the regular sawtooth (Figure 5.6), a plot of the pressure amplitude against time of flight, shown in Figure 5.8, shows the comparison of the results of the SPRID predictions of the

attenuation of the BPF tone at the specified axial stations versus expected attenuation calculated from equation (3.29).

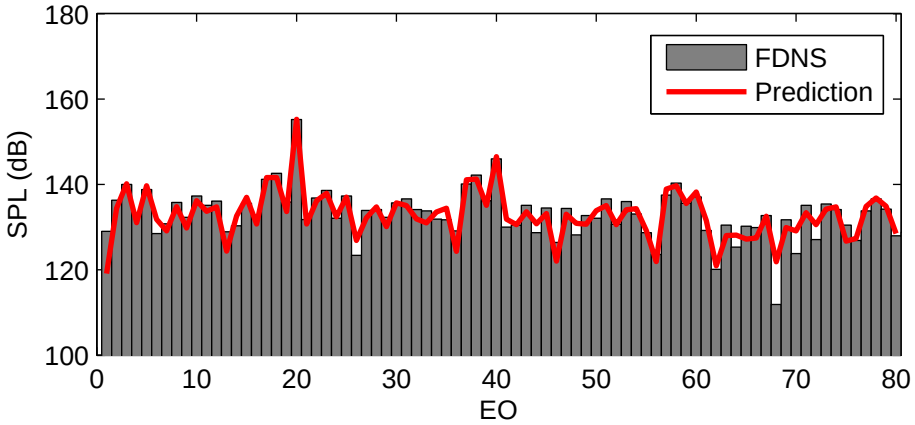

Figure 5.10: Frequency spectra 0.5m away from start point for irregular sawtooth 1

The propagation agrees exactly with nonlinear theory. The initial shock amplitude is observed to be attenuated rapidly until about axial station 5 (0.5m), and thereafter, the attenuation falls off. This agrees with the theory that the attenuation becomes independent of the shock amplitude at large values of the time of flight.

Figures 5.9 - 5.11 show the comparison between the results of the SPRID and the FDNS model. For the irregular sawtooth profiles, the spectra at the axial stations were compared. Presented here (Figures 5.9 - 5.11) are the spectra at the fan plane and at two axial stations (0.5m and 1m). Generally the agreement of the two methods (Figures 5.9 - 5.11) is very good at all the stations specified. Perfect agreement can be observed for the initial spectra; see Figures 5.9.

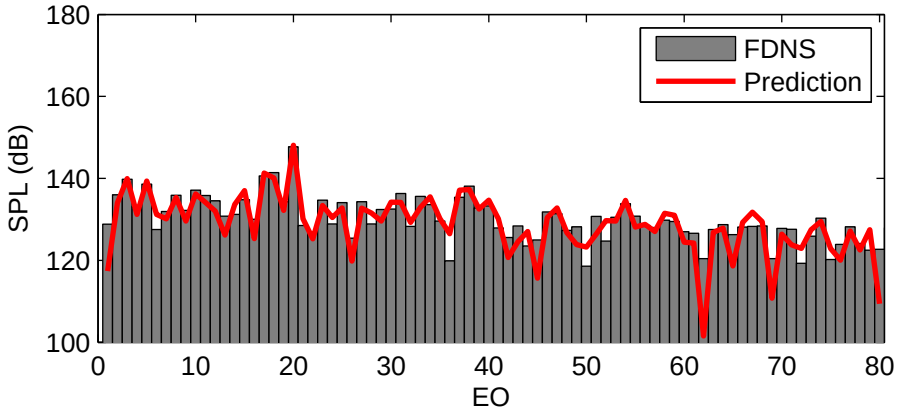

Figure 5.11: Frequency spectra 1m away from start point for irregular sawtooth 1

As the propagation proceeds further upstream, the perfect agreement observed at the initial stage is not seen. This is most likely due to the different approaches used in the two models because the SPRID propagates the sawtooth in time domain while the FDNS is a frequency domain numerical method, and therefore, they employ different approaches. The different approaches cause slight numerical differences in the simulations. Notwithstanding, comparison of the range of magnitudes of values show both codes agree to a reasonable degree.

5.3.1 Comparisons with measured data

Results of SPRID are also compared with results from an experimental scaled-rig engine test, carried out by Rolls Royce in the AneCom anechoic test facility in Germany. The experimental data provides the frequency spectrum at an axial position about $0.1z/D$ forward of the fan plane (referred to here as 'fan-case') for the rigid inlet duct. These

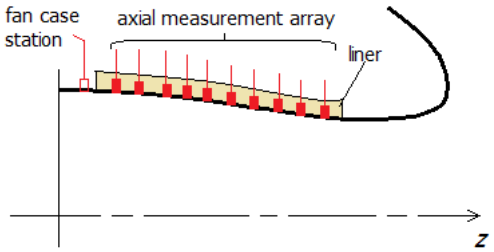

Figure 5.12: Illustration of the AneCom modular fan rig: measurement locations and lined region

fan-case SPL values of the engine orders in the frequency spectrum were employed to construct a sawtooth pressure profile that was propagated using the SPRID to various axial stations corresponding to the axial stations where measurements were taken in the scaled-rig engine test carried out in the AneCom modular fan rig(schematic diagram of the fan rig in figure 5.12. Note, this excludes the location of fan-case measurement). Frequency spectra of predictions and measurements at these axial stations were compared. Predictions are averaged results obtained taking 100 simulations and calculating the mean value of the SPL.

It is important to point out here again that the SPL values from the measured data only provide the magnitude of the complex Fourier coefficients, and therefore, the sawtooth propagated to obtain results discussed in this section was generated through the scaling method (see section 4.2.2.1) utilizing the measured data. The figures 5.13-5.15 show the results of propagation in SPRID against measured data at various axial stations in the intake duct for the rigid wall case. Although the predictions do not match tone-for-tone at all engine orders, the general noise levels are similar. The differences between predictions and measurements at the axial stations is not far-removed from the differences

already present at the start (i.e. at the fan case) and various other physical phenomena present in the real-life propagation that are not represented in the model. A notable attribute of the SPRID model is the relatively good agreement of its prediction of the BPF tone (Engine order 20 in figures 5.13-5.15) at the axial stations. It can therefore be said that the SPRID model agrees with the measured data to a reasonable degree for the idealized sawtooth waveform approximation employed in the model.

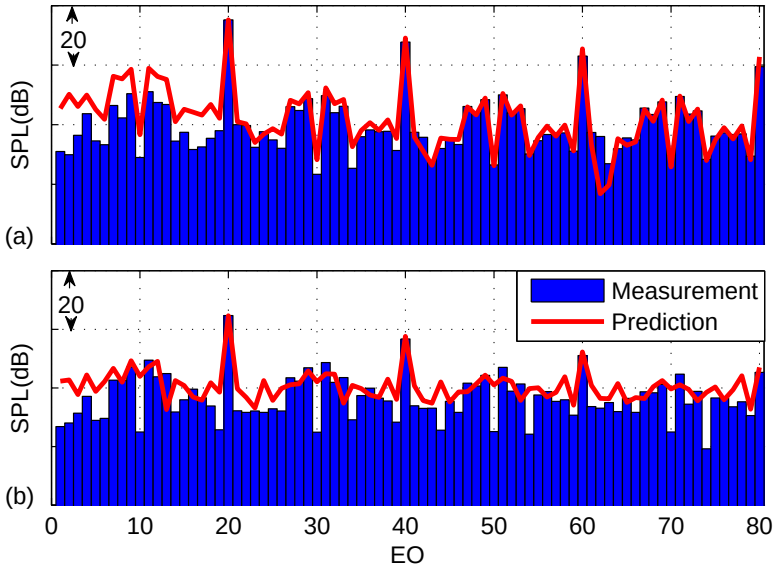

Figure 5.13: Prediction against measurement at (a) fan-case (b) axial distance 0.1m [Note: Prediction is the average of 100 simulations and calculating the mean value of the SPL]

5.4 Summary

Results from the code written to evaluate modes in cylindrical and annular ducts have been presented. Comparisons are made with results from an existing code developed in the ISVR, University of Southampton. Results from both codes match for the azimuthal orders considered. Also, results from the simulation of nonlinear propagation for regular and irregular sawtooth waveforms. These results have been generated by the time-domain nonlinear propagation code developed. Comparisons are made with theory, benchmark frequency-domain nonlinear propagation code FDNS, and with measured data acquired from a model-scale rig test.

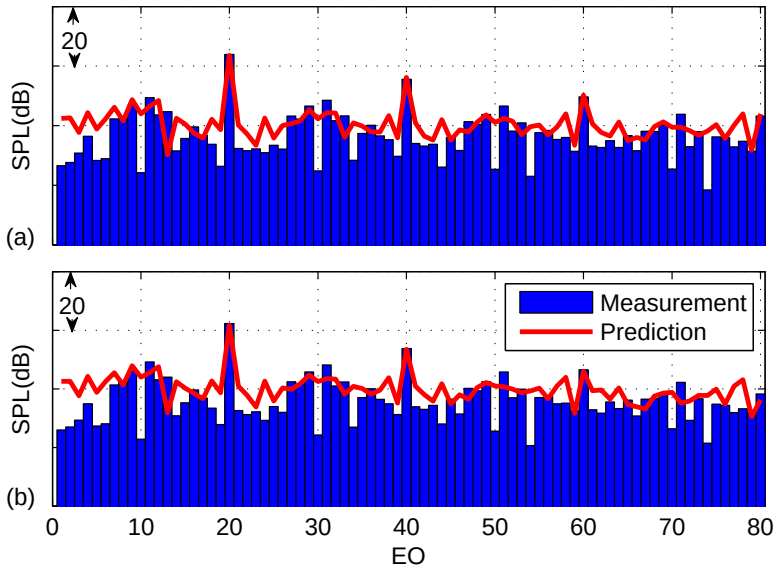

Figure 5.14: Prediction against measurement at (a) axial distance 0.12m (b) axial distance 0.15m [Note: Prediction is the average of 100 simulations and calculating the mean value of the SPL]

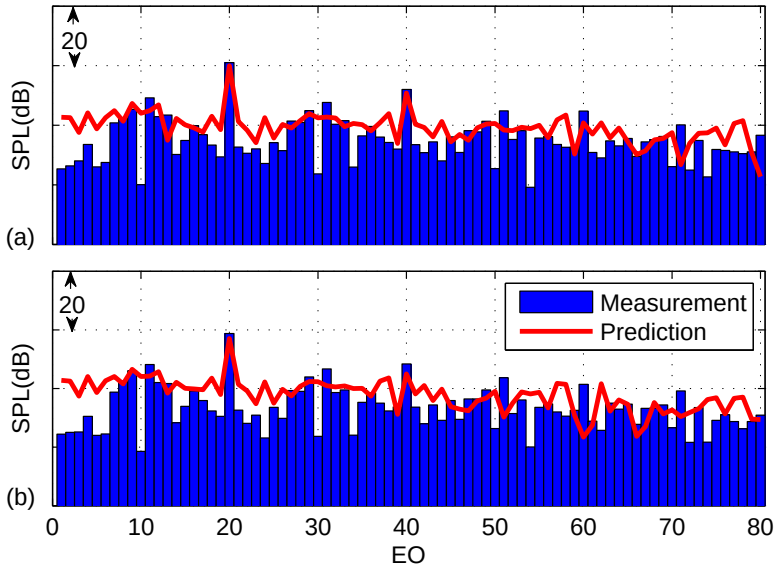

Figure 5.15: Prediction against measurement at (a) axial distance 0.19m (b) axial distance 0.25m [Note: Prediction is the average of 100 simulations and calculating the mean value of the SPL]

Chapter 6

Time-Frequency Domain Supersonic Fan Noise Propagation

6.1 Background

The time domain nonlinear propagation model, based on the weak shock theory, discussed in chapter 5 can only predict the propagation of the pressure waveform in a rigid inlet duct. In the actual aircraft engines, inlet ducts are treated with some form of acoustic liners. This acoustic liner ensures the attenuation of specific tones in the inlet duct before the pressure field is radiated out of the nacelle. The attenuation of specific tones actually implies that the acoustic liners are tuned to attenuate a particular limited range of frequencies. The range of frequencies attenuated by the acoustic liner is carefully chosen by the aircraft manufacturers based on in-depth research on the characteristics of the noise produced by the engine.

Generally, the acoustic liners installed in the intake of aircraft engines have their optimum attenuation around the most dominant tones in the intake duct. With the knowledge of the physics of the propagation of the pressure waveform generated at the fan blade tips, the number of fan blades and various other design and flow factors, the acoustic liners are manufactured to reduce the dominant tones.

In the research on the prediction of supersonic fan noise, the model for prediction must be one that takes into account the effect of installed acoustic liners on the propagation of the pressure field in the aircraft intake. In the time domain, the nonlinear propagation of the pressure field is well represented, and a reliable model has been developed (chapter 5). To include the effects of acoustic liners in the propagation model, the frequency dependence of the acoustic lining must be included. It is therefore useful to find a

means of changing to the frequency domain in order to model the effect of the acoustic liners, implemented in the propagation scheme.

This need brought about the use of the time-frequency domain algorithm in a new propagation model. The nonlinear propagation of the pressure field is achieved in the time domain while the acoustic liner effects are added in the frequency domain. This is referred to as the hybrid approach [57] or a modified weak shock theory [58]. 'Modified' implies that the conversion to the frequency domain, addition of acoustic liner effects, and conversion back to the time domain, are added to the steps established for the weak shock theory. In the remaining sections of this chapter, the procedure and results of this time-frequency domain approach are discussed.

6.2 The Propagation Model

The time-frequency domain scheme also is a one-dimensional propagation model which predicts the propagation of the pressure field from the fan plane up to the point of radiation from the intake duct. The finite difference method is used in this propagation model as this allows for the discretization of the waveform, and the use of algorithms which facilitate quicker conversion between the time and frequency domains. The model was developed in two phases; the first phase is the nonlinear propagation of the sawtooth waveform and the second, the addition of the acoustic liner into the model. This two-phase approach allows the validation of the model against already existing models, including the Time-domain model (SPRID) and the FDNS model for propagation in a lined intake ducts. In the first phase, validation without the lining is undertaken. Then scaled-rig test measurements will be used as part of the second validation phase.

6.2.1 Nonlinear Distortion in the Time Domain

Nonlinear propagation of the pressure field generated at the fan blade tips, idealized as a sawtooth, is implemented in this model using the weak shock theory (section 3.2) in a finite difference scheme.

6.2.1.1 The Grid

Due to the presence of shocks in the pressure field to be propagated, there is a need of carefully evaluating the number of nodes on the finite difference grid which will enable a acceptable level of resolution for the shocks present. In this model, the number of nodes on the finite difference grid is N (Figure 6.1. The nodes on the grid are uniformly spaced and individually mark discrete points in the pressure waveform.

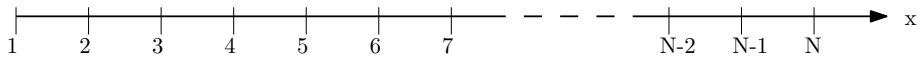

Figure 6.1: Illustration of the one dimensional finite difference grid

Another factor affecting the choice of N is the application of acoustic liner absorption. As this model applies the absorption in the frequency domain and employs the FFT algorithm to take the discrete Fourier transform of the pressure field, the determination of N also rests of the requirements of this process. The determination of an appropriate N for the model is discussed in section 6.3.1.1 later in this chapter.

6.2.1.2 Nonlinear Propagation

Using the Burger's Equation in the one-dimensional form,

$$\frac{\partial p}{\partial z} = \frac{\beta p}{\rho_0 c_0^3}\frac{\partial p}{\partial \tau} + \frac{\delta}{2c_0^3}\frac{\partial^2 p}{\partial \tau^2} \tag{6.1}$$

where β is the coefficient of nonlinearity, ρ_0 is the ambient density, c_0 is the local sound speed and δ is the sound diffusivity. $\tau = t - \frac{z}{c_0}$ is the retarded time and z is the direction of propagation. The equation can be expressed in non dimensional variables by using $\bar{p} = p/P_0$; $\bar{z} = z/\hat{z}$; $\bar{\tau} = \omega_0\tau$ and $\Upsilon = \alpha_0\hat{z}$. For signal source $p(\omega_0 t)$ and thermo-viscous attenuation coefficient α_0 at frequency ω_0, $\hat{z} = \frac{\rho_0 c_0^3}{\beta P_0 \omega_0}$ (the lossless shock-formation distance) [59]. Using these in equation (6.1) yields,

$$\frac{P_0\partial\bar{p}}{\hat{z}\partial\bar{z}} = \frac{\beta\bar{p}P_0^2\omega_0}{\rho_0 c_0^3}\frac{\partial\bar{p}}{\partial\bar{\tau}} + \frac{\delta P_0\omega_0^2}{2c_0^3}\frac{\partial^2\bar{p}}{\partial\bar{\tau}^2} \tag{6.2}$$

On dividing through by P_0, multiplying through by $\hat{z}$ and substituting for $\hat{z}$ and Υ, we obtain

$$\frac{\partial\bar{p}}{\partial\bar{z}} = \bar{p}\frac{\partial\bar{p}}{\partial\bar{\tau}} + \Upsilon\frac{\partial^2\bar{p}}{\partial\bar{\tau}^2} \tag{6.3}$$

where $\bar{p}$ is the acoustic pressure of the waveform and Υ is the coefficient of the diffusive losses.

An approximate solution can be obtained for equation (6.3) by the method of fractional steps [60] over incremental steps $\Delta\bar{\tau}$. This is achieved by separating equation (6.3) into two equations (referred to as operator splitting)[57] and solving these equations separately over each time step to obtain an approximate solution for equation (6.3).

This model makes use of the distortive term of the Burger's equation for the nonlinear propagation. The diffusive term is ignored in the model as no viscous effects considered in the distortion of the waveform. It is notable that the re-sampling of the waveform

to the finite difference grid implicitly adds an amount of dissipation which may be commensurate to the losses expected from the diffusive part of the Burger's equation [57, 58] albeit this is a function of the resolution of the waveform by the grid. The equation (6.3) then reduces to

$$\frac{\partial \bar{p}}{\partial \bar{z}} = \bar{p}\frac{\partial \bar{p}}{\partial \bar{\tau}}. \tag{6.4}$$

The waveform to be propagated is discretized into N waveform samples and these are represented by p_ι $(\iota = 1, 2, \ldots, N)$. To use equation (6.4) in the time-domain finite difference propagation, for the grid described in section 6.2.1.1, the equation is discretized as

$$\bar{\tau}_\iota^{j+1} = \bar{\tau}_\iota^{j} + \bar{p}_\iota^{j}\Delta\bar{z} \tag{6.5}$$

where subscript ι marks each position in N and superscripts j and $j+1$ signify the values before and after a propagation step respectively.

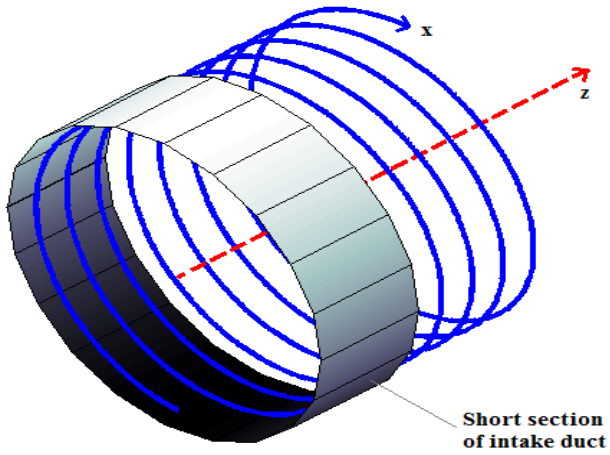

Figure 6.2: Helical path of waveform along the intake duct axial direction

Figure 6.2 is an illustration of the pressure field in an intake duct advancing along a characteristic helical path in the x direction which is related to the axial distance z in the direction of propagation by

$$x = \frac{zK\lambda M_{rel}}{D} \tag{6.6}$$

where K is defined in equation (3.26) in chapter 3, $\lambda = \pi D/B$, M_{rel} and D are the shock spacing, relative Mach number and duct diameter respectively.

Using knowledge of the weak shock theory and (6.5), the nonlinear distortion of the points on a discretized pressure waveform in a frame moving at the speed of sound, c_0, is expressed, in dimensional variables, as;

$$x_\iota^{j+1} = x_\iota^j + \frac{\gamma+1}{2\rho_0 c_0} p_\iota^j \Delta t \tag{6.7}$$

where x_ι^j is the initial position, $\frac{\gamma+1}{2\rho_0 c_0} p_\iota^j$ is the expression of the velocity and Δt is the time step corresponding to the propagation step $\Delta\bar{z}$.

For the shocks that are present in the pressure waveform, the corresponding expression is;

$$x_\iota^{j+1} = x_\iota^j + \frac{1}{2}\frac{\gamma+1}{2\rho_0 c_0}\left(p_{\iota,1}^j + p_{\iota,2}^j\right)t \tag{6.8}$$

where $\frac{1}{2}\left(p_{\iota,1}^j + p_{\iota,2}^j\right)$ is the mid-point pressure of each shock wave (1 and 2 describe the point just ahead and behind the shock respectively).

Using equations (6.5), the pressure waveform is advanced in space by propagation steps ($\Delta\bar{z}$) chosen within the limits of the Courant–Friedrichs–Lewy (CFL) condition which explains that for stability in the simulation, the displacement of the highest pressure value in the discretized waveform over a the propagation step should be less than a step space between two consecutive points on the finite difference grid; this can be expressed as[57];

$$\Delta\bar{z} < \left(\max\frac{\partial\bar{\tau}}{\partial\bar{p}}\right). \tag{6.9}$$

For each step of propagation, the waveform samples are no longer uniformly spaced because each point on the waveform moves with respect to the magnitude of the acoustic pressure at that point on the waveform. The waveform is therefore resampled to the finite grid by linear interpolation to restore the uniform intervals of points on the waveform (see illustration in figure 6.3). Figure 6.4 (differences exaggerated for clarity) shows the added amplitude reduction that occurs during the resampling procedure. This additional attenuation introduced by the resampling process is the main reason for the omission of the diffusive part of the Burger's equation from the nonlinear process [57, 58, 61].

In a situation where a propagation time-step larger than that specified by the CFL condition is employed, during propagation, the waveform may become multivalued because of the distortion of waveform. This is a non-physical and hence must be corrected before propagation continues. The waveform becomes multivalued when

$$\bar{\tau}_\iota^{j+1} < \bar{\tau}_\iota^j. \tag{6.10}$$

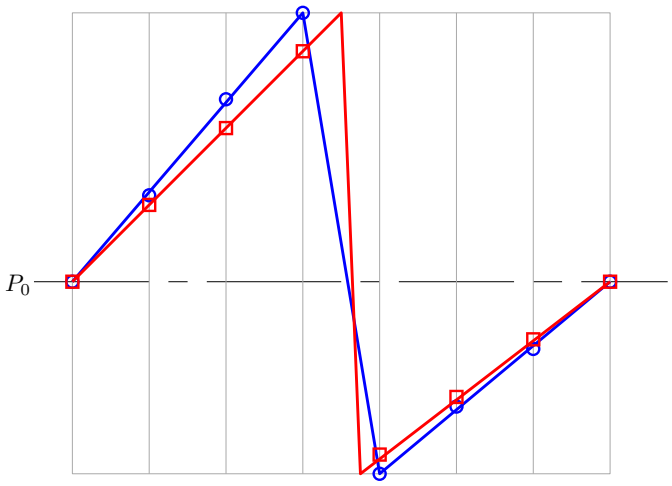

Figure 6.3: Resampling of points on waveform back to the base grid

The multivalued waveform is resolved by the removal of all multivalued points using the position of the mid-point of the shock. All points on the expansion waves (before and after a shock) that have overshot the shock mid-point are deleted, the waveform is then reordered and thereafter, resampled on the grid. Figure 6.5) shows an illustration of the initial sawtooth and the region of sample points to be removed from multivalued sawtooth obtained after that propagation. It also shows the mid-points of shocks used to determine the multivalued samples to be removed and gives a picture of the resultant 'corrected' sawtooth. After the removal of the multivalued wavelets, the number of samples in the waveform becomes less than N. This is resolved by resampling the waveform back to grid of N samples.

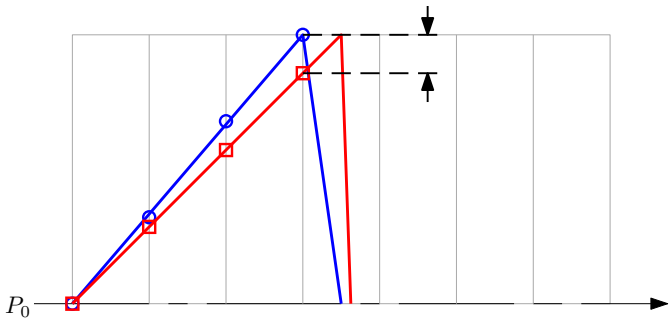

Figure 6.4: Illustration of the reduction in amplitude due to resampling waveform back to the grid

In the event that two shocks merge, the location of the shocks is coincident and the number of shocks present is adjusted, and waveform is resampled to the base grid ready for onward propagation.

With the linear interpolation, resolution of multivalued parts of the waveform and the sorting of the merging of shocks, the nonlinear propagation part of the model is fulfilled.

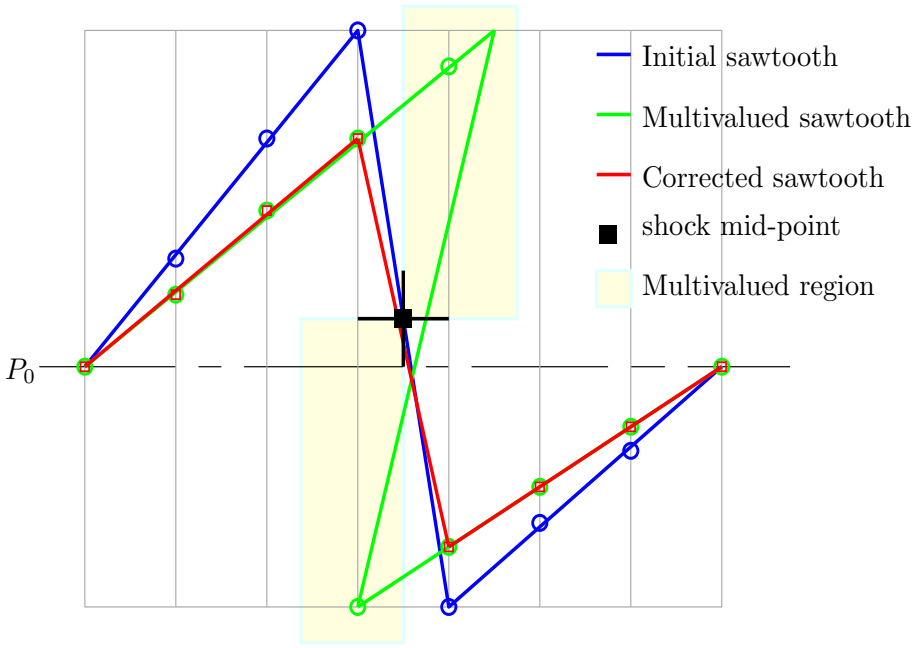

Figure 6.5: Resolution of a multivalued part of the waveform

The sequence of main steps in the nonlinear distortion part of the model are ordered in the figure 6.6.

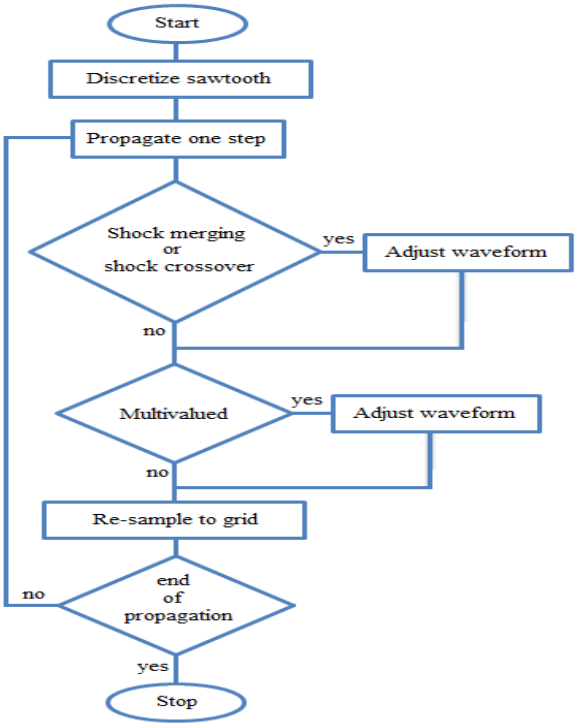

Figure 6.6: The main steps in the nonlinear distortion process

6.2.2 Absorption in the Frequency Domain

In order to add an absorption effect to the model, knowledge of all the acoustic liner's characteristic parameters is essential. The values of various parameters related to the intake duct (in which the liner is installed) and the flow within the duct are also very important. These enable the generation of predicted liner absorption rates performance values for the specific intake duct configuration and flow conditions. These values form inputs into the propagation model. In this case, the liner decay rates are given by the axial wavenumbers of modes in the duct, which has the liner installed. These are provided from a duct-mode code[62] written by Dr. Alan McAlpine[1].

Addition of acoustic liner absorption to the model is achieved in the frequency domain. The discretized pressure waveform is converted to its harmonic amplitudes by taking the discrete Fourier transforms (DFT) of the wavelets using the fast Fourier transform (FFT) algorithm in MATLAB. The transform is implemented in MATLAB by

$$C_m = \sum_{n=1}^{N} \omega_N^{(n-1)(m-1)} p_n \tag{6.11}$$

where m are the integer multiple of the rotating shaft frequency, $n = 1, 2, \ldots, N$ and $\omega_N = e^{-2\pi i/N}$ is a complex Nth root of unit [63].

Thereafter, absorption is added to the frequency spectrum using the equation[58, 64, 65]

$$C_m^{j+1} = C_m^j \exp\big[-\big(A_m + iS_m\big)\Delta\bar{z}\big], \tag{6.12}$$

where C_m^{j+1} is the resultant harmonic amplitudes, C_j^k is the initial harmonic amplitudes, A_m are the imaginary parts of the axial wavenumber (absorption), and S_m are the real parts of the axial wavenumbers (phases) at each azimuthal order m.

After the acoustic liner absorption has been applied to the harmonic amplitudes, the 'treated' harmonic amplitudes are converted back to a pressure waveform using the inverse fast Fourier transform. The resulting pressure waveform is that which has gone through the nonlinear distortion and liner absorption processes.

6.2.3 Model Overview

All the processes discussed in the earlier sections for the nonlinear propagation and acoustic liner absorption are implemented in a MATLAB code to form a propagation model, utilizing the time-frequency domain approach, which will be referred to as 'NP-SWIND' which stands for Nonlinear Propagation of Sawtooth Waveform in Intake Duct. The main activities within the model are

[1] Dr. McAlpine is the author's research supervisor at the ISVR, University of Southampton, UK.

- A step-in-space distortion of the wave in the time domain.
- Fourier integral to obtain the harmonic amplitudes of the sawtooth wave.
- Application of absorption to the harmonic amplitudes.
- Repetition of the above steps until required position in space is achieved.

Figure 6.7 shows an illustration of the whole propagation process. The step-by-step implementation of the processes in the code is laid out in the flow chart in Appendix A.

6.3 Results and Validations

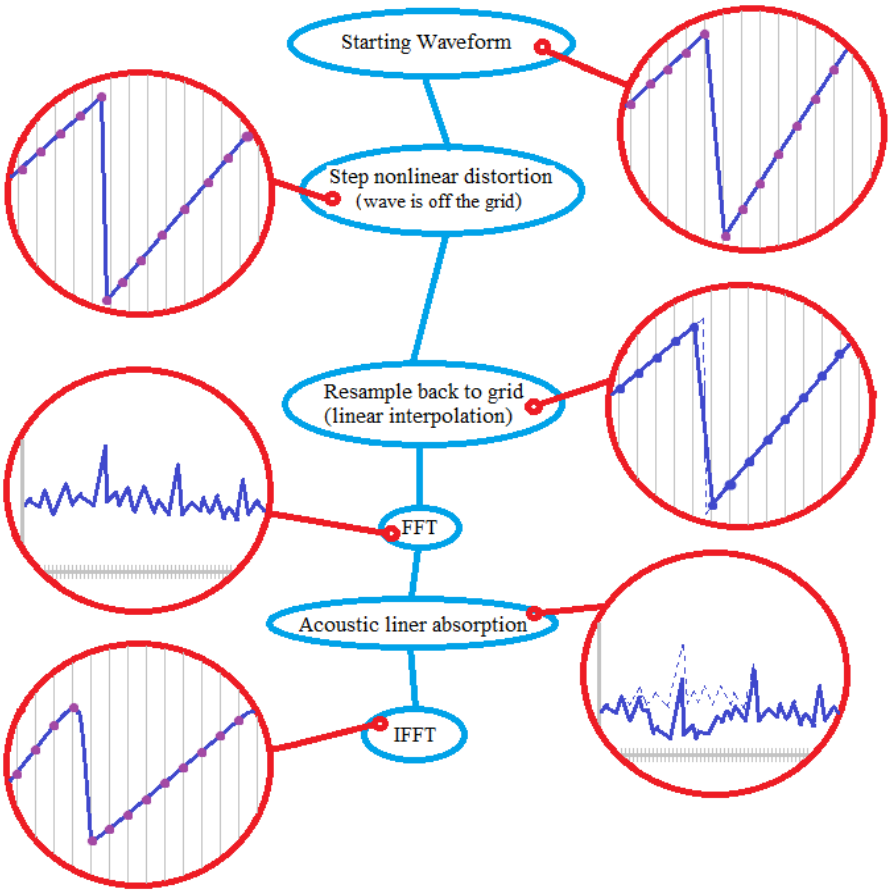

Figure 6.7: Illustration of the main elements in the model

6.3.1 Convergence Studies and Comparison with Benchmarks

In order for the model to reliably predict the propagation of the pressure field, various parts of the finite difference model is tested to ensure that satisfactory results are

obtained. These checks were made against benchmark solutions obtained from the aforementioned validated models (SPRID and FDNS), or analytical results. Due to the fact that shocks are present in the pressure waveform it is expected, as recommended in literature [58, 61], for the grid resolution to be carefully chosen. Another important factor is the simulation time. Taking the FFT of the pressure waveform to obtain its harmonic amplitudes and converting back through IFFT to get back the pressure waveform for every propagation step, implies that simulation time will vary as NlogN [58, 61, 66, 67]; where N is the number of grid points. This shows the dependence of the computational time on the grid resolution. It is hence necessary to first sort out the grid resolution. Pestorius in his work [58] suggested that it may be advantageous and a gain on computation time if the FFT and IFFT transforms are implemented after a fixed number of steps. If the total number of propagation steps is s, the time of simulation for nonlinear distortion process will be proportional to sN. In the event that the FFT and IFFT transform are taken after ζ steps, the simulation time for the absorption process will vary as $(s/\zeta)NlogN$. The total simulation time will therefore be proportional to $sN + (s/\zeta)NlogN$.

The acceptable number of steps before the transforms to and from the frequency domain are performed must be found out with respect to the benchmark solutions. The two major convergence studies necessary for the proper execution of the model are on the grid resolution and the appropriate number of propagation steps before FFT and IFFT transforms are performed.

6.3.1.1 Grid Resolution and First-phase testing

Since the fast Fourier transform algorithm is being used, the number of grid points is preferred to equal $2^{\bar{N}}$ where $\bar{N}$ is a positive integer. Having a benchmark which provides an exact result enables various values of $\bar{N}$ be trialled for the model, and checking the variance of the results of this model and the benchmark. It is important to note that as expected, the higher the value of $\bar{N}$ chosen the closer the result will be to the benchmark with respect to the amplitudes of the shocks present in the waveform. A decision has to be made on an acceptable level difference in the results between the model and the benchmark. Higher-amplitude shocks would require finer grids in order not to lose significant portions of the shocks at every step of propagation.

Also, the studies on resolution of the grid allowed the testing of the nonlinear propagation part of the model (referred to earlier as the first-phase). Using the high grid resolution the output of the nonlinear propagation part of the model can be compared with analytical results (for regular sawtooth waveforms only) or the results from FDNS to validate that part of the model. This is discussed fully in section 6.3.2.

Figure 6.8 shows the error in propagation of a regular sawtooth with 20 shocks, synonymous with a pressure profile from a turbofan with 20 perfectly matched blades, over a typical intake duct length, for grid resolution of values $\bar{N}$ up to 20, when checked against analytical results for the same case. It is evident from the figure that the higher the grid resolution the closer the result to the analytical results. The error is evaluated with respect to the difference between the exact analytical value of harmonic amplitudes and those of each grid resolution. This can is expressed

$$error = \sqrt{\frac{\sum^{N} |C_{m_{grid}} - C_{m_{analytic}}|^2}{\sum^{N} |C_{m_{analytic}}|^2}} \tag{6.13}$$

where $C_{m_{grid}}$ are the amplitudes obtained at each grid resolution and $C_{m_{analytic}}$ are corresponding amplitudes obtained from the analytic solution.

To further appreciate the differences the logarithmic value of the percentage error is plotted on the vertical axis in figure 6.9.This figure enables the magnitude of the error to be appreciated and it can be observed that there is a linear decline of logarithm of error as the grid resolution is increased.

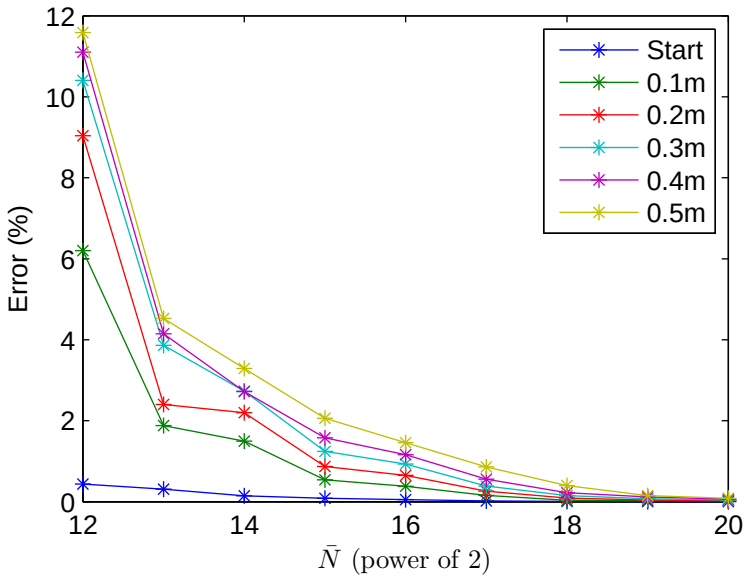

Figure 6.8: Percentage error for propagation of regular sawtooth in rigid duct for various grid resolutions compared to analytical results

Setting a strict limit of maximum error less than 2 percent at the highlight plane (furthermost point of propagation, i.e. $z = 0.5D$), the least resolution that can be employed in this propagation model was determined as that with $\bar{N}$ equal to 18 that is, a grid with $N = 2^{18} + 1$ points for the discretization of the waveform. An additional point is added to the number because the last point in the waveform is exactly equal to the first point but these two point are represented separately in the sample space.

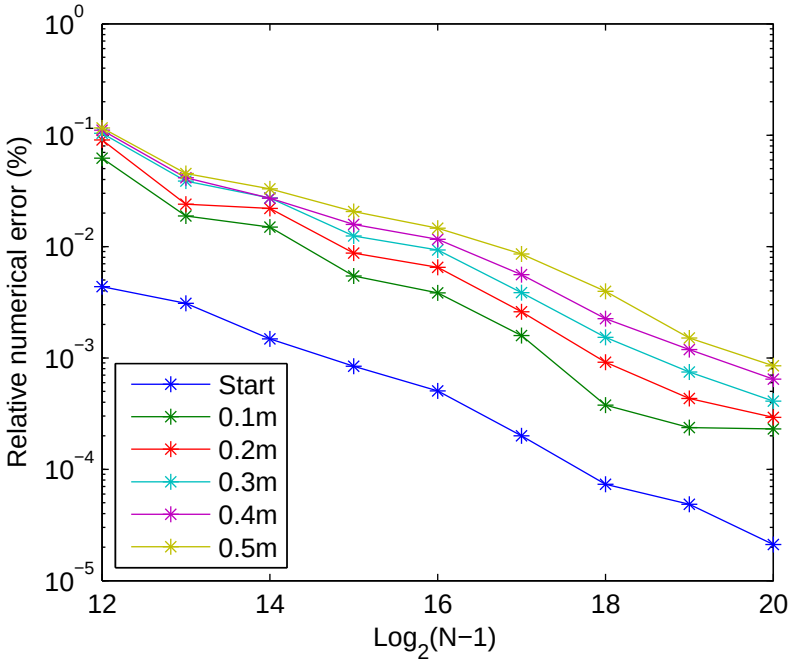

Figure 6.9: Relative percentage error (on logarithm scale) for propagation of regular sawtooth in rigid duct for various grid resolutions compared to analytical results

6.3.1.2 Evaluating Propagation Distance before Application of Absorption

After obtaining a suitable finite difference grid resolution for the sawtooth, studies to find out the number of propagation steps that can be taken before FFT and IFFT transforms can be performed was carried out. The propagation steps directly translate to a finite distance in the inlet duct. The ability to propagate the waveform over some distance induct before applying the absorption of the liner saves a significant amount of computational time[58]. Depending on the computational power of the computer employed for running the simulation, several minutes may be saved in computation time for this $2^{\bar{N}}$ grid resolution. To incorporate the possibility of propagating for a number of steps before implementing the Fourier transforms, equation (6.12) can be rewritten as

$$C_m^{j+1} = C_m^j \exp\big[-\big(A_m + iS_m\big)\zeta\Delta\bar{z}\big], \tag{6.14}$$

where ζ is the number of propagation steps taken before the FFT Transform is performed. The model simulation was run for a typical intake duct length with FFT and IFFT performed at various propagation step intervals. Figures 6.10 (and 6.11) show the results with these FFT and IFFT performed at various intervals (of 0.0006D, 0.006D and 0.06D respectively) on a regular sawtooth with high amplitude shocks, and how they compare with analytic results for a rigid intake duct.

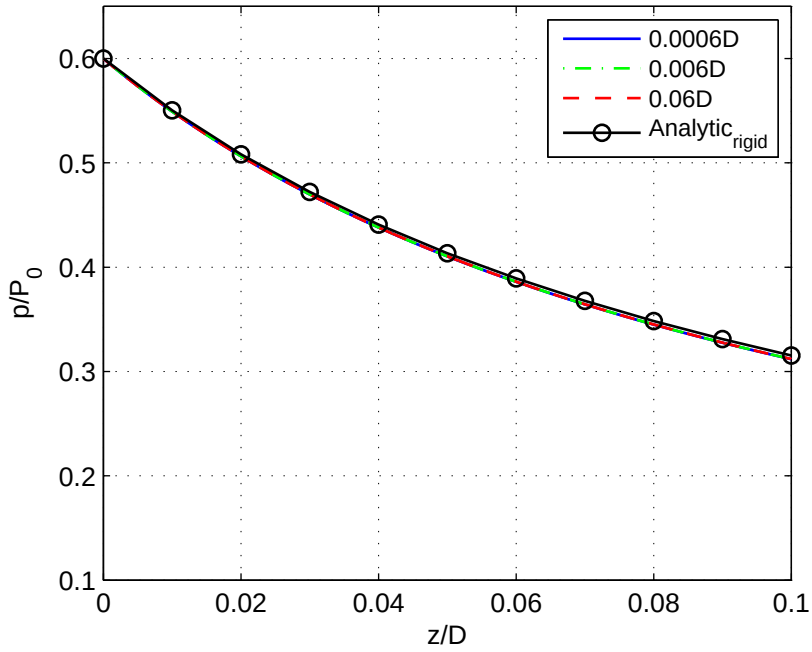

Figure 6.10: Shock amplitude attenuation for FFT and IFFT performed at various intervals for rigid intake duct

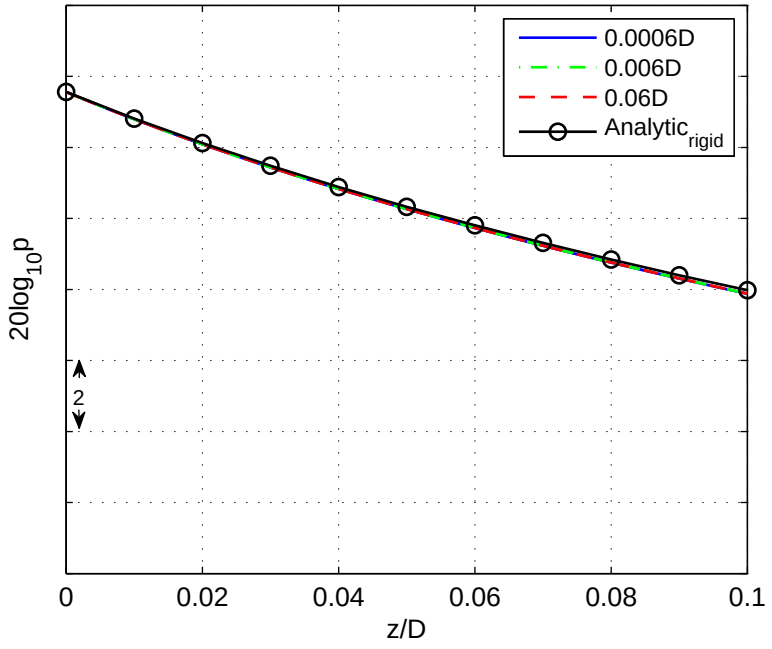

Figure 6.11: Sound level attenuation for FFT and IFFT performed at various intervals for a rigid intake duct

There exist very little difference between the analytical result and each propagation. Another interesting observation is that although the Fourier transforms were performed at varying intervals, the result for the simulation for this intervals do not show any clear difference. This may be because there are no changes to the frequency spectrum between the FFT routine and the IFFT routine as no acoustic liner effects are present in this rigid duct case. For the lined wall case, figures 6.12 (also 6.13), still utilizing the same regular sawtooth and intervals used in the rigid wall case, the effects of performing the Fourier transforms at different intervals can now be seen. When compared with the analytical result, it is clear that when the transforms are performed more regularly the closer the result is to the analytic solution. The step points are the points in the propagation where the transforms and acoustic liner absorption process are implemented. The results for the 0.06D interval case clearly shows the biggest differences throughout the length of propagation, while the 0.0006D interval case closely matches the analytic solution.

It can be inferred that as long as the axial station at which results are required are not specified to two decimal places (in meters), an interval of about 0.006D will give acceptable results.

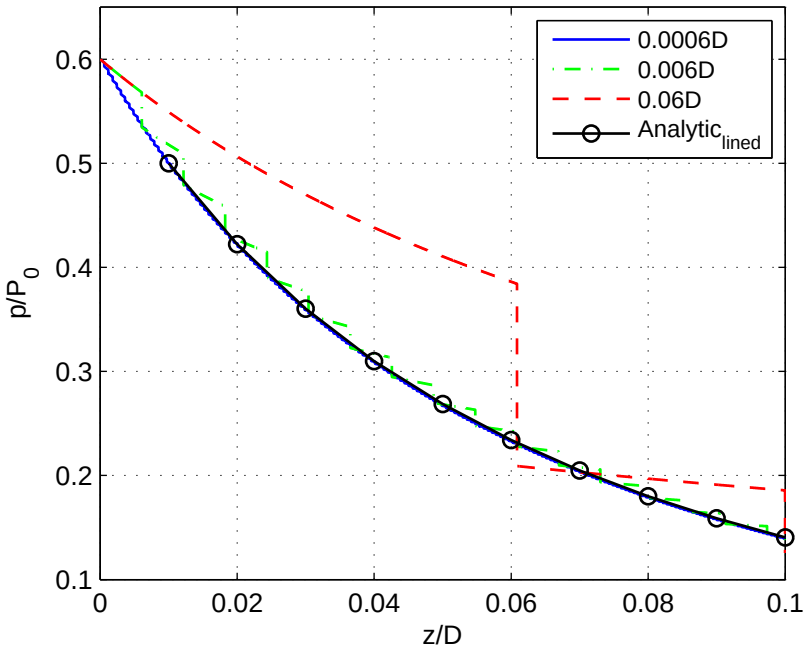

Figure 6.12: Shock amplitude attenuation for FFT and IFFT performed at various intervals with constant absorption in a lined duct compared to analytical results

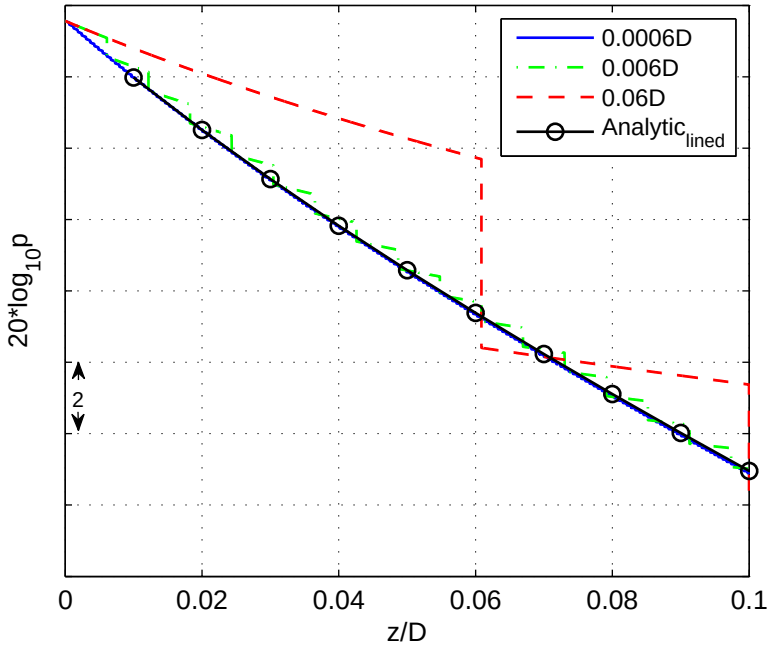

Figure 6.13: Sound level attenuation for FFT and IFFT performed at various intervals with constant absorption in a lined duct compared to analytical results

6.3.2 Validation of Nonlinear Propagation

The model development was in two phases. The nonlinear propagation of the pressure waveform was first completed, and then the application of liner absorption was examined. The results of the nonlinear propagation process was validated against an analytical result and against results from benchmarks (the time-domain model for rigid duct and the frequency-domain based FDNS). The results of nonlinear propagation were compared with those of the benchmarks at all axial positions up to a typical duct length of 0.5D. Very good agreement is observed between the benchmarks and the NP-SWIND. Figure 6.14 shows one of such comparisons at the final axial station (at $z = 0.5D$ from the fan plane).

The validation of the whole model which incorporates the acoustic liner absorption is planned to be done using the FDNS model as a benchmark, and thereafter also comparisons with measured data will be carried out.

6.3.3 Simulation Results

The following are results from the propagation model for a rig-scale type intake duct with radius equal to 0.5m, and a fan with 20 blades. The fan and duct parameters used as input in this model are those of the rig-scale test measurements carried out by

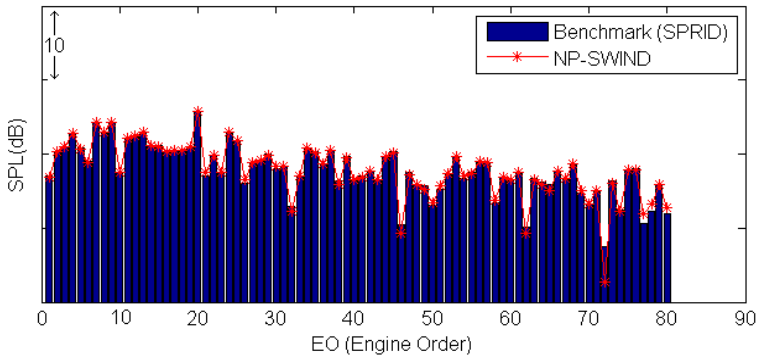

Figure 6.14: Comparison between results of Benchmark SPRID and the NP-SWIND model at $z = 0.5D$

Rolls-Royce. These values are used in order to be able to validate results against these measurements provided by Rolls-Royce. The results shown in the following figures are outputs of the NP-SWIND model for realistic acoustic liner attenuation rates. Applying the model axial wavenumbers gives the absorptive part and the phase as seen in following equation in which the exponential of the axial component of pressure has been isolated for convenience

$$e^{-ik_z z} = e^{i(k_{z_r} - ik_{z_i})z} = e^{(k_{z_i} - ik_{z_r})z} \tag{6.15}$$

where z is the axial direction, k_z is the axial wavenumber with real and imaginary parts k_{z_r} and k_{z_i} respectively.

The waveform employed for propagation is shown in figure 6.15, together with its frequency spectrum. As this wave is propagated by the model, the acoustic liner absorption effect is also applied. It was observed that as this acoustic liner effects were being applied, the initially straight expansion waves which exist between the shocks started to become wavy (figure 6.16) and this waviness increased with distance due to the combined effect of the acoustic liners and the nonlinear distortion of the waveform.

In figures 6.17-6.19 the progressive effect of absorption by the acoustic liner on the waveform and SPL-frequency spectrum is obvious especially around the BPF tone. The realistic acoustic liner modelled here is optimized around the BPF tone. The amplitudes of the shocks have greatly reduced (though still distinguishable) and the expansion waves have become wavy. It is important to point out that the phases (S_m in equation (6.14)) were set to zero in the simulation that generated these results. Equally, it is important to note that of the $(N-1)/2$ frequency bins in the spectrum, absorption is applied to only the first 200 due to the frequency limits of the realistic absorption coefficients available. The vertical axis of figures 6.18 and 6.19 has been adjusted hence, the —— line indicates the minimum of the vertical scale of the previous figures. This holds for subsequent figures with adjusted vertical axes.

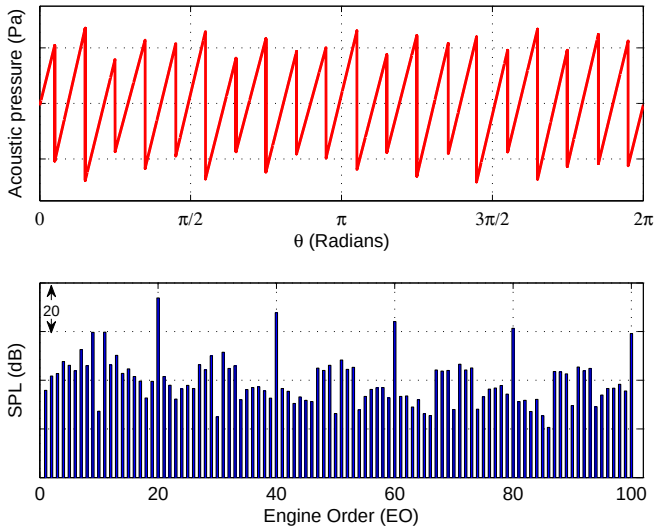

Figure 6.15: Pressure waveform and its frequency spectrum at the start of propagation $z = 0$

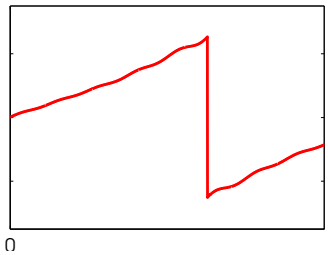

Figure 6.16: Waviness of expansion waves commences as acoustic liner absorption is being applied

The full axial wave-number (absorption and phase) information were applied to the first 200 tones in the generation of the results displayed in figures 6.20 and 6.21. In these figures, the additional effect of the phase is observed in the rounding off of the tops on the shocks. Comparison of these figures with figures 6.17 and 6.18 shows no significant differences. The rounding of the top of the shocks does not translate to significant changes in the frequency spectrum at $z = 0.1D$. At $z = 0.2D$, the observable differences occur mainly at the higher frequencies were lower levels are predicted when absorption and phase values are used.

6.4 Summary

The NP-SWIND model which uses the combined time-frequency domain approach to combine the nonlinear distortion and acoustic liner absorption in a single model has

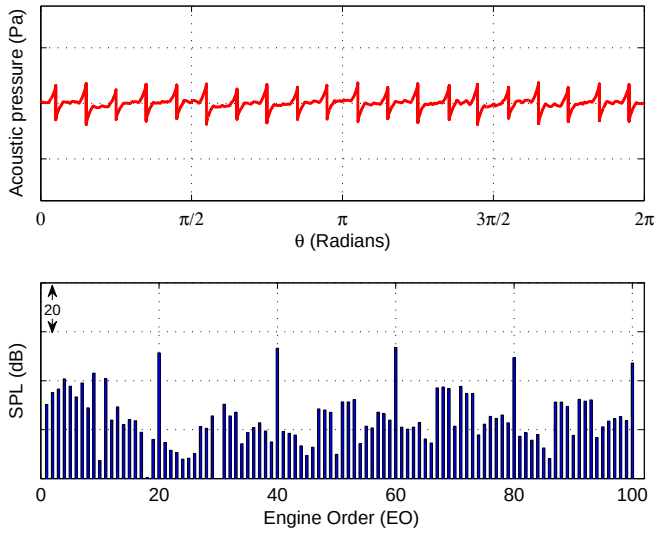

Figure 6.17: Pressure waveform and its frequency spectrum at $z = 0.1D$ using absorption k_{z_i} only

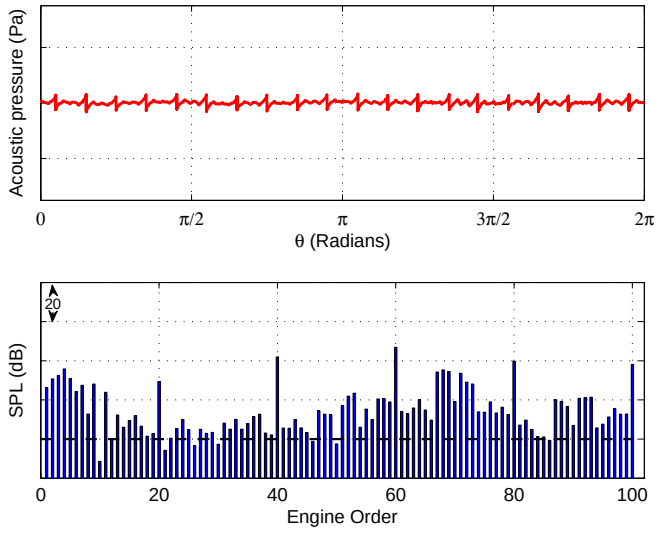

Figure 6.18: Pressure waveform and its frequency spectrum at $z = 0.2D$ using absorption k_{z_i} only [- - - line indicates the minimum of the vertical scale of the figure showing spectrum at $z = 0$]

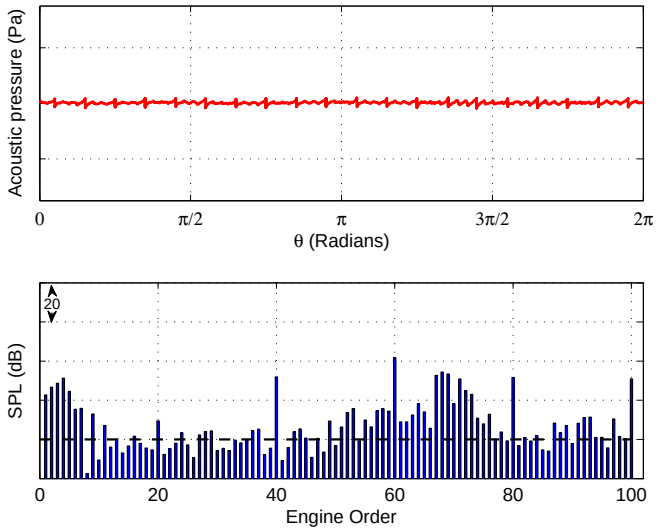

Figure 6.19: Pressure waveform and its frequency spectrum at $z = 0.3D$ using absorption k_{z_i} only [- - - line indicates the minimum of the vertical scale of the figure showing spectrum at $z = 0$]

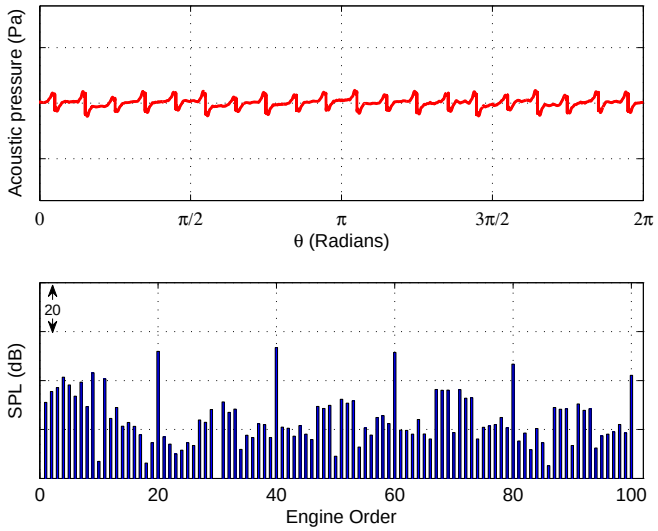

Figure 6.20: Pressure waveform and its frequency spectrum at $z = 0.1D$ using whole axial wavenumber; absorption and K_{z_i} and phase K_{z_r}

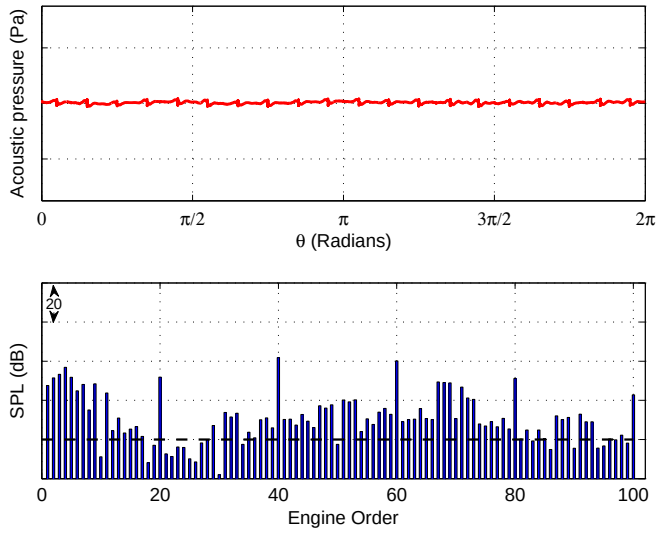

Figure 6.21: Pressure waveform and its frequency spectrum at $z = 0.2D$ using whole axial wavenumber; absorption and K_{z_i} and phase K_{z_r} [- - - line indicates the minimum of the vertical scale of the figure showing spectrum at $z = 0$]

been developed. The nonlinear propagation part of the model has been validated with various benchmark solutions after studies of the suitable number of grid points for the finite difference grid, and the evaluation of the propagation distance that is allowable between Fourier transforms. The validation against the benchmark solutions certifies the model for rigid ducts. Various results have been shown for the whole model with both the nonlinear distortion and acoustic liner absorption processes combined. This results are yet to be validated against the benchmark (FDNS) and measured data. The validation of NP-SWIND will open the way to the further development of the model.

Chapter 7

Validation of Aircraft Intakes Time-Frequency Domain Nonlinear Propagation Code

In the previous chapter, the propagation of a sawtooth pressure waveform in an aircraft intake with installed acoustic liners was investigated. The results from the time-frequency domain model employed to account for the nonlinear attributes of the propagation of shock waves and the absorptive effect of the acoustic liners requires some verification. It is common practice to validate models with measurements or in some instances with well-established empirical or analytical models. In this chapter, the propagation results obtained for lined intakes will be validated with measurements. It is useful to first test the results of the model in the absence of acoustic liners. The availability of measurements for this rigid-wall configuration allows the validation of the nonlinear propagation of the shocks without needing to account for the absorption introduced by the acoustic liners. After this, validation of results for a lined-wall configuration is undertaken.

7.1 Information on measured data

The measured data employed in this study and particularly in the validation of the time-frequency domain model were acquired by Rolls-Royce in a scaled-engine test carried out in an anechoic test rig in AneCom, Berlin. This data is proprietary and has been used according to laid down standards. The static model-scale rig test entailed the acquisition of data inside the intake duct, in the near-field and in the far-field. Pressure transducers were mounted on the wall inside the intake duct. These pressure transducers were installed at varying distance along the axis of the duct from very close to the fan up to the periphery of the highlight plane of the intake duct. Figure 7.1 shows an

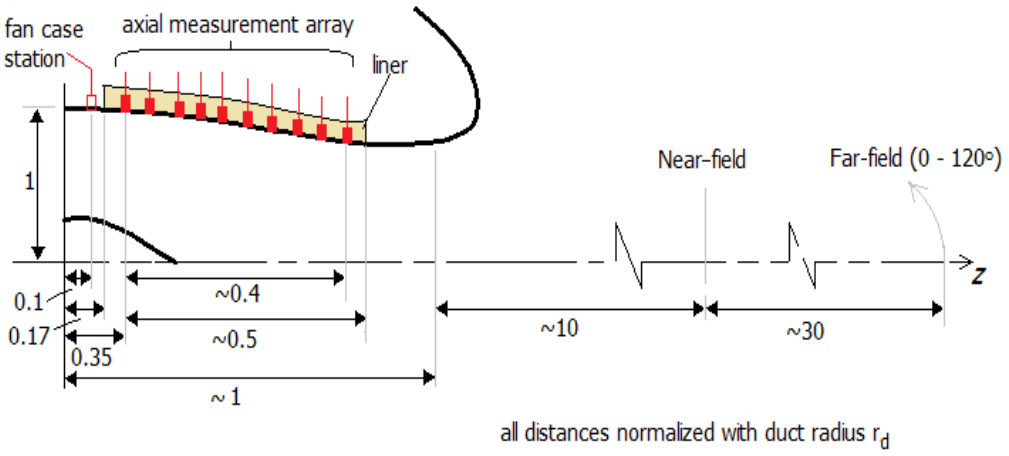

Figure 7.1: Illustration of the model-scale fan rig and measurement stations

illustration of the location of the measurements in-duct and outside the intake duct. All the distances are normalised with respect to the radius, r_d, of the intake duct. The measurements that are of interest here are those acquired in the intake along the axial direction and the far-field measurements. These measurements are used in this thesis for the validation of the time-frequency domain propagation of the sawtooth waveform generated at the fan plane.

In the intake duct(figure 7.1), the measurement acquired closest to the fan-plane at about $0.104r_d$ is the starting location for propagation in the model. At this location, a number of measurements were taken with microphones places around the azimuth. The advantage of this arrangement ensures a well resolved starting waveform input into the time-frequency domain model. Data was also measured at ten different location between $0.35r_d$ and $0.75r_d$ upstream in the intake duct. Only in-duct measurements are required at this stage. Measurements outside the duct in the region of propagation covered in the time-frequency domain model are used later in chapter 8.

The liner is installed in the duct from about $0.17r_d$ to $0.82r_d$. From the fan plane to the highlight plane, the intake duct is about the length equal to its radius. The near- and far-field measurements are at about 10radii and 40radii from the centre of the highlight plane.

7.2 Waveform near the fan

In order to adequately predict the evolution of the pressure field generated by the supersonic fan at any upstream location it is important to, at the beginning, check the agreement of the input-sawtooth to the propagation model against that measurement in the scaled-engine test rig. The first measurement closest to the fan taking at $0.1r_d$

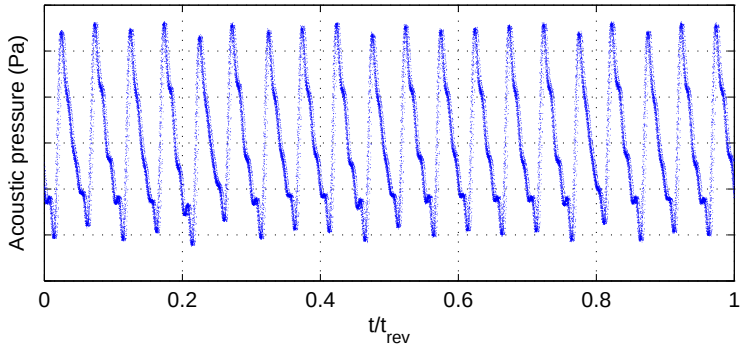

Figure 7.2: Measurement near the fan at distance $0.05r_d$

marks the reference point from which propagation is commenced. Due to the sensitivity of the nonlinear process to minute differences in shock amplitudes it is essential to closely approximate the sawtooth at the start location as this may progressively affect to a significant degree the level of agreement of prediction and measurement.

7.2.1 Measured against averaged-centred sawtooth

The availability of pressure measurements very close to the fan allows for a starting waveform to be generated from the measurements. Data was acquired over a time $\tilde{t}$ for a sampling frequency $\tilde{f}$ with a total number of samples, $\tilde{N}$. The number of revolutions marked by tachometer measurements is $\tilde{s}$. Number of the samples per cycle is

$$N_s = \frac{\tilde{N}}{\tilde{s}} \tag{7.1}$$

Using the tachometer measurements as trigger for a new revolution, the measurements can be overlaid over the duration of a single cycle to get the distribution such as that shown in figure 7.2 This is repeated for measurements at each location of measurements around the azimuth and in the axial direction.

After putting all the measurements together at all axial stations, it is necessary to sort out the relative scatter of the points along the sawtooth form by describing a smooth trend line over the distribution. First, for the good resolution of the shock waves, it was necessary to capture the peaks. Also, it is important to carefully resolve the azimuthal position of the shock waves themselves within a full revolution.

An algorithm was written to scan through the data picking the peaks and troughs for each shock and the corresponding circumferential position. The shock values are then sorted by picking the maximum value and minimum value for each shock and the position for the shock is the average between the position of the maximum value and the

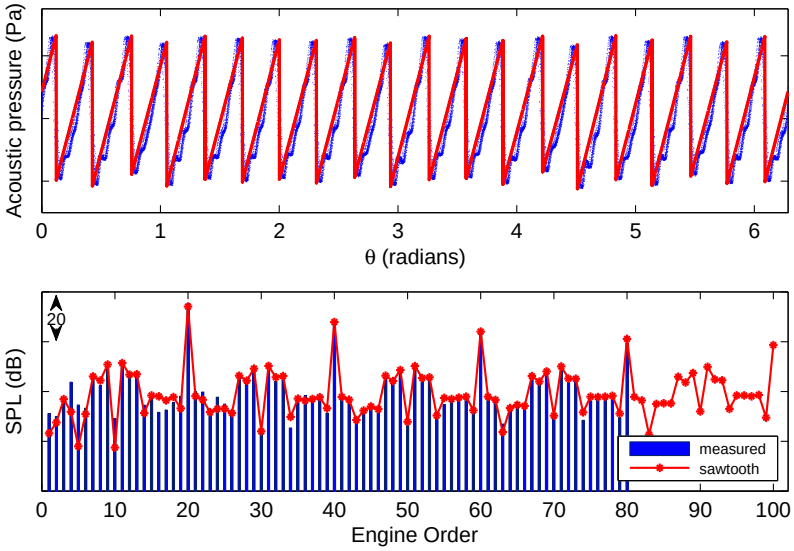

Figure 7.3: Comparison of measurement and idealized sawtooth at distance $0.05r_d$

minimum value. Concisely, for any shock with maximum measurement $\tilde{p}_{max}$ at position $\tilde{\theta}_{max}$ and minimum measurement $\tilde{p}_{min}$ at position $\tilde{\theta}_{min}$, the shock position is taken to be

$$\tilde{\theta}_n = \left(\tilde{\theta}_{max} + \tilde{\theta}_{min}\right)/2. \tag{7.2}$$

One example of the smooth waveform that results from the algorithm is shown in figure 7.3. Figure 7.3 shows the sawtooth described over the measurement acquired closest to the fan. The frequency spectrum of the smooth sawtooth is compared against the spectrum from the measured data in the bottom plot in figure 7.3. There is very good agreement showing that the algorithm for fitting smooth sawtooth to the measured data is reliable. The measured spectrum data are are only provided up to about Engine order 80.

7.2.1.1 Making use of frequency spectrum of measured data

Another means of obtaining a smooth waveform from the measurements acquired closest to the fan is achieved by using the frequency spectrum of the measured time series in the optimization routine explained in detail in section 4.2.2. Using this method generates a waveform with shock waves differently distributed, and with slightly different shock amplitudes, but accurate representing the frequency spectrum. For clarity 'differently distributed shock waves' means that the order of the shock waves in the sawtooth waveform using this method is different from that of the measured.

This indicates that the character of the sawtooth is retained whatever the order may be as long as the amplitudes and relative shock spacing among the shocks are retained. Any significant variation of these two characteristics, that is, the shock amplitudes and relative shock-to-shock spacing will yield a significantly different frequency spectrum. To put the sensitivity of the sawtooth in good perspective, if the shock amplitude of any one shock is significantly altered in a given a sawtooth or if two shocks are moved significantly closer or further apart, the frequency content will be significantly different.

7.2.1.2 Correction for variations over each revolution

As expected, there are slight fluctuations in the measured data due to the resolution given by the sampling frequency. Over each revolution, the number of points captured varies from an average by one data point. This describes a situation where it appears that a revolution has been marked as completed by the tachometer but the last point expected for that revolution is then logged immediately after. It is not strange that the number of point per revolution differs as the fan's revolution over a fixed period is not an integer and the limitation of instrumentation coupled with unpredictable operation conditions will not allow the resolution of data acquisition to be tailored exactly to the fan's speed.

In order to accurately represent each period of revolution, it was useful to get an average time for one revolution and mark this as the time over which the acquired data is ordered over the sampling time. The average time forms a platform to attached time signatures to every acquired data and to be able to successful represent the distribution of the measurements circumferentially in the azimuthal direction.

In summary, having a data sample (with $\tilde{N}$ data points and $\tilde{s}$ revolutions) spanning a period $\tilde{t}$, if the average time for a revolution is $\tilde{t_r} = \tilde{t}/\tilde{s}$ and , a data point with serial number $\tilde{n_N}$ has a time allocation,

$$\tilde{t_N} = \frac{\tilde{n_N}\,\tilde{t}}{\tilde{N}} \tag{7.3}$$

on the sampling time line. To make sure every data point falls within a revolution, the time $\tilde{t_N}$ is adjusted to vary only over a period equal to $\tilde{t_r}$. Hence, the time of a data point is adjusted with respect to the specific revolution $\bar{s}$ it falls within as

$$\tilde{t}_{N_r} = \tilde{t_N} - \bar{s}\tilde{t_r}. \tag{7.4}$$

This allows each time allocation for each data point fall within the range 0 to $\tilde{t_r}$. Plotting the data against $\tilde{t}_{N_r}$ then yields the pressure distribution over the circumference of the

duct at the axial position where the measure in taken. As seen in figure 7.2, the pressure distribution over one revolution can be obtained.

7.2.1.3 Measurements in Rigid Duct

The waveform at selected locations where measurements were taken along the duct axis are shown in figure B.1(in Appendix B).

As shown in figure 7.1, measurements were acquired in the fan case close to the fan at ten different locations on the duct wall along the duct axis. These measurement locations are the same for the rigid and lined wall configurations. In figure B.1, a measurement in the fan case ($0.1r_d$)and measurements at $0.35r_d$, $0.483r_d$, $0.616r_d$ and $0.75r_d$ are shown. This figure shows the changes that have taken place in the pressure field from a point close to the fan to a distance about three-quarters of the duct radius.

7.2.1.4 Measurements in Lined Duct

Similarly, the figure B.2 shows the measurements at the same stations (fan case, $0.35r_d$, $0.483r_d$, $0.616r_d$ and $0.75r_d$) for the lined duct wall configuration. The changes from fan case measurement to the furthermost axial microphone is obvious more in the lined duct as expected due to the combined effect of nonlinear attenuation and liner absorption of the pressure field waveform as it propagates upstream. The variations in the waveform at different stations along the duct axis are discussed in the next section 7.2.2.

7.2.2 Spatial representation of measured data

In order to spatially represent the pressure distribution, the time axis is converted to the direction of travel of the waveform as it spirals along its helical path. The waveform propagates along a helical path in the direction x (figures B.1 and B.2) and consequently, propagates upstream in the axial z direction. The azimuth position along the helical path is represented by angle θ (in radians), the pressure waveform can be re-oriented in space for the range $\theta = 0$ to 2π. Figure 7.4, a spatial representation of figure B.1, shows the waveforms at fan case, and four axial stations along the duct axis.

For the fan case measurement, figure 7.4(a), the acoustic pressure normalized with the maximum value of the acoustic pressure at this station is plotted against azimuthal angle. The irregular distribution of the shock waves is obvious. This differences in shock amplitudes and consequently, the extent or span of the expansion waves accentuate the blade-to-blade differences.

Figure 7.4(b) shows the measurement acquired at $0.17r_d$, the basic form of the waveform is retained but the shock amplitudes are about a fifth of their values at the previous

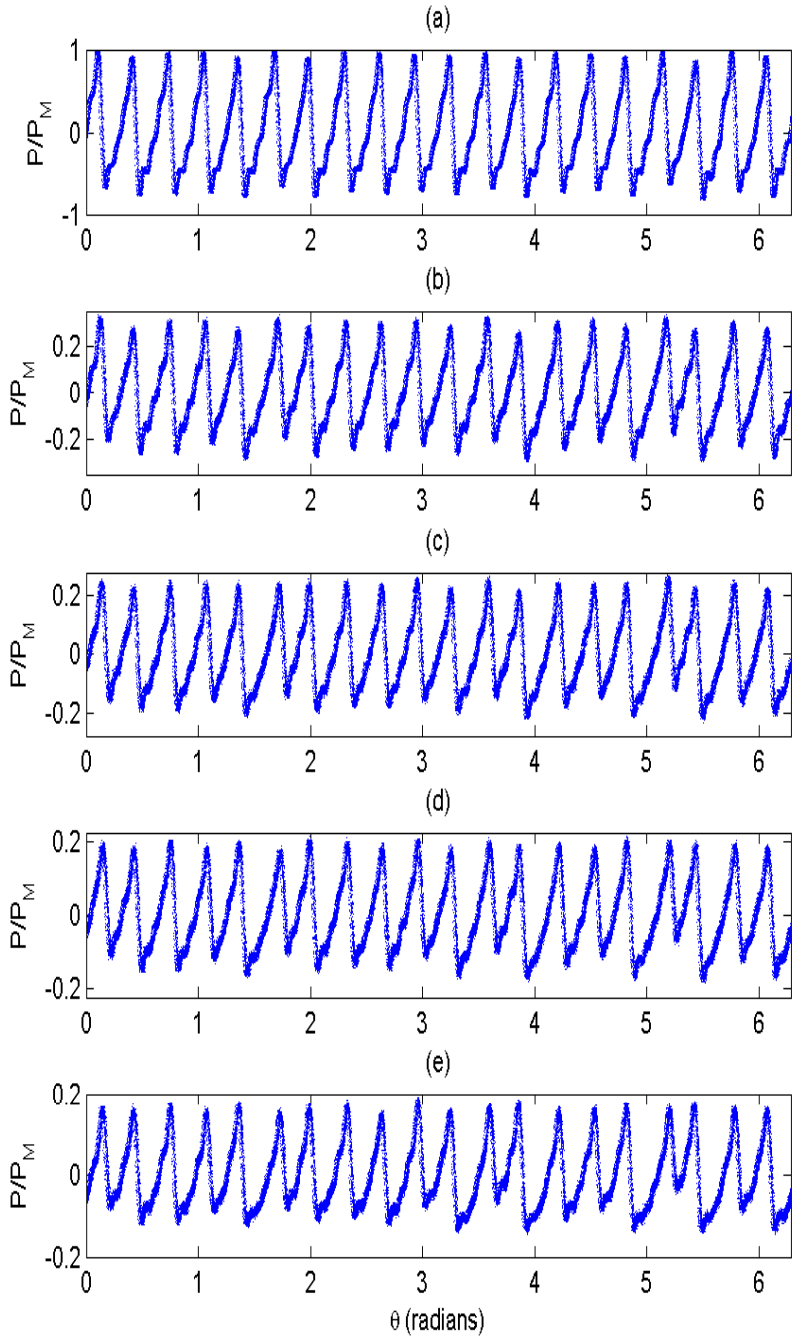

Figure 7.4: Spatial representation of measurement (a) near the fan (b) at $0.35r_d$ (c) at $0.483r_d$ (d) at $0.616r_d$ (e) at $0.75r_d$ [Note: pressure P normalized by measured ambient pressure P_M]

station.A closer look reveals that the shock waves with mid points with greater positive values have moved closer to neighbouring shock waves with mid points which comparably less positive values. This observation is more evident at the following stations shown (figure 7.4(c)-(e)). At these stations, the shock wave have been increasingly attenuated. At the last station shown here (figure 7.4(e)), the shock amplitudes are just over 10 percent of their starting values at the fan case measurements. The shock waves which have more positive values of mid point pressures are now even more positively displaced. Elongation of the expansion waves can be observed between shock waves with greater difference in their mid point pressures. For the length of the duct considered here, the shock waves are well defined at each axial station over the whole length of the duct although they have been considerably attenuated and displaced from their original positions.

For the measurements acquired for the lined duct wall configuration (figure 7.5(a)-(e)), the same stations are shown as for the rigid wall configuration. Although the experimental set up is the same except for the inclusion of the acoustic liner, slight differences can be observed for the fan case measurement when compared against the same for the rigid duct. The minute differences are seen on close examination as little changes in the shock amplitudes and positions over the whole waveform. This could have been due to experimental rig operation conditions and changes in ambient atmospheric values owing to the fact that the data acquisition were carried out on separate days.

Overall, the waveform for the two fan case measurements are similar. The waveforms captured in the measurements upstream are well attenuated compared to the measured waveform at fan case. At the stations $0.35r_d$, $0.483r_d$, $0.616r_d$ and $0.75r_d$, there has been an overall reduction of the shock amplitudes to about 15%, 10%, 7.5% and 6% respectively. Compared to the attenuation to about 35%, 25%, 20% and 18% observed in the rigid wall duct. The additional attenuation provided by the liner resulted in the greater distortion of the waveform. Since the acoustic liner is optimized for a particular frequency range, as components in this range are well absorbed, their continued is evident as the increased waviness of the expansion waves (Figure 7.6) coupled to the effects the limit of data sampling rate may add to to the resolution of the waveforms.

The waviness can be first sighted at the top ends of the expansion waves (figure 7.5(b)). It then develops along the expansion waves as propagation continues upstream. By the last of the ten axial stations, figure 7.5(e), the waveform has significantly different outlook from the well defined sawtooth as the fan case – figure 7.5(a). This waviness is analogous to what is observed as well in propagation model in figure 6.16 in section 6.3.3. Comparison of these two figures show that the waviness in the measurements is more pronounced than observed in the propagation model. As expected, the waviness of the expansion waves continue to get more accented as the nonlinear propagation, together with the absorptive effect of the acoustic liners, progresses.

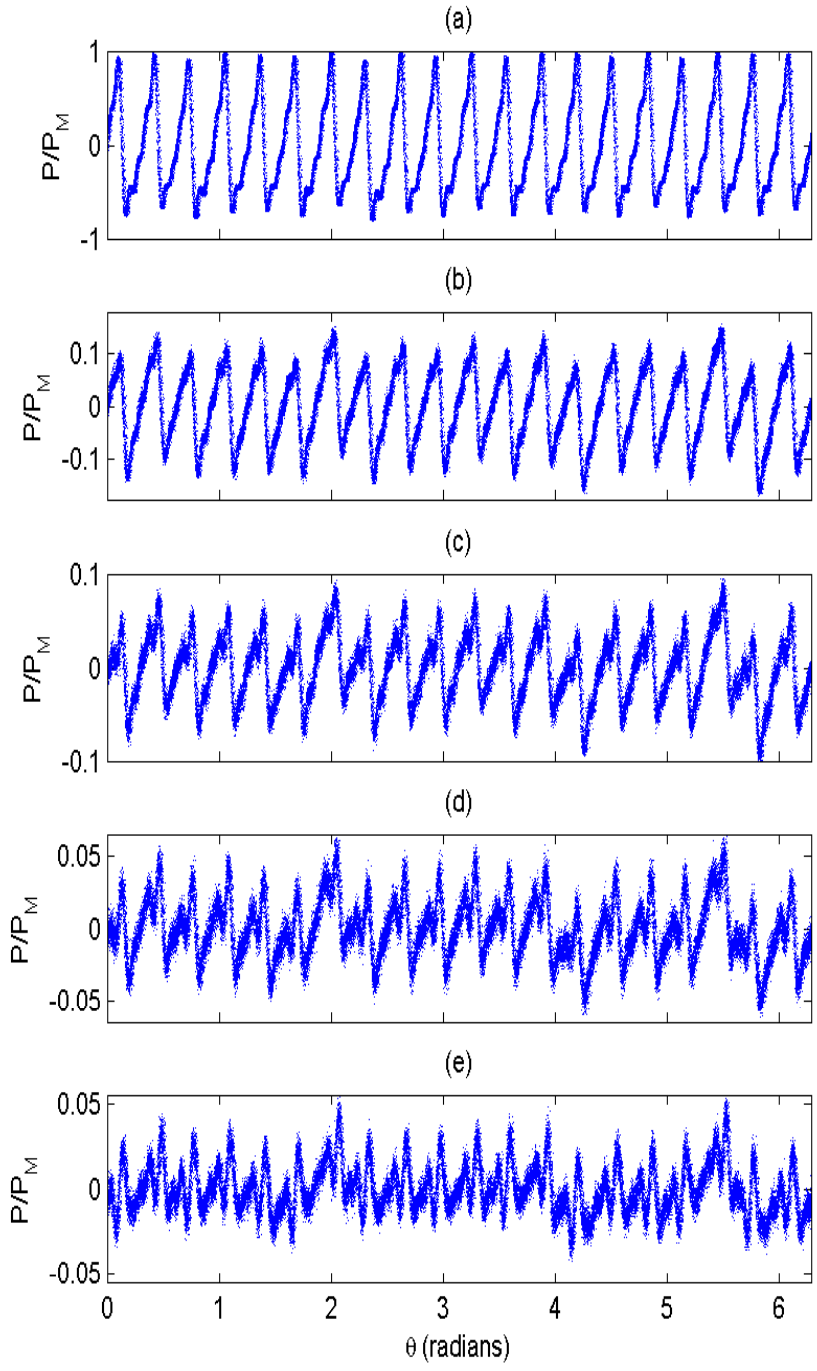

Figure 7.5: Spatial representation of measurement (a) near the fan at distance $0.05r_d$ (b) at $0.35r_d$ (c) at $0.483r_d$ (d) at $0.616r_d$ (e) at $0.75r_d$ [Note: pressure P normalized by measured ambient pressure P_M]

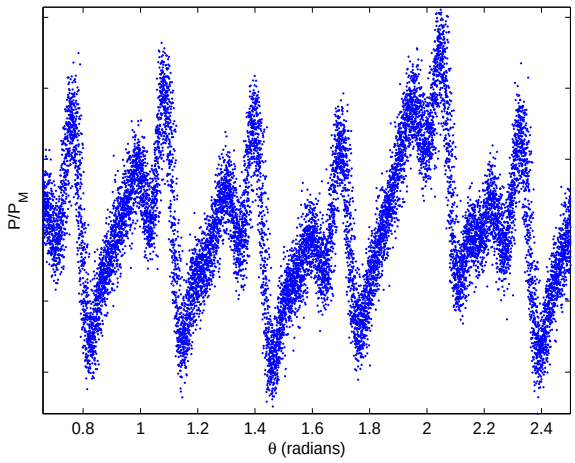

Figure 7.6: Waviness of the expansion waves for the lined duct

7.3 Comparisons: Measurement against prediction

Using the measurements closest to the fan, a smooth sawtooth which is used in the propagation model is generated. The position of the measurement near the fan marks the starting point, $z = 0$ of propagation for the predictions. The other distances of the points where measurements were acquired along the duct were corrected for the propagation model using this reference point. The propagation model, NP-SWIND (discussed in chapter 6) is used to generate the results shown in this chapter.

For propagation in the rigid duct-wall case, only the nonlinear evolution of the sawtooth is considered. This is achieved in the model by turning the liner stage off by specifying a rigid wall configuration. In the case of the lined wall duct, liner properties are obtained from a liner impedance model for the frequency range of interest. The liner performance properties form an input and are applied only over the section of the duct which is lined. Consequently for the lined-wall configuration, there are three stages. A first stage which is rigid followed by a second stage where a liner is installed. It is this area where the liner attenuation is implemented in the model. This stage is followed by another rigid wall stage upstream leading to the inlet of the duct where propagation of the waveform ends.

The results presented in this chapter are direct comparisons between the prediction results obtained from NP-SWIND and the measured data. Comparisons are shown at selected stations over the whole propagation length. The waveforms have been centred for better visualization of the comparisons. The waveform generated from the fan case measurement (figure 7.2) is used as the starting waveform for the predictions. Hence,

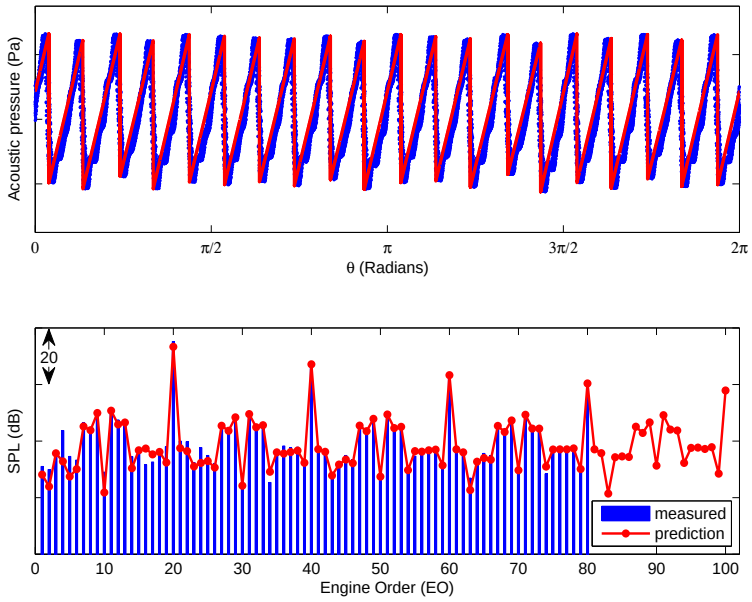

Figure 7.7: Measurement against prediction: Fan case station

all the results compared here were generated using this waveform as input into NP-SWIND propagation model. Similarities, level of agreements and observable differences are discussed.

7.3.1 Rigid Duct-wall Configuration

In this section, the comparisons from the results of the prediction model and the measurements are shown for the rigid wall intake duct. For consistency, the comparisons have been done for the same axial stations shown in section 7.2.2. At the start of the simulation, which is the same as the station where the fan case measurements were taken, figure 7.7 shows the comparison between measurement and prediction at this point. The agreement here is very good. However, some slight differences can be seen in the form of the two waveforms. In the measurements, the expansion waves are not exactly linear as there is a noticeable concave downwards. The linear expansion waves used in the prediction model does not capture this feature but assumes that the expansion waves are linear from shock-to-shock.

Another noticeable feature in the measurement here is that the shock peaks and troughs are sightly spread out and do not terminate at a single point but the propagation model clearly represents the shock amplitude over a finite jump from peak to trough. Turning attention to the SPL-frequency spectrum, it is observed that there is very good agreement between measurement and prediction at this fan case station. The results of prediction at axial station 1 is compared against measurement in figure 7.8. At this

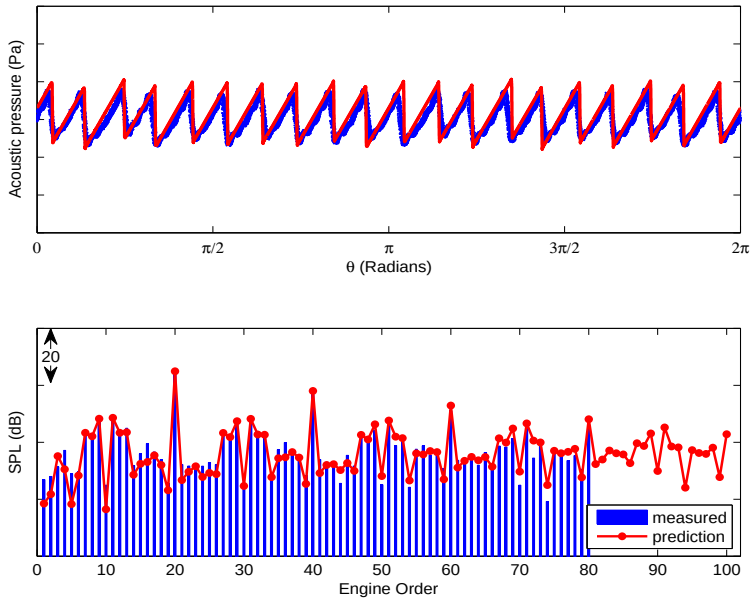

Figure 7.8: Measurement against prediction: axial station 1

station, the waveform has been propagated for a distance $0.25r_d$ and the shock amplitudes are less than half their previous values. The waveform shape is consistent with that of the previous station. The effect of nonlinear propagation is seen in the reduction of shock amplitudes and the change in shock position as shocks with higher mid-point pressures propagate faster. There is very good agreement of propagation results with measurements at this station both in the waveform generated and the frequency spectrum. The expansion wave curvature and spread of the shock peaks and troughs in the measured waveform pointed out in the fan case station are much more evident at this station, but, overall, the prediction model captures the waveform to a high degree of agreement and clearly represents the pressure field well in the frequency spectrum.

As the waveform is further propagated to axial stations 4, 7 and 10, a distance of $0.483r_d$, $0.616r_d$ and $0.75r_d$ respectively, the results of the propagation model agrees closely with measurements (figures 7.9, 7.10 and 7.11). The rate of decay of the shock waves lessens with distance as observed and pointed out in the literature [17, 18, 33, 34, 36, 41]. Over this propagation distance, the shock amplitudes are seen to gone through a reduction to about 25%, 20% and 18% of the fan case waveform respectively at these stations.

Despite the curvature in the expansion waves in the measured data, a feature which continues to be accented as the pressure field progressed against the incoming flow upstream, the one-dimensional waveforms from the prediction model agree very well with measurements at these axial stations. The level of agreement is observable in the SPL-frequency spectra at these three axial stations. The general trend of the measured

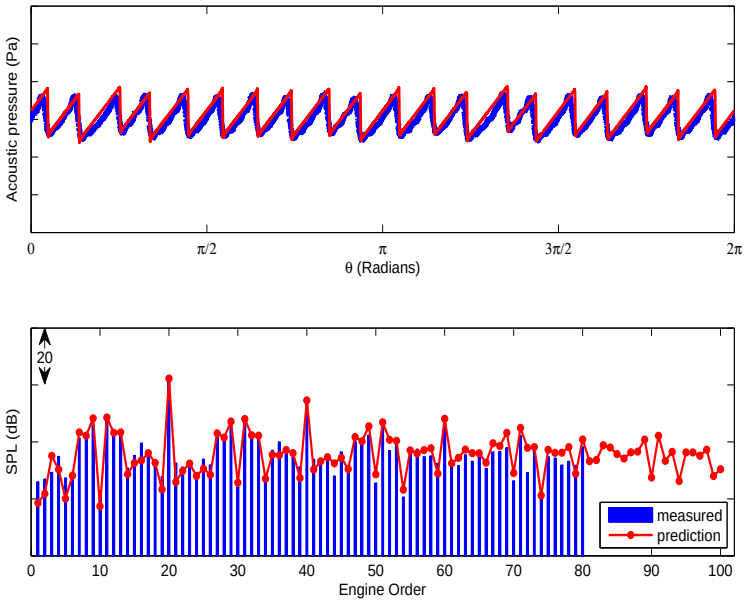

Figure 7.9: Measurement against prediction: axial station 4

spectra agree well and there is good agreement when the amplitudes of the tones in each frequency spectrum are compared against those obtained from measurements.

The rapid decay of the BPF tone and its harmonics is accurately captured by the propagation model. All features of the nonlinear propagation of sawtooth waveform such as shock amplitude attenuation, shock position displacement, are well handled by the propagation model as evident in the result comparisons. About 20dB attenuation is observed for the BPF for the propagation of the waveform fan case to axial station 10.

Comparisons of the measured and predicted attenuation of the first four BPF harmonics over a distance (normalized with duct radius at the fan plane r_f) are shown in figure 7.12(a)-(d). There is very good agreement most especially for the BPF and 2BPF tones. The overall trend and levels are well predicted. The measured 3BPF and 4BPF tone levels are similar with only slight differences at the measurement points particularly for the 4BPF tone.

7.3.2 Lined Duct-wall Configuration

Owing to the fact that the fan case measurement was acquired in a rigid section before the installed acoustic liner, the fan case comparison for the lined intake duct is exactly as that of the rigid duct – figure 7.7. As shown in figure 7.1, the liner is installed from about $0.17r_d$ to $0.82r_d$ in the duct. All the other ten axial stations where measurement

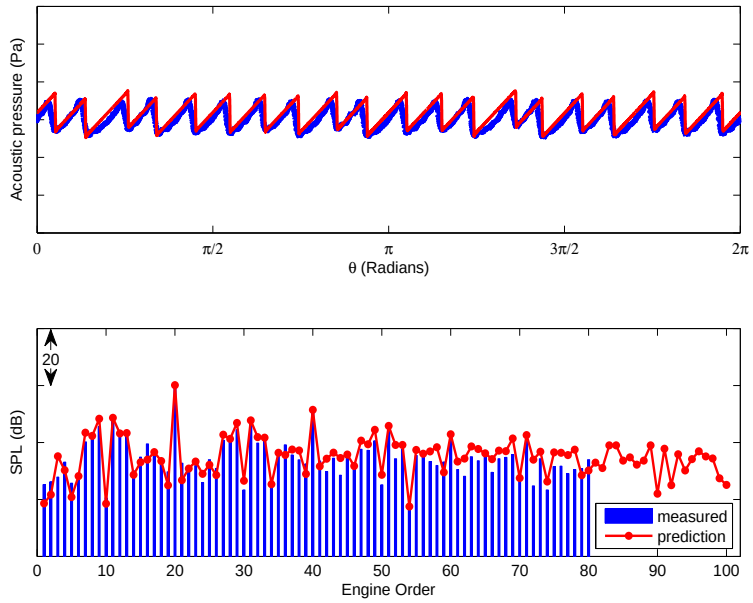

Figure 7.10: Measurement against prediction: axial station 7

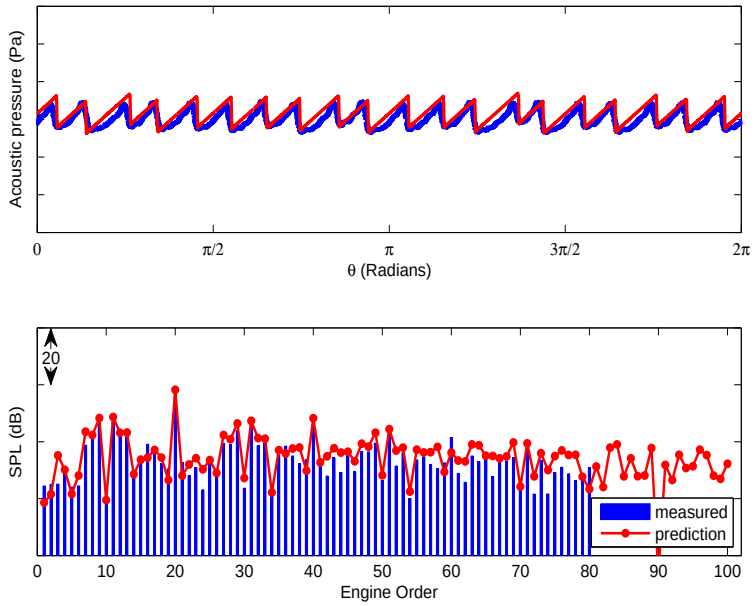

Figure 7.11: Measurement against prediction: axial station 10

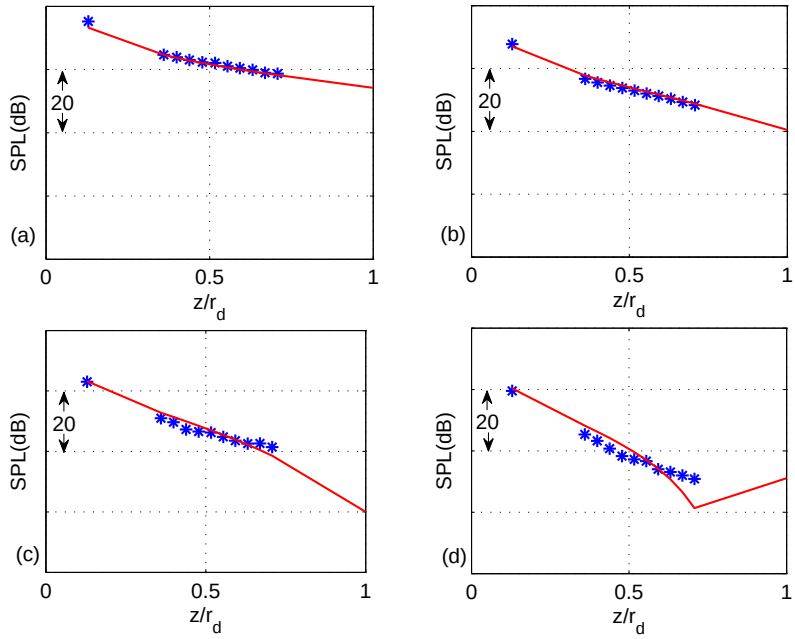

Figure 7.12: Measurement (*) against prediction (—) in rigid-wall intake: BPF harmonics attenuation (a) BPF (b) 2BPF (c) 3BPF (d) 4BPF

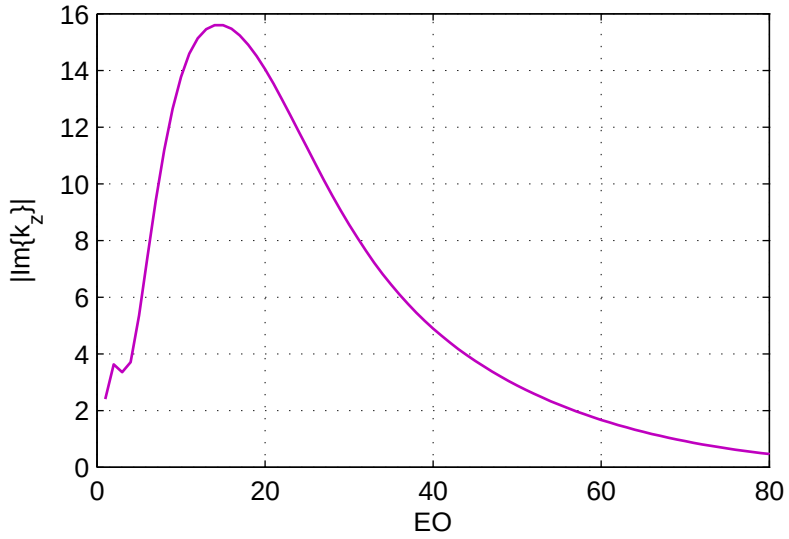

Figure 7.13: Liner decay rates

were acquired are within this lined range. Results are compared at the axial stations 1,4,7 and 10.

A single-degree-of-freedom (SDOF) liner was installed for the experiments details of which are proprietary. A linear SDOF lined-wall duct mode code developed by Dr. Alan McAlpine, in the Institute of Sound and Vibration Research at the University of Southampton, was used to generate liner decay rates for the prediction model. This liner decay rates are provided for a flow condition with a boundary layer thickness of about 4% of the radius. The decay rates are shown is figure 7.13.

Figure 7.14 is the comparison at axial station 1. The agreement of the prediction with measurement at this station is good. The amplitudes of the tones agree closely with the measurements. The waveform at this station is much more attenuated than that at the same station in the rigid duct. This is principally a result of the inclusion of the effect of the acoustic liner. The shock amplitudes in the waveform are, overall, just about an average of 18% of the waveform of the previous fan case station. To clearly see the comparison of the waveforms, the vertical scale has been halved in figure 7.15. It is clearly seen that for the predicted waveform, the peaks and troughs of the shock extend further than those which are measured. This is the residual effect of the spread that is observed at the peaks and troughs of the measured waveform. The prediction model clearly defined the peaks and troughs whereas for the measurements, the capture of the peaks and troughs are dependent on the resolution of sampling. It was also observed that there is a downward displacement of the measured sawtooth wave form in the lined duct configuration when compared to that measured in the lined intake duct. Hence, the fan case measurements for the rigid and lined intake duct configurations, although having all shock amplitudes the same, have a slight vertical difference in the position of the waveform. This is clearly evident in figure 7.14 as the measured waveform is not centered with the predicted sawtooth waveform. This is corrected in figure 7.15 and in subsequent comparisons as well.

In figure 7.16, the comparison at axial station 4 shows good agreement. The increased dissipation of the tones around the BPF (engine order 20) is easily observable. The acoustic liner was tuned to attenuate this frequency range. The waveform shows pointed shock ends which is not evident in the measured waveform. The waviness of the expansion waves, a result of the attenuation of certain frequencies is evident in the measured waveform and the predicted waveform as well. It should be noted that the folds in the expansion waves of the measured waveform are displaced closer towards the shock peaks while that of the predicted waveform is smooth and symmetrical along the length of the expansion wave. This may difference in the location of the fold may be due to the curvature which is observed in the measured waveform at the start fan case station but not represented in the input waveform for propagation.

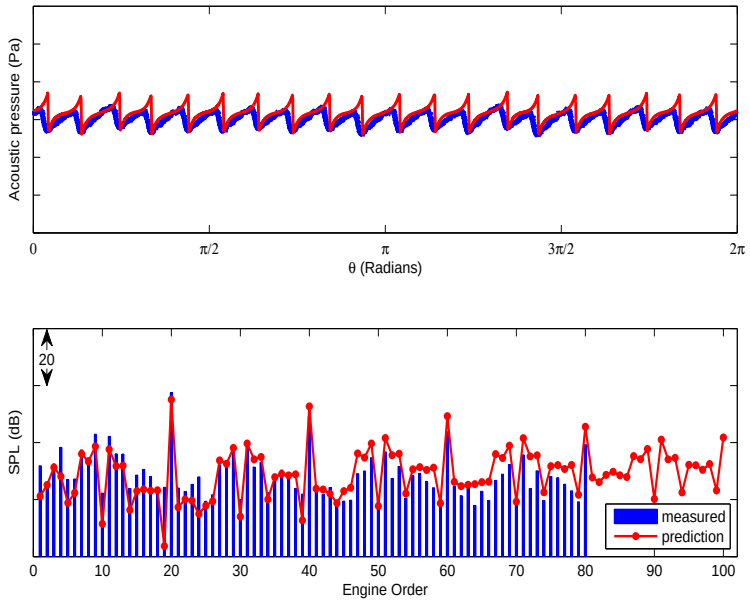

Figure 7.14: Measurement against prediction: axial station 1

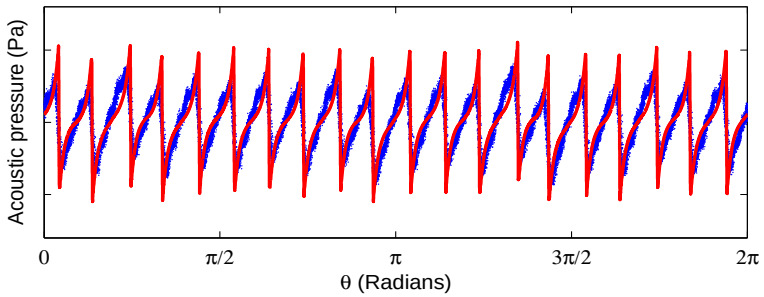

Figure 7.15: Measurement against prediction: axial station 1

At the axial stations 7 and 10 (7.17 and 7.18), the waveforms shown are four times the scale used in the fan case comparison. This is because the waveform has been greatly attenuated. The agreement of measurement and predictions at these stations are good. The absorptive effect of the acoustic liner is slightly overpredicted at these axial stations. This is seen for the BPF tone and tones close to the BPF. Other tones' levels match almost accurately. The - - - - - line in the SPL-frequency plots mark the lower limit values of the comparison plots shown for the fan case and axial stations 1 and 4. In the waveform the waviness of the expansion waves have increased for both the measured and predicted waveforms. By the time the wave has propagated to axial station 10, the features of the expansion waves are dominant as the shock amplitudes have been reduced to about 6% of the initial waveform captured in the fan case. A closer look at the measured waveform at this station shows that the wavy folds of the expansion waves

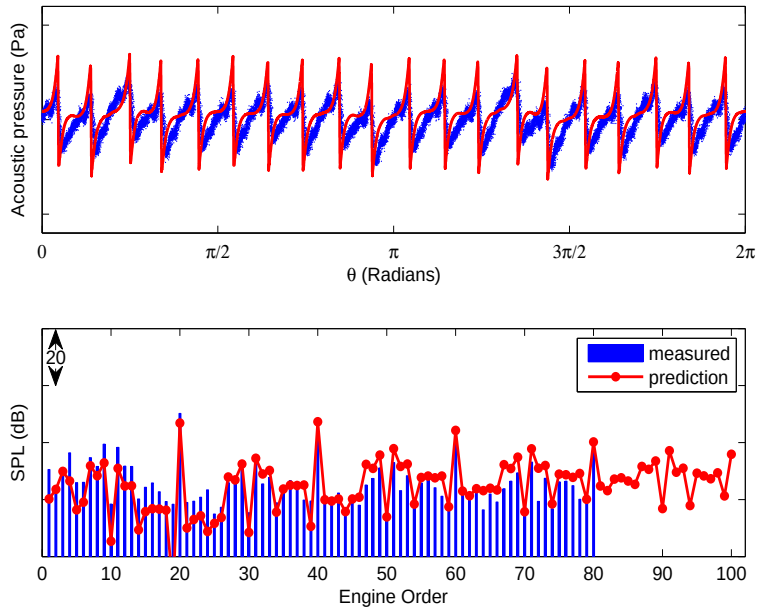

Figure 7.16: Measurement against prediction: axial station 4

have actually developed to have wave peaks and troughs. The prediction waveform, as it starts with a linear expansion wave, has expansion waves which have their central section flattened out. The continuous attenuation of certain frequencies by the acoustic liner brought about a increasing change in the features of the expansion waves. Ultimately, the agreement of the prediction and measured data for the lined wall intake duct showed good agreement at all the axial station of which a few were shown in this section.

Compared to the 20dB attenuation suffered by the BPF tone in the rigid intake duct propagation, the lined intake duct reduces the BPF tone by about 46dB.

Comparisons of the measured and predicted attenuation of the first four BPF harmonics over a distance (normalized with duct radius at the fan plane r_f) are shown in figure 7.19. The is relatively good agreement at the BPF and 2BPF (figure 7.19(a) and (b)). The BPF tone attenuation is overpredicted with about 2 to 5dB difference between measurement and prediction at the 10 axial stations were measurements were acquired. The levels predicted at some stations for the 3BPF and 4BPF tone are close to measurements. The variations observed in the measurements, which may be due to flow and geometry changes, are not seen in the predictions for which a cylindrical duct is used.

Figure 7.20, shows BPF tone attenuation measurements against predictions for both the rigid and lined ducts. The nonlinear decay is represented in the rigid case, the additional attenuation achieved by liner absorption is the difference between the rigid and lined results for this dominant BPF tone.

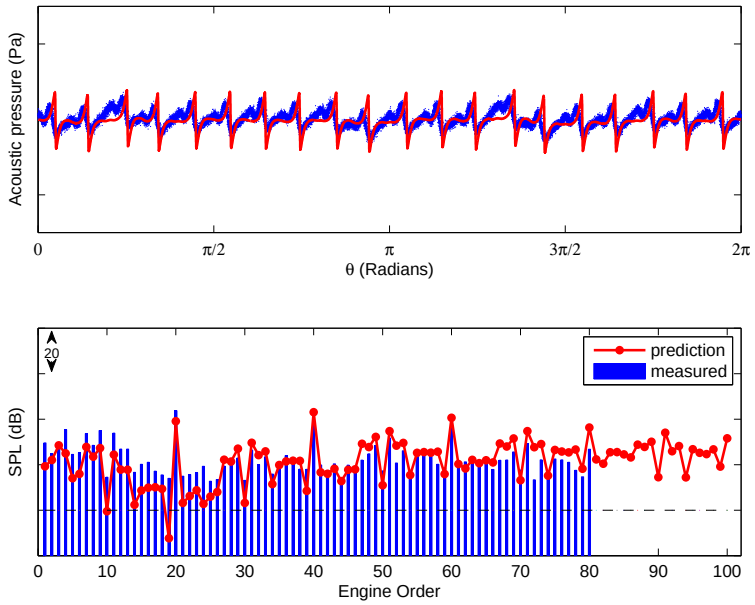

Figure 7.17: Measurement against prediction: axial station 7

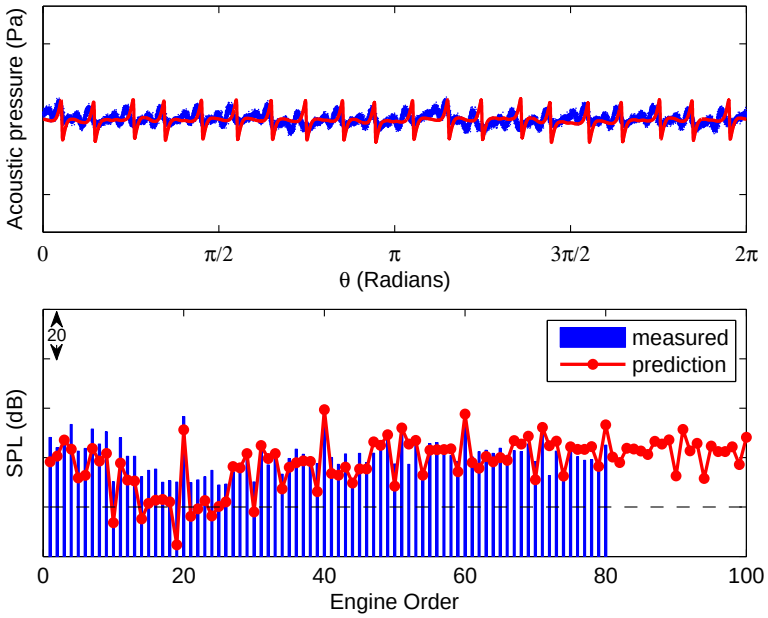

Figure 7.18: Measurement against prediction: axial station 10

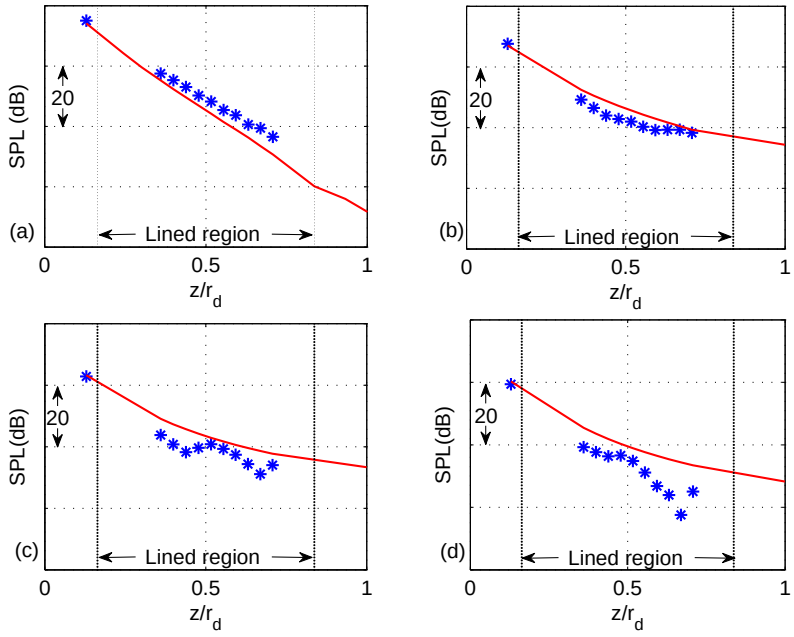

Figure 7.19: Measurement (*) against prediction (—) in lined-wall intake: BPF harmonics attenuation (a) BPF (b) 2BPF (c) 3BPF (d) 4BPF

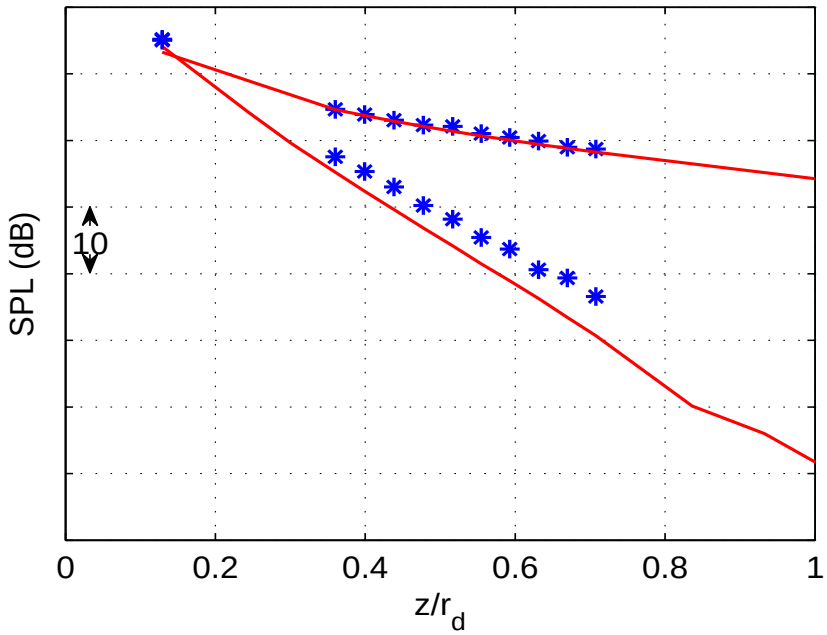

Figure 7.20: Measurement (*) against prediction (—) for both rigid and lined-wall intake: BPF tone attenuation

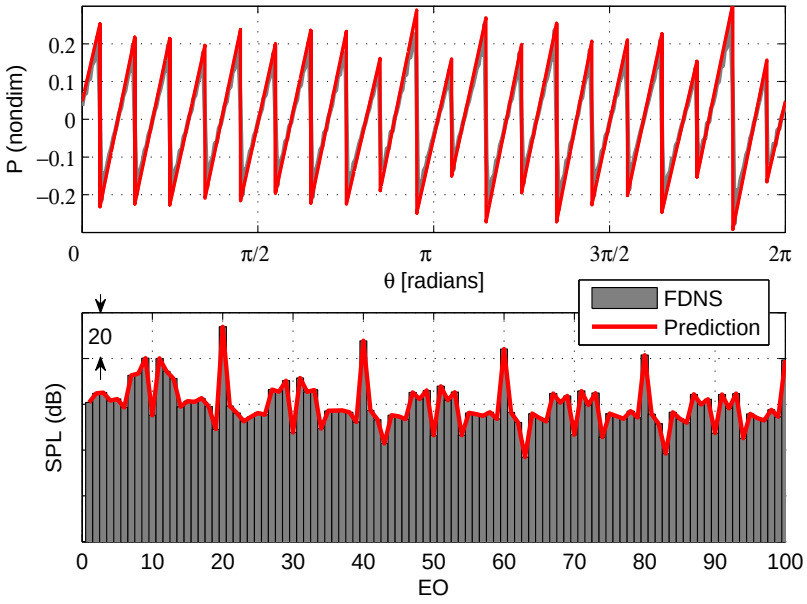

Figure 7.21: FDNS results against prediction: initial source waveform

7.4 Comparisons against FDNS

Results of the time-frequency domain model were compared against results of the frequency domain model FDNS using an idealized sawtooth waveform (figure 7.21 similar to that for realistic fans. The sawtooth waveform was the input into the time-frequency domain model while its spectrum was the input for the FDNS model. Comparisons are shown for both rigid (figure 7.22) and lined wall (figure 7.23)at the end of propagation for a axial distance 0.5m in a cylindrical duct with radius 0.5m. There is good agreement for both the rigid and lined cases with matching overall trends and small tone-to-tone differences. The absorption of the liner, optimized for halfBPF tone attenuation, was well represented as results show in SPL-EO spectrum in figure 7.23.

7.5 Summary

The good agreement observed between the measured data and the prediction at each axial station both for the rigid wall and lined duct wall intakes validate the propagation model presented. As seen in the comparisons for the rigid duct, the propagation model results agreed very well with the measured data, this validated the correct representation of the nonlinear propagation process. Also the good agreement of the comparisons made for the lined intake duct illustrate that the addition of the acoustic liner to the nonlinear propagation is successful and is captured reasonably well in the propagation

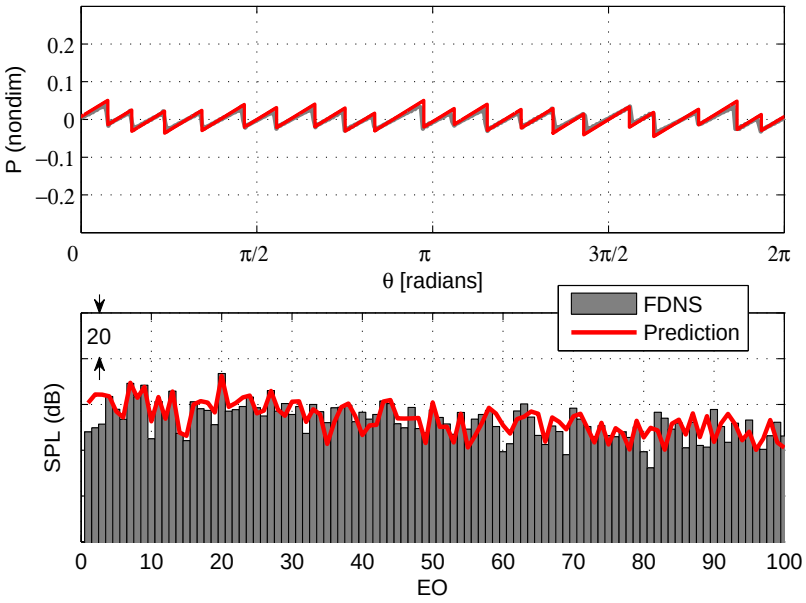

Figure 7.22: FDNS results against prediction for rigid walled duct at distance 0.5m

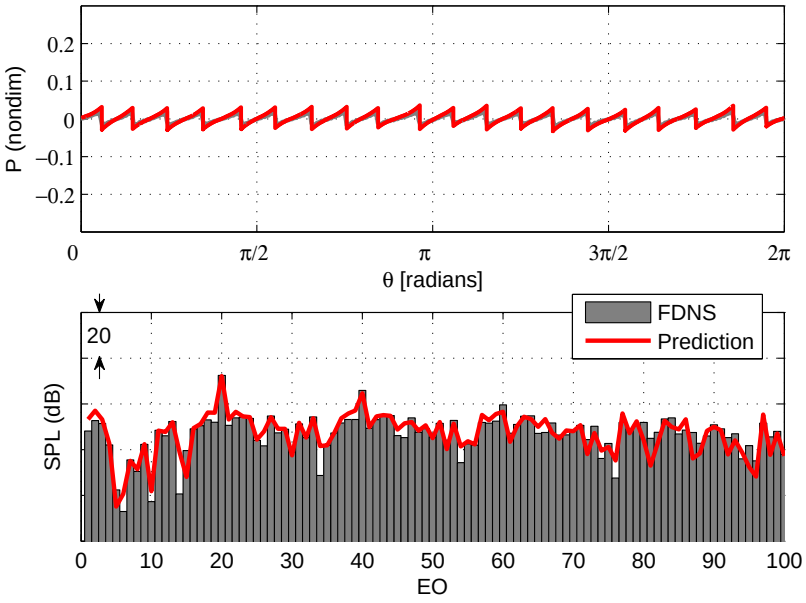

Figure 7.23: FDNS results against prediction for lined walled duct at distance 0.5m

model. The time-frequency domain sawtooth propagation model, referred to as NP-SWIND, has been validated with the model-scale rig test data. Subtle features which are seen in measurement, for example,the slight curvature in the expansion wave, is not represented in the input waveform of the propagation model. Despite the presence of this feature in measurement, the one dimensional sawtooth approximation employed by this time-frequency domain propagation model yields results which agreed very well with measurements in both the rigid and lined intake ducts. In reality, there are geometry and flow speed and varying boundary effects, which may significantly affect the propagation of the pressure field and most especially influence the attenuation provided by the installed liner. Inclusion of these features in prediction model may further improve the prediction capabilities especially for the lined-wall ducts.

Chapter 8

Radiation of Supersonic Fan Noise from Aircraft Intakes

The focus of previous chapters is the prediction of the radiation of the pressure field generated at the fan upstream against the incoming flow in an intake duct for both the rigid wall and acoustically lined wall configurations. Propagation of this pressure field terminates at the intake duct lip. After this point, the pressure field is radiated from the intake duct to the far-field. In the civil aviation certification process[2, 3], the noise measured is the perceived noise, that is, the noise radiated from the aircraft. The engine contributes a significant part of the effective perceived noise. The level of contribution of engine noise to the overall noise levels varies with aircraft and aircraft engine operation conditions (as discussed in section 1.1).

In order to be able to predict the contribution of the engine noise to the overall aircraft noise, the various sources within the aircraft engine are considered separately. The focus of previous chapters has been on supersonic fan noise, generated by the rotor-locked pressure field, and likewise, this chapter is focussed on the radiation of this pressure field from the intake duct.

8.1 Far-Field Radiation

As the pressure field exits the intake duct, it is radiated into free space. The radiation of the pressure field is a radically different process from the propagation in the intake duct. In the intake duct the propagation is bounded by the walls and this physical boundary, which also houses the source – the fan, preserves the helical propagation path of the pressure field. The wall also create a defined passageway for the incoming flow. As the pressure field emerges from the intake duct, it ceases from following the helical path it followed in the intake duct as there are no external structures to support this path. Also,

the external flow speed just forward of the intake may be significantly different from the flow speed in the intake duct. It should be noted the helical path of propagation in the duct is influenced by the flow. A fast flow speed results in a tighter helical path, and hence, a longer propagation time within the intake duct, while a slow flow speed will allow for the spread out of the helical path and consequently a shorter transit time. The change in flow speed from the intake to the external field will without fail affect the radiation of the pressure field. In the region just ahead of the intake duct, the pressure field goes through a lot of change owing to the free space it has exited into, the spin out ejection from the intake duct and the interaction with the external flow.

The radiation of the pressure field is studied here as that emerging from a cylindrical intake duct. Incoming flow is assumed to be uniform throughout the length of the duct. This cylindrical intake duct is also considered to have negligible wall thickness. The model is based on model radiation from a semi-infinite cylinder (figure 8.1) for which an analytic solution is known.

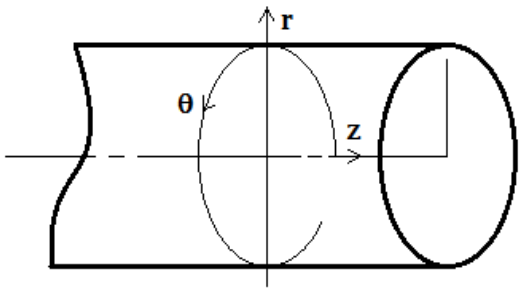

Figure 8.1: Intake duct approximation for radiation

8.1.1 Principal angle of radiation

A pressure field in a cylindrical duct described in terms of spinning modes is given by,

$$P_{mn} = A_{mn} J_{mn}\left(\kappa_{mn} r\right) e^{i\left(\omega t - k_{z_{mn}} z - m\theta\right)} \tag{8.1}$$

with the dispersion relation described as in equation (3.13).

The solutions near the wall can be approximated for all three directions (radial r-direction, azimuthal θ direction and axial z direction)as [68, 69]

$$\cos\phi_r = \frac{\kappa}{k\left(1 - M\frac{k_z}{k}\right)}$$
$$\cos\phi_\theta = \frac{k_\theta}{k\left(1 - M\frac{k_z}{k}\right)}$$
$$\cos\phi_z = \frac{k_z}{k\left(1 - M\frac{k_z}{k}\right)}$$

where angle ϕ has its components ϕ_r, ϕ_θ and ϕ_z in the radial, azimuthal and axial directions. Knowing that the axial wavenumber, k_z, is given as in the dispersion relation equation 3.13, the modal propagation angle in the axial direction can be re-written, after substitution for k_z and further simplification, as

$$\cos\phi_z = \frac{-M \pm \sqrt{1 - (1 - M^2)\frac{\kappa^2}{k^2}}}{1 - M\sqrt{1 - (1 - M^2)\frac{\kappa^2}{k^2}}} \tag{8.2}$$

where $\pm$ represents the positive and negative directions. Equation (8.2) can be written in terms of the mode cut-off ratio,

$$\eta = \frac{k}{\kappa\sqrt{1 - M^2}}. \tag{8.3}$$

substituting equation (8.2) into equation (8.3) leads to

$$\cos\phi_z = \frac{-M \pm \sqrt{1 - \frac{1}{\eta^2}}}{1 - M\sqrt{1 - \frac{1}{\eta^2}}}. \tag{8.4}$$

For a spinning mode, the angle at which maximum pressure amplitude is observed in the far-field is equal to the axial angle of propagation if there is no flow [68]. In reality, there is a convective effect of the flow, and this flow effect should be factored in.

The effect of the uniform flow is to change the direction of propagation from the normal of the wavefronts. The propagation is shifted to the direction of a resultant vector, c_p, of the propagation speeds (radial and axial) taking into account the convectional effect of the flow. Assuming a flow in the positive axial z direction, the effect of the flow can be seen as illustrated in figure 8.2.

For a flow u (of Mach number M), the angle of radiation where the peak of the principal lobe in the far-field will be obtained by solving

$$\cos\phi_p = \frac{c_z + u}{c_p} \tag{8.5}$$

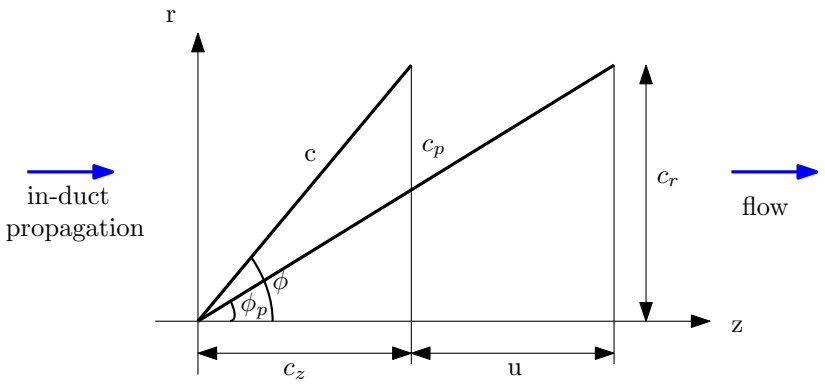

Figure 8.2: Effect of external flow on radiation angle

for which $c_r = csin\phi_z$ and $c_z = ccos\phi_z$ are the group velocities and u is From figure 8.2, for a flow velocity, u,

$$c_z = c\cos\phi = \frac{c\left[-M + \sqrt{1-\frac{1}{\eta^2}}\right]}{1 - M\sqrt{1-\frac{1}{\eta^2}}}. \tag{8.6}$$

using the cosine rule, $c_p^2 = c^2 + u^2 - 2cu\cos\phi_z$ and after substitution for $\cos\phi_z$ and rearrangement the expression yields

$$c_p = \sqrt{c^2 + u^2 - 2cu\cos\phi_z} = \frac{c\sqrt{\left(1-M^2\right)\left[1 + M\sqrt{1-\frac{1}{\eta^2}}\right]}}{\sqrt{1 - M\sqrt{1-\frac{1}{\eta^2}}}}. \tag{8.7}$$

Using equations (8.6) and (8.7) in (8.5) gives the angle of the principal lobe in the far field as [68]

$$\cos\phi_p = \left[\frac{\left(1-M^2\right)\left(1-\frac{1}{\eta^2}\right)}{1 - M\sqrt{1-\frac{1}{\eta^2}}}\right]^{\frac{1}{2}}. \tag{8.8}$$

In the case of a turbo fan engine, the incoming flow is against the direction of propagation in the duct which will give push-back effect to indicate its direction. For an intake duct, there is a external duct outside the duct, say M_E, if this external flow speed in exactly equal to the flow speed in the duct, the equation (8.8) describes the angle of the principal lobe in the far-field. Otherwise, if the external flow speed, of Mach number M_E, is the not equal to in-duct flow speed, M, angle of radiation where the peak of the principal lobe in the far-field, $\bar{\phi_p}$ will be at

$$\cos\bar{\phi_p} = \frac{c_z + cM_E}{c_p} \tag{8.9}$$

$$= \frac{M_E - M + (1 - MM_E)\sqrt{1 - \frac{1}{\eta^2}}}{\left[\left[1 - M\sqrt{1 - \frac{1}{\eta^2}}\right]\left[1 + M_E\left(M_E - 2M\right) + \left(2M_E - M - M{M_E}^2\right)\right]\sqrt{1 - \frac{1}{\eta^2}}\right]^{\frac{1}{2}}}$$

It is useful to mention that in real aircraft applications, the external flow is in a direction opposite to the axial direction of propagation in the duct. It is essential, therefore, to use the negative value for the external flow Mach number.

Rice [70]gives an extended study on the single-mode radiation pattern and a method using equal acoustic power per mode to determine the radiation pattern in multi-modal conditions. The single-mode radiation pattern is evaluated with respect to the cut-off ratio. For the multi-modal radiation pattern, using a biasing function unequal acoustic power can be assigned to shift power from one mode to another. It is pointed out that the duct termination loss reduces the principal lobe for the multi-modal content at high angles especially for the near cut-off modes and the radiation pattern major lobes are then those of modes with principal lobes near the duct (axial) axis.

Moreover, the presence of acoustic liners suppresses the principal lobe over a range of angles in the far-field and may not be evident as the side lobes of modes with less attenuation may have formed a noise floor higher in value than the principal lobe [70, 71]. For the rotor-locked field of an aircraft engine, the single-mode radiation pattern for each engine order is expected as supersonic relative fan speed conditions facilitate the propagation of these single modes. Multi-modal structures are more prevalent in subsonic fan relative speeds due to their complex interaction sources in which case the separation of the modes excited at the fan plane will needed at the lip end of the duct [72].

The study in [68] also shows that there can be as much as 10 to 15 degrees difference in the angle of the principal lobe of radiation between the static (no external flow) case and a case with external flow speed of Mach number 0.2.

8.2 Radiation Model

The cylindrical duct is a simplification to the actual geometry of aircraft intakes. The symmetry of the cylindrical duct allows for the use of a simple radiation model unlike asymmetric intakes such as drooped or scarfed intakes [73] which have geometry particularly primed to influence the sound radiated to particular directions by using the

asymmetry in duct geometry to change the directivity pattern of the sound radiated to the far-field.

A number of studies [22, 74–79] have been carried out on radiation from semi-infinite cylindrical or annular, unflanged ducts or pipes. Some of these studies are based on analytic modeling of the radiation [22, 78] or computational using numerical methods [79–81] (finite element, boundary element and infinite element schemes) based on the linearized Euler Equations in the near-field and Ffowcs Williams-Hawkings integral for the far-field radiation. The analytical solutions of Homicz and Lordi [82] generated for the canonical problem are used as benchmark for comparisons. There has also been studies using computational fluid dynamics CFD for a cylindrical duct with low Mach number flow speeds [83] and for axisymmetric realistic duct geometry with and without acoustic liners for near field radiation [84, 85]. Moreover, the computational aeroacoustics studies carried out by Tam et al [86] provide a good insight into the physical processes of refraction and diffraction observable in radiation from inlets. The effect of changing flow speeds and forward flight are discussed in the study for particular radiated modes. It is quite computationally costly to run non-analytical models. Although they better model the real life case, using them as a parametric model in which parameters can be quickly changed and results generated reasonably quickly on standard computers is presently not feasible. The need to resolve all elements and boundary conditions, perform integrals such as the Kirchhoff Integral or the Ffowcs Williams and Hawkings formulation for far-field radiation boundaries [87–89] make these models elaborate and computationally expensive. As the aim of this project is to have models for reliable predictions, both in-duct propagation and onward radiation, in a short space of time, the far-field radiation prediction which can quickly give reliable results, allowing for change of input parameters is desired. Only an analytical radiation model fits this picture. This radiation model based on the Weiner-Hopf Technique [90] as used in references [22, 77, 78].

The intake duct is a special case of the radiation from flow ducts presented by Rienstra [78] and Gabard et al [22] as there is no vorticity shed from the duct because the flow is in the opposite direction. Also, the external flow is in the opposite direction as well and hence, the convectional drift is in the opposite direction to that of a duct with internal flow (uniform) and external flow in the direction of propagation of the sound in the duct.

The investigation of far-field radiation discussed in this chapter is based on the work done by Gabard et al [22]. In the theoretical solution to radiation from jet pipes presented, the analytical model assumes a semi-infinite unflanged annular duct, which can be modified for various annular configurations, with a uniform internal flow. A zero radius centre body implies a cylindrical duct. This configuration approximates an aircraft intake duct, neglecting the spinner. It is useful to note, albiet not used in this thesis, that in the model, the cylindrical centre body is allowed to project further than the annulus to directly capture the effects in a by-pass duct configuration. The interaction of the

acoustic field and the instability wave of the vortices shed are incorporated into the model.

Starting from the convective wave equation (3.12) and having defined an intake configuration which has both the internal and external flows of equal velocity and in an opposite direction to the direction of propagation, the Weiner-Hopf technique [90]is employed to solve for the hard wall cylindrical duct with continuity conditions in the direction of propagation [91]. It is important to note that in practice, the Mach number in duct at the fan will be about double the Mach number of the external flow but a uniform Mach number is prescribed everywhere in the Weiner-Hopf model. From this procedure, the Weiner-Hopf equation for the semi-infinite annular duct was obtained as

$$G(u) = G^{+}(u) + G^{-}(u) = \omega \frac{\bar{K}(u)F^{+}(u)}{\kappa_{\infty}\kappa} \tag{8.10}$$

where

$$\bar{K} = D_{\rho}(1-uM)^{2}\kappa_{\infty}\frac{Y'_{m}(\kappa\omega h)J_{m}(\kappa\omega) - J'_{m}(\kappa\omega h)Y_{m}(\kappa\omega)}{Y'_{m}(\kappa\omega h)J_{m}(\kappa\omega) - J'_{m}(\kappa\omega h)Y_{m}(\kappa\omega)} - (1-uM_{\infty})^{2}\kappa\frac{H_{m}(\kappa_{\infty}\omega)}{H'_{m}(\kappa_{\infty}\omega)} \tag{8.11}$$

This equation is then solved by the analysis and evaluation of its kernel which inherently is as a dispersion relation is its character; having distinct relations for the upstream and downstream axial modes[22]. The process is well detailed in [22, 78]. The general solutions as presented in [22] are the pressure field $p_p(r,z)$ and acoustic field particle velocity $V_p(r,z)$.

$$p_p(r,z) = \frac{\omega^2}{2\pi}\int_{\Gamma}\frac{\left(1-uM_{\infty}\right)^{2}F^{+}}{\kappa_{\infty}}L_{\infty}\ e^{(i\omega uz)}du, \quad r>1 \tag{8.12}$$

$$p_p(r,z) = \frac{\omega^2 D_{\rho}}{2\pi}\int_{\Gamma}\frac{\left(1-uM\right)^{2}F^{+}}{\kappa}L_{d}\ e^{(i\omega uz)}du, \quad h<r<1 \tag{8.13}$$

where $D_{\rho} = \rho_d/\rho_{\infty}$ is the ratio of the jet and ambient densities

$$V_p(r,z) = \frac{p}{i\omega}, \quad r>1 \tag{8.14}$$

$$V_p(r,z) = \frac{p}{i\omega D_{\rho}}, \quad h<r<1 \tag{8.15}$$

where for an intake configuration, the first parts of (8.13) and (8.15) apply,

$$F^{+}(u) = \frac{\kappa_{\infty}^{-}\kappa^{-}\bar{K}^{-}\kappa_{\infty}^{+}\kappa^{+}}{\omega(u-u_{\infty})^{2}\bar{K}^{+}}\left[G_{\infty}^{+} - G_{d}^{+}\right]$$

$$L_\infty(r,u) = \frac{H_m(\kappa_\infty \omega r)}{H'_m(\kappa_\infty \omega)} \quad \text{and}$$

$$L_d(r,u) = \frac{Y'_m(\kappa\omega h)J_m(\kappa\omega r) - J'_m(\kappa\omega h)Y_m(\kappa\omega r)}{Y'_m(\kappa\omega h)J'_m(\kappa\omega) - J'_m(\kappa\omega h)Y'_m(\kappa\omega)}$$

where also, H_m and H'_m is the Hankel function and its derivative, G is the Weiner-Hopf equation and $\bar{K}$ is the split function.

The main highlight of the solutions which is of direct importance to this study is the far-field approximation which describes the radiated sound field far away from the duct. The complex general solutions are simplified by using the stationary phase approximation and taking the limit $\omega R \to +\infty$. For spherical coordinates defined as $z = R\cos\phi$ and $r = R\sin\phi$, and in-duct pressure field defined as in (3.17), at a farfield distance R, the solutions is, as in reference [22],

$$q_s(R,\phi) = \frac{\tilde{q}(u_s)}{\pi R(1 - {M_E}^2 \sin^2\phi)^{1/2}} e^{[i\omega RS(\theta) - i(m+1)\frac{\pi}{2}]} \tag{8.16}$$

$S(\theta) = \left[(1 - M_E^2 \sin^2\theta)^{1/2} - M_E \cos\theta\right]/(1 - M_E^2)$ adds the effect of stretching caused by the external flow. The static solution u_s was obtained to be [22]

$$u_s = \frac{\cos(\tan^{-1}\left[(1 - M_\infty^2)^{\frac{1}{2}} tan\phi\right]) - M_\infty}{(1 - M_\infty^2)}. \tag{8.17}$$

and $\tilde{q}(u_s)$ is the pressure or the velocity potential evaluated from (8.16) and (8.17).

Therefore, the directivity functions for the pressure and the velocity potential in the far-field at a distance R are $D_p(\phi) = |p|R$ and $D_v(\phi) = |V_p|R$.

Some of the equations above are general and reduce to simpler expressions when applied to the intake duct configuration owing to the fact that the hub radius $h = 0$ for the cylindrical duct case. The Weiner-Hopf kernel $\bar{K}$ simplifies to

$$\bar{K} = D_\rho(1 - uM)^2 \kappa_\infty \frac{J_m(\kappa\omega)}{J'_m(\kappa\omega)} - (1 - uM_\infty)^2 \kappa \frac{H_m(\kappa_\infty \omega)}{H'_m(\kappa_\infty \omega)} \tag{8.18}$$

and L_d reduces to $L_d = J_m(\kappa\omega r)/J'_m(\kappa\omega)$. The numerical method of solution to the Weiner-Hopf kernel split function and the implementation of the equations for the radiation of sound is discussed in detail in references [22, 78].

This analytical study on radiation from cylindrical or annular jet pipes carried out in reference [22] by Gabard et al was written in a code named 'GX-Munt'. This analytic code allows for various configurations of flow; in the direction of flow or against the direction of flow. Also, it includes vorticity shedding effects for jets and allows for external flow outside the cylinder to be in the direction of propagation (positive z direction) or against the direction of propagation in the duct. These options make the code adaptable to the intake duct case where the in-duct flow and the external flow are both counter-directional to the direction of propagation of the sound in the intake duct. For this intake configuration, GX-Munt only allows the same value for the the in-duct and the external flow speeds. The radiation code GX-Munt has both near-field and far-field capabilities [92].

To generate the results discussed in this chapter, the far-field solver is used to obtain the far-field radiation from the intake duct considered. It is useful to note that GX-Munt takes as input, the diameter, source information in the form of the revolution per minute of the installed fan, the range of azimuthal and radial orders required. The directivity outputs from GX-Munt, based on modes with unit amplitude pressure for the specified azimuthal and radial orders, over the polar angle range of interest. GX-Munt also computes the velocity potential and the radial intensities in the far-field [92].

GX-Munt was originally developed as a model to predict the fan noise radiation from bypass ducts of high-bypass-ratio turbofan engines with particular focus of aft fan noise. It was aimed to capture the effect of the shear layer which is at the interface between the external free field and the bypass flow. The problem is tackled as that of a cylindrical or annular duct using the Weiner-Hopf technique which requires the factorization of the Weiner-Hopf kernel. This factorization is mostly done numerically [77, 78, 93]. A no-flow semi-infinite cylindrical duct case with analytical solutions is discussed in ref [74]. The complexity is raised when mean flows in-duct and external are considered with the consequent convective and refraction effects [78, 82]. The approach used by [22] was a build up on the works on [78, 94] where solutions were generated to realistic high frequency and Mach numbers observable in real cases.

The model takes inputs of the duct radius r, the flow properties (in-duct velocity v_d, speed of sound c_d and density ρ_d) and the ambient velocity, speed of sound and density. For this inlet case, the velocities in-duct an external are equal and are entered as negative values to indicate the direction of flow in the negative z direction [92]. The incident modes (pressure and velocity potential) are[92]

$$\begin{aligned} p_p(r,\theta,z,t) &= AJ_m(\kappa r)e^{im\theta+ik_z z-i\omega t} \\ V_p(r,\theta,z,t) &= BJ_m(\kappa r)e^{im\theta+ik_z z-i\omega t} \end{aligned} \tag{8.19}$$

where amplitudes A and B are related by $A = -i\rho_d(\omega - v_d k_z)B$. Note that $A = 1$ in as the pressure mode has a unit amplitude for the intake duct case under study.

The directivity functions of pressure, velocity potential and radial intensity are the output of the model. They are given by [92]

$$p_p(R,\phi,\theta,t) = \frac{1}{R} D_p(\phi) e^{i\omega RS(\theta)/c_0 + im\theta - i\omega t} \tag{8.20}$$

$$V_p(R,\phi,\theta,t) = \frac{1}{R} D_v(\phi) e^{i\omega RS(\theta)/c_0 + im\theta - i\omega t} \tag{8.21}$$

$$I_R(R,\phi,\theta) = \frac{1}{R^2} D_I(\phi) \tag{8.22}$$

where $D_p(\phi)$, $D_v(\phi)$, and $D_I(\phi)$ are the directivity function for pressure, velocity potential and radial intensity respectively.

8.2.1 Using in-duct pressure with unit amplitude directivity

The amplitudes A_m at each engine order (EO) are obtained from the magnitude of the pressure field, p_m (where $m = EO$), at the termination of the duct propagation by

$$|p_m| = A_m |J_m(\kappa r)|. \tag{8.23}$$

The unit amplitude pressure values p_u for each engine order can be evaluated from the directivity function D_p as

$$p_u(\phi) = \frac{1}{2}\frac{1}{R^2} |D_p(\phi)|_m{}^2. \tag{8.24}$$

The far-field pressure at each engine order for all angles ϕ is expressed as

$$p_{ff_m} = A_m p_u(\phi). \tag{8.25}$$

Examples of unit amplitude output of the GXMunt radiation model are shown for the first radial order in figure 8.3 for m(20,1) and m(40,1), and figure 8.4 for m(60,1) and m(80,1).

8.3 Far-field measurements

Measurements were acquired in the far-field at a number of engine operation conditions over a polar angle range 0 to 120 degrees in 5 degree intervals. The engine speed

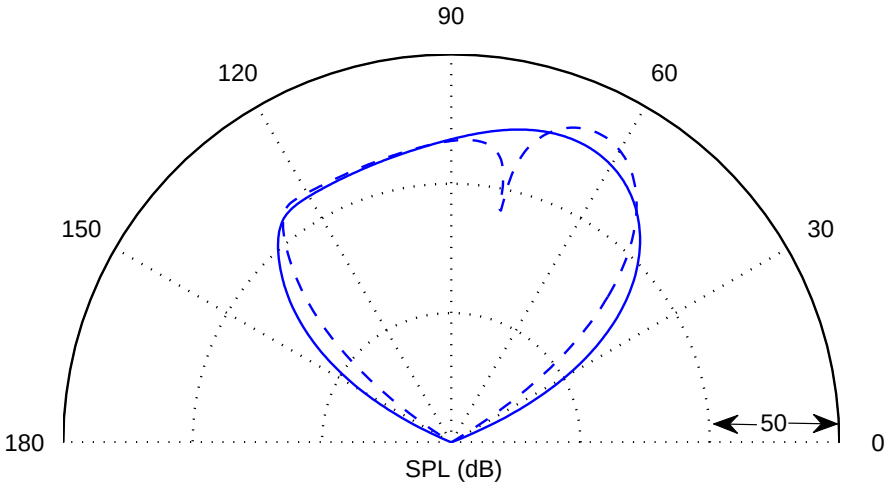

Figure 8.3: Unit amplitude far-field directivities for EO 20 (—) and E0 40 (- -)

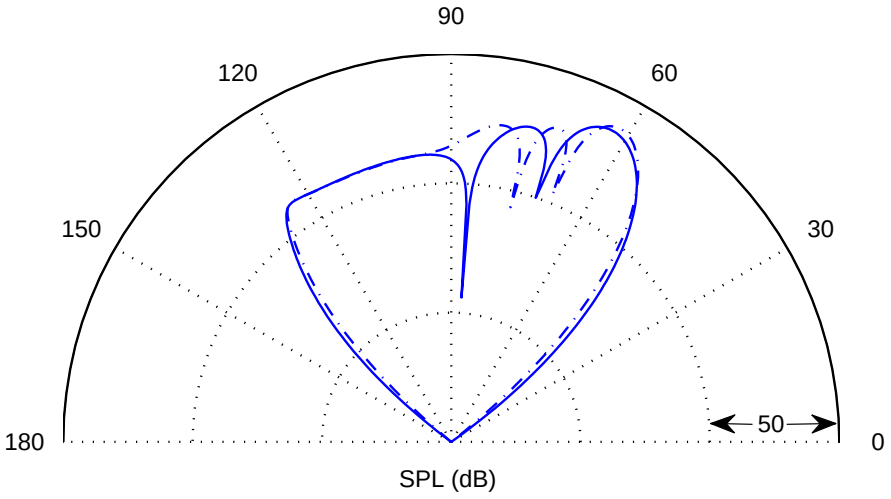

Figure 8.4: Unit amplitude far-field directivities for EO 60 (—) and E0 80 (- -)

was raised from conditions where the tip speeds were subsonic (70% and 80% of engine optimum) to 90% operation which has the relative fan blade tip speeds in the supersonic regime.

Figure 8.5 shows the comparisons between the far-field directivities at the three engine operation conditions. Only the BPF and its next three harmonics are shown. It is obvious, most especially, from the BPF tone directivity (figure 8.5(a)) that the rotor-locked field radiated to the far-field when relative tip-speeds are supersonic is absent at the two lower engine operation conditions. The clear hump in the 90% plot shows the rotor-locked field which is dominant from about polar angle 50^o. The range of prominence of the rotor-locked field varies over the range of engine orders considered. The multi-modal field is dominant at subsonic conditions and remains prominent at angles close to the duct axis. The amplitudes at each engine order falls off for higher angles unlike the rotor-locked field which appears to have a characteristic peak between the angles 60^o and 90^o at all engine orders up to 4BPF.

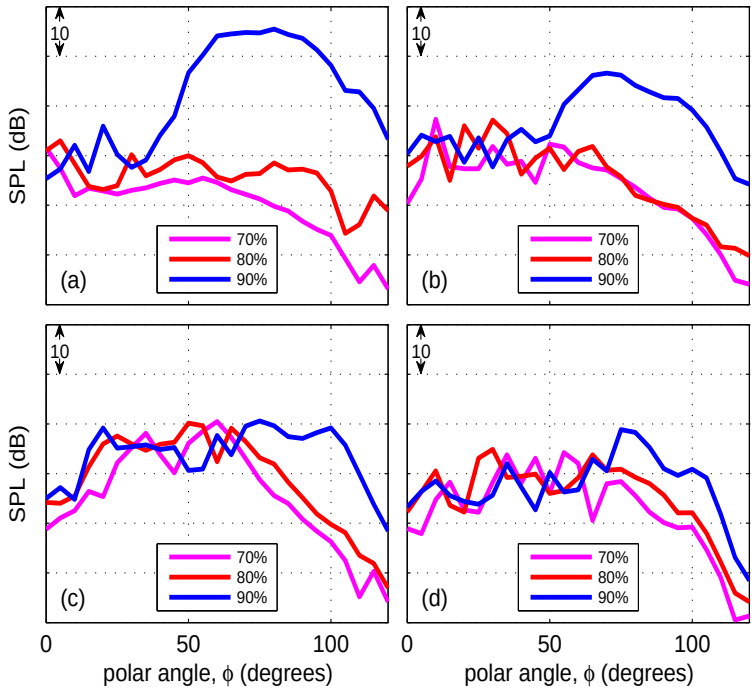

Figure 8.5: Measured far-field directivity at 70, 80 and 90 % engine operation: rigid duct (a) BPF (b) 2BPF (c) 3BPF (d) 4BPF

A number of the far-field SPL-frequency spectra are shown in figures 8.6 and 8.7, at 30, 60, 90 and 120 degrees respectively. At low angles such as 30^o, there is very little to separate among the three engine operation conditions. This is because the multi-modal field is dominant in this region and increase in the engine power has not significantly altered this field. Going to a higher angle such as 60^o (figure 8.6(b)), the presence of

the rotor-locked field is obvious with a BPF tone over 20dB higher than that of the lower engine power measurement. Similar differences are observed from engine order 7 to 50. After this, at the higher frequencies, the sound levels for each engine order for the different engine operation conditions are similar. From figure 8.7(a) and (b), the rotor-locked field maintains its dominance through out the whole spectrum at 90^o and at 120^o even though the mean sound level is much lower, about $20dB$ less than at 90^o.

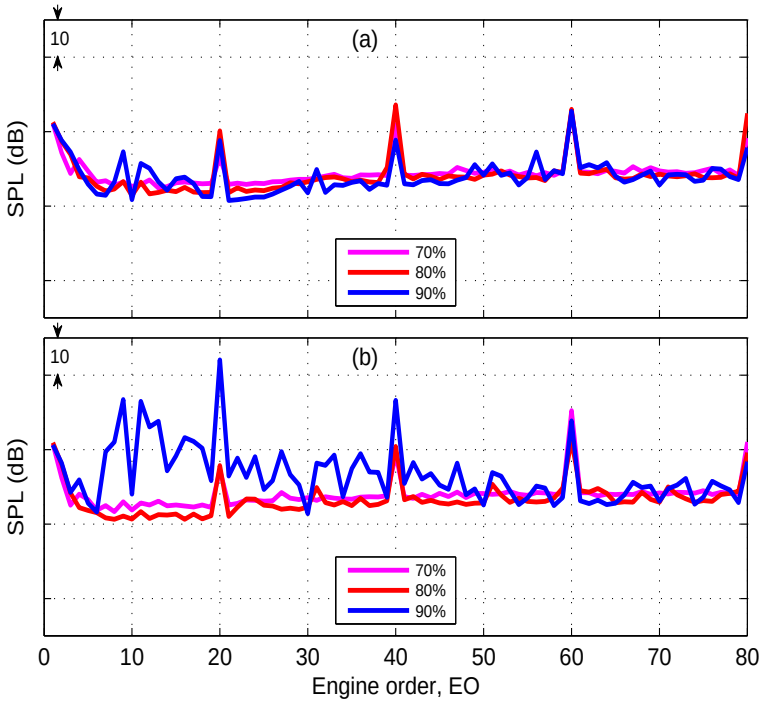

Figure 8.6: Measured SPL-EO spectrum at 70, 80 and 90 % engine operation for a rigid duct at polar angle (a) 30^o (b) 60^o

In contrast to the measurements for rigid duct configuration (figure 8.5), the lined duct results, figure 8.8, show a well attenuated BPF tone over all angles with a little residual of the dominance of the rotor-locked field left at higher angles. The effect of the liner, which is optimized for the frequencies around BPF is obvious and still appears significant at 2BPF on comparison of figure 8.5(b) with figure 8.8(b). For higher frequencies, 3BPF and 4BPF in figure 8.8(c) and (d), the shapes and levels are similar to those measured in the rigid intake duct and there is less attenuation of these frequencies and there will also be boundary layer shielding giving a lower liner absorption at these high frequencies.

8.4 Radiation results and comparisons

The output from the radiation model is used together with the results at the duct lip from the NP-SWIND time-frequency domain nonlinear propagation model. The output

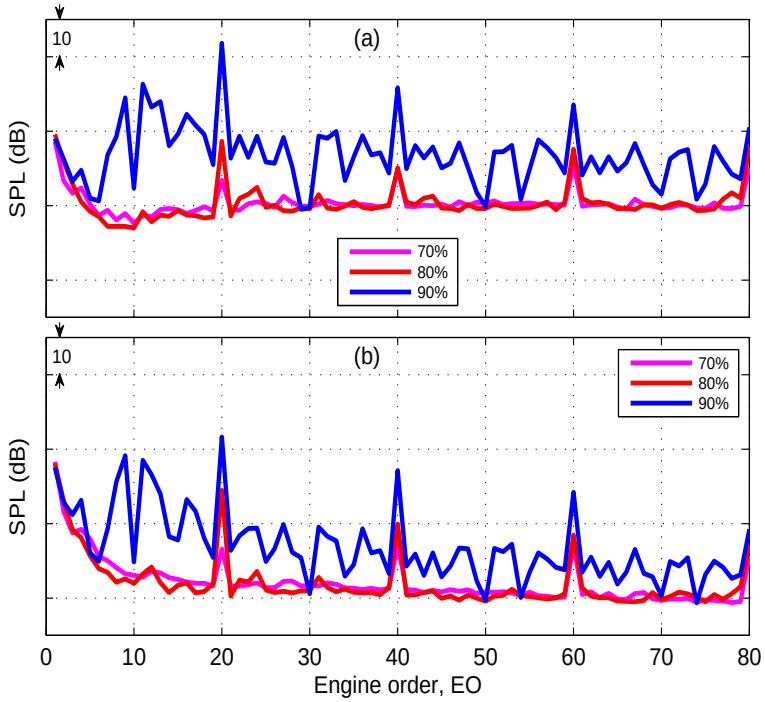

Figure 8.7: Measured SPL-EO spectrum at 70, 80 and 90 % engine operation for a rigid duct at polar angle (a) 90^o (b) 120^o

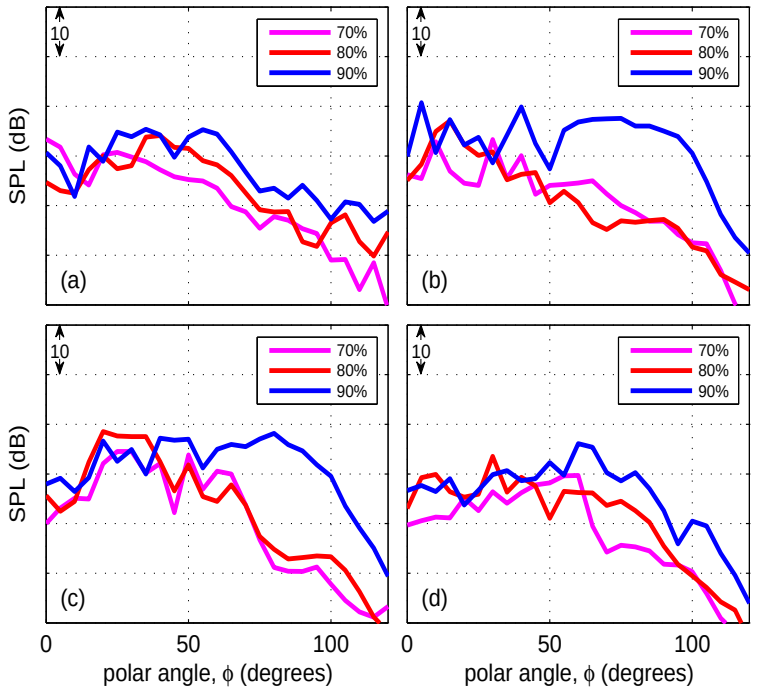

Figure 8.8: Measured far-field directivity at 70, 80 and 90 % engine operation: lined duct (a) BPF (b) 2BPF (c) 3BPF (d) 4BPF

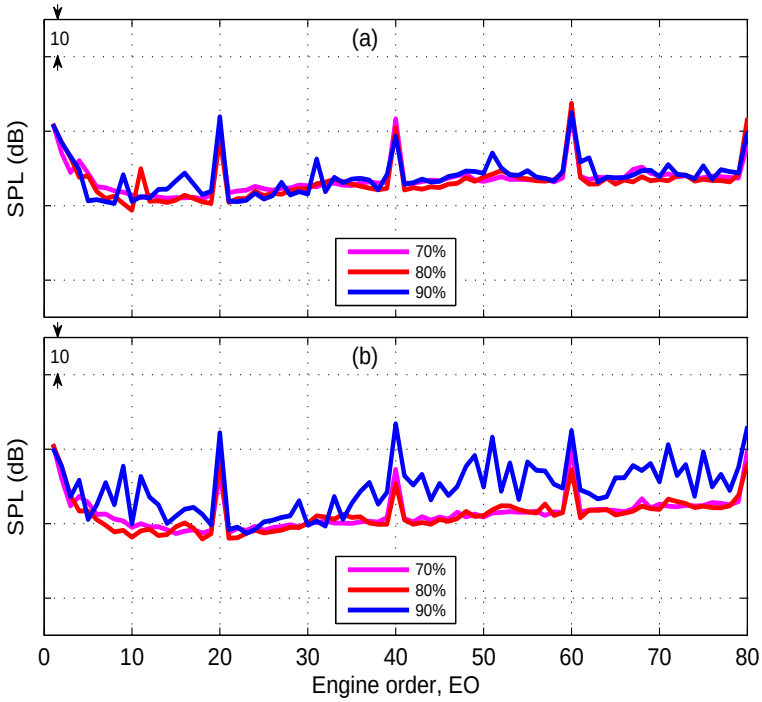

Figure 8.9: Measured SPL-EO spectrum at 70, 80 and 90 % engine operation for a lined duct at polar angle (a) 30^o (b) 60^o

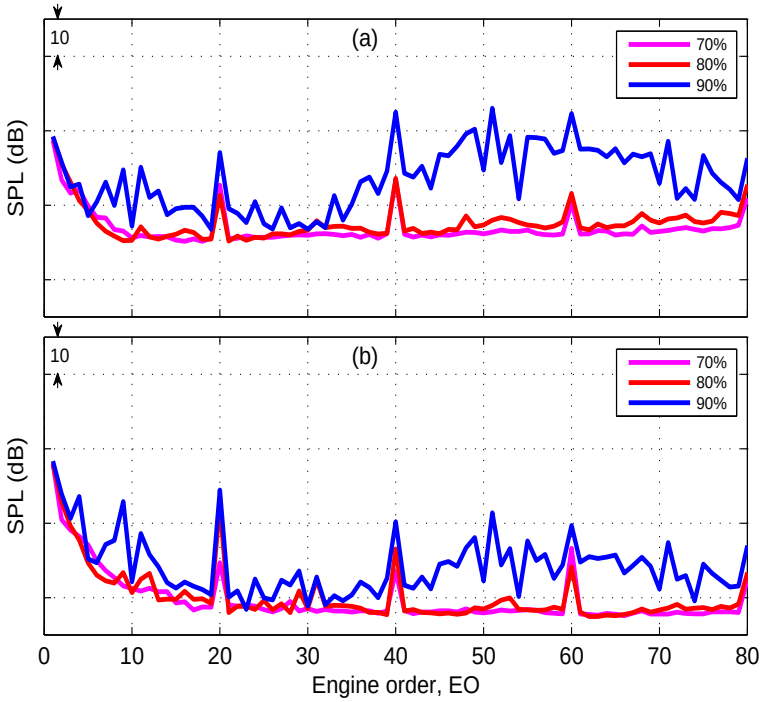

Figure 8.10: Measured SPL-EO spectrum at 70, 80 and 90 % engine operation for a lined duct at polar angle (a) 90^o (b) 120^o

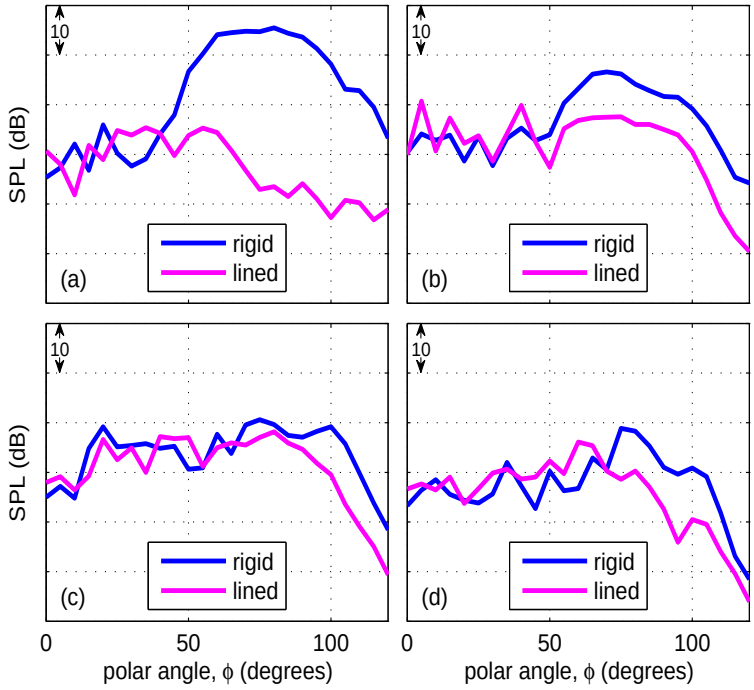

Figure 8.11: Rigid against lined measured directivities at 90% engine operation (a) BPF (b) 2BPF (c) 3BPF (d) 4BPF

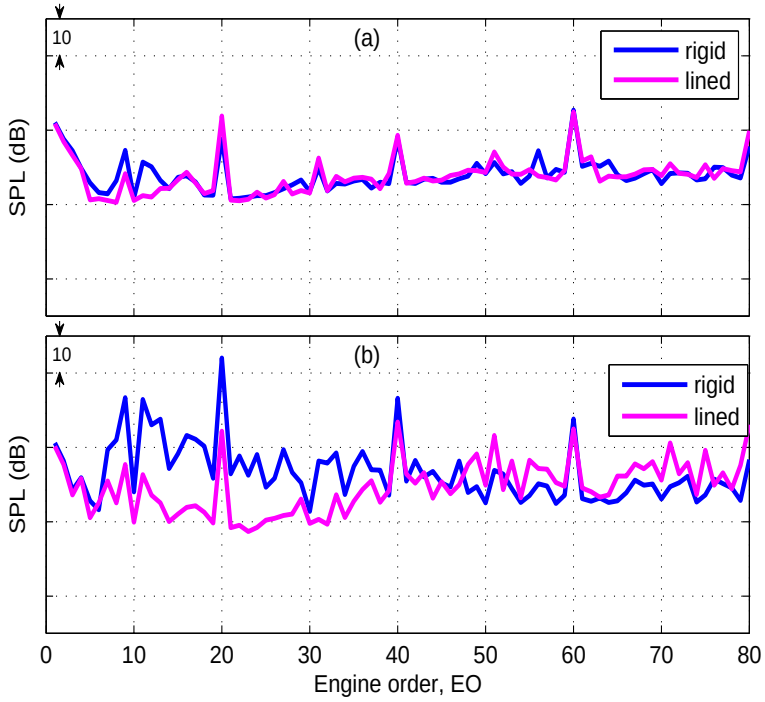

Figure 8.12: Rigid against lined measured SPL-EO spectrum at 90% engine operation for polar angle (a) 30^o (b) 60^o

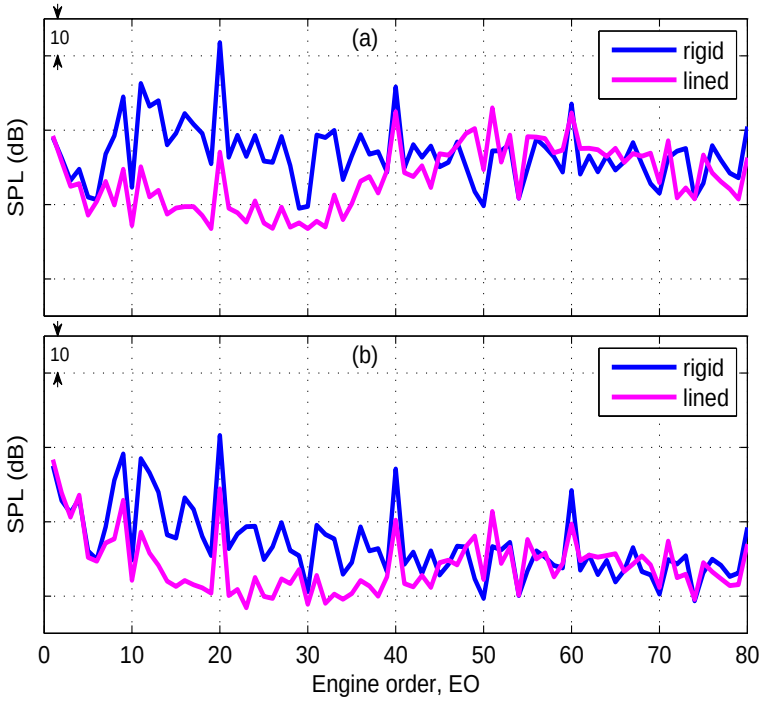

Figure 8.13: Rigid against lined measured SPL-EO spectrum at 90% engine operation for polar angle (a) 90^o (b) 120^o

pressure values from GX-Munt have unit amplitudes. The required pressure amplitude to predict far-field data for the duct of interest are determined from the pressure field which exits the intake duct as predicted by NP-SWIND using equation (8.25). The prediction results in the following comparisons between measurements and predictions are obtained by this algorithm. All comparisons are made with measurements acquired at 90% engine speed where the rotor-field is observed.

8.4.1 Radiation from rigid intake duct

Prediction results are shown in figures 8.14 to 8.16. The comparison between experimental measurements and predicted directivities for the BPF and its next three harmonics (figure 8.14(a)-(d)) indicate that at low polar angles up to about 50 to 55^o, the rotor-locked field is not the principal source radiated at these low polar angles for the 90% engine operation. In this polar angle range, the multi-modal and interaction noise component are present for all frequencies considered. Above 50^o, the rotor-locked field gains dominance at most EOs. The region for which the rotor-locked field is expected to be dominant is between 60^o to 80^o polar angle [69]. Within this region, the prediction for the BPF tone is within $5dB$ of the measurement and actually matches measured sound levels at the start of the region at about 50^o and from about 75^o to 100^o. The predicted 2BPF directivity, figure 8.14(a), has two lobes. The first of which (the main

lobe) matches closely with measured values. The inter-lobe region clearly fall-short of the measurements within that region. Similar observation is seen at 3BPF. Above 90^o, at all the BPF harmonics, there is very little change in predicted levels but a rapid decline in measured values.

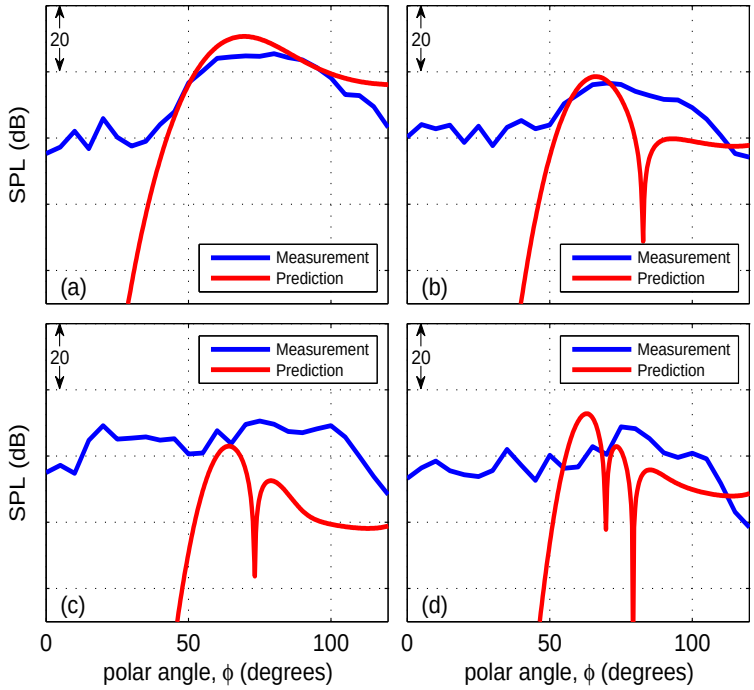

Figure 8.14: Far-field directivity: measurements against prediction: rigid duct (a) BPF (b) 2BPF (c) 3BPF (d) 4BPF

The SPL-EO spectra, figures 8.15 and 8.16 show that the agreement between the predicted sound levels with measurement is good up to BPF except for the spectrum at 30^o where no significant rotor-locked field is present. This agreement is much poorer at higher frequencies. Conversely, the prediction and measurement levels are similar at 90^o for most EOs except for higher BPF harmonics [figure 8.16(a)]. As observed in the directivities, at polar 120^o far higher levels are predicted. The reason for this occurrence at high angles is discussed in section 8.5.

The SPL-EO spectra at polar angles 55^o and 75^o, figure 8.17, represent the polar angle regions where the rotor-locked field starts to be dominant and just after the directivity peak respectively. It is observed that the agreement between prediction and measurements for these polar angles is good up to BPF, and just slightly higher in levels at other EOs. The drop in levels in the spectrum at 75^o, figure 8.17(b), marks a region close to the inter-lobe null at that frequency.

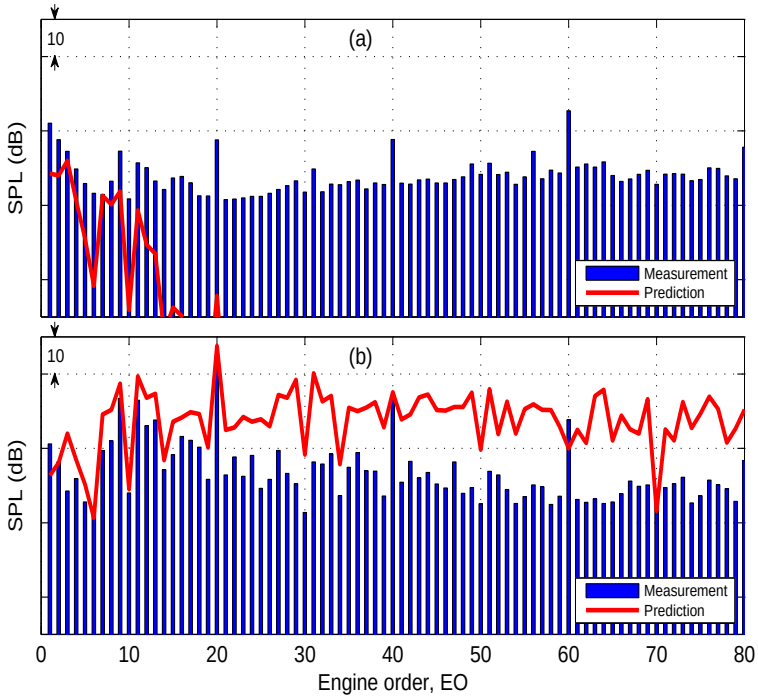

Figure 8.15: Measured against predicted SPL-EO spectrum for rigid intake duct at polar angle (a) 30^o (b) 60^o

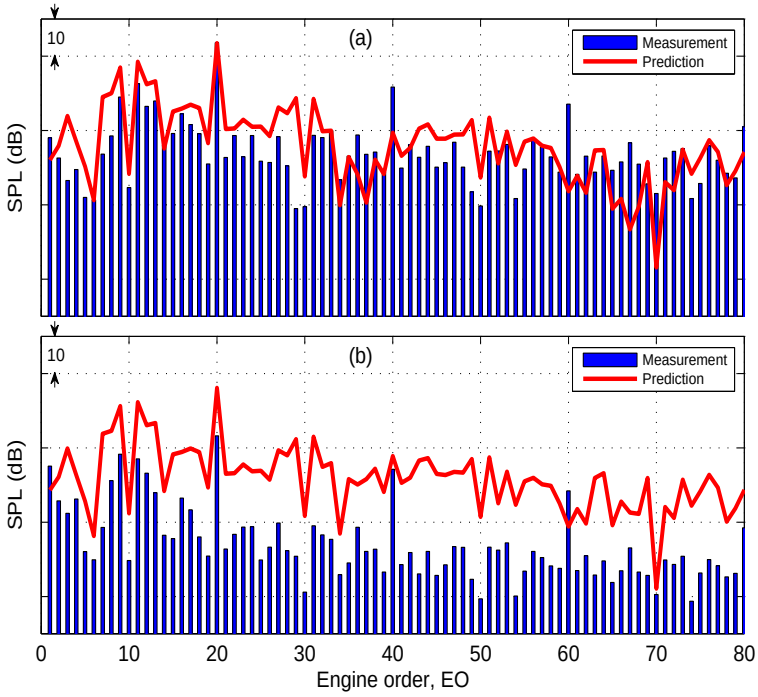

Figure 8.16: Measured against predicted SPL-EO spectrum for rigid intake duct at polar angle (a) 90^o (b) 120^o

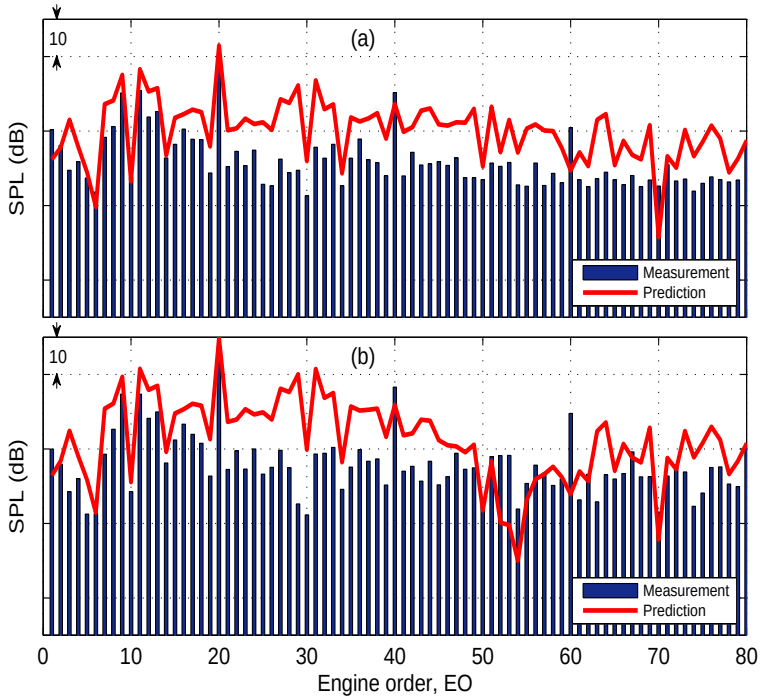

Figure 8.17: Measured against predicted SPL-EO spectrum for rigid intake duct at polar angle (a) 55^o (b) 75^o

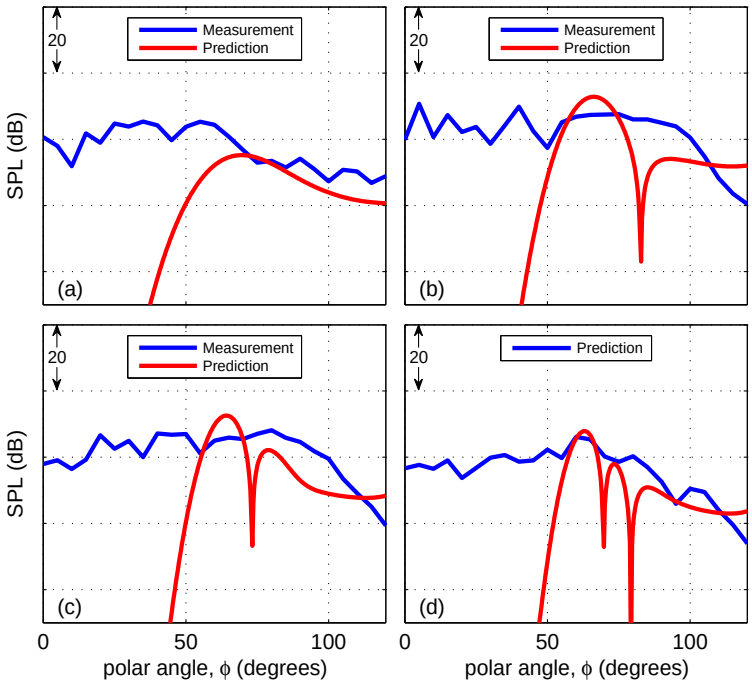

Figure 8.18: Far-field directivity: measurements against predictions: lined duct (a) BPF (b) 2BPF (c) 3BPF (d) 4BPF

8.4.2 Radiation from lined intake duct

The far-field directivities at the BPF harmonics for the lined wall duct figure 8.18 show that the overall trend of the measurement is well captured except at the inter-lobe null points, where at these angles the predictions diverge from the measured levels. For 2BPF and 3BPF, the peaks of the main lobes overshoot the measured level by about 5dB but the peak almost matches the measured level at 4BPF (figure 8.18(b)). As seen for the rigid duct, the higher angle (greater than 90^o) rapid sound level drop in the measurement is not observed in predicted directivities for higher EOs.

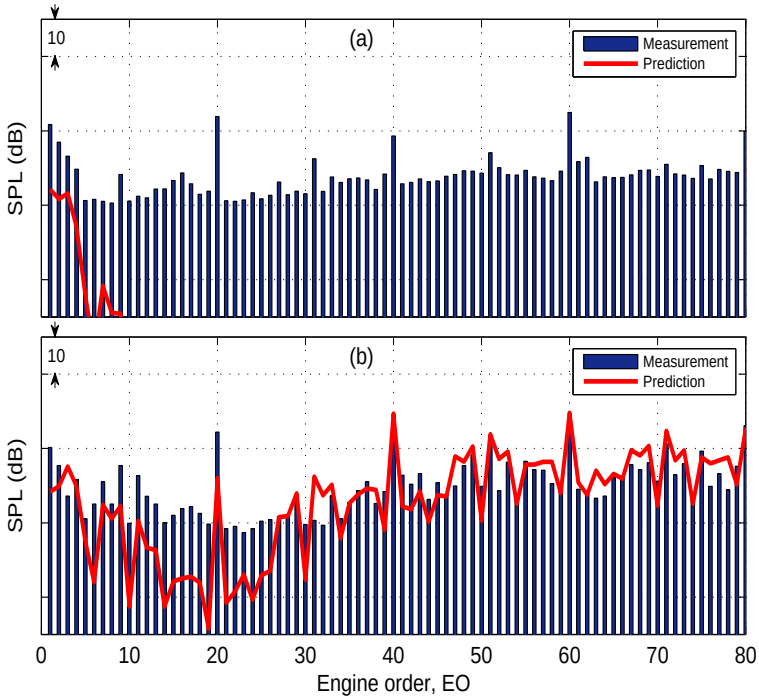

Figure 8.19: Measured against predicted SPL-EO spectrum for lined intake duct at polar angle (a) 30^o (b) 60^o

Good agreement between the predicted sound pressure levels and measurements is observed in the SPL-EO spectra shown for polar angles 30^o to 120^o in 30^o intervals in figures 8.19 and 8.20. Similar to the rigid duct results, the rotor-locked field is not significant at 30^o. For other polar angles higher than 55^o, the higher EOs of the measurements are closely matched by predictions except at 90^o [figure 8.20(b)] where the levels are much lower in the predictions. There is an over-prediction of the attenuation of the liner evident in levels of EOs around BPF (EO 20). There is a smaller variance between measurement and prediction at 120^o, figure 8.20(b), compared to observation for the rigid duct. Figure 8.21(a) shows the levels at the start of the polar angle region where the rotor-locked field is dominant (polar angle 55^o) and figure 8.21(b) captures the predicted levels aft the peak of the main lobe of the directivity.

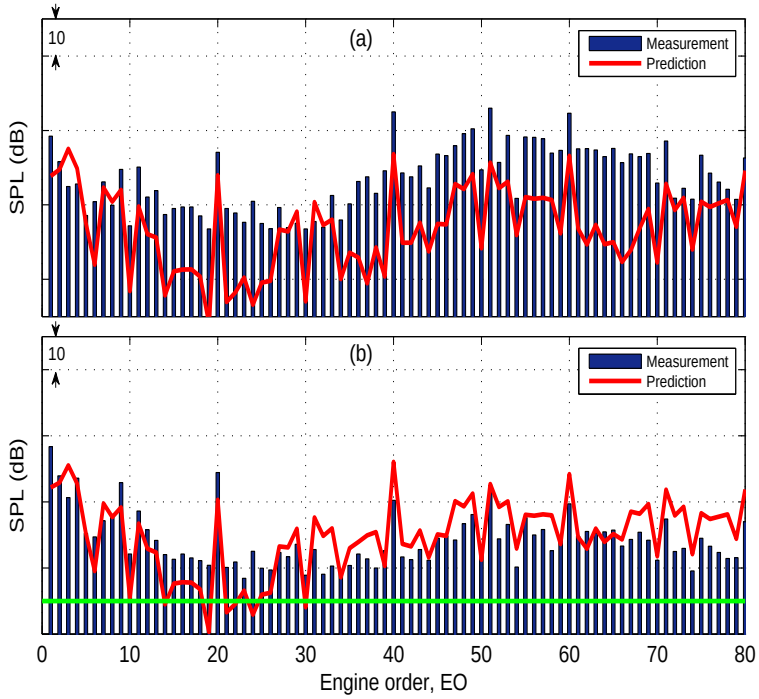

Figure 8.20: Measured against predicted SPL-EO spectrum for lined intake duct at polar angle (a) 90^o (b) 120^o. [NOTE: the green line marks the lower limit of the vertical axis in previous plots]

Overall, the agreement with measurement is good around the region where the rotor-locked field is dominant except for the over-prediction of liner attenuation which still appears to be reflected in the EOs close to BPF. At higher angles, above 75^o, the level of agreement reduces but improves at close to 120^o. The rigid and lined cases both show the region of dominance of the rotor-locked field. Various levels of agreement with measured data are observed for the two wall conditions with the best agreements still seen for polar angles 55^o and higher.

8.4.2.1 Incoherent sum of higher radial orders

Observations from the comparison of measurement against prediction of the far-field directivities (figures 8.14 and 8.18) show that for high frequencies/engine orders the levels predicted are much lower than the measurements. The amplitudes assigned to each engine order are obtained from the pressure field at the wall in the intake duct near the intake throat. The assumption that all the energy is contained in the first radial order was extended to the far-field radiation in this case. However, from the output of the radiation model, the second radial order is cut-on at about 2BPF - engine order 40. Also, the third radial order is observed to be cut-on at frequencies higher than 3BPF. Moreover, appraisal of the measured directivities reveal that unlike the single radial order

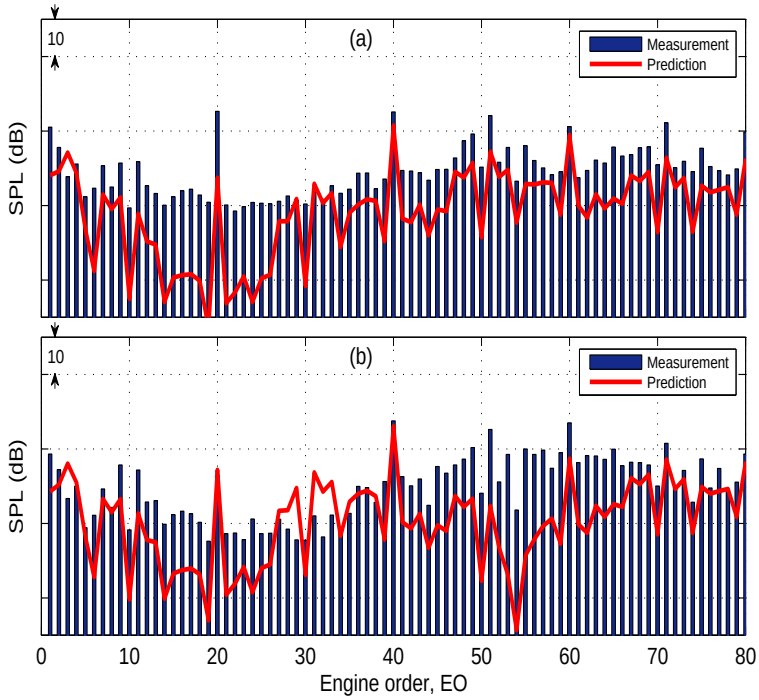

Figure 8.21: Measured against predicted SPL-EO spectrum for lined intake duct at polar angle (a) 55^o (b) 75^o

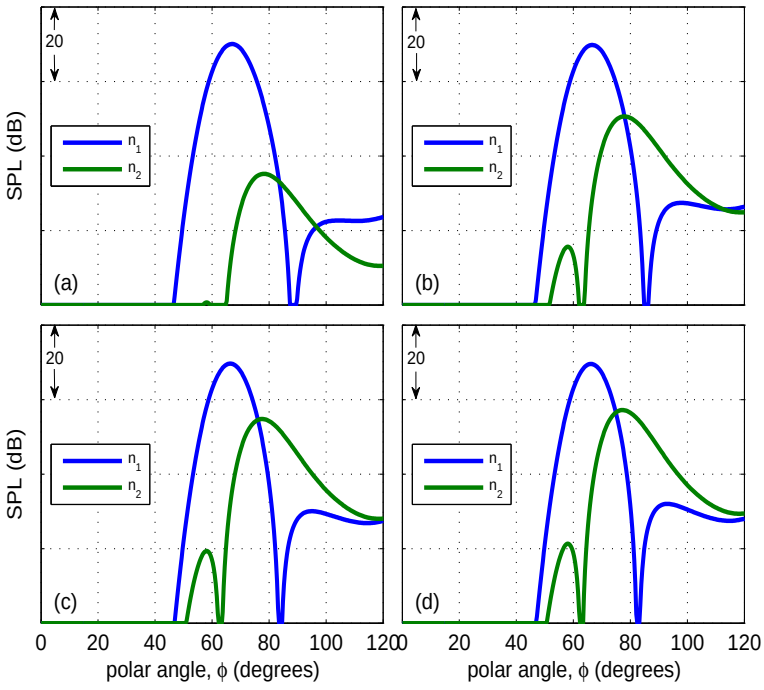

Figure 8.22: Unit amplitude directivities (a) EO 37 (b) EO 38 (c) EO 39 (d) 2BPF

patterns in the predictions which have an identifiable principal lobe, the measurement does not have nulls and may contain several peaks. Knowing that the rotor-locked field does not radiate at low, near-axis, angles eliminates the need for comparisons at these angles. The multimodal field is the principal source at the lower polar angles. At higher polar angles, the sound levels in the measurements are thought to be mostly influenced by the rotor-locked pressure field. In reality, various factors will be contributing at these angles as well. These factors include background noise from experimental set up, noise from other sources and some multimodal content residual spanning to high angles.

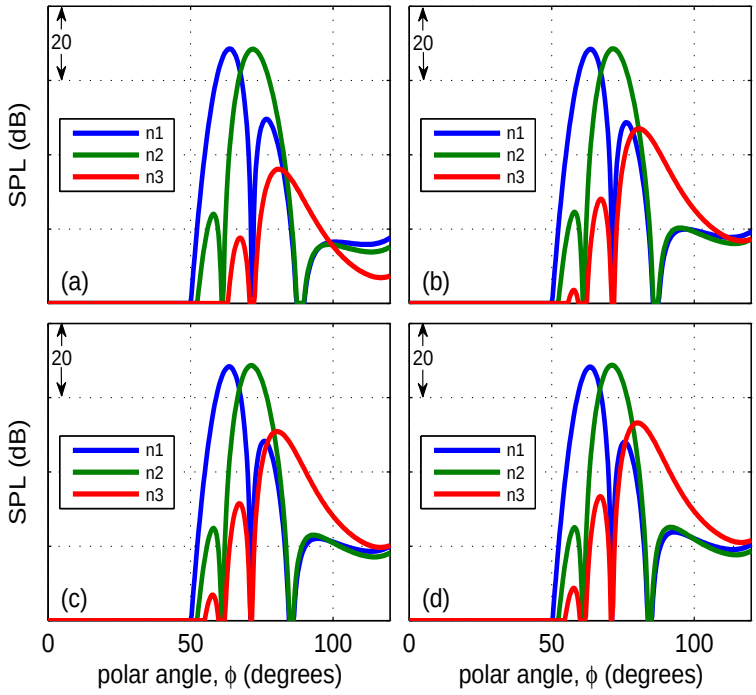

Figure 8.23: Unit amplitude directivities (a) EO 67 (b) EO 68 (c) EO 69 (d) EO 70

It is useful to look more closely at the comparisons at higher angles. Figures 8.22 shows the unit amplitude plots for the first and second radial order for engine order 37 to 40. Each radial order is seen to have a distinct principal lobe at about a specific angle. This peak coincides with the null of the other radial order. This implies that, with the assumption that the rotor-locked field is dominant at these polar radiation angles, the type of trend seen in measurements across the angles of interest can only be produced if there is a shift in dominance from one radial order to the other as higher angles are reached.

Figure 8.23 further reveals the locations of the peaks for the first three radial orders for engine orders 67 to 70. The peaks for higher radial orders are at higher angles and they occur where other radial order have their null values in that region; most observable in

figure 8.23(d). Another notable observation from figures 8.22(a)to(d) and 8.23(a)to(d) is that as frequency value increases the definition of the peaks and the null points between the lobes become clearer and, depending on the amplitude levels, the main lobes of the higher radial orders may encompass the side lobes of the lower orders.

For example, in the rigid wall configuration, at BPF figure 8.14(a), the prediction and measurement agree well at the angles expected for rotor-locked field. Good agreement is also observable at 2BPF to 4BPF 8.14(b),(c) and (d) at the initial regions but at higher angles, the disparities may be the result of the absence of higher radial orders in the prediction.

From the intake wall measurements, it is unknown how energy is distributed amongst different radial orders and hence, it is not certain how much these various orders contribute to measured values in the far-field. Holding on that the pressure values at the wall in the intake duct mainly contains energy in the first radial order, the inclusion of the higher radial orders in the far-field directivities will mean that the power of the in-duct wall pressure will have to be distributed among the radial orders considered in the far-field. The implication of this is that the contribution of higher radial orders in the far-field can be investigated by distributing power to higher orders and observing the effect on predicted directivities. This is possible by incoherent addition of the contribution of all cut-on radial orders with parametric variation, that is, for example, allowing the shift of power by varying the percentage contribution of each radial order. In figure 8.24, (a) and (b) are the comparisons at EO 37 for the rigid and lined duct respectively while (c) and (d) are the for the EO 67. These have been chosen as examples for two radial orders cut-on (EO37) and three radial orders cut-on (EO67). In the figure, the predictions are based on the inclusion of the first radial order. The procedure about to be introduced will allow for acoustic power to be allocated to all the cut on radial mode orders. Rice [68] proposed the use of equal energy per mode in order to be able to sum the contribution of each mode to obtain an overall value. Summing the contribution incoherently allows a weighting of individual contributions of each radial order. A case where there is equal contribution among the radial orders can be likened to the equal energy analogy.

The modal power of mode (m,n) can be expressed as [73]

$$W_{mn} = \frac{|p_{mn}|^2}{2\rho_0 c_0}\pi\left[a^2 - \left(\frac{m}{\kappa_{mn}}\right)\right]J_m^2(\kappa_{mn}a)\left[(1+M^2)Re\{\zeta_{mn}\} - M(1+|\zeta_{mn}|^2\right]. \quad (8.26)$$

where a is the duct radius, κ_{mn} is the radial wave number, in-duct Mach number $M = u/c_0$ and $\zeta_{mn} = k_{z_{mn}}/(k + k_{z_{mn}}M)$.

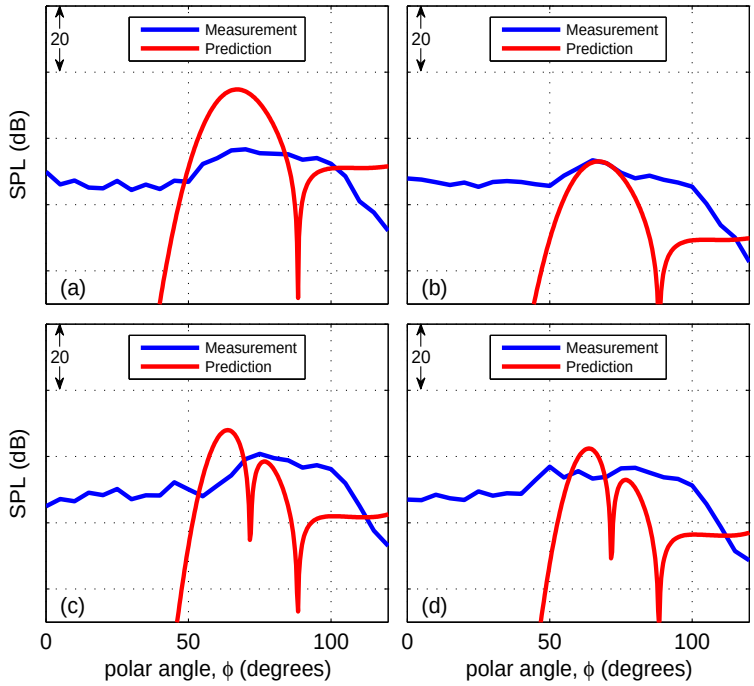

Figure 8.24: Measurement against prediction (a) EO 37 rigid (a) EO 37 lined (a) EO 67 rigid (a) EO 67 lined

For $\check{n}$ radial orders are cut-on, define a weighting coefficient α_{w_n} which is the ratio of modal powers (of the power of radial order n to that of radial order 1) expressed as

$$\alpha_{w_n} = \frac{W_{mn}}{W_{m1}} \quad \text{for any} \quad n = 2, 3, \ldots, \check{n}. \tag{8.27}$$

Using the definition (8.26) in (8.27) and rearranging yields

$$\left|\frac{p_{m1}}{p_{mn}}\right|^2 = \frac{\left[a^2 - \left(\frac{m}{\kappa_{mn}}\right)\right] J_m^2(\kappa_{mn}a)\left[(1+M^2)Re\{\zeta_{mn}\} - M(1+|\zeta_{mn}|^2\right]}{\alpha_{w_n}\left[a^2 - \left(\frac{m}{\kappa_{m1}}\right)\right] J_m^2(\kappa_{m1}a)\left[(1+M^2)Re\{\zeta_{m1}\} - M(1+|\zeta_{m1}|^2\right]}. \tag{8.28}$$

Let the right hand side of (8.28) be Ξ_n^2, then

$$|p_{m1}| = \Xi_n |p_{mn}| \quad \text{for any} \quad n = 2, 3, \ldots, \check{n}. \tag{8.29}$$

Assumption of an incoherent sum gives that the root-mean-square pressure at the wall can be expressed as a combination of the pressure values of all cut-on radial orders as

$$\overline{p^2} = \overline{p_{m1}^2} + \overline{p_{m2}^2} + \ldots + \overline{p_{m\check{n}}^2}$$

which implies

$$|p|^2 = \frac{1}{2}|p_{m1}|^2 + \frac{1}{2}|p_{m2}|^2 + \ldots + \frac{1}{2}|p_{m\check{n}}|^2. \tag{8.30}$$

To obtain $|p_{m1}|$, substitute in for $|p_{mn}|$ to give

$$|p|^2 = \frac{1}{2}|p_{m1}|^2\left[1 + \frac{1}{\Xi_2^2} + \frac{1}{\Xi_3^2} + \ldots + \frac{1}{\Xi_{\check{n}}^2}\right] \tag{8.31}$$

Hence,

$$|p_{m1}| = \frac{|p|}{\sqrt{(1 + \frac{1}{\Xi_2^2} + \frac{1}{\Xi_3^2} + \ldots + \frac{1}{\Xi_{\check{n}}^2})/2}}. \tag{8.32}$$

Consider a case where two radial orders are cut on ($\check{n} = 2$), with the modal power of each order given by W_{m1} and W_{m2}. From equation (8.32),

$$|p_{m1}| = \frac{\Xi_2|p|}{\sqrt{(\Xi_2^2 + 1)/2}} \tag{8.33}$$

and substituting equation (8.33) into equation (8.31),

$$|p_{m2}| = \frac{|p|}{\sqrt{(\Xi_2^2 + 1)/2}} \tag{8.34}$$

The effect of allocating some modal power to other cut-on radial modes can be seen for the BPF harmonics in a rigid intake duct; far-field directivities in figures 8.25 and the SPL-frequency spectrum at various angles (figures 8.26, 8.27 and 8.26).

The error bars in the figures range over the frequencies for which two or more orders are cut-on. The error bars are calculated using equation (8.31) while allocating from 0 to 100% of the power to each cut-on radial order while maintaining the 100% total, that is, ranging each $\Xi_{\check{n}}$ in equation (8.32) from 0 to 1 for every cut-on radial mode.

In figure 8.28, the SPL-frequency spectrum for angles 55^o and 75^o give an insight to the levels at the beginning and end of the polar angle region where the rotor-locked field is most dominant. It is observed at these angles that the measured values fall within or are close to the range prescribed by the error bars for the EOs for which two or three radial orders are cut-on.

Allocation of modal power to other radial orders yields similar effects in the lined wall intake duct, figures 8.29, as in the rigid wall duct. The mean for the range of α_{w_n} (labelled 'Prediction(Mod)') is plotted against measured valued and the original single radial order prediction. The agreement between predictions and measurements for the polar angles 55^o to 80^o is slightly improved as the peak of the prediction curve spreads

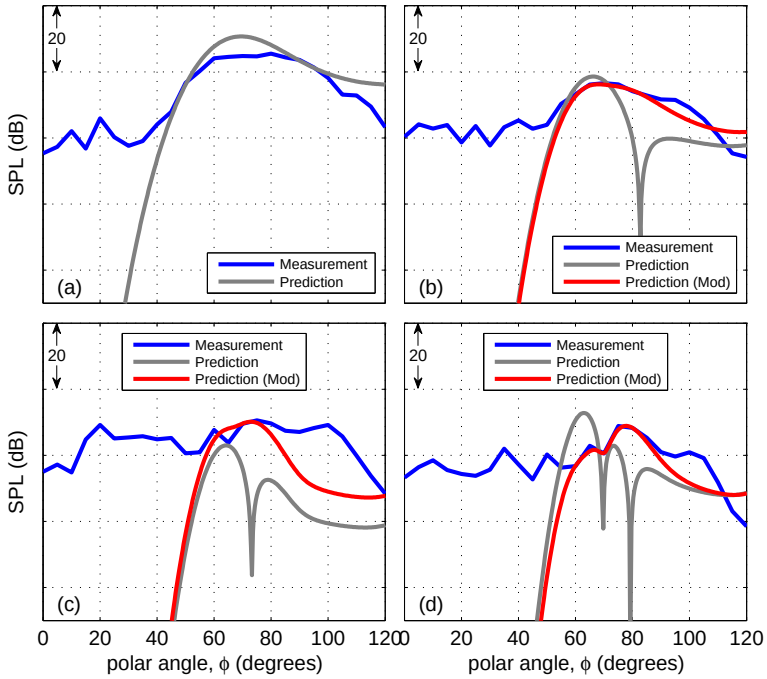

Figure 8.25: Far-field directivities of measurements against predictions: rigid duct (a) BPF (b) 2BPF (c) 3BPF (d) 4BPF [Prediction: single radial order; Prediction(Mod): all cut-on radial orders assuming equal power per mode]

to higher polar angles due to the filling of the null points between lobes by subsequent radial orders.

Figures 8.30 and 8.31 are the SPL-frequency spectrum at 30^o intervals for the lined wall case. At polar angle 30^o, similar to the rigid case, there is no significant rotor-locked field levels at most EOs. Allocation of modal power to higher radial orders gives EO level ranges as shown by the error bars in the spectra at each EO. The lower limits of range of possible values in the lined wall case are much lower than the measured values (figures 8.30(a),(b) and 8.31(a))except at very high angles close to 120^o (figure 8.31(b)). This is opposite to the observation made for the rigid wall case where the lower limits seemed to improve agreement between prediction and measurement at EOs other than the BPF harmonics.

8.4.2.2 Inclusion of almost cut on radial orders

The results from section 8.4.2.1 begged for further investigation of how closely the directivity functions, generated from predictions for the cut-on radial orders, can predict the measured levels of the radiated field if the amplitudes of each radial component was known. The approach employed is based on the incoherent addition of the pressure

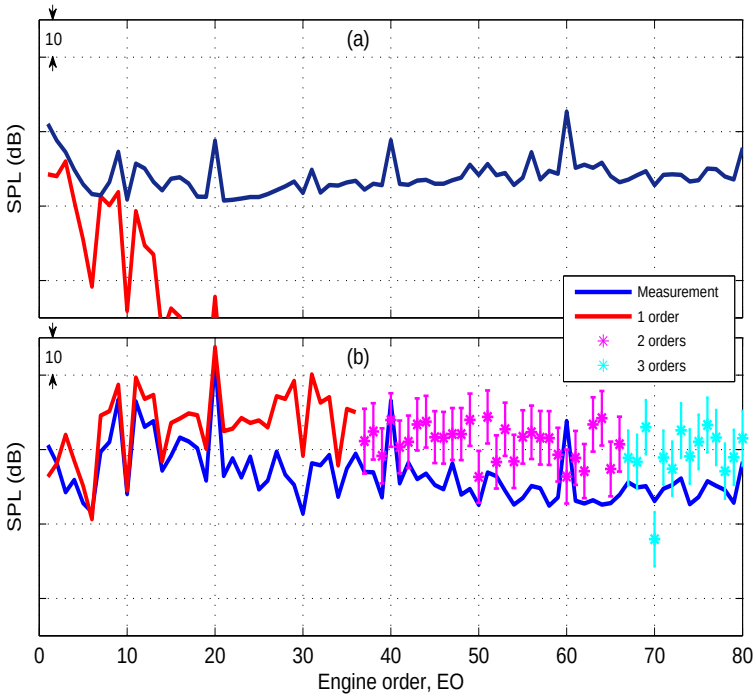

Figure 8.26: Measured against predicted (with all cut-on radial orders) SPL-EO spectrum for rigid intake duct at polar angle (a) 30^o (b) 60^o [Error bars show the range of prediction for variation of power among all cut-on radial orders]

contributions of all cut-on radial orders for each EO as in section 8.4.2.1. The main difference is the evaluation of the amplitude of each cut-on radial order for each EO at the null points. As discussed earlier, the principal lobe of a radial order coincides with the inter-lobe null points of the other radial orders. It can be assumed at this point that only that radial order is contributing to the sound level at that polar angle. With this assumption, the actual amplitude, required to match measured far-field data, of the various EOs for all cut-on radial orders can be evaluated by

$$A_{mn}|_{EO} = \frac{p_{msrd}}{p_{gx}} \tag{8.35}$$

where p_{msrd} and p_{gx} are the measured values of pressure and the predicted unit amplitude pressure values at each inter-lobe null points for $m = EO$ and each n cut-on radial order at that EO. On obtaining the amplitudes at the null points for each EO and for each cut-on radial order at that frequency, these are then taken as the contributions of the various cut-on radial orders added incoherently. The comparison with measurements in the previous section also alludes to the contribution of 'not-yet-cut-on' or 'almost-cut-on' radial order at high angles close to 90^o and above. Hence, in order to add the effect of these 'almost-cut-on' orders, equation (8.35) is evaluated at 90^o because of the absence of a definite inter-lobe null points at which the amplitudes can be evaluated.

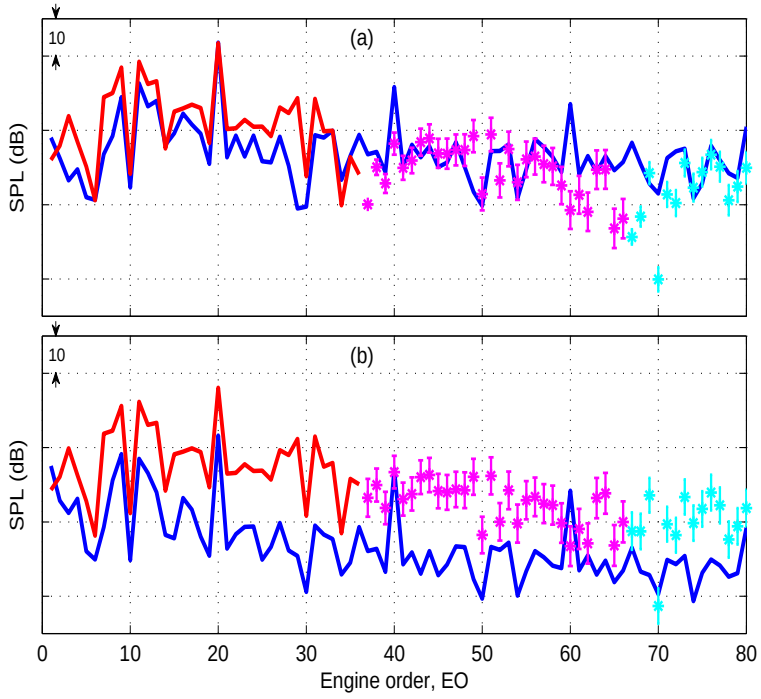

Figure 8.27: Measured against predicted (with all cut-on radial orders) SPL-EO spectrum for rigid intake duct at polar angle (a) 90^o (b) 120^o [Error bars show the range of prediction for variation of power among all cut-on radial orders]

Another reason for evaluation at 90^o, is the rapid fall off of the measured directivities at angles above 90^o. It should be noted that the contributions of these 'almost-cut-on' order have no significance at lower angles as the lobes at lower angles are minuscule and have negligible sound levels.

Knowing that using values of the modal amplitudes derived from measurements will definitely improve the predictions at the null points, in fact the measurements and prediction will be the same at the inter-lobe nulls, the question to be answered here is to what extent does having the correct amplitude for each cut-on radial order improve the predictions at various polar angles and for the range of frequency of interest?

The results of this investigation are evident in figures 8.32 through to 8.39 for both the rigid and lined wall configurations.

The first observable contribution of using the amplitudes from the measured pressure values is that the peak values in the prediction are now comparable to the same sound level as measurements 8.32(b)-(d) and 8.36(b)-(d). This is expected as the null points at which the first radial order is evaluated coincide with the peak values in the directivities or are points very close to the peak values. For the rigid wall intake duct, the addition of the contribution of cut-on radial orders gives a very good agreement from angles 60^o to 90^o, which is the region of dominance of rotor-locked field, as observable in the

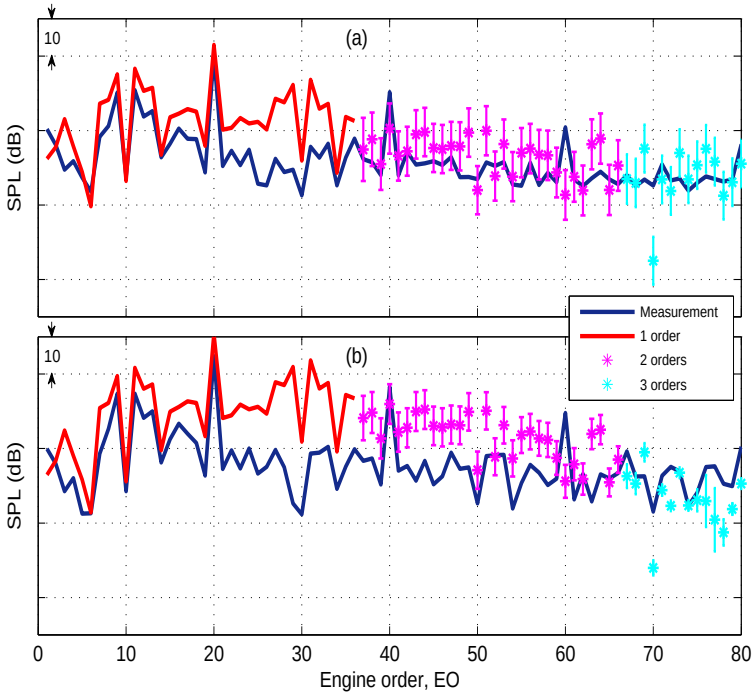

Figure 8.28: Measured against predicted (with all cut-on radial orders) SPL-EO spectrum for rigid intake duct at polar angle (a) 55^o (b) 75^o [Error bars show the range of prediction for variation of power among all cut-on radial orders]

SPL-EO spectrum at angles 60^o and 90^o [figures 8.33(b), 8.34(a)] and also at angle 75^o [figure 8.35(b)]. As observed earlier, the rotor-locked field is almost non-existent at polar angle 30^o as seen in the comparison of the SPL-EO spectrum [figure 8.33(a)] but it progressively becomes more evident as the polar angle increases. As seen in figure 8.35(a), the SPL-EO spectrum at 55^o indicates the start of the rise of rotor-locked sound levels above the multi-modal field. As observed in previous sections, the prediction of sound levels for polar angles above 90^o is always much higher that measurements. This is believed to be as a result of geometry effects (discussed in section 8.5).

Similar to the observations in the rigid duct, the lined duct results for the inclusion of all cut-on radial orders and the next non-yet-cut-on radial order gives better agreement with measurements for the BPF harmonics [figure 8.36] and at the polar angles where the rotor-locked field is dominant [figures 8.37(b), 8.38(a)]and also at angle 75^o [figure 8.39(b)]. The absence of the rotor-locked field at very low angles and comparatively high sound levels at polar angles greater 90^o from the duct axis is similar to the observations in the rigid duct wall case. It is important to say that the use of measured amplitudes with the unit-amplitude directivities from GXMunt also fills in for the over-prediction of the attenuation of the installed acoustic liner (figure 8.36). This is seen to be a result of the second radial order added at the EOs close to BPF. As the second radial order, in theory, is actually not cut-on at near-BPF frequencies, the results may only be

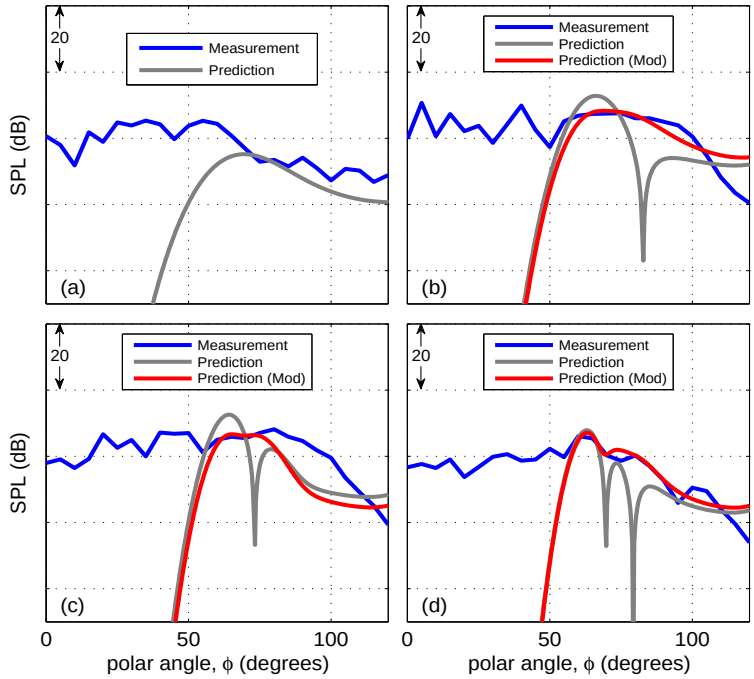

Figure 8.29: Far-field directivities of measurements against predictions: lined duct (a) BPF (b) 2BPF (c) 3BPF (d) 4BPF [Prediction: single radial order; Prediction(Mod): all cut-on radial orders assuming equal power per mode]

representative if geometric and flow effects not captured in the radiation model mean that this mode is reasonably well radiated from the intake.

8.5 Geometry and flow effects on radiation

The influence of duct geometry on the radiation results appears significant at angles greater than 90^o. In the measured directivities for the BPF tone and its harmonics, figure 8.5 and 8.8, the continuous drop in sound level is observed at these high polar angles of directivity for both the rigid and lined intake ducts. This is not the case in the prediction results in figures 8.14 and 8.18. Prediction results show sound level stay relatively unchanged, or marginally increase in some instances at high frequencies, at polar angles greater than that of the highlight plane. This was evident in the SPL-EO spectra as well. Comparisons between prediction and measurement, for example at 120^o [figure 8.16(b)], showed significant differences at most EOs (although the differences are much less for the lined wall intake figure 8.20(b)). These differences still exist even when measured amplitudes were used with together with predicted unit-amplitude pressure directivities – figure8.38.

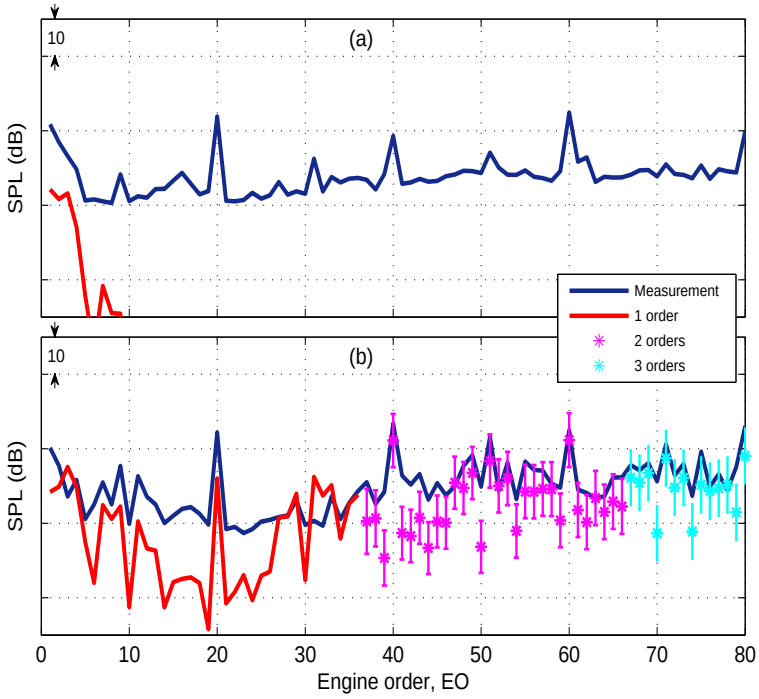

Figure 8.30: Measured against predicted (with all cut-on radial orders) SPL-EO spectrum for lined intake duct at polar angle (a) 30^o (b) 60^o [Error bars show the range of prediction for variation of power among all cut-on radial orders]

An illustration of the uniform flow in the cylindrical duct with a thin duct wall (used in the radiation model) and a realistic flow in an axisymmetric intake duct is made in figure 8.40. A single flow speed is set inside and outside the cylindrical duct whilst the axisymmetric duct has varying flow speeds especially along the wall. A region can be seen near the lip where flow speeds are very high due to the turning in of the flow around the duct lip. It can be inferred that the radiation pattern at range of polar angles of interest may be influenced by the rounded duct lip due to the diffraction of the radiated field around the curvature of the duct lip. This is consistent with the observation in computational studies in references [38, 86, 95] which show that flow speed up occurs at the inner curvature of the lip causing a refraction of the sound field towards and around the curvature[95]. It can be argued that the flow speed up around the lip may also influence the transfer of energy to among radial orders and make otherwise cut-off modes cut-on. This features present in reality are not captured in the radiation model. The extent of the effect of geometrical variation at the duct lip on the radiation to other angles less than 90^o is not known but good agreement between prediction and measurement at some angles suggest that it does not have as much significant effects as at higher angles.

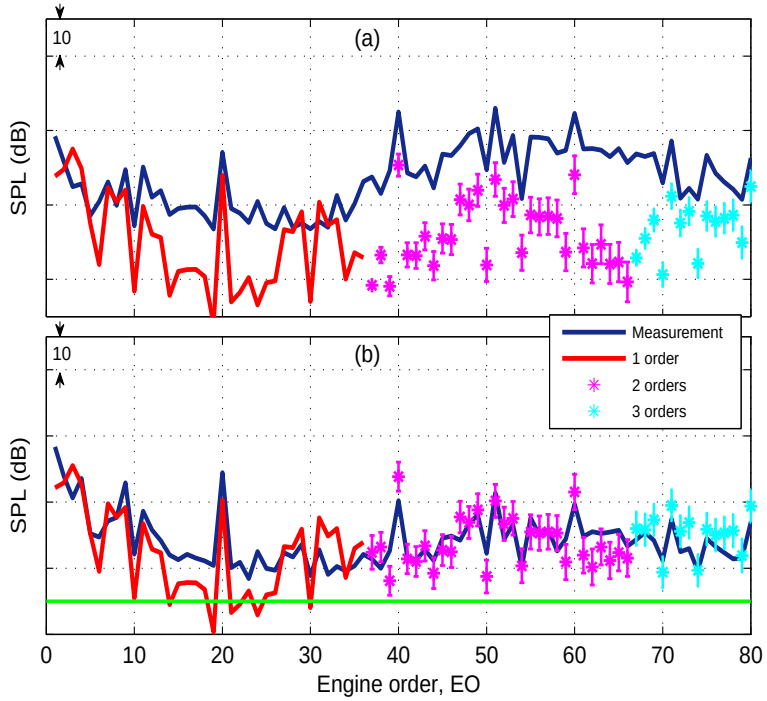

Figure 8.31: Measured against predicted (with all cut-on radial orders) SPL-EO spectrum for lined intake duct at polar angle (a) 90^o (b) 120^o [Error bars show the range of prediction for variation of power among all cut-on radial orders]

8.6 Summary

An analytical model based on a cylindrical-thin-walled duct has been used to predict the radiation of the rotor-locked field to the far-field. Relatively good agreement is observed between measured sound levels and predictions, most especially at polar angles between 60^o and 80^o where the rotor-locked field is dominant. The differences observed at high polar angles are a result of the geometry of the duct lip as the propagated pressure field is radiated out of the intake duct. There is no significant presence of the rotor-locked field at low angles close to the duct axis and indeed no significant contribution of the rotor-locked field was seen until about 55^o to 60^o polar angle for both the rigid and acoustically lined intakes.

The flow speed up around the duct lip for realistic geometry duct, as observed in figure 8.40(b) and in computational aeroacoustic simulations of mean flow in realistic ducts [85, 86, 95], is not represented in this model which assumes the duct is a thin walled cylinder. The diffraction along the flare installed at the inlet of the intake duct is all not captured for the same reason. This makes the prediction at high polar angles above 90^o significantly different from measurements.

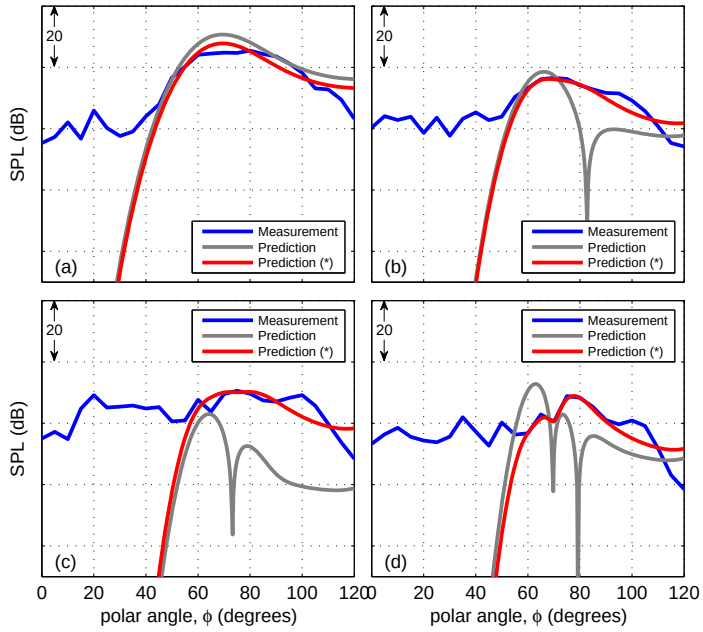

Figure 8.32: Far-field directivities with all cut-on radial orders: measurements against prediction(*): rigid duct (a) BPF (b) 2BPF (c) 3BPF (d) 4BPF [Prediction: single radial order. Prediction(*): prediction using pressure amplitudes from measured data with predicted unit amplitude directivities.]

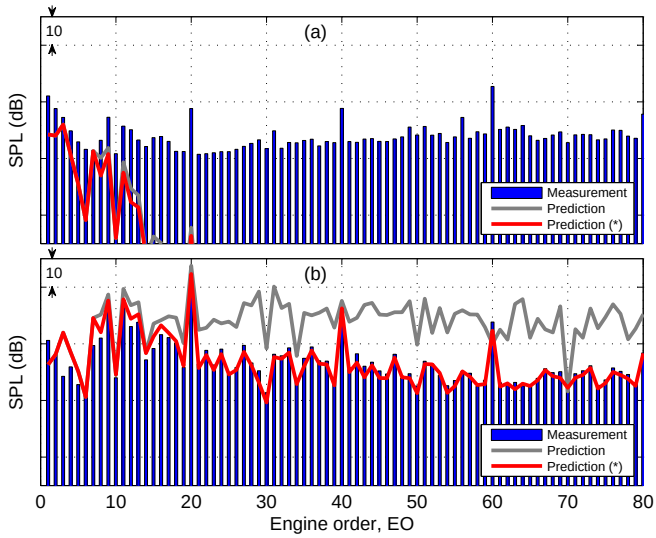

Figure 8.33: Measured against prediction(*) SPL-EO spectrum for rigid intake duct at polar angle (a) 30^o (b) 60^o [Prediction: single radial order. Prediction(*): prediction using pressure amplitudes from measured data with predicted unit amplitude directivities.]

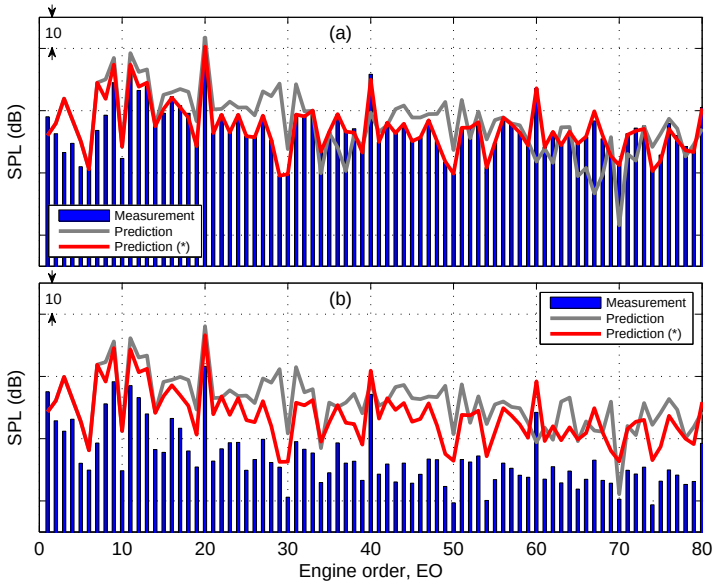

Figure 8.34: Measured against prediction(*) SPL-EO spectrum for rigid intake duct at polar angle (a) 90^o (b) 120^o [Prediction: single radial order. Prediction(*): prediction using pressure amplitudes from measured data with predicted unit amplitude directivities.]

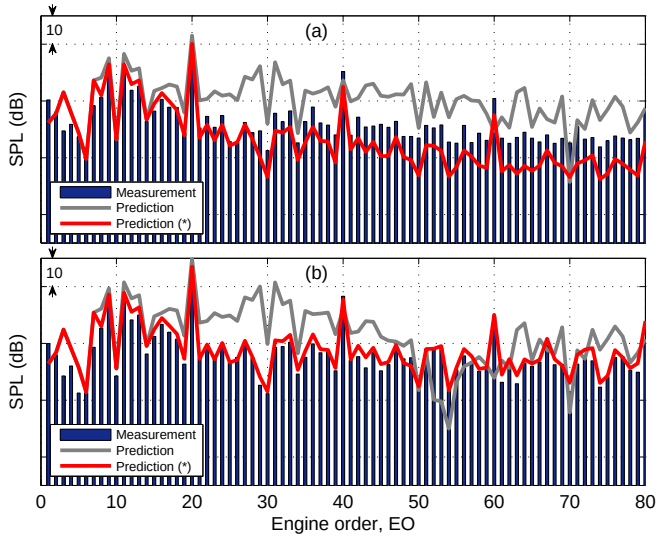

Figure 8.35: Measured against prediction(*) SPL-EO spectrum for rigid intake duct at polar angle (a) 55^o (b) 75^o [Prediction: single radial order. Prediction(*): prediction using pressure amplitudes from measured data with predicted unit amplitude directivities.]

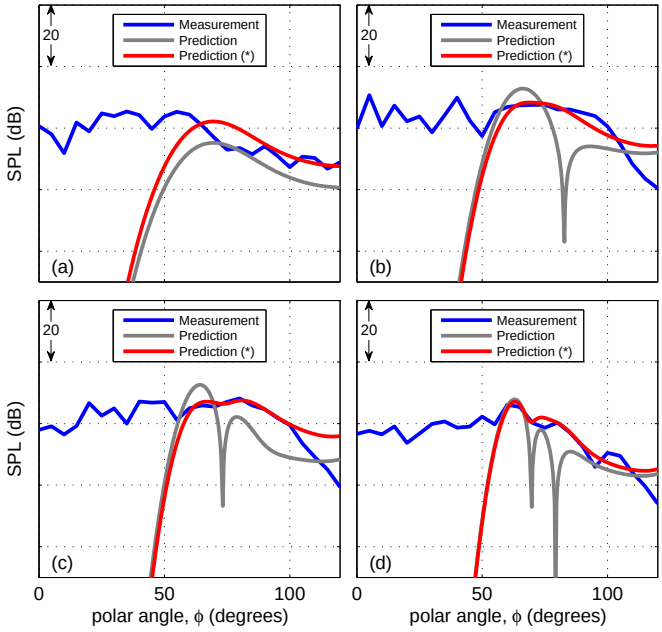

Figure 8.36: Far-field directivities with all cut-on radial orders: measurements against prediction(*): lined duct (a) BPF (b)2BPF (c) 3BPF (d) 4BPF [Prediction: single radial order. Prediction(*): prediction using pressure amplitudes from measured data with predicted unit amplitude directivities.]

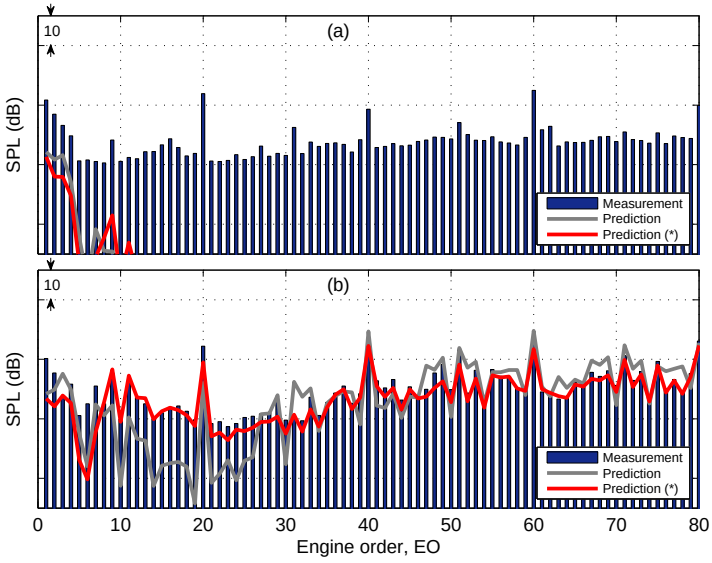

Figure 8.37: Measured against prediction(*) SPL-EO spectrum for lined intake duct at polar angle (a) 30^o (b) 60^o [Prediction: single radial order. Prediction(*): prediction using pressure amplitudes from measured data with predicted unit amplitude directivities.]

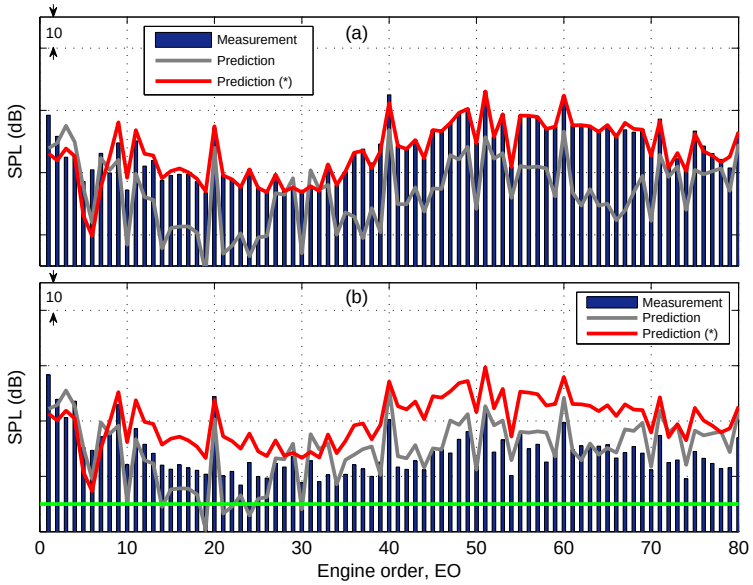

Figure 8.38: Measured against prediction(*) SPL-EO spectrum for lined intake duct at polar angle (a) 90^o (b) 120^o [Prediction: single radial order. Prediction(*): prediction using pressure amplitudes from measured data with predicted unit amplitude directivities. NOTE: the green line marks the lower limit of the vertical axis in previous plots]

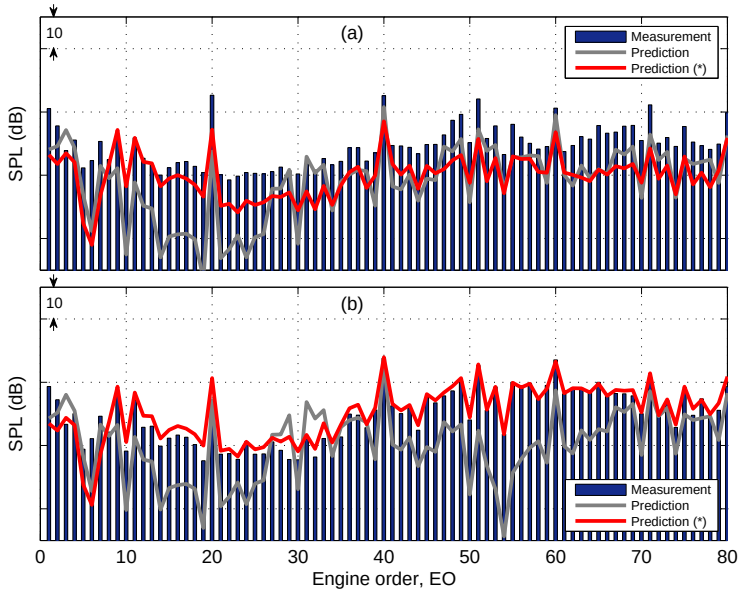

Figure 8.39: Measured against prediction(*) SPL-EO spectrum for lined intake duct at polar angle (a) 55^o (b) 75^o [Prediction: single radial order. Prediction(*): prediction using pressure amplitudes from measured data with predicted unit amplitude directivities.]

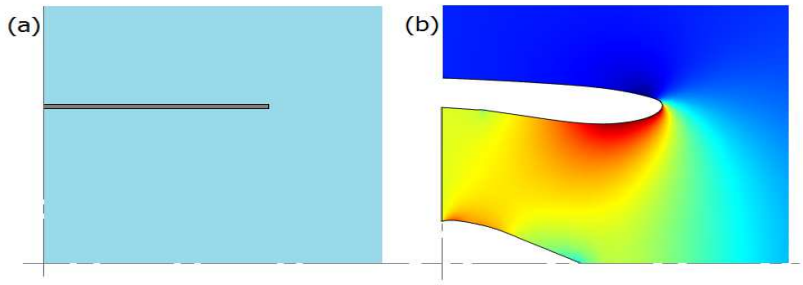

Figure 8.40: Illustration of flow in and around (a) cylindrical duct (b) Axisymmetric duct

There are many flow and geometry effects than may influence the sound levels in the far-field as various interaction and change in modal powers can significantly affect radiation angles and indeed, the levels perceived at different polar angles. As the sound levels predicted for the far-field are in direct relation with the sound levels predicted at the highlight plane of the duct, the proper capture of the effect of geometrical changes in the duct and the resultant change in flow parameters may be necessary in the achieving better prediction of the propagation and radiation of buzz-saw noise. Effects of variation in geometry (radius) on nonlinear propagation is covered in chapters 10 and 11.

Two points are to be stressed. First, the diffraction around the duct lip is much different from what is model in GXMunt radiation model used. Second, owing to the high-speed flow region around the lip, it is presumed that energy is scattered into higher-order radial modes. This has been demonstrated that in principle, if the individual contribution of each radial order is known, good prediction can be achieved. The prediction results with only one radial order considered yielded much better agreements for the lined wall duct results. This may be due to less interactions and modal power changes as a much lower sound levels exits the duct and is radiated to the far-field in this case. The addition of higher radial order gave significant improvement to predictions, especially in the rigid wall duct, stretching the region of good agreement over larger range of polar angles for most EOs.

Chapter 9

Development of Irregular Sawtooth Propagation Equations for Axisymmetric Ducts with Axially Non-uniform flows

Equations for the regular sawtooth propagation in cylindrical ducts have been presented [17, 18, 36]. An analytic formula for regular sawtooth propagation with a fixed decay rate independent of frequency also has been presented [18, 21]. Moreover, the propagation of a regular sawtooth in an example duct with varying geometry in the duct axis direction is found in the study by Mathews and Nagel [23]. As a real fan generates a pressure field with shocks with an irregular sawtooth pattern, it is useful to extend this analytical formulation to an irregular sawtooth waveform.

The simplicity afforded by the regular sawtooth pattern in that describing a single shock wave is sufficient for all other shocks in the pressure field is no longer present as every shock wave is in reality unique. As the regular sawtooth analytical solutions are based on a single shock wave which is representative of the other shock waves in the waveform, the same analogy is put to use in the simplification of the complexity for the irregular sawtooth problem.

9.1 Analytical equations for propagation in axisymmetric rigid ducts

First, it is useful to go through the basic steps in the generation of the analytical equation for the nonlinear decay of a regular sawtooth as found in [17].

9.1.1 Basic derivation for regular sawtooth propagation in a rigid duct

For a regular sawtooth with starting shock amplitude $p_s(0)$ at time of flight $T = 0$, consider the propagated to a time of flight, T. The velocity of the shock wave will be

$$v_s = c_0 + \frac{\gamma+1}{2\rho_0 c_0} p_m, \tag{9.1}$$

where p_m is the mid point pressure of each individual regular shock wave. Assuming that the sawtooth waveform is centred at the ambient pressure, the shock velocity will reduce to

$$v_s = c_0. \tag{9.2}$$

The expansion waves, however, will span from $\frac{1}{2}p_s(0)$ to -$\frac{1}{2}p_s(0)$. Hence, the top end of the expansion wave behind the shock will travel at velocity

$$v_{e_t} = c_0 + \frac{\gamma+1}{2\rho_0 c_0}\frac{1}{2} p_s(0) = c_0 + \frac{\gamma+1}{4\rho_0 c_0} p_s(0), \tag{9.3}$$

while the bottom end of the expansion wave ahead of the shock will be propagate at velocity

$$v_{e_b} = c_0 - \frac{\gamma+1}{2\rho_0 c_0}\frac{1}{2} p_s(0) = c_0 - \frac{\gamma+1}{4\rho_0 c_0} p_s(0). \tag{9.4}$$

Assuming a moving reference frame travelling at speed c_0, i.e. $\bar{x} = x - c_0 t$, the velocities can be re-written as

$$v_s = 0, \tag{9.5}$$

$$v_{e_t} = \frac{\gamma+1}{4\rho_0 c_0} p_s(0), \tag{9.6}$$

$$v_{e_b} = -\frac{\gamma+1}{4\rho_0 c_0} p_s(0). \tag{9.7}$$

Note that the time of flight

$$T = \frac{c_0 t}{\lambda} = \frac{zK}{D} \tag{9.8}$$

where $\lambda = \frac{2\pi}{B}$ is the shock spacing, D is the duct diameter and K is defined in equation (3.26). Hence,

$$T = \frac{c_0 t B}{2\pi}, \tag{9.9}$$

which implies

$$t = \frac{2\pi T}{c_0 B}, \tag{9.10}$$

where B is the number of shock waves equal initially to the number of fan blades. The propagated distance of the shock and its related expansion wave end points over a time of flight T are

$$x_s = v_s t = 0, \tag{9.11}$$

$$x_{e_t} = v_{e_t} t = \frac{\gamma+1}{4\rho_0 c_0} p_s(0) \times \frac{2\pi T}{c_0 B} == \frac{(\gamma+1)\pi T}{2\rho_0 c_0^2 B} p_s(0), \tag{9.12}$$

$$x_{e_b} = v_{e_b} t = -\frac{\gamma+1}{4\rho_0 c_0} p_s(0) \times \frac{2\pi T}{c_0 B} = -\frac{(\gamma+1)\pi T}{2\rho_0 c_0^2 B} p_s(0). \tag{9.13}$$

Figure 9.1 captures these points at time of flight T. The shock remains stationary in the moving frame (hence $\bar{x}_s = x_s$). The expansion waves must then be resolved to the shock position to correct for the distortion otherwise the pressure will be multi-valued (and consequently ensure the decay of the shock amplitude over distance axial distance z reached at time of flight T).

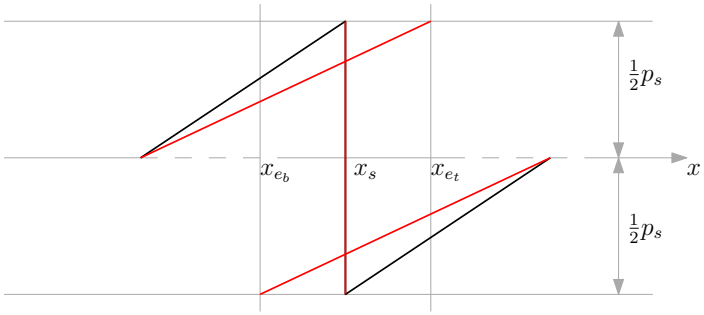

Figure 9.1: Distortion of waveform

From figure 9.2, we can use the similar triangle ratios to arrive at

$$\frac{\frac{1}{2}p_s(T)}{\frac{1}{2}p_s(0)} = \frac{\frac{\pi}{B}}{\frac{\pi}{B} + \frac{(\gamma+1)\pi T}{2\rho_0 c_0^2 B} p_s(0)}. \tag{9.14}$$

Rearranging yields

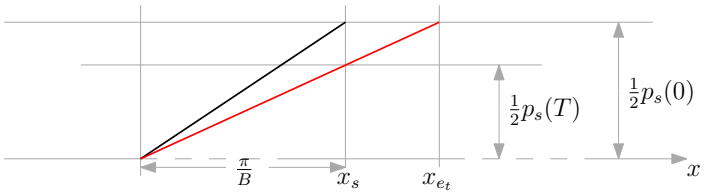

Figure 9.2: Resolution of waveform by removal of distorted multi-valued regions

$$p_s(T) = \frac{p_s(0)}{1 + \frac{(\gamma+1)}{2\rho_0 c_0^2} T p_s(0)}, \tag{9.15}$$

but $\gamma P_0 = \rho_0 c_0^2$, therefore,

$$p_s(T) = \frac{p_s(0)}{1 + \frac{(\gamma+1)}{2\gamma} T \frac{p_s(0)}{P_0}} \tag{9.16}$$

The initial shock strength is defined as $s = \frac{p_s(0)}{P_0}$, hence

$$p_s(T) = \frac{p_s(0)}{1 + \frac{(\gamma+1)}{2\gamma} T s},$$

which is the equation 3.29.

9.1.2 Propagation of a regular sawtooth in a rigid duct with varying duct geometry

This is covered in detail in Mathews and Nagel's work [23], where a regular sawtooth pressure amplitude decay as a function of distance of propagation was presented. Starting at a point i, where the shock amplitude attenuation according to propagation in a cylindrical duct is expressed via equation (3.29). If both sides are divided by the P_0, we have that an expression in shock strength, s as

$$s_i = \frac{s}{1 + \frac{(\gamma+1)}{2\gamma} T s}. \tag{9.17}$$

Substituting in for $T = zK/D$, rearranging and remembering that K and D vary in the direction of propagation, we have [23]

$$\frac{1}{s_i} = \frac{1}{s} + \frac{(\gamma+1)}{2\gamma} \int_0^{z_i} \frac{K}{D} dz. \tag{9.18}$$

The diameter $D_i = 2R_i$ at any point i. Equation 9.18 can then be written for stepwise propagation from i to $i+1$ as

$$\frac{1}{s_{i+1}} = \frac{1}{s_i} + \frac{(\gamma+1)}{2\gamma}\left\{\left[\frac{K_i}{R_i} + \frac{K_{i+1}}{R_{i+1}}\right]\frac{z_{i+1}-z_i}{2}\right\}. \tag{9.19}$$

Equation (9.19) is the shock attenuation analytical equation for regular sawtooth propagation in rigid wall ducts with varying inlet geometry.

9.1.3 Propagation of irregular sawtooth in a rigid duct

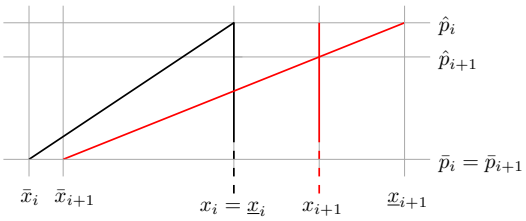

Figure 9.3: Illustration for upper half of a single shock wave

Following the same analogy used for the regular sawtooth, an 'analytical' equation can be obtained for a single 'irregular' shock sawtooth waveform, and this can be then be solved for a given set of nonidentical shock waves in an irregular sawtooth. Consider a single shock wave as shown in two parts in figures 9.3 and 9.4, propagated from x_i to x_{i+1}. $\bar{x}$ and $\hat{x}$ represent the positions of starting point and the top point of the pre-shock expansion wave. While, $\breve{x}$ and $\underline{x}$ represents positions of bottom point and the end point of the post-shock expansion wave. Focusing on the top part of the waveform gives figure 9.3, and using the similar triangle ratios, we have that

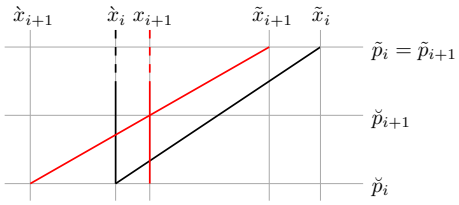

Figure 9.4: Illustration for lower half of a single shock wave

$$\hat{p}_{i+1} = \frac{\hat{p}_i - \bar{p}_i}{1 + \frac{\underline{x}_{i+1} - x_{i+1}}{(x_{i+1}-\bar{x}_{i+1})+(x_{i+1}-x_i)-(\bar{x}_{i+1}-\bar{x}_i)}} + \bar{p}_i, \tag{9.20}$$

which yields

$$\hat{p}_{i+1} = \frac{\hat{p}_i - \bar{p}_i}{1 + \frac{\underline{x}_{i+1} - x_{i+1}}{x_{i+1} - \bar{x}_{i+1}}} + \bar{p}_i. \tag{9.21}$$

For the bottom part of the waveform, using the illustration given in figure 9.4, for the lower part of a shock wave with all the values taken as negative to represent a bottom section below the mid-point pressure, we obtain

$$\frac{\breve{p}_{i+1} - \breve{p}_i}{\tilde{p}_i - \breve{p}_i} = \frac{x_{i+1} - \grave{x}_{i+1}}{\tilde{x}_{i+1} - \grave{x}_{i+1}}, \tag{9.22}$$

which yields

$$\breve{p}_{i+1} = \frac{(\tilde{p}_i - \breve{p}_i)(x_{i+1} - \grave{x}_{i+1})}{\tilde{x}_{i+1} - \grave{x}_{i+1}} + \breve{p}_i. \tag{9.23}$$

It is important to note the the start and end positions of the fore and after expansion waves are taken to be the mid-points of the span of these expansion waves. The positional values x, $\bar{x}$, $\tilde{x}$, $\underline{x}$ and $\grave{x}$ are all evaluated as the product of the velocity equations based on the mid-point pressure of the shock

$$v_s = c_0 + \frac{\gamma + 1}{2\rho_0 c_0} p_m, \tag{9.24}$$

and the end points on the expansion waves, as expressed in equations

$$v_{e_t} = c_0 + \frac{\gamma + 1}{2\rho_0 c_0} p_s \tag{9.25}$$

$$v_{e_b} = c_0 - \frac{\gamma + 1}{2\rho_0 c_0} p_s \tag{9.26}$$

with the time from point i to $i + 1$ given as in equation (9.10).

Equation (9.21) and (9.23) are together the equations for the advancement of an irregular sawtooth where the (9.21) and (9.23) evaluate the values of the top end and bottom end of the shocks after a time step. The shock amplitude for the particular shock propagated is the difference calculated by subtracting the result of (9.23) from that of equation (9.21). For a sawtooth with B shocks, the equations are evaluated for each shock and checks for shock crossover and merging is checked at every step. In the event of shock crossover, the shock order is corrected. When two shocks merge, the top shock value of the shock with a higher mid-point and bottom shock value of the other shock are used to form the new shock. Hence, the effective number of shocks in the waveform is adjusted accordingly to reflect the actual number of shock waves now present.

This is only applicable for propagation in a rigid duct as the assumption that the expansion waves are linear is factored into the resolution of the propagation using the distortion of the propagated expansion waves and their corresponding shock wave.

9.1.4 Propagation of irregular sawtooth in a rigid duct with varying duct radius

Consider a simple converging duct, figure 9.5, the pressure p, velocity u, density ρ and sound speed c varying along the duct axis.

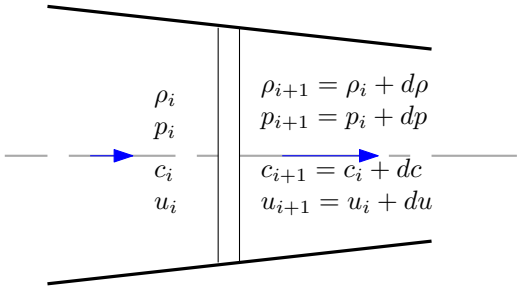

Figure 9.5: Illustration of converging duct using nozzle analogy

$$v_s = c_i + \frac{\gamma + 1}{2\rho_i c_i} p_m \tag{9.27}$$

and the points on the expansion waves, as expressed in equations

$$v_{e_t} = c_i + \frac{\gamma + 1}{2\rho_i c_i} p_{s_i} \tag{9.28}$$

$$v_{e_b} = c_i - \frac{\gamma + 1}{2\rho_i c_i} p_{s_i} \tag{9.29}$$

evaluated at the initial positions and the time it takes to advance one propagation step in the axial direction to the next position. A moving frame based on a mean sound speed (c_0) can be described, modifying the equations as

$$v_s = (c_i - c_0) + \frac{\gamma + 1}{2\rho_i c_i} p_m \tag{9.30}$$

and the points on the expansion waves, as expressed in equations

$$v_{e_t} = (c_i - c_0) + \frac{\gamma + 1}{2\rho_i c_i} p_{s_i} \tag{9.31}$$

$$v_{e_b} = (c_i - c_0) - \frac{\gamma + 1}{2\rho_i c_i} p_{s_i} \tag{9.32}$$

Taking into account the variation in duct geometry with axial position and all the consequent changing parameters such as inflow speed and rate of change of time of flight, from axial position z_i to z_{i+1}, and using v_s, v_{e_t} and v_{e_b}, then, for the shock

$$x_{i+1} = \left[c_i + \frac{\gamma + 1}{2\rho_i c_i} p_{m_i} \right] dt \tag{9.33}$$

where $t = \pi z K / B c_i$ and hence,

$$x_{i+1} = x_i + \frac{\pi}{B}\Big[1 + \frac{\gamma+1}{2\rho_i c_i} p_{m_i}\Big] \int_{z_i}^{z_{i+1}} K(z) dz, \tag{9.34}$$

$$x_{i+1} = x_i + \frac{\pi}{B}\Big[1 + \frac{\gamma+1}{2\rho_i c_i^2} p_{m_i}\Big] \big[K_i + K_{i+1}\big](z_i - z_{i+1}). \tag{9.35}$$

Similarly, for the position of the ends of the expansion waves

$$\underline{x}_{i+1} = x_i + \frac{\pi}{B}\Big[1 + \frac{\gamma+1}{2\rho_i c_i^2} p_{s_i}\Big] \big[K_i + K_{i+1}\big](z_i - z_{i+1}) \tag{9.36}$$

$$\grave{x}_{i+1} = x_i + \frac{\pi}{B}\Big[1 - \frac{\gamma+1}{2\rho_i c_i^2} p_{s_i}\Big] \big[K_i + K_{i+1}\big](z_i - z_{i+1}) \tag{9.37}$$

$$\bar{x}_{i+1} = \bar{x}_i + \frac{\pi}{B}\Big[1 + \frac{\gamma+1}{2\rho_i c_i^2} \bar{p}_i\Big] \big[K_i + K_{i+1}\big](z_i - z_{i+1}) \tag{9.38}$$

$$\tilde{x}_{i+1} = \tilde{x}_i + \frac{\pi}{B}\Big[1 - \frac{\gamma+1}{2\rho_i c_i^2} \tilde{p}_i\Big] \big[K_i + K_{i+1}\big](z_i - z_{i+1}) \tag{9.39}$$

In addition to these equations, it is necessary to have few checks for each step of propagation. First, a check for shocks merging, that is, when

$$x_{i+1}|_j \geq x_{i+1}|_{j+1}$$

where $j = 1, ..., B$ is the order of the shock. Also, a check on shock crossover, when the first shock in the series has a position

$$x_{i+1} < 0,$$

or when the last shock in the series is at a position

$$x_{i+1} > 2\pi.$$

The first is corrected by moving the first shock to the rear in the series and adding 2π to the value of its position while the other is rectified by making the shock the first in the series by subtraction of 2π from its position.

9.2 Analytical equations for propagation in axisymmetric lined ducts

9.2.1 Propagation of regular sawtooth in a lined duct

A similar procedure, as in section 9.1.1, can be followed for the lined duct case to obtain

$$p_s(T) = \frac{p_s(0)\ e^{-\sigma_B T}}{1 + \frac{(\gamma+1)}{2\gamma}\frac{s}{\sigma_B}(1 - e^{-\sigma_B T})} \tag{9.40}$$

where σ_B is the liner decay rate of the BPF tone [18, 21].

9.2.2 Propagation of regular sawtooth in a lined duct with varying geometry

Following from equation (9.19), the equation for the attenuation of regular sawtooth shock amplitude in a lined duct with varying inlet geometry can be derived. This follows the same analogy used in [17] for a regular sawtooth propagating in a lined cylindrical duct. For a fixed liner decay rate independent of frequency, σ_B, the shock strength at a point on the duct axis can be written as

$$s_i = \frac{s\ e^{-\sigma_B T}}{1 + \frac{(\gamma+1)}{2\gamma} T s \frac{1-e^{-\sigma_B T}}{\sigma_B T}}, \tag{9.41}$$

$$s_i = \frac{s\ e^{-\sigma_B T}}{1 + \frac{(\gamma+1)}{2\gamma}\frac{s}{\sigma_B}(1 - e^{-\sigma_B T})}. \tag{9.42}$$

Rearrange equation (9.42) to obtain

$$\frac{1}{s_i} = \frac{1}{s\ e^{-\sigma_B T}} + \frac{(\gamma+1)}{2\gamma}\frac{1}{\sigma_B\ e^{-\sigma_B T}} - \frac{(\gamma+1)}{2\gamma}\frac{1}{\sigma_B}, \tag{9.43}$$

$$\frac{1}{s_i} = \Big[\frac{1}{s} + \frac{1}{\sigma_B}\frac{(\gamma+1)}{2\gamma}\Big] e^{\sigma_B T} - \frac{1}{\sigma_B}\frac{(\gamma+1)}{2\gamma}. \tag{9.44}$$

The time of flight $T = \frac{zK}{D} = \frac{zK}{2R}$ and $K = K(z)$ and $R = R(z)$ are functions of z. Hence,

$$\frac{1}{s_i} = \Big[\frac{1}{s} + \frac{1}{\sigma_B}\frac{(\gamma+1)}{2\gamma}\Big] \exp\{\frac{\sigma_B}{2}\int_0^{z_i}\frac{K}{R}dz\} - \frac{1}{\sigma_B}\frac{(\gamma+1)}{2\gamma}. \tag{9.45}$$

This can be written for stepwise propagation from point i to a subsequent point $i+1$ as

$$\frac{1}{s_{i+1}} = \Big[\frac{1}{s_i} + \frac{1}{\sigma_B}\frac{(\gamma+1)}{2\gamma}\Big]\ \exp\Big\{\frac{\sigma_B}{2}[\frac{K_i}{R_i} + \frac{K_{i+1}}{R_{i+1}}]z_{i+1} - z_i\Big\} - \frac{1}{\sigma_B}\frac{(\gamma+1)}{2\gamma}, \qquad (9.46)$$

for a duct with radius varying along the duct axis.

9.2.3 A Note on Analytical Equations and Acoustic Liners

Due to the complexity of the interactions and energy transfer among various harmonics it is difficult to have a set of analytic equation that will conveniently predict the nonlinear distortion of the waveform and the absorption by a realistic acoustic liner for an irregular sawtooth. The simplification of taking a constant (liner) absorption rate for the regular sawtooth enables absorption directly to be applied to the shocks amplitudes.

9.3 Summary

The equations presented in this chapter are sufficient to predict the nonlinear attenuation of a pressure field simplified to a one dimensional sawtooth (regular or irregular) in a cylindrical or axisymmetric duct with rigid walls. Also presented is an analytical equation for propagation of regular sawtooth in a duct with absorption σ_B set for the BPF tone. The analytical representation of the sawtooth is not able to incorporate the effect of a real acoustic liner which have different decay rates at different frequencies. For the irregular sawtooth, each shock wave is unique resulting in tones not only present at harmonics of the BPF, but at the harmonics of the shaft rotation frequency. Unlike for the regular sawtooth where one N-wave represents all the waveform, the equations presented for the irregular sawtooth propagation in a rigid intake are applied to a full waveform due to the inherent inter-shock interactions. Equations are presents for propagation in axisymmetric ducts with rigid wall and for a lined wall case with fixed absorption for all frequencies.

Chapter 10

Axisymmetric Ducts with Varying Radius and Effects of Nonlinear Propagation

Prior to the study on axisymmetric ducts of varying radius in the previous chapter, the propagation models presented had employed the approximation of the aircraft intake duct as a cylindrical duct with a constant radius. This approximation allowed for the simplification of the complexity of the nonlinear propagation of the rotor-locked pressure field, which is represented as a sawtooth waveform. Although, the constant cross section approximation of the intake for the nonlinear propagation has been shown to yield results that agree reasonably well with measurements, most especially in the rigid wall intake configuration, it is important to improve the model to correctly represent reality. Typical aircraft intakes are contoured along the axial direction from the fan plane to the duct lip. The shape of the intake ensures that the cross-section varies in the axial direction. This variation in cross-sectional area influences the flow in the duct, and, hence, the propagation of the pressure field from the fan to the highlight plane (duct lip). This shows that including the geometric variation of the duct is useful in the improvement of the prediction of the evolution of the fan's pressure field. Inclusion of the geometrical variation of the intake also fits well with the aim of this project which is to improve the prediction capabilities for buzz-saw noise.

10.1 Duct Geometry

As the rotor-locked field generated at the fan face propagates against incoming air flow in the intake, any changes in the flow affect the upstream propagation to various levels depending on the magnitude of the changes. Buzz-saw noise levels obtained are influenced by the flow in the intake which is directly linked to the geometry of the intake.

A change in duct cross section is mainly reflected as a change in the axial flow Mach number, as the flow slows or speeds up along the streamlines.

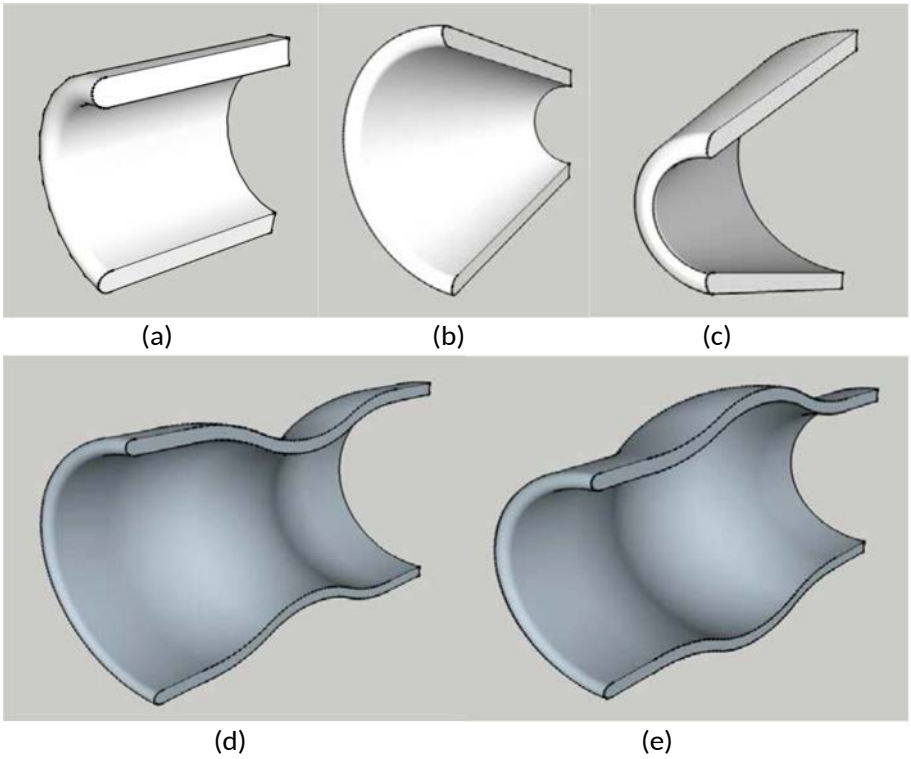

Figure 10.1: Ducts with varying cross-section: (a) Cylindrical (b) Converging (c) Diverging (d) Converging-Diverging (e) Diverging-Converging

Two intake ducts with the same fan installed but with different inlet contours will inevitably produce different sound levels at the termination of the duct after sound propagation through the inlet. The axial flow speeds directly influence a number of quantities. Owing to the fact the the flow in contrary to the direction of propagation, the higher the flow speeds, the higher more negative convective effect on the pressure waveform and may result in a longer propagation time within the duct. As the pressure field generated by a supersonic fan propagates in a helical path, which can be likened to a spring, for a duct with a fixed radius (figure 10.1(a)), a higher flow speed implies a tighter coil. The higher flow speed will act to compress the spring and allows more coils within a fixed axial distance. In the same way, a lower flow speed will translate to more spaced-out coils resulting in a shorter length when the spring is stretched out. Various levels of compression or expansion will be observed if the same analogy is used for different ducts such as illustrated in figure 10.1(b)-(e).

10.2 Real Flows and the Boundary Layer

The knowledge of the flow speed at every point within the aircraft inlet is useful for a more precise prediction of the propagation of the rotor-locked pressure field. With this knowledge, the interaction of the pressure field as it travels along its helical path through the inlet against the incoming flow can be better represented. Depending on the inlet contour and overall design of the aircraft intake, the flow around the duct is described. The amount of mass flow the fan achieves together with the inlet geometry dictate the levels of the flow speeds obtainable in various regions in the duct.

In the previous chapters, the focus has been on a cylindrical duct with constant cross-sectional area. In this case, the flow was assumed to be a plug flow with no radial variations. In reality, there is variation in the radial direction and notably a boundary layer where the the velocity varies from the mean flow freestream velocity to zero velocity at the wall. This is contrary to uniform flow where the flow is kept constant everywhere in the duct. Prior to investigating propagation through real flow profiles in axisymmetric ducts, one-dimensional flows were investigated. This study allows the appreciation of the extent of the effect of variation in flow speed.

10.2.1 Nozzle flow approximation

In the cylindrical duct, the flow was simplified to a uniform flow. For an axisymmetric duct, the flow can be simplified by the assumption that the flow varies only along the duct axis, and that the variation is primarily only influenced by the change in cross sectional area. This assumption reduces the complexity of the incoming flow to one-dimensional nozzle flow. Although this is not the case in reality, it was useful for the investigation of variation in flow speed on propagation of the system of shock waves generated at the fan.

From the continuity equation, we have that for two points z_1 and z_2 along the duct axis separated by a distance dz, the variation from z_1 to z_2 can be written as

$$\rho_1 A_1 v_1 = \rho_2 A_2 v_2, \tag{10.1}$$

where the variation of the density ρ, cross-sectional area A and the velocity v are $d\rho$, dA and dV respectively, that is,

$$\rho A v = (\rho + d\rho)(A + dA)(v + dv). \tag{10.2}$$

On differentiating

$$\frac{dv}{v} + \frac{dA}{A} + \frac{d\rho}{\rho} = 0. \tag{10.3}$$

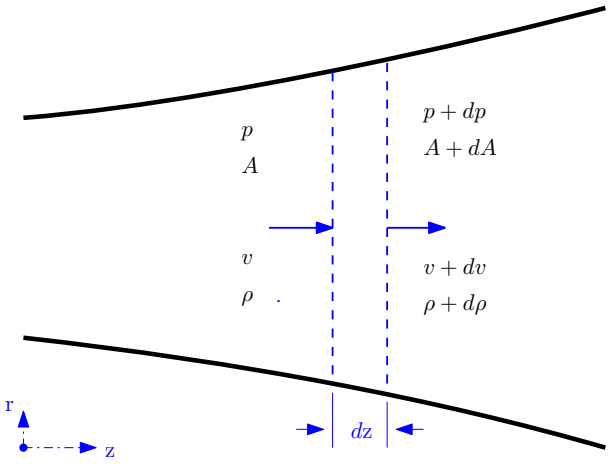

Figure 10.2: Nozzle flow

Figure 10.2 shows a nozzle with a subsonic flow. The flow is taken to be steady, uniform and isentropic. If the conduit is expanding, the flow is decelerating whereas a converging conduit will imply the flow is accelerating. Using the continuity equation and energy equation for an isentropic flow, we obtain

$$\frac{dv}{v}(M^2 - 1) = \frac{dA}{A}, \tag{10.4}$$

which allows for the changes in the flow Mach number to be related to the change in the cross-sectional area. This approximation does not represent the reality in intake duct but it is useful for study purposes as discussed later in section 10.4.

10.2.2 Non-uniform flow

In reality, the flow in aircraft intakes will be fully developed with a boundary layer at the walls, and various flow regimes in the axial direction [96, 97]. Studies on flow in ducts, particularly aircraft intakes[98], show that the flow speed varies from the fan face to the duct lip, and there is an over-speed region close to the duct lip. This is a result of the converging of the the streamlines as the flow turns into the aircraft intake. The mean flow levels in the aircraft intake can be even more varied if there is ingestion of any form of turbulence, at high angle of attack and with particular intake designs such as a drooped configurations [99]. All these features of the incoming flow result in a very complex inflow into the aircraft intake, making all regions seemingly unique in their flow characteristics.

10.3 Acoustic Liner

As mentioned in the previous section, the flow in an aircraft intake is non-uniform and could include varying levels of turbulence[98, 100]. The non-uniform mean flow will be taken to be axisymmetric in an axisymmetric intake. Owing to the change in the radius along the duct axis, and the consequent change in flow speed at the wall, it is expected that the attenuation rates owing to absorption by the installed acoustic liner will also vary along the direction of the duct axis. Also, critically the increase or decrease in the boundary layer thickness will impact on the level of attenuation the acoustic liners can achieve due to the shielding effect of the boundary layer[18, 101, 102].

At a particular radius, a thicker boundary layer over the acoustic liner results in more refraction away from the liner thereby causing a lower attenuation rate compared to the decay rate with a thinner boundary layer. These effects of boundary layer thickness on liner attenuation are an addition to the changes to the modes propagating in the duct which the variation in duct radius would have caused. These coupled effects, a simplification of the real case, of impact of the variation in duct cross section and boundary layer thickness on the liner attenuation, give a hint of the complexities in reality and an appreciation of the difficulty in the prediction of such propagation.

10.4 Geometry effects

The variation in internal geometry of a duct may have significant effects on the propagation of a pressure field within that duct. Variation in geometry is not isolated as it results in a consequent variation in flow and can considerably affect the effectiveness of installed acoustic liners as well. In a duct without flow, various studies[23, 103, 104] suggest that a change in geometry can cause significant changes in sound propagation of the pressure field. This is directly due to the continuous interaction between the propagated sound field and any guides, surfaces or enclosures within which the sound field is propagating.

In aircraft intakes at supersonic relative tip speeds, the shock waves travel in a helical path adjacent to the intake duct wall. The helical path follows the variations in the contour of the duct wall, and as the cross-sectional area changes, the helical path changes as well, giving rise to a longer or shorter time of flight for the spiralling pressure field. Thus, for an intake ducts with variation of internal geometry along the duct axis, there are essentially two variations that may occur in the duct. The first variation occurs when the radius of the duct reduces with respect to axial distance, and, the second when the duct radius increases along the axis. Realistic aircraft intakes have intake wall geometries that are a combination of convergent and divergent regions, and may also have regions with constant cross-sectional area. The effects of these two types of intake

geometry variation on nonlinear propagation are discussed separately in sections 10.4.1 and 10.4.2, with a focus on the changes in flow speed, and resultant changes in results of nonlinear propagation.

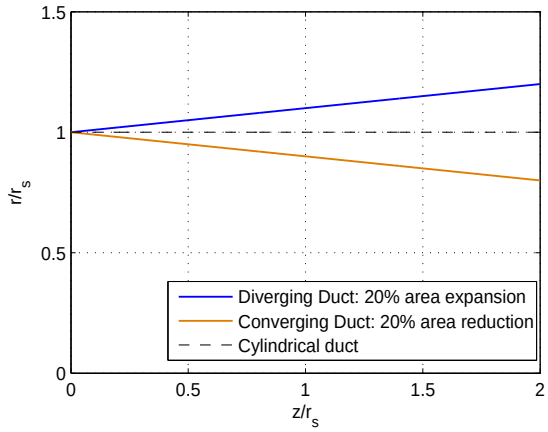

Figure 10.3: Variation of duct radius compared to constant area duct

Figure 10.3 shows the extents of the variations used in this study. All the duct have the same starting parameters at $z = 0$. The converging ducts vary by the extent of the reduction in their areas at the duct lip. The area reduction varies from 1% to 20% of the area at $z = 0$. For the diverging ducts, the area expands with increasing z and the expansion varies from 1% to 20% of the area at $z = 0$. The same reduction and expansion ranges are used for the converging-diverging and the diverging-converging ducts but unlike the linear gradient on the converging and diverging ducts, a cosine function smoothing is applied to the avoid unrealistic abrupt changes in internal geometry of the converging-diverging and the diverging-converging ducts. Taking the radius of the duct at $z = 0$ to be r_s, the radius of the converging-diverging and the diverging-converging ducts are generated by

$$r(z) = r_s \quad \forall\ 0 \leq \frac{z}{r_s} < 0.1 \text{ and } 1.9 < z/r_s \leq 2$$
$$r(z) = r_s \pm \frac{a_s r_s}{2}\left\{\cos\left[\frac{\pi}{0.9}\left(\frac{z}{r_s} - 0.1\right)\right] - 1\right\} \quad \forall\ 0.1 \leq z/r_s \leq 1.9$$

where a_s is the percentage reduction or expansion as a ratio of 100.

10.4.1 Converging ducts

Consider a duct with radius r reducing as axial distance z increases as shown in figure 10.1(b), with the conditions at the fan plane ($z = 0$) known. As z increases upstream, the flow conditions change. Assuming an axial flow with flow speed dictated only by

the changes in the duct radius, the flow speed observed increases as the axial distance increases. The flow speed variation will scale with the gradient of the inlet geometry.

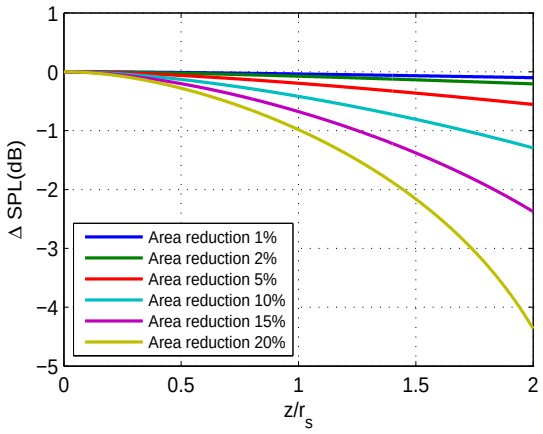

Figure 10.4: Difference in attenuation of rigid converging duct compared to rigid constant area duct

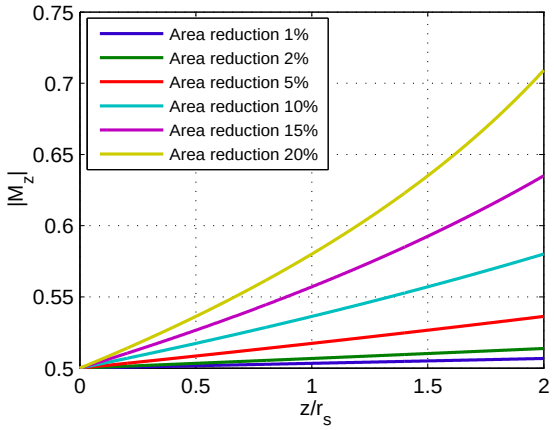

Figure 10.5: Axial Mach number for the converging ducts

To see the effect of this simple inlet geometry variation, we considered a series of converging ducts with different duct-end area reductions with respect to the area at $z = 0$. With all the necessary parameters of geometry and flow known at $z = 0$, the propagation of a regular sawtooth was carried out. The difference between the BPF tone attenuation and that of a cylindrical duct having the same parameters at $z = 0$ is shown in figure 10.4. The flow Mach number for the ducts is plotted against duct axis distance normalized with the radius, r_s, at $z = 0$, in figure 10.5. From these two figures it is observable that the nonlinear attenuation is higher for larger area reductions due to the higher flow speeds which have resulted in more nonlinear decay. An extra 4.4dB attenuation was observed for the propagation of a regular sawtooth up to a distance equal to the initial diameter of the duct. A considerably higher attenuation is expected for an

irregular sawtooth due to more pronounced nonlinear effects and energy transfer among the various frequencies.

An appreciation of the time it takes the pressure field from the start of the duct to the end can be seen in the time of flight shown in figure 10.6. Although the radius of the duct reduces as the cross sectional area of the duct end is reduced, the increase in the inflow Mach number, owing to the area reduction increases the overall propagation time the pressure field in the duct.

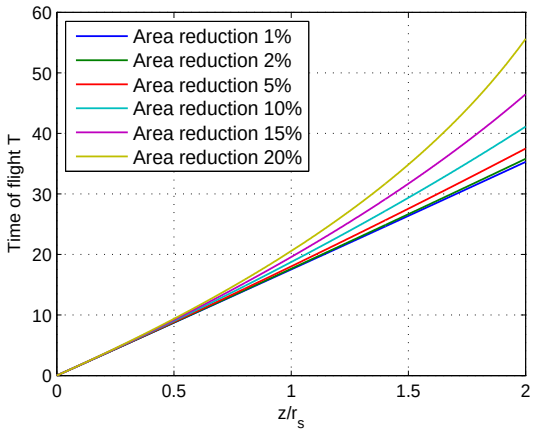

Figure 10.6: Time of flight for various converging ducts

A simple case of the combined effect of geometry variation and liner attenuation can be constructed. Consider a cylindrical duct lined entirely on the internal surface and propagating a regular sawtooth in the duct for a range of fixed liner decay rates σ_B 0.001 to 0.1 for the BPF tone. The effect of the liner can be isolated by finding the difference in BPF attenuation in the lined and the rigid ducts as shown in figure 10.7. In this figure, for various liner decay values, it is observed that additional attenuation can be provided by the liner to varying levels from an almost insignificant amount (as in $\sigma_B = 0.001$) to considerably more than the nonlinear attenuation as with the result for $\sigma_B = 0.1$.

The change in geometry translates into a change in the time the pressure field spends propagating in the duct. For the converging duct being considered, the increase in time of flight also impacts on the liner attenuation as the increase in the time of flight implies that the pressure field has more time to interact with the liner resulting in more attenuation in the lined duct as seen in figure 10.8. This figure, which is the result for liner decay $\sigma_B = 0.1$, shows that for this case, an additional attenuation of up to about 35dB was achieved for a cross sectional area reduction of 20% over a lined cylindrical duct. And checking the difference in attenuation against the rigid cylindrical duct yields figure 10.9, showing a variation of about 27 to 62dB more attenuation for

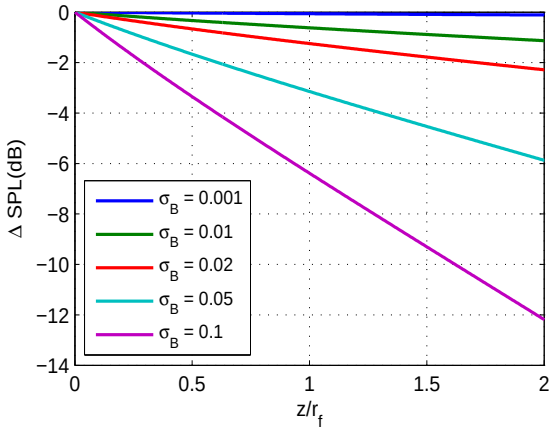

Figure 10.7: Cylindrical duct with variations in BPF tone attenuation

various converging ducts, for propagation of a regular sawtooth over a length equal to the initial diameter of the duct.

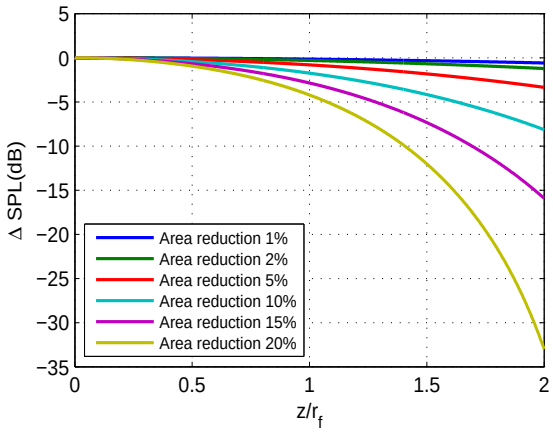

Figure 10.8: Difference in BPF tone attenuation of lined converging duct compared to lined constant area duct

10.4.2 Diverging ducts

Another variation that occurs is an increase of the duct radius along the duct axis. A number of diverging ducts with area increase of 1% to 20% were studied, and the effect of the duct variation is shown in the figures 10.10-10.13. Figure 10.10 shows the various BPF tone attenuation plots for the diverging ducts. Unlike the results for the converging ducts in the previous section, it is observed that the diverging ducts reduce the nonlinear attenuation suffered by the pressure field propagating in the duct. This is due to the reduction in the time of flight (see figure 10.11), of the pressure field as the area increases and inflow speed decreases (see figure 10.12), resulting in reduced nonlinear attenuation.

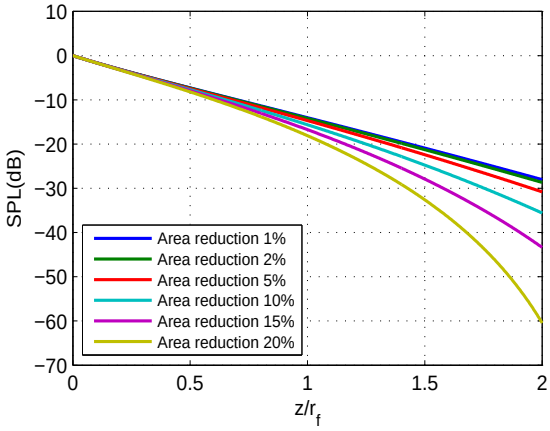

Figure 10.9: Difference in attenuation of the BPF tone for lined converging ducts with variations in throat contraction compared to a rigid constant area duct

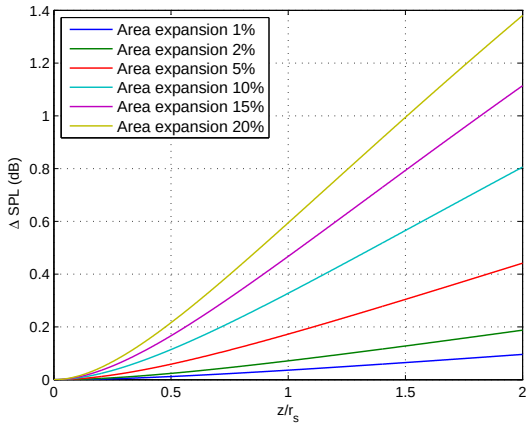

Figure 10.10: Difference in BPF tone attenuation of diverging duct compared to constant area duct

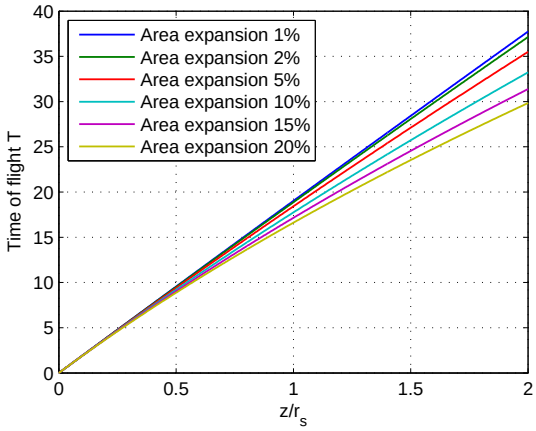

Figure 10.11: Time of flight for various diverging ducts

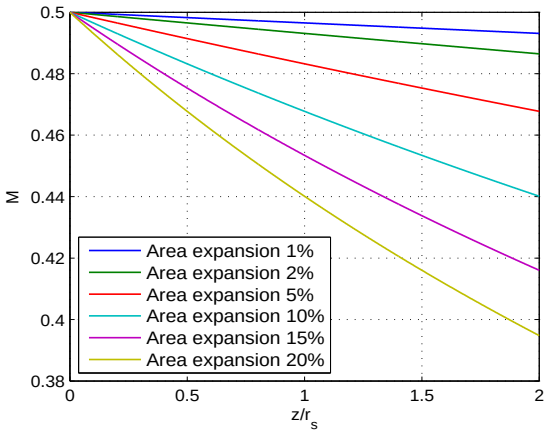

Figure 10.12: Mach number variations for various diverging ducts

For the range of area expansions 1% to 20%, only about 1.4dB difference is seen compared with the cylindrical duct. This illustrates that there is not a very strong effect on the divergence of the duct. The Mach number reduces by about only 20% of the initial value for the highest expansion area. Since this variation in Mach number drives the time of flight, it is observed from figure 10.11 that the time of flight dropped only to 30 for the 20% expansion from about 37 for the 1% expansion. Using a similar process to the lined converging duct, fixed BPF tone liner decay was applied to the propagation of a regular sawtooth. Figure 10.13 indicates the difference in SPL values compared to a lined cylindrical duct. With the liner, the impact of the reduction of time of flight by the increased divergence in cross sectional area of the duct is more pronounced. The duct with 20% expansion now has about $8dB$ has higher sound level of the BPF tone than cylindrical duct owing to the shorter time the pressure field spends in the duct.

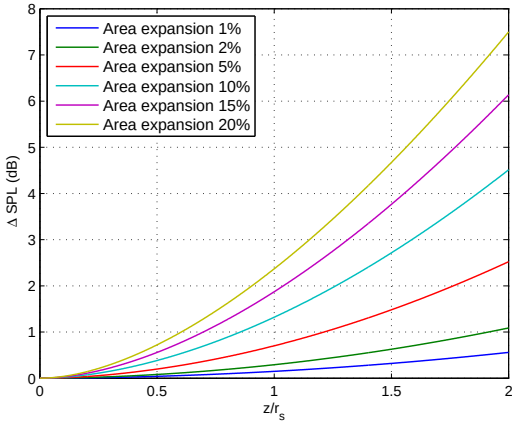

Figure 10.13: Difference in BPF tone attenuation of lined diverging duct compared to lined constant area duct

10.4.3 A Note on Converging and Diverging Ducts

A notable observation is that for the same percentage area reduction or expansion for the converging or diverging ducts, the effect of the change in geometry is more pronounced in the converging duct. The reduction in nonlinear attenuation in the diverging duct is not the same value as the increase in nonlinear attenuation in the corresponding converging duct. The Mach number considerably increases in the converging duct with a change up to about 44% from the starting value more than double the change observed for the diverging duct having the same parameters at the start of the duct. This is reflected as well in the plots of time of flight variations.

10.4.4 Converging-Diverging and Diverging-Converging Ducts

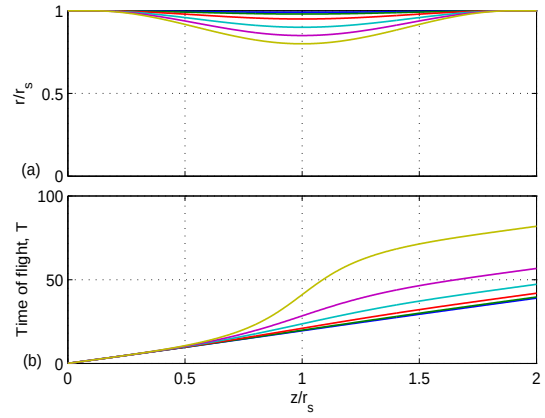

Figure 10.14: Converging-diverging ducts (a) radius variation (b) time of flight variation

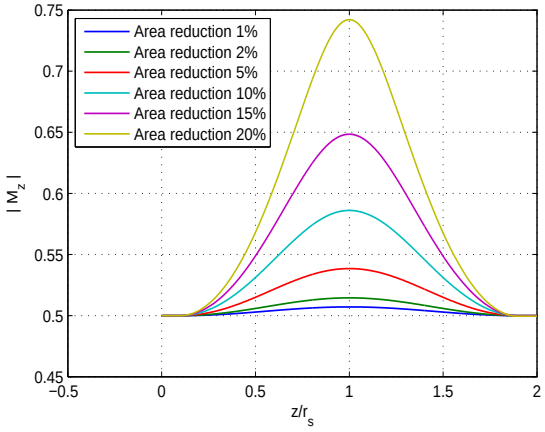

Figure 10.15: Mach number variations for various converging-diverging ducts

To further explore the effects of geometry and flow changes, regular sawtooth waveform simulations were performed in ducts with both converging and diverging sections. Owing to the observations of the significant differences between the effects of converging and diverging ducts, two model ducts were investigated; one starting with a converging section and the other starting with a diverging section. A series of throat contraction and expansions from 1% to 20% of the initial duct cross-sectional area were used.

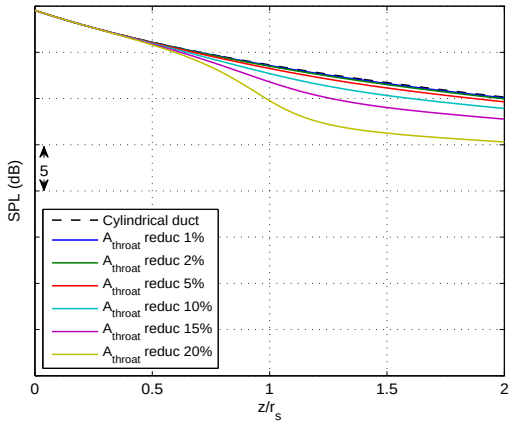

Figure 10.16: Regular sawtooth BPF tone attenuation in a rigid Converging-Diverging ducts with variations in throat contraction

For the converging-diverging duct, the variation of the duct geometry and time of flight over the whole length of propagation is shown in figure 10.14(a) and (b). As the propagation advanced along the duct axis, there is a short cylindrical section then the radius reduces in the converging section of the duct. In this converging section, the rate of change of the time of flight is observed to increase. As the end of the converging section is reached, this steep gradient reduces as the diverging section of the duct begins and continues so until the end of propagation. The flow Mach numbers along the duct wall for the converging-diverging ducts for the various throat reductions are shown in figure 10.15.

For this idealized case, the flow speed increases up to the throat and decreases back to the starting level over the diverging section. This example gives an insight into what is expected where there are convergent and divergent section in a typical aircraft engine intake. Although the flow speed will be very different from the uniform plug flow assumption, convergent sections will act to give more time of flight to the pressure field, whereas divergent sections appear to shorten the total propagation time when compared to the duration in a cylindrical duct. The effect of these changes in geometry can be seen in the attenuation of the BPF tone for the rigid wall case in figure 10.16 and the lined wall duct in figure 10.17. In the rigid wall case, there is no significant difference up to about 5% area reduction when compared to the cylindrical duct. Higher area reductions showed differences up to 5dB for the 20% area reduction. The differences between the

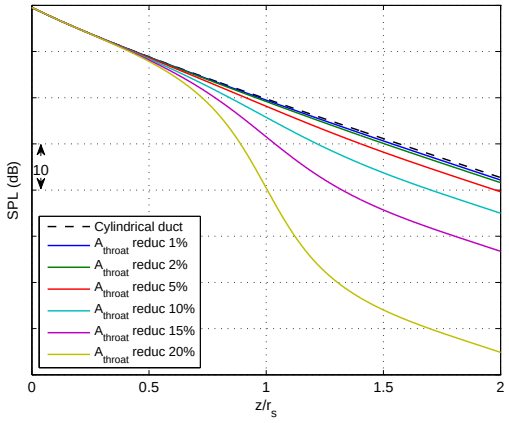

Figure 10.17: Regular sawtooth BPF tone attenuation in a lined Converging-Diverging ducts with variations in throat contraction

converging-diverging ducts and the cylindrical ducts are significantly more, up to $35dB$ for the 20% area reduction, for the lined case where the BPF tone decay σ_B was set equal to 0.1.

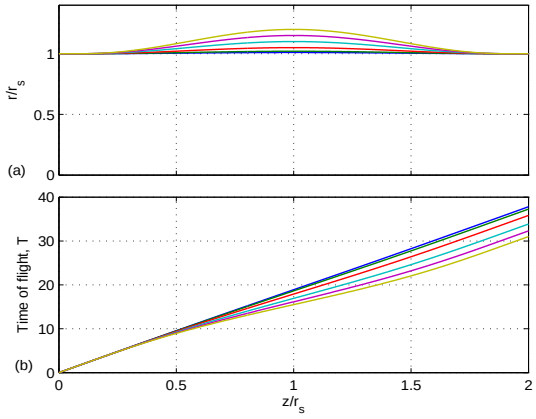

Figure 10.18: Diverging-converging ducts (a) radius variation (b) time of flight variation

The variation of geometry and corresponding changes in the time of flight along the duct axis are shown for the diverging-converging ducts in figure 10.18. The variations in this duct configuration are not as pronounced as the converging-diverging duct owing to the divergent section yielding values not very dissimilar to the cylindrical duct. By the time the converging section of the duct begins, the sawtooth has been significantly attenuated leaving the variations observed within the converging region much less than would be observed if the converging section was closer to the start. This is also evident in the flow mach number plots (see figure 10.19). With this arrangement the BPF tone attenuation for the rigid wall case (see figure 10.20) is similar to that for the rigid

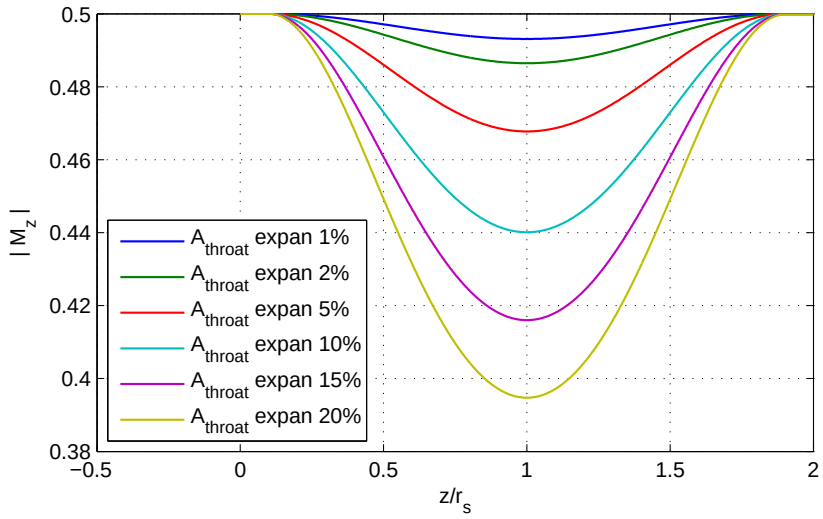

Figure 10.19: Mach number variations for various diverging ducts

cylindrical duct with less than 2dB difference at a distance twice the starting radius for a 20% area expansion. The lined wall case (see figure 10.21) affords a clearer look at how the attenuation of the BPF tone progresses. The gradient is lower and attenuation progresses slow up to about an axial distance equal to one radius, from this point where the converging section begins and forwards, the gradient steepens as the converging section drives the flow speed higher, which allows for longer time for the sawtooth to decay by nonlinear attenuation and liner absorption.

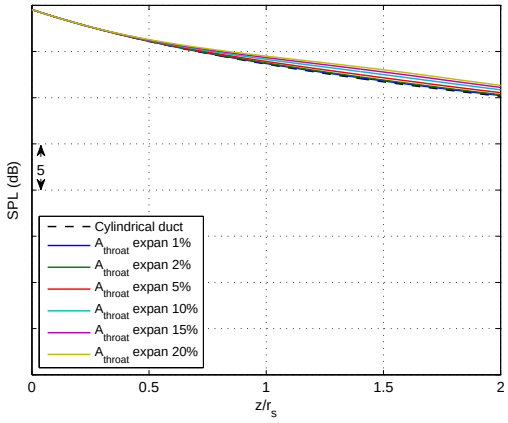

Figure 10.20: Regular sawtooth BPF tone attenuation in a rigid Diverging-Converging ducts with variations in throat contraction

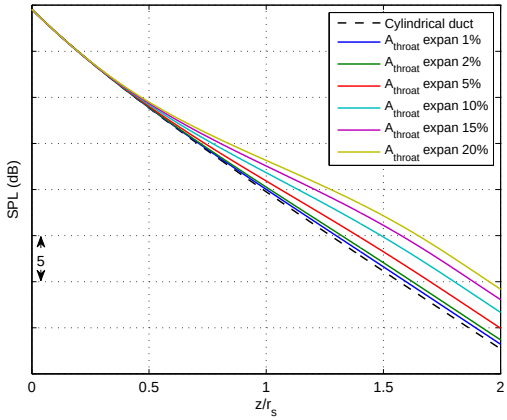

Figure 10.21: Regular sawtooth BPF tone attenuation in a lined Converging ducts with variations in throat contraction

10.5 Propagation effects

10.5.1 Significance of Geometry and Flow effects

A considerable amount of insight into the nature of nonlinear propagation of the pressure field generated at supersonic relative fan speeds in ducts with varying inlet geometry can be drawn from the investigations on the converging, diverging, converging-diverging and diverging-converging ducts. With a change in cross sectional area, there is a change in the flow speed. This change in flow speed acts to reduce or increase the time of flight of the pressure field in the duct, being mindful of the fact that the flow is in the direction against the direction of propagation. The increase or decrease in the time of flight implies the pressure field may be attenuated more or less than otherwise in a cylindrical duct. This effect can be significant in rigid wall ducts and even more so in lined wall ducts because the change in time of flight also impacts on the total amount of liner absorption over the propagation distance.

The changes in duct geometry can be translated as effectively a change in the time of flight for every step of propagation. In reality, the variation in flow speed along the internal wall is much more varied than one-dimensional nozzle flow assumption implies. This fact implies that the effects on the propagation may be more pronounced. The possibility of reaching higher or lower flow speeds in realistic aircraft intake ducts, depending on the gradient of the variation in the inlet geometry, suggest that incorporation of geometry and flow effects into the prediction models will be very important to achieving more realistic prediction.

10.5.1.1 Time of Flight and Equivalent Cylindrical Ducts

As it has been established that the change in geometry and flow result in a change in time of flight in the propagation, a question may be asked, 'is there an equivalent cylindrical duct for an axisymmetric duct with varying duct radius?'. The total time of flight for a duct with varying radius can be calculated, and for a constant radius cylindrical duct, its length can be adjusted to give the same time of flight. The propagation with the same start conditions can be evaluated using the equation for the nonlinear sawtooth propagation model presented in previous chapters and the equations in chapter 9.

10.5.2 Rigid duct with varying radius and its equivalent cylindrical duct

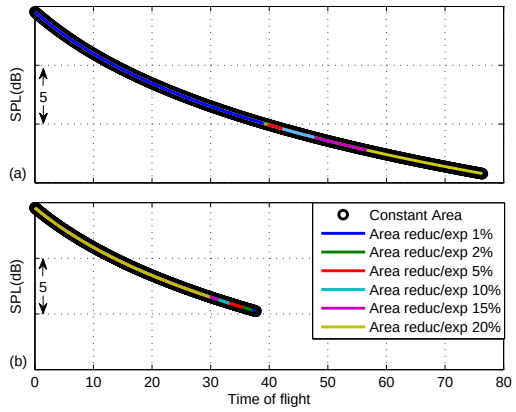

Figure 10.22: Equivalent cylindrical duct for (a) converging ducts (b) diverging ducts

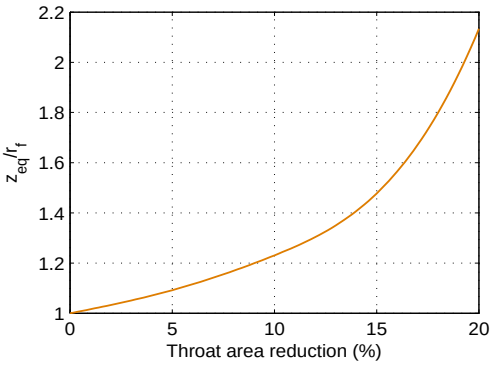

Figure 10.23: Trend line for equivalent length of cylindrical duct for converging ducts

In order to further appreciate how the effects of varying intake geometry result in time of flight changes, the BPF tone attenuation for converging ducts of different end area

Table 10.1: Equivalent Cylindrical duct for various converging ducts

Area Reduction (%)	Equivalent length of Cylindrical duct (normalised with radius)
1.0000	1.0159
2.0000	1.0329
5.0000	1.0918
10.0000	1.2306
15.0000	1.4774
20.0000	2.1336

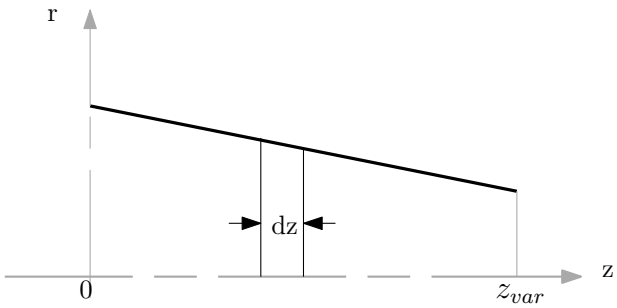

Figure 10.24: Evaluating the time of flight over small axial steps dz

reductions are shown in figure 10.22(a). In the figure, the SPL is plotted against the time of flight for rigid wall cases. The otherwise different nonlinear attenuation curves for the different ducts have collapsed to the same curve when plotted against the time of flight with the throat reductions showing up exclusively as different lengths of propagation. This case points out that, although the ducts are different one from another, the differences in geometry are actually equivalent to different times of propagation. This is consistent with the propagation in cylindrical ducts, which in the figure have been carried out up to the time of flight of the duct with the highest area reduction. Also, it is important to point out that the higher the reductions in area, the lengthier the time of flight; an agreement with earlier figures. The equivalent length of cylindrical duct for various converging duct are plotted in figure 10.23. Table 10.1 shows the normalized cylindrical duct length of the area reductions used in the study.

The length of an equivalent cylindrical duct can be found as

$$z_{cyl} = \frac{T_{var} D_{cyl}}{K_{cyl}} \tag{10.5}$$

where T_{var} is the time of flight in a varying duct, D_{cyl} is the diameter of the cylinder and K_{cyl} is the constant for the cylinder as evaluated from equation 3.26. While T_{var}

can are evaluated as a summation with respect to the variation in the cross section of the duct (see figure 10.24) to be matched as

$$T_{var} = \sum_{0}^{z_{var}} \frac{K_{var}(z)}{D_{var}(z)} dz \tag{10.6}$$

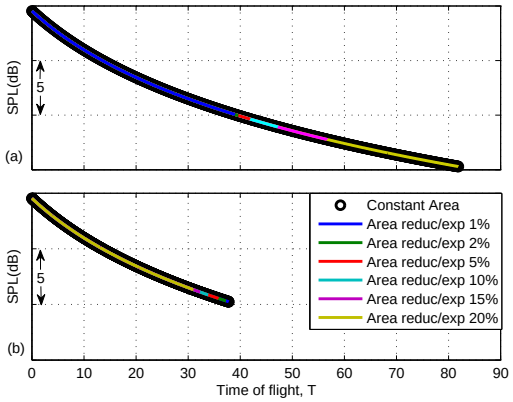

Figure 10.25: Equivalent cylindrical duct for (a) converging ducts (b) diverging ducts

Similar observations were made for the diverging (figure 10.22(b)), converging-diverging and the diverging-converging ducts (figure 10.25(a)-(b) respectively). All the nonlinear attenuation curves can be traced using a cylindrical duct with the same starting parameters and the required time of flight equal equivalent to that for each duct.

10.5.3 Lined duct with varying radius and its equivalent cylindrical duct

The study of the equivalent cylindrical duct was extended to lined ducts with a fixed attenuation rate for the BPF tone. In agreement with the results and observations for the rigid wall cases, all the ducts (converging, diverging, converging-diverging and diverging-converging) can be represented by an equivalent cylindrical duct, based on propagations for a respective time of flight. An example of this is shown in figure 10.26 for lined converging ducts. The results for the lined cases are consistent with the findings for the rigid case.

In a realistic aircraft intake typically there are rigid wall regions adjacent to both ends of the lined section. An extension of the study to part-lined ducts shows that an equivalent cylindrical duct can be used to represent a part-lined duct as long as the liner is applied starting at the same time of flight and over the same range of time of flight as in the duct with varying radius. The time of flight at the start and end of the lined area and

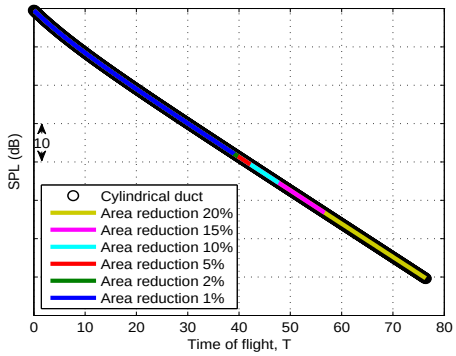

Figure 10.26: Trend line for equivalent length of cylindrical duct for converging ducts

the total time of flight together with the all flow and geometry parameters at the start of propagation form a sufficient set of values to determine an equivalent cylindrical duct. Using this method, equivalent cylindrical ducts are evaluated for different converging ducts (figure 10.27), diverging ducts (figure 10.28), converging-diverging ducts (figure 10.29) and diverging-converging ducts (figure 10.30). All these ducts have a lined section inbetween two rigid sections.

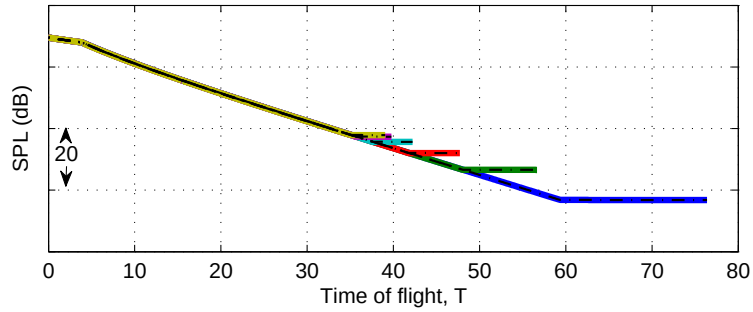

Figure 10.27: Equivalent cylindrical duct (- - -) for converging ducts (——)

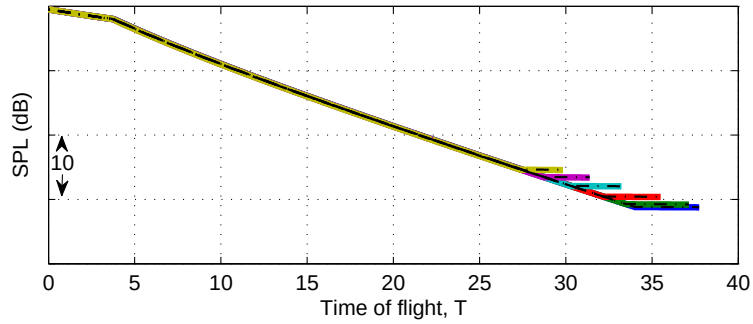

Figure 10.28: Equivalent cylindrical duct (- - -) for diverging ducts (——)

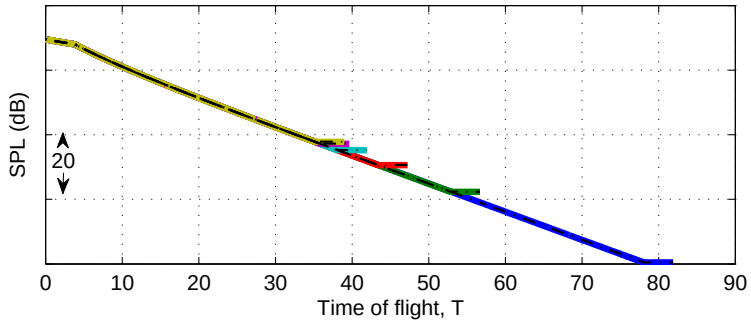

Figure 10.29: Equivalent cylindrical duct (- - -) for converging-diverging ducts (——)

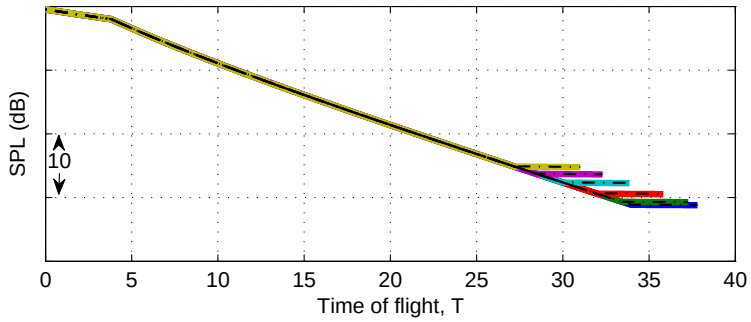

Figure 10.30: Equivalent cylindrical duct (- - -) for diverging-converging ducts (——)

10.6 Summary

An investigation of the propagation of sawtooth waveforms in axisymmetric ducts with varying radius has shown the effect of the geometry changes on flow speed and the consequent effect on the time of flight of propagation. The converging regions increase the flow speeds while the diverging regions reduce the flow speeds. The increase or reduction in flow speeds result in an increase or decrease in the effective time the waveform spends spiralling in the duct before it is radiated (referred to by the time of flight). With the inclusion of the liner, an increase or decrease in the time of flight can be more significant as there is a combined effect of the attenuation by the nonlinear distortion of the shock waves and the absorption provided by the acoustic liner. This suggests that the amount of attenuation of buzz-saw noise in an aircraft intake could be influenced by the careful design of the intake duct geometry, albiet changes to the intake also would affect the aerodynamics, fan pressure ratio, and may also other operation and performance factors.

Chapter 11

Advanced Supersonic Fan Noise Model

11.1 Overview of the Advanced Model

Throughout the previous chapters, different aspects of prediction of supersonic fan noise have been presented. A step-by-step advancement approach has been undertaken with the addition of various features to develop a prediction model which is more representative of the real situation. The time-frequency domain model in chapter 6 has been improved by the incorporation of variation of the duct radius for axisymmetric intakes. This improvement also incorporated the variation in flow speeds and acoustic liner decay rates with axial distance. In order put together these improvements to the model, a new layout for the time-frequency domain model is presented.

For an axisymmetric intake the geometry and flow parameters such as duct radius or diameter, flow speed are all a function of the axial direction of propagation z. All variables dependent on them; tangential and relative tip Mach numbers, time of flight and other variables of nonlinear propagation, vary with z. Owing to axial variations, the inputs to the propagation model were changed to include the internal duct geometry, a more representative mean flow profile, and non-constant acoustic liner decay rates along the span of the liner.

In order to keep the structure of the time-frequency domain model, these three parameters will be permitted to vary in the direction of propagation are evaluated at an initial stage prior to the commencement of the propagation simulation. Also, this decision was spurred by the availability of various other platforms or models for evaluation of the mean flow in ducts and the acoustic liner decay rates. Moreover, this fits the aim to make a much faster and less computational expensive model for prediction of supersonic fan noise as opposed to the fully numerical computation models.

The mean flow calculations were carried out using the finite element code COMSOL while the liner decay rates were evaluated by an duct mode code used in the Institute of Sound and Vibrations Research (ISVR) written by Dr. Alan McAlpine. The entire structure of the advanced supersonic fan noise model is illustrated in figure 11.1

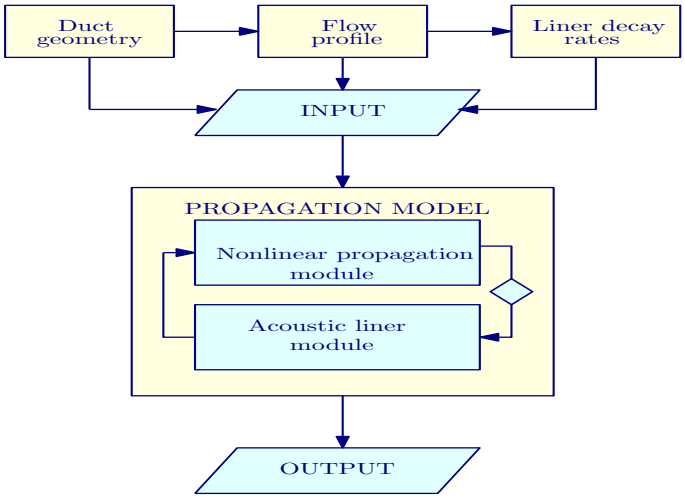

Figure 11.1: Illustration of structure of the advanced supersonic fan noise model

Equations (6.7) and (6.8) still describe the distortion of the waveform for every step propagation step, but the parameter K in (3.26) now varies along the duct axis for each step, owing to the variation of the duct radius and axial, tangential and relative Mach numbers along the duct axis.

11.2 Axisymmetric Ducts

Propagation using the advanced supersonic fan noise model focuses on axisymmetric ducts. The model is developed to predict the buzz-saw noise propagation for ducts where the radius is solely a function of the distance along the duct axis. Any point along the axis, the cross-sectional area is described by the circumference of this radius.

The results of prediction for supersonic fan noise propagation that will be shown in this chapter are for two different axisymmetric ducts. Both ducts are models of aircraft inlet ducts. The first is the geometry of a 22inch radius flight inlet used in experimental work presented by Hodder [105]. Three different profiles were presented for this drooped aircraft intake; for the north side, south side and the east side. Here the east side geometry is rotated around the duct's axis forming a volume of revolution which provides an axisymmetric intake duct. The other inlet profile is the model-scale intake rig used in static tests already introduced in chapters 5 and 7 for validation of previous prediction models, and also found in the computational aeroacoustic studies in [106]. This rig intake geometry is proprietary information and only illustrations are shown. These two

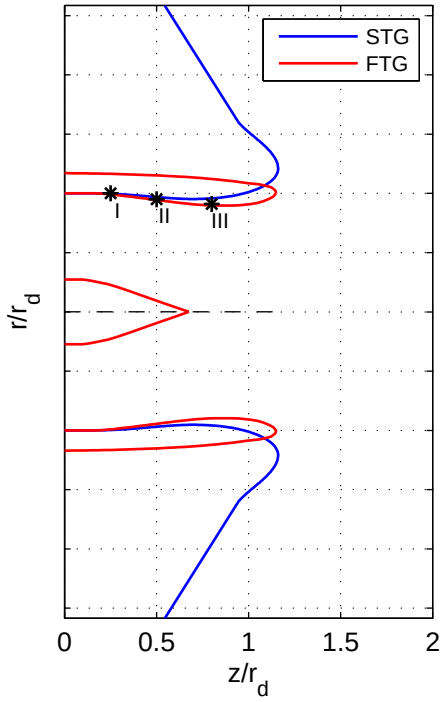

Figure 11.2: Static-test and flight-test Intakes Ducts

ducts have been scaled to have the same radius at the fan plane (start of propagation) and are referred to as flight-test-geometry (FTG) and static-test-geometry (STG) for easy identification. Figure 11.2 shows the two ducts on axis normalized with the radius r_d at $z = 0$. The main difference between these duct, apart from their different inner geometry, is that the static case STG has a mini-flare installed to tailor the inflow. These ducts enable the advanced model to be tested for both a flight and static test duct configuration. The points marked I, II and III are the stations for which waveform and spectrum results are shown.

11.3 Intake flow simulation

The non-uniform flow in the intake duct is taken to be axisymmetric. Flow profiles were generated for both the static test STG and flight test FTG configurations. The mean flow for these ducts was simulated using the compressible flow simulator in the duct flow package in COMSOL Multiphysics ® Modeling Software.

The compressible flow simulation in COMSOL is fairly straightforward to set up due to the easy-to-follow graphic user interface and hence, only a brief description of the set up is given (for details and equations see COMSOL documentation [107]). With an axisymmetric model environment set in COMSOL, the inner boundaries of the intake

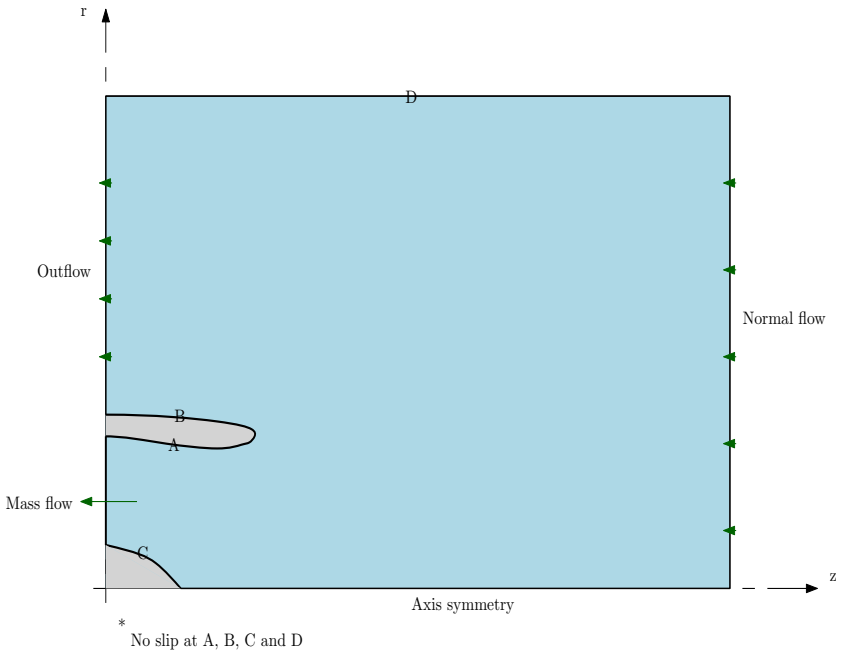

Figure 11.3: Flow simulation for an axisymmetric flight test duct: compressible flow domain

and an external flow domain are defined (as illustrated in figure 11.3 for the FTG). The appropriate surfaces are set as solid with appropriate wall conditions. It should be noted that as this is a duct flow package, boundaries were required to describe a finite volume for simulation. To mimic a far-field boundary and ensure both internal flow and external flow to the intake duct, a large domain space was defined. At the fan plane, a mass flow which gives the velocity required at the fan plane is defined using continuity equations. No slip wall conditions are imposed at the inner walls and over the spinner. The axisymmetric condition is defined along the centre-line (duct axis) and a normal flow with zero velocity potential is defined at the termination of the external domain added forward of the intake duct.

For the flight test case, an outflow is defined at the boundary of the external domain in-line with the fan plane. This is to give same effect for the flow over the outside of the aircraft nacelle in flight. Appropriate outflow conditions are set to match realistic flight measurements. For the static test case, a no-slip condition is imposed on this boundary to reflect the reality that the aircraft engine is enclosed within test space.

A fine mesh of triangular elements is defined for the mean flow simulations with finer resolution at regions where there is significant curvature in the geometry at the exit in order to capture the changes in the flow properly. Element size range was between 8.0×10^{-4} to about 5.0×10^{-2}m with a curvature factor of 0.25. The mesh generated for the simulation of the flow in the duct (figure 11.4) was set to have appropriate resolution of the simulation at curved surfaces. This setting allows for smaller elements in regions

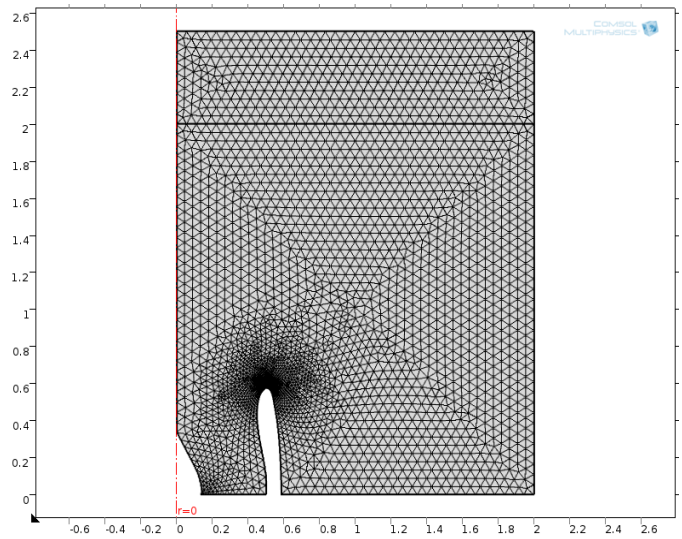

Figure 11.4: Flow simulation mesh for FTG

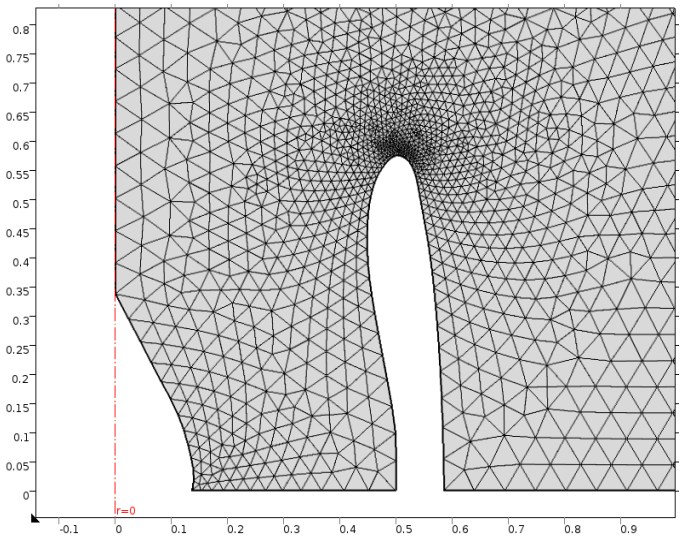

Figure 11.5: Flow simulation mesh for FTG: intake region

with curved surfaces in the intake duct region (figure 11.5), notably the duct lip (figure 11.6). The mesh for the STG is similar to these examples shown for the FTG.

The result of the simulation of the compressible flow in the intake duct is shown in figure 11.7. A closer look at the variation in flow Mach number in the intake duct can be seen in the zoomed in version in figure 11.8. A variation of about 0.4 is observed in flow Mach number at the wall from the fan plane to the duct lip. The region where the flow speeds up is observed close to the lip of the duct for this flight test configuration. This is consistent with observations from literature on CFD studies and measurements of flow in aircraft intakes [39, 98].

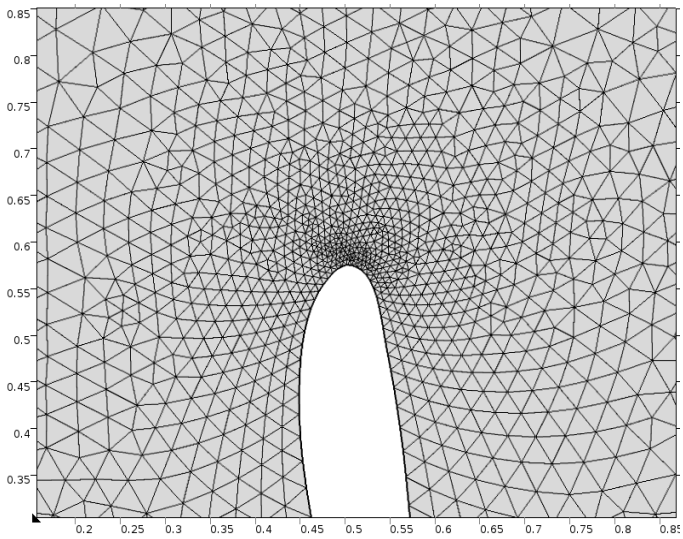

Figure 11.6: Flow simulation mesh for FTG: duct lip elements

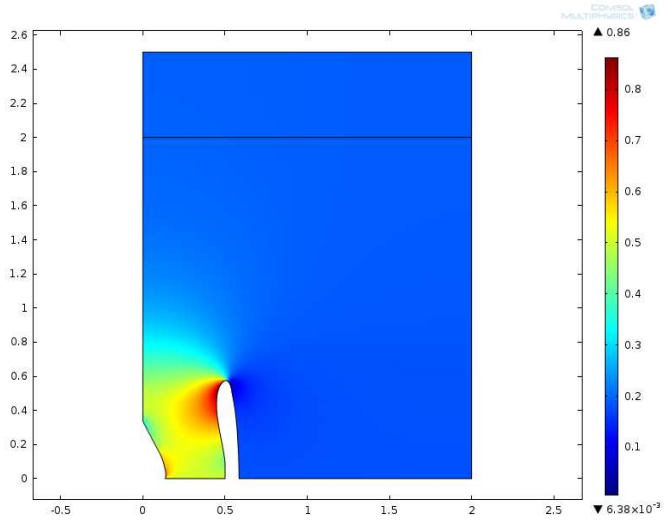

Figure 11.7: Mean flow in FTG duct

Similar procedure was carried out for the STG and the variation mean flow in and just outside the duct are shown in figure 11.9. Features seen for the FTG are present in the mean flow of the STG but with a smaller range in the variations. The flow at the duct lip are different owing to the flare at the entry of the STG.

The one dimensional sawtooth representation of the pressure field at the fan allows that the pressure field is concentrated at the wall without a shock span in the radial direction. Hence, the required flow speed values are those at the wall of the intake ducts. The flow velocity at the wall is extracted from the mean flow calculations by specifying to export the data along a specific boundary, in this case, the intake contour. COMSOL exports these values along the contour of the intake. Adjustments are made using the geometry

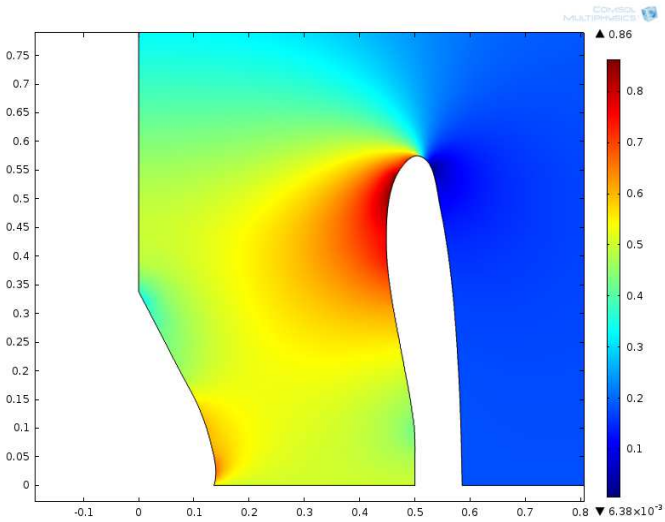

Figure 11.8: Mean flow in FTG: intake region

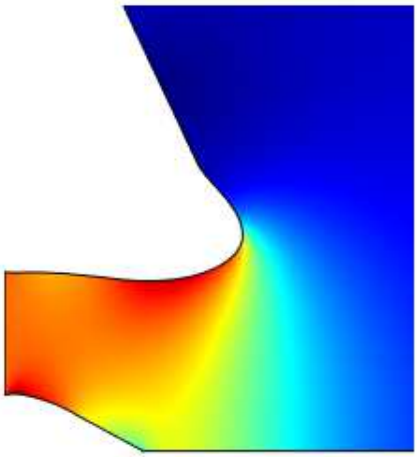

Figure 11.9: Mean flow distribution in STG: intake region [not to scale]

data to obtain the flow speeds with respect to the duct axis. These then form the input to the propagation model. The resultant wall flow speeds, normalized with the starting value, for the two ducts considered are shown in figure 11.10 for the entire length of the inner geometries of the ducts. The flow speed for the FTG first reduces in the initial diverging section and then increases as the duct then converges. The peak of the flow speed is seen at the region near the duct lip where there is a high-speed flow as it enters the duct. In the STG, the flare eases the flow into the duct and appears to spread out the region where the flow speeds up. The greater contour variations in the FTG achieves higher Mach number values, increasing by over 150% of the starting Mach number at an axial distance equal to the duct radius.

The result of flow simulations for the duct show much more features of flow development from the duct lip to the fan plane. The assumption of uniform flow in the study in the

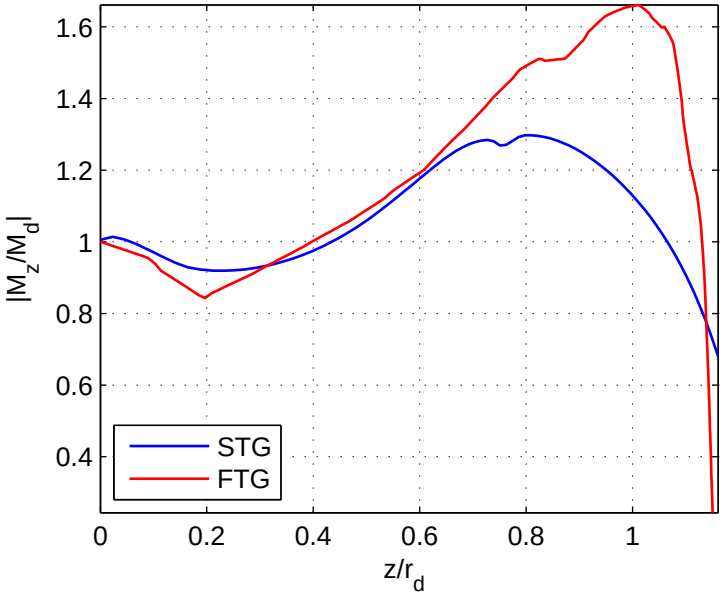

Figure 11.10: Static-test and flight-test Intakes Ducts

previous chapter, misses out on features such as the flow speed up region, but it did allow reduction of flow speed for regions where the radius is increasing and higher flow speeds where duct radius is reducing.

11.3.1 Acoustic Liner effects

The modeling of the nonlinear propagation of supersonic fan tones in aircraft intakes, although most often developed first with rigid wall ducts, is not complete without the incorporation of the installed acoustic liners. The addition of the acoustic liner was discussed in chapter 6. In this chapter, we look at the effects of variation in the modal attenuation rates predicted for the acoustic liner due to variations in the thickness of the boundary layer over the liner. A range of boundary layer thicknesses, δ, were studied from 0.0% to 10% of the radius of the duct. For a shear flow profile defined by the 7th power law,

$$\frac{\bar{u}}{U} = \left(1 - \frac{y}{r_d}\right)^{1/N_p}, \tag{11.1}$$

where $\bar{u}$, U, y and r_d are the mean velocity, free stream velocity, radial distance from the wall and duct radius respectively and $N_p = 7$, the corresponding displacement thickness, δ^* is given as

$$\delta = \frac{N_p + 1}{\delta^*}. \tag{11.2}$$

This results in displacement thicknesses in the range 0 to 1.25.

Table 11.1: Liner parameters for acoustic liner model

	BPF	1/2 BPF
Facing Sheet porosity	0.03	0.05
Liner depth (m)	0.0125	0.025
Mass reactance (m)	0.01	0.02

A linear liner model for axial flow of Mach number 0.5 was used. Two liners were considered; one tuned to have a maximum attenuation at about the BPF and the other tuned to have a maximum attenuation at half-BPF. The porosity of the facing sheet, σ, is set to achieve acoustic resistance within a target range, while keeping the optimum liner decay around the required frequencies (BPF or half-BPF). Acoustic reactance is the imaginary part of the acoustic impedance,

$$Z_a = R_a + i(km_r - cot(kh)) \tag{11.3}$$

where $R_a = 0.3M/\sigma$ is the resistance, k is the wave number, h is the liner depth and m_r is the mass reactance; defined as $m_r = (\varrho + \varepsilon d)/\sigma$. The quantities ϱ, ε and d are the thickness of the facing sheet, end correction and the diameter of each pore on the facing sheet [21, 51, 108]. An existing duct mode code (details not discussed here) based on the Pridmore-Brown equations, for lined annular ducts, is used to obtain the modal decay rates for the various boundary-layer thicknesses and liner impedance models. These liner modal decay rates are used in the simulation of propagation for boundary layers that are 0, 2, 4 ,6, 8 and 10 percent of the duct radius, and with respect to the variation in the radius along the duct axis.

For a duct of radius 0.5m, axial flow Mach number 0.5 and an installed fan with 20 blades, figures 11.11 and 11.12 show examples of the output of the liner modal decay rates (the imaginary part of the axial wavenumber) for the two liners optimized to BPF and to half-BPF. Table 11.1 shows the various parameters used in the characterization of the two liners. These plots are for the uniform (plug) flow for a cylindrical duct. In can be observed that the peak is at about EO20 or EO10 (BPF or half-BPF for these two cases). Also the resonance points for the liner can be observed at intervals. At antiresonance, in uniform flow, the reactance approaches zero and the liners provide no attenuation as they are acting like a rigid wall when this occurs[109–111]. These points of no absorption are not observed so clearly when there is a non-uniform flow with a boundary layer as these are smoothed out by the presence of of boundary layer as the absorption liner decay rates assymptote to zero with increase in frequency [108, 112–115].

Figure 11.13 shows the effect of boundary layer thickness on the level of decay rates obtained for the acoustic liner optimized for the BPF. For this liner optimized, in uniform flow conditions, to attenuate the BPF tone, the performance of the liner is seen to vary

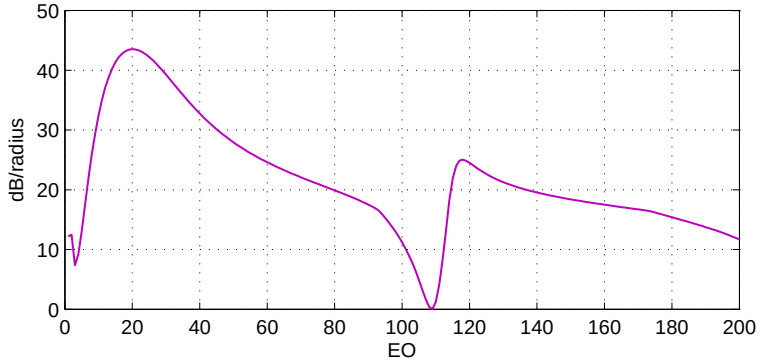

Figure 11.11: Acoustic liner optimized to attenuate BPF (EO20) tone

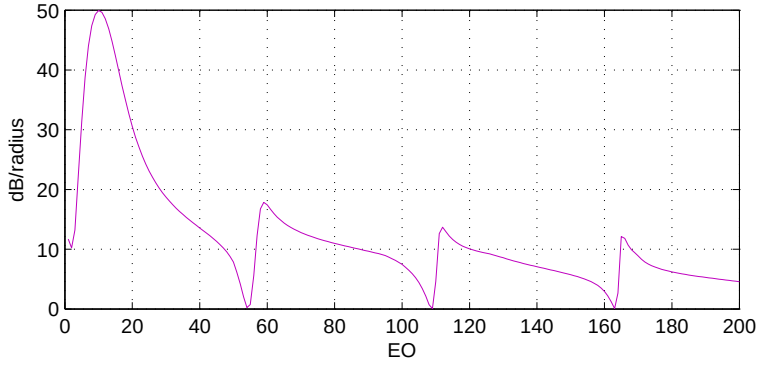

Figure 11.12: Acoustic liner optimized to attenuate half-BPF (EO10) tone

depending on the thickness of the boundary level over the liner. As the boundary layer thickens, the decay rates drop. Not only this but the peak attenuation moves away from the targeted EO to lower frequencies. This reduction in the decay rate values, and shift of the peak, is due to the refraction of sound away from the liner by the boundary layer[108, 108, 114, 115]. The refraction increases with increasing thickness of the boundary layer. The boundary layer can be said to be acting as a shield to the acoustic liner, reducing the incidence of the pressure field on the liner.

Hence, in order to satisfactorily predict the nonlinear propagation of the pressure field in lined intake ducts, it is necessary to have a good estimation of the thickness of the boundary layer at the wall, as this may significantly affect the prediction result. In reality, the boundary layer thickness will vary all along the duct inner contour. For example, the thickness of the boundary layer at the fan plane may be significantly different from that at the mid-regions and the duct lip. A good knowledge of the extent of the shielding which the boundary layer causes will enhance more accurate predictions. Measurements on aircraft intakes carried out on test beds, outdoor or indoor rigs and chambers mostly focus of the pressure and flow speed measurements. Although there exist studies on isolated liners with various types of flows[109, 111], it is not common to

see literature or reports on investigation into the boundary-layer thickness in real intake ducts, making this type of data for predictions unavailable. In section 10.5, the effects of the variation in boundary-layer thickness on the propagation results is shown and discussed.

From figure 11.13, it can also be seen than there is significant reduction in the decay rates at higher frequencies when a boundary layer is present. As the boundary layer was increased from 2% to 10% of the duct radius, the resonance point is not decipherable any longer and the liner decay at higher frequencies tend to zero. At about a boundary layer thickness of 5% of the radius and above, there is no longer any attenuation predicted by the liner for frequencies in excess of EO = 80 (4BPF).

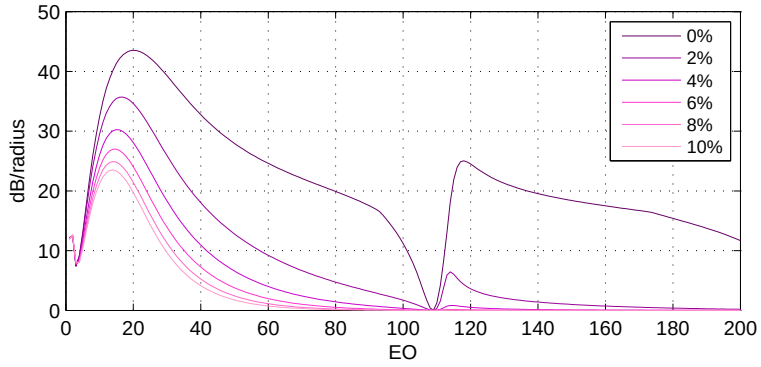

Figure 11.13: Acoustic liner optimized to attenuate BPF (EO20) tone absorption for different boundary layer thicknesses

11.4 Results from Advanced Model

In addition to the two duct geometries, two different source sawtooth waveforms were also used in the study referred to here for easy identification as IR1 and IR2. These are irregular sawtooth waveforms with different levels of shock-to-shock variations; IR1 has a greater level of differences among the shock waves than IR1, allowing for representation of two different fan blade sets with 20 blades each. The results presented are for the FTG and STG shown in figure 11.2 with the acoustic liner placed in the duct wall from $z/r_d = 0.1$ and $z/r_d = 1$ along the duct axis. The nonlinear propagation of the rotor-locked pressure field was simulated for the whole length of each duct and the model prediction results are shown over this range. The other quantities set at the fan plane are listed in table 11.2.

Table 11.2: Information quantities for propagation at fan plane

Radius (m)	0.5
Air density (kg/m^3)	1.2
Speed of sound (m/s)	340
Specific heat ratio	1.4
Fan rpm	7500
Number of blades	20

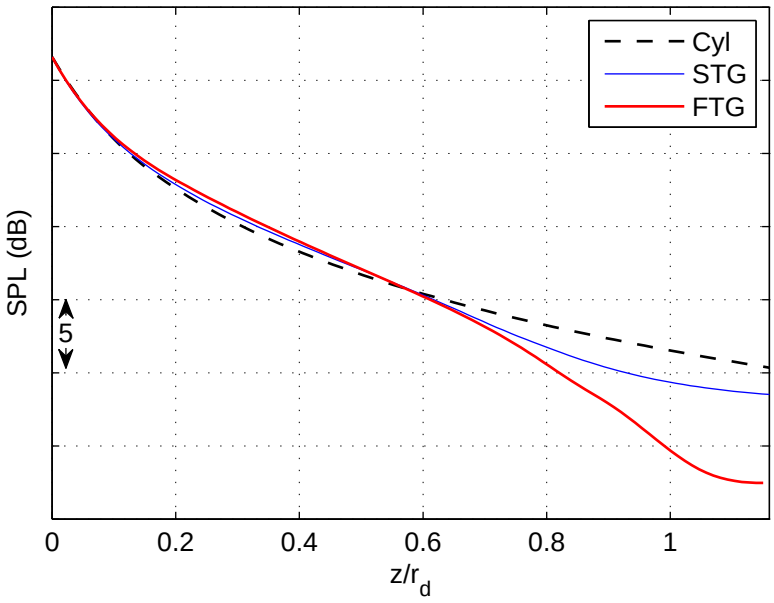

Figure 11.14: Comparisons of regular sawtooth BPF tone attenuation in rigid wall ducts

11.4.1 Results for rigid wall ducts

Comparisons for the rigid wall cases are shown for the cylindrical duct, the STG and FTG. In figure 11.14, the effect of geometry variation is exclusively seen for the propagation of a regular sawtooth which leaves out the effect of shock-to-shock differences. The three values of the SPL start at the same level since the levels are prescribed at the fan plane. As the propagation progresses, slightly higher sound levels are observed in the divergent regions of the STG and FTG. This continues until about a distance of z/r_d =0.3, where the cross sectional area of the STG and FTG began to reduce giving an effectively higher nonlinear decay. Consequently, at z/r_d =0.6, the three ducts have similar sound pressure levels. The cross sectional areas of the STG and FTG continue to reduce, much more in the FTG, giving rise to even stronger attenuation. The waveform eventually reaches the flow speed-up region, at about z/r_d =0.8 for the STG and later for the FTG, where higher flow speed cause a much rapid decay to be predicted.

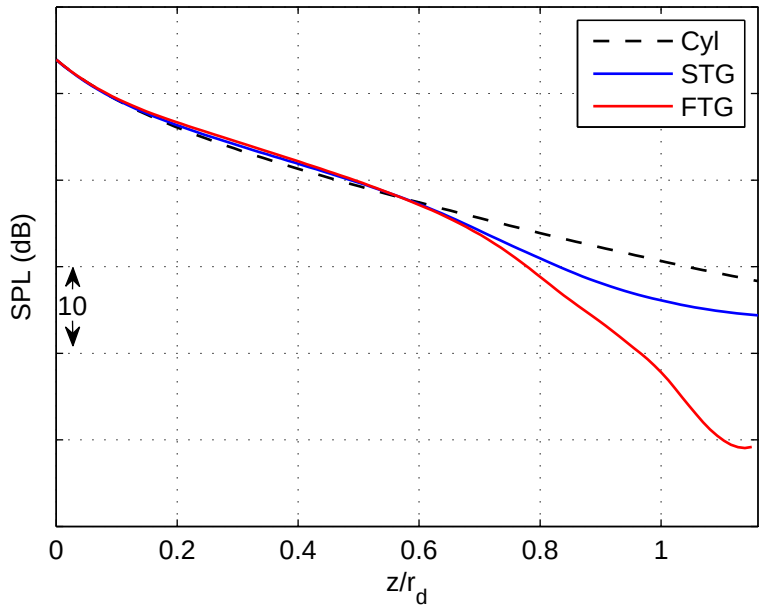

Figure 11.15: Comparisons of IR1 BPF tone attenuation in rigid wall ducts

Figures 11.15 and 11.16 show the attenuation of the IR1 and IR2 in the three ducts respectively. Although the irregular sawtooth waveforms are different from each other, and much more from the regular sawtooth, a similar trend is seen as for the regular sawtooth but with larger attenuation overall and different features in the flow speed-up region.

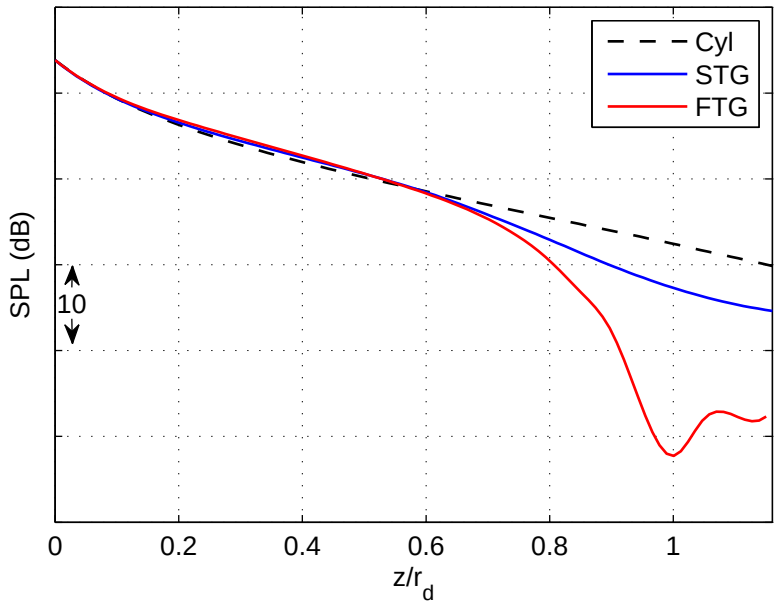

Figure 11.16: Comparisons of IR2 BPF tone attenuation in rigid wall ducts

11.4.2 Results for lined wall ducts

For the lined wall case, two liners were used in the propagation simulations – one optimized at about BPF and the other optimized for the half-BPF tone. Propagation was performed for the whole length of the ducts for the range of boundary-layer thicknesses mentioned.

11.4.2.1 Lined cylindrical duct

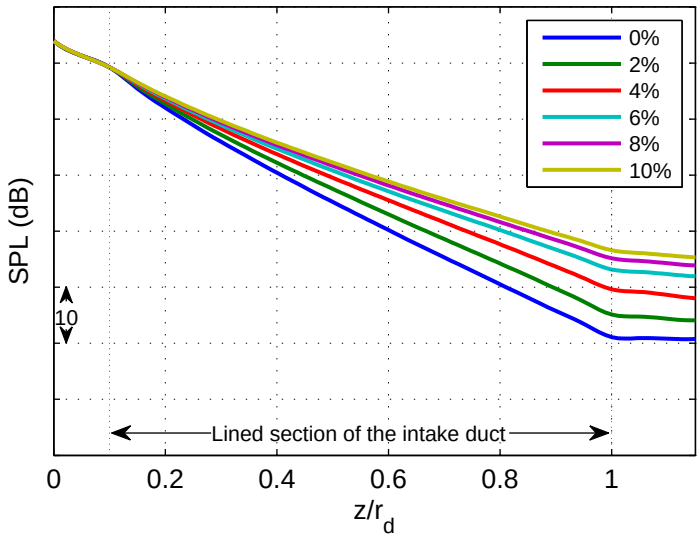

Figure 11.17: IR1 BPF tone attenuation in lined wall cylindrical duct: BPF-optimized liner

Figure 11.17 shows the BPF tone attenuation from the propagation of IR1 in a lined cylindrical duct. The liner decay rates reduce with increasing boundary layer thickness. The plot of SPL against axial distance clearly shows this as the zero boundary layer case is most attenuated while the 10% boundary-layer thickness was least attenuated. From $z/r_d = 0$ to 0.1 on the duct axis, the duct is rigid. This is reflected in the result as similar levels are seen for all the boundary-layer thicknesses. The effect of the liner becomes evident as soon as the lined region is reached. A steady almost linear gradient is seen until $z/r_d = 1$ where the other rigid region starts. At this location, the rate of attenuation drops causing an obvious change in the gradient of the curves. Similar observations are seen for the BPF tone attenuation when the liner is tuned to half-BPF (figure 11.18), but with significantly less attenuation for all the different boundary-layer thicknesses, and considerably less variation from 0% to 10% thickness. Results for IR2 (see figures 11.19 and 11.20) appear similar but the plot show that the IR2 is slightly less attenuated compared to the IR1 when the final value at the ends are compared. Owing to the fact that exactly the same liner absorption is applied to the two waveforms,

difference may be traced to the slight increase in the IR2 BPF tone after $z/r_d = 1$ observed in figure 11.16. The effect of variation in radius is absent in these results and hence, these results form a basis for comparison for the axisymmetric intake ducts.

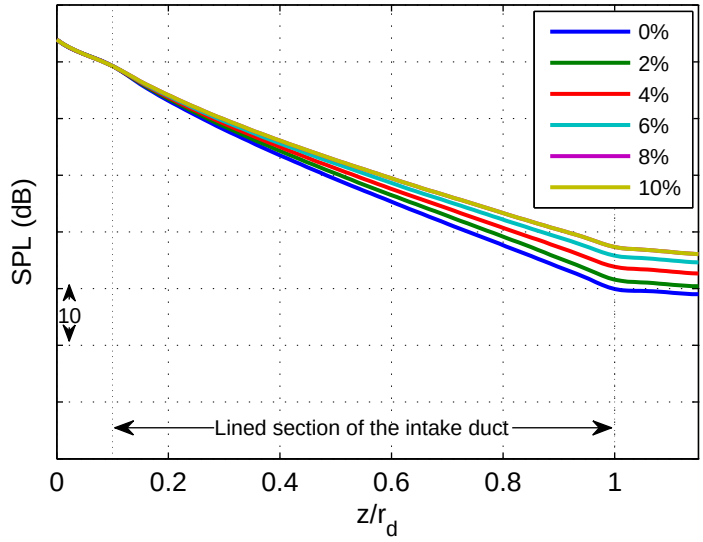

Figure 11.18: IR1 BPF tone attenuation in lined wall cylindrical duct: half-BPF optimized liner

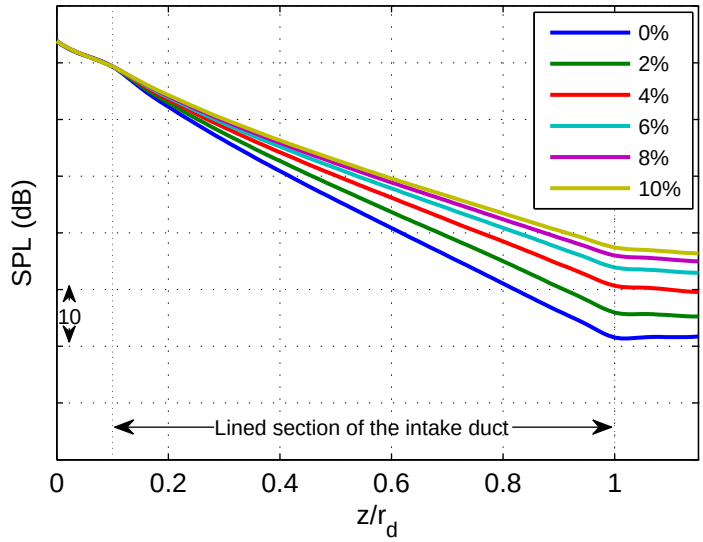

Figure 11.19: IR2 BPF tone attenuation in lined wall cylindrical duct: BPF-optimized liner

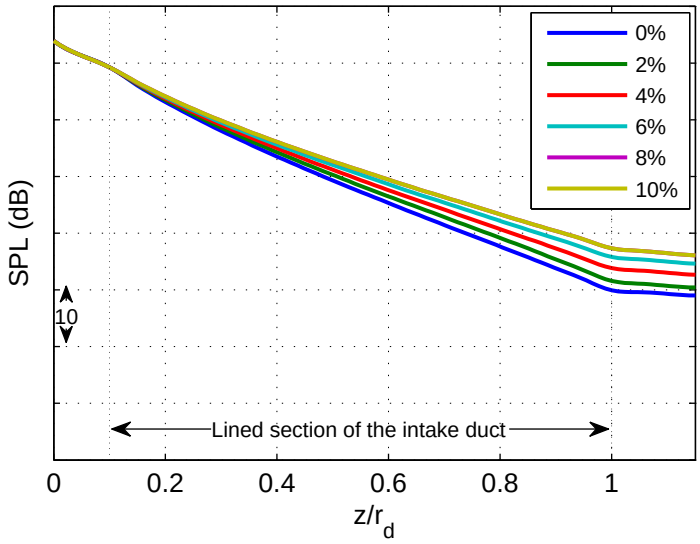

Figure 11.20: IR2 BPF tone attenuation in lined wall cylindrical duct: half-BPF optimized liner

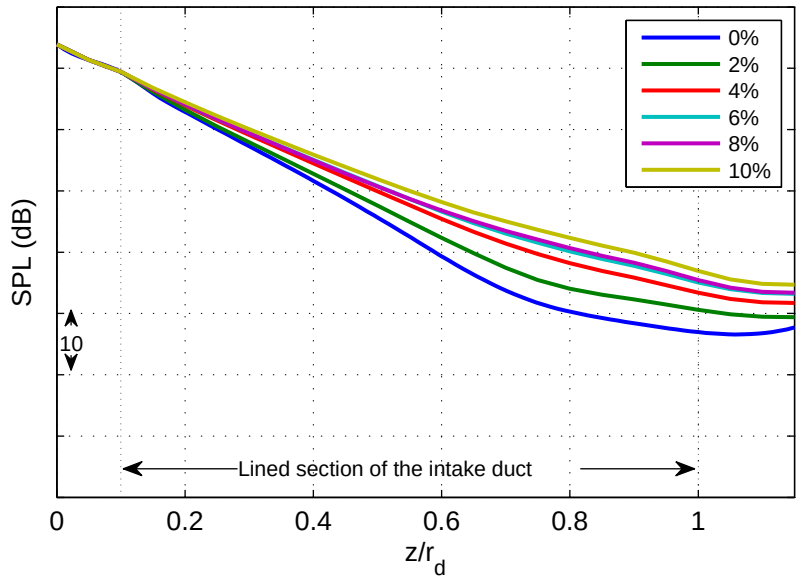

Figure 11.21: IR1 BPF tone attenuation in lined wall FTG: BPF-optimized liner

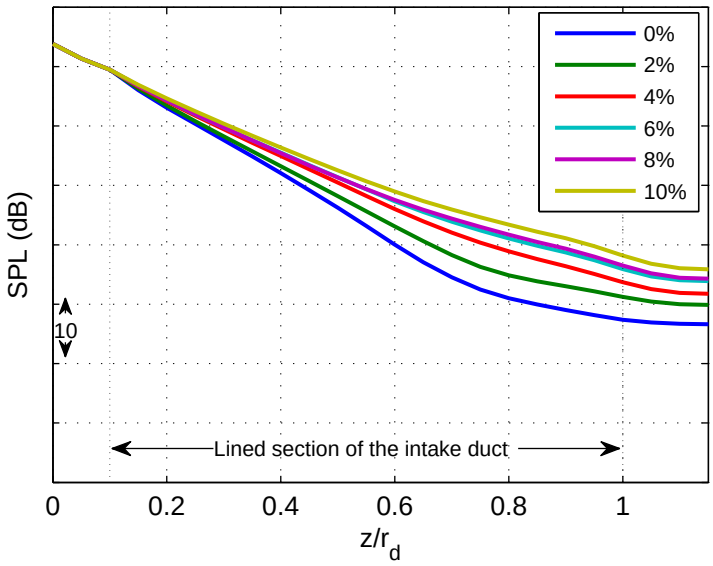

Figure 11.22: IR2 BPF tone attenuation in lined wall FTG: BPF-optimized liner

11.4.2.2 Lined FTG duct

Plots of the BPF tone attenuation along the duct axis were generated for the FTG for the two sawtooth waveforms and all the different boundary layer thicknesses for the two different acoustic liners. These can be seen in figures 11.21 to 11.24. In all cases, less attenuation of the BPF tone is observed for a thicker boundary layer. The initial rigid section gives the same results as expected since there is no liner attenuation in addition to the nonlinear shock decay in this region. The lined region has notable observations. In figures 11.21 and 11.22 where the acoustic liner is optimized for the BPF tone, there is more variation in the different curves for different boundary layers with about 10dB variation at the end of propagation compared with only 2 to 3dB between the 2% to 10% boundary layer thickness in figures 11.23 and 11.24 for which the acoustic liner is optimized to half-BPF.

The variation of the attenuation by the liner is prominent between the distance $z/r_d = 0.6$ to $z/r_d = 0.8$. This reflects the rapid changes in flow speeds (see figure 11.10) in this region. As the duct radius changes, and the flow speed varies, the liner decay rates also vary giving the waviness in the plots in this region. The attenuation reduces in the subsequent rigid region, but owing to the fact that the waveform has been well attenuated, a less obvious transition was observed when compared to the plots for a cylindrical duct (figure 11.17). The differences between the results for the IR1 and IR2 are discussed in section 11.4.3.

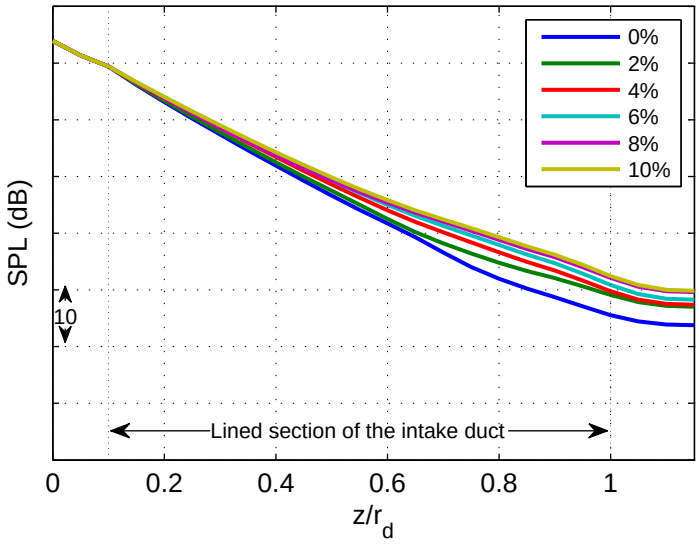

Figure 11.23: IR1 BPF tone attenuation in lined wall FTG: half-BPF-optimized liner

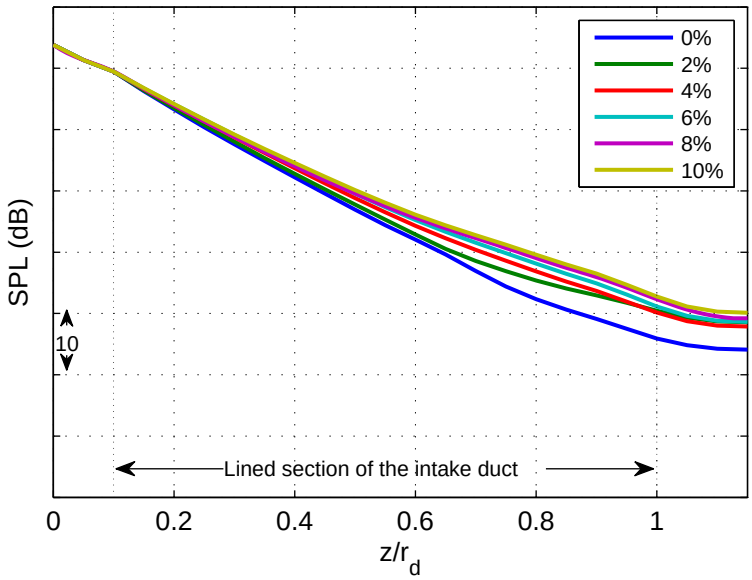

Figure 11.24: IR2 BPF tone attenuation in lined wall FTG: half-BPF-optimized liner

11.4.2.3 Lined STG duct

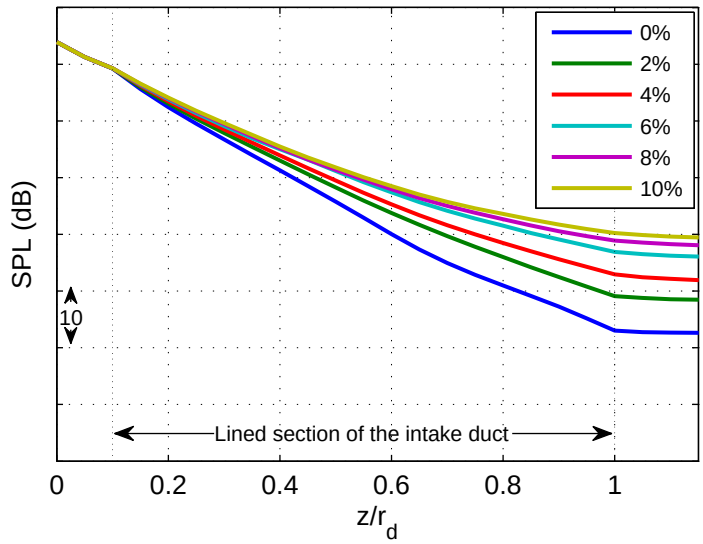

Figure 11.25: IR1 BPF tone attenuation in lined wall STG: BPF-optimized liner

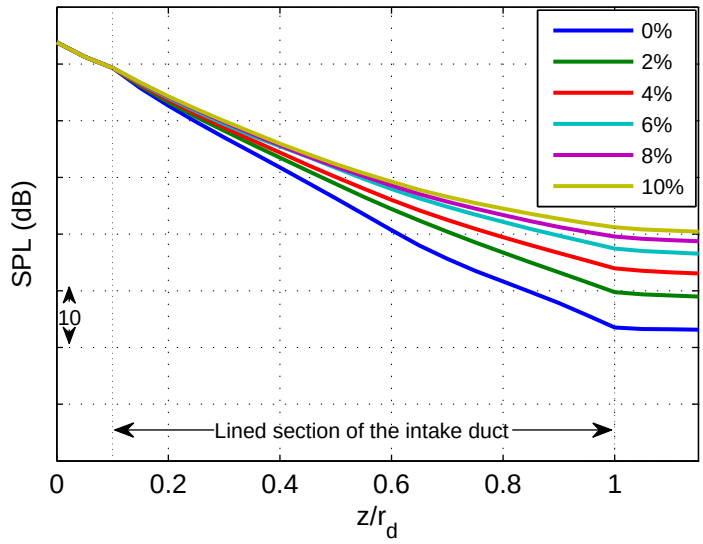

Figure 11.26: IR2 BPF tone attenuation in lined wall STG: BPF-optimized liner

As the BPF tone is the most dominant tone, plots of BPF tone attenuation are shown for the STG intake in figures 11.25 to 11.28. The first observation is that the attenuation plots have traces of the features of the cylindrical duct and the FTG intake duct. The initial rigid wall region where all curves are the same is seen as in the cylindrical duct. Also, the region where there are larger changes in flow speed are where the changes in tone attenuation are higher. These observations are related to the STG's wall contour not being as varied as the FTG, and the resultant lower peak flow speed, which may

be traceable to the flare installed for the STG set-up, to guide the flow into the duct. There is about 18dB difference at $z/r_d = 1$ comparing the zero boundary layer case to the 10% boundary layer case with the BPF optimized liner. This is a higher variation than is observed for the flight test FTG intake duct. Less variation is observed for the propagation results for the acoustic liner optimized for half-BPF attenuation.

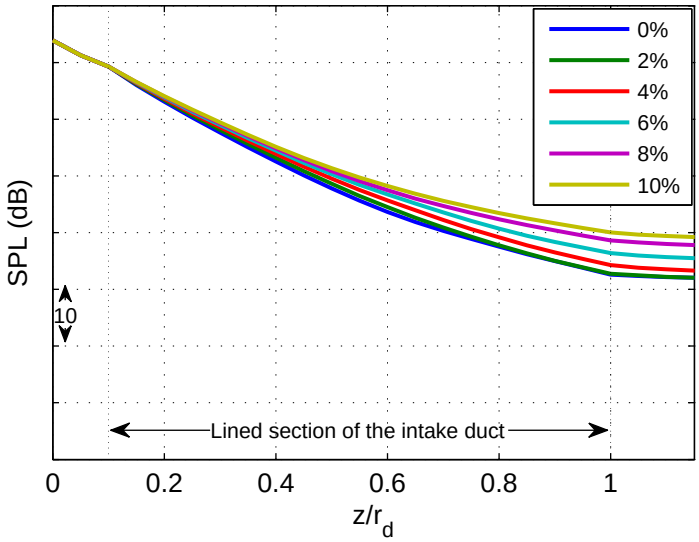

Figure 11.27: IR1 BPF tone attenuation in lined wall STG: half-BPF-optimized liner

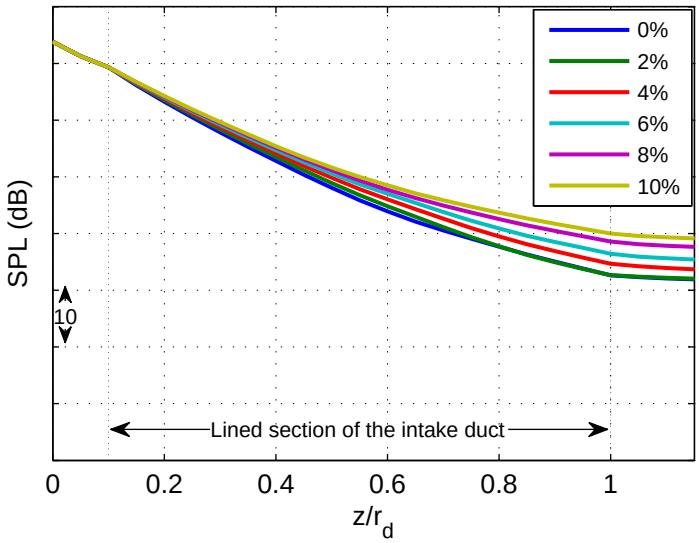

Figure 11.28: IR2 BPF tone attenuation in lined wall STG: half-BPF-optimized liner

11.4.3 Comparison of results: IR1 versus IR2

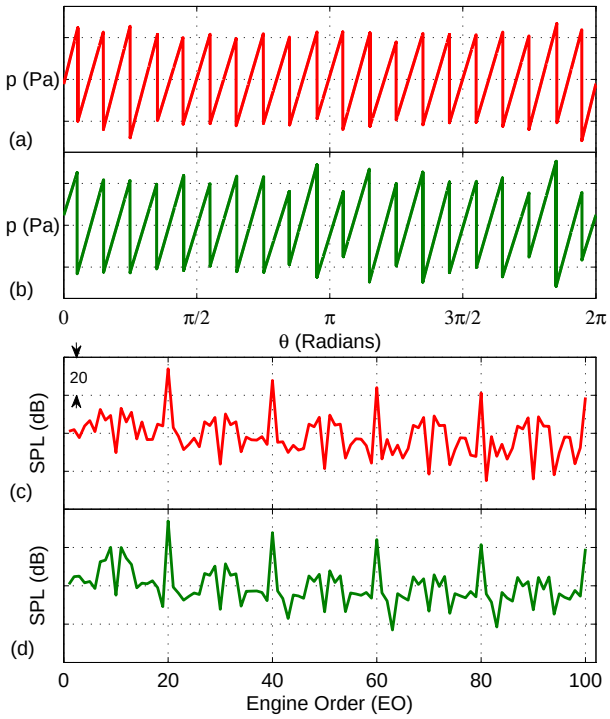

Figure 11.29: Initial waveforms (a) IR1 (b) IR2 and initial spectrum (c) IR1 (d) IR2

The two sawtooth waveforms IR1 and IR2 (see figure 11.29) employed in the study presented in this chapter were propagated in the FTG and STG ducts. The weakly irregular sawtooth waveform IR1 shows less shock-to-shock difference compared to the strongly irregular sawtooth waveform IR2. There also is greater variation in shock spacing and shock mid-point pressure for the IR2 as observable in figure 11.29(a) and (b) and also evident in the spectrum plots. The differences between the propagation of the weakly irregular and the strongly irregular sawtooth waveforms are evident in the results presented. The inter-harmonic tones in sawtooth IR2 are much more prominent than those of sawtooth IR1 showing the greater energy contained in the other frequencies other than the BPF harmonics, due to the greater irregularity in the waveform.

Sawtooth waveforms IR1 and IR2 in the FTG duct

Results are shown at the three stations marked in figure 11.2. First, for the simulations in the rigid wall duct and then for the lined wall. Figures 11.30 to 11.32 show the waveform and corresponding SPL-EO spectrum for the stations I to III for the FTG duct. At station I, figure 11.30, the amount of nonlinear attenuation are comparable for the two waveforms. Further at stations II and III (figures 11.31 and 11.32, the differences

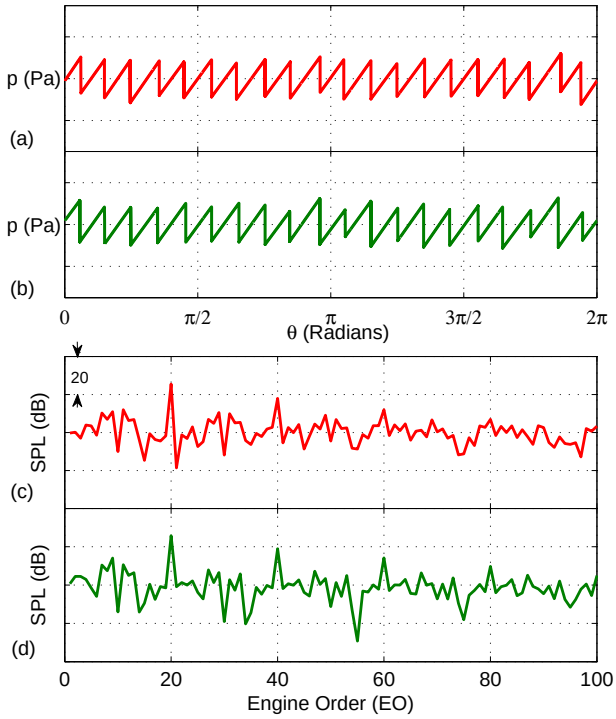

Figure 11.30: Simulation for rigid wall FTG: station I waveform (a) IR1 (b) IR2 and spectrum (c) IR1 (d) IR2

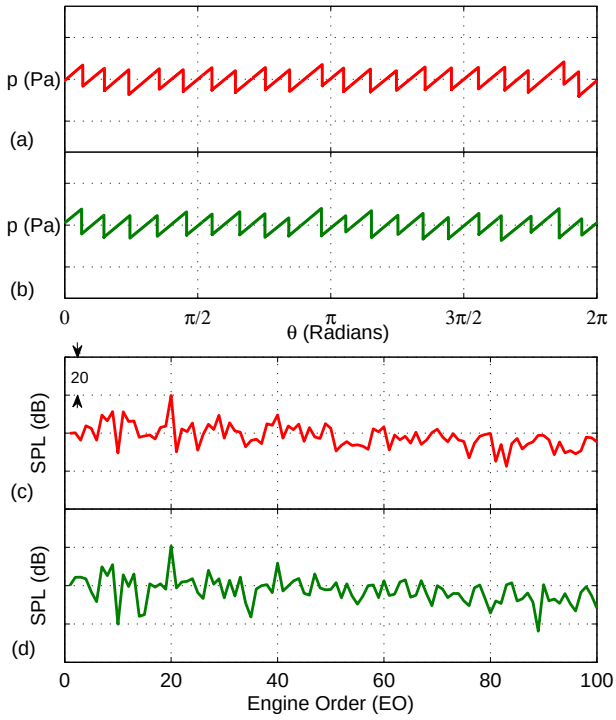

Figure 11.31: Simulation for rigid wall FTG: station II waveform (a) IR1 (b) IR2 and spectrum (c) IR1 (d) IR2

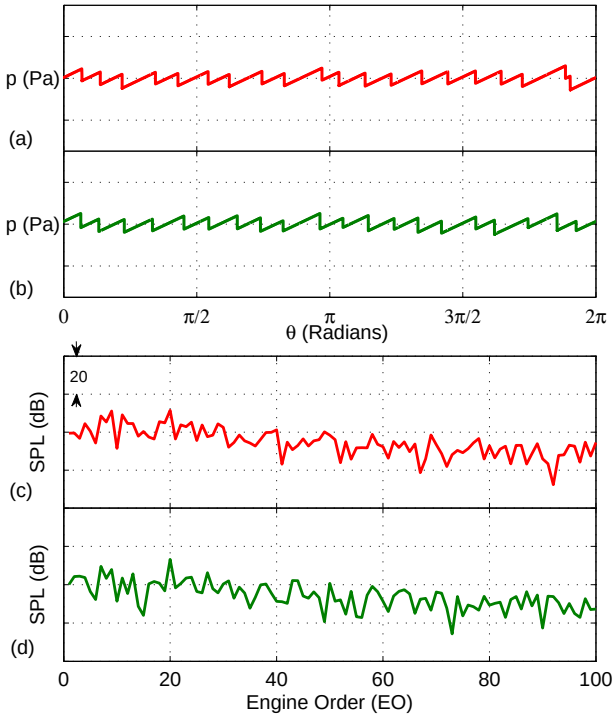

Figure 11.32: Simulation for rigid wall FTG: station III waveform (a) IR1 (b) IR2 and spectrum (c) IR1 (d) IR2

begin to show and various features appear in the waveforms and the spectra. A common feature of shocks with higher variation in the mid-point pressures is that they move further away from adjacent shocks, thereby increasing shock spacing is observed. The spectrum of sawtooth IR2 is much more varied with lower levels for the BPF harmonics at station III owing to greater energy transfer. The dominance of low-frequency tones are much more pronounced in sawtooth IR2 compared to sawtooth IR1.

Observations of the results for simulations in the lined duct (figures 11.33 to 11.35) are similar to those made for the simulation results for the rigid wall ducts, except there is additional attenuation of the tones by liner absorption of the BPF-optimized liner. It is of note that since the same flow conditions and liner absorption rates are used for the two ducts the observable differences are still mainly traceable to the initial nonlinear interactions. The results are only presented for the boundary-layer thicknesses of 0% and 10% of the duct radius, which are the lower and upper ends of the range of boundary-layer variations considered. As discussed earlier, lower liner attenuation is achieved for thicker boundary-layer due to boundary-layer shielding. Results show a considerable difference in the spectrum over the range of boundary-layer thicknesses. Up to about 10dB for some tones at stations II (figure 11.34(c) and (d)) III (figure 11.35(c) and (d)).

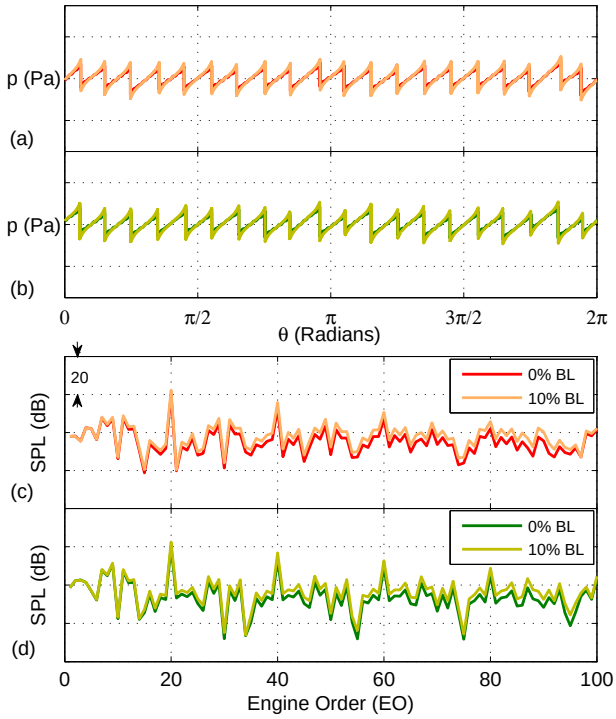

Figure 11.33: Simulation for lined wall FTG: station I waveform (a) IR1 (b) IR2 and spectrum (c) IR1 (d) IR2

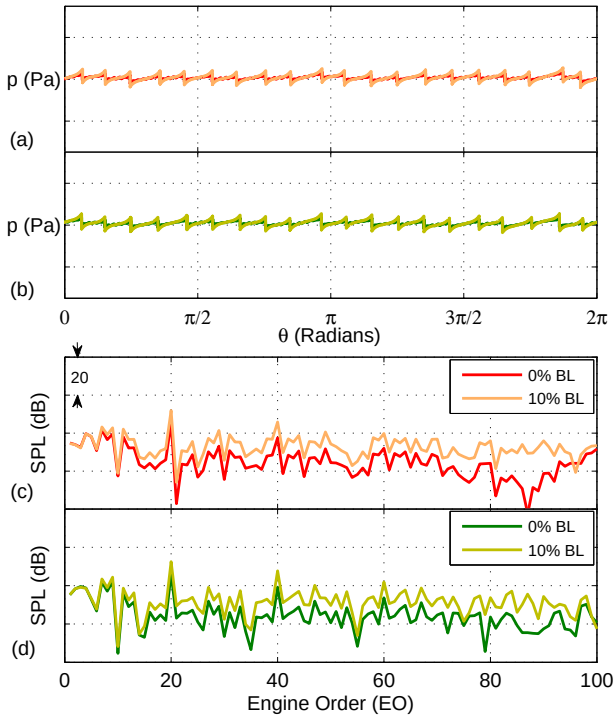

Figure 11.34: Simulation for lined wall FTG: station II waveform (a) IR1 (b) IR2 and spectrum (c) IR1 (d) IR2

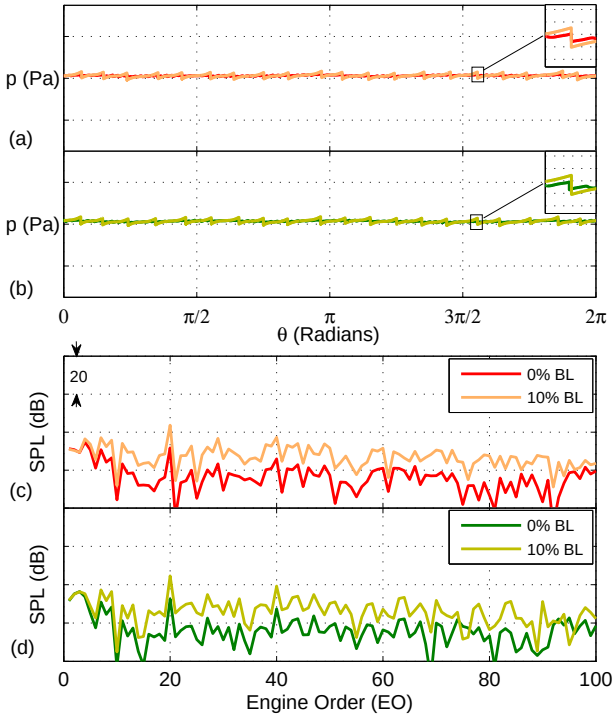

Figure 11.35: Simulation for lined wall FTG: station III waveform (a) IR1 (b) IR2 and spectrum (c) IR1 (d) IR2

Sawtooth waveforms IR1 and IR2 in the STG duct

Results for simulations in the rigid wall STG intake are shown for stations I, II and III in figures 11.36, 11.37 and 11.38. The waveforms and spectra clearly show the attenuation of the shocks as they propagate in the duct. A rapid decay of the amplitude is observed from the start to station I which is consistent with the observations that the rate of attenuation is proportional to the inverse of the distance [19, 26, 28]. Since, the range of variation in the radius along the duct axis and lower flows speeds are present in the STG intake compared to the FTG intake, less attenuation is observed by station III. The SPL-EO spectra at each station also show higher tone levels for the STG for the same length of propagation when compared to results from the FTG.

The waveforms and EO spectra for the lined wall STG results are shown for IR1 and IR2 in figures 11.39 to 11.41. The effect of the inclusion of liner absorption and different boundary layer thicknesses are obvious from the figures. Results are presented for the BPF-optimized liner, and so much more attenuation is seen around this tone in the SPL-EO spectra. As the same liners and flow speeds are used in simulations for the two waveforms, the differences in tone levels are primarily due to the nature of the waveforms and the nonlinear propagation.

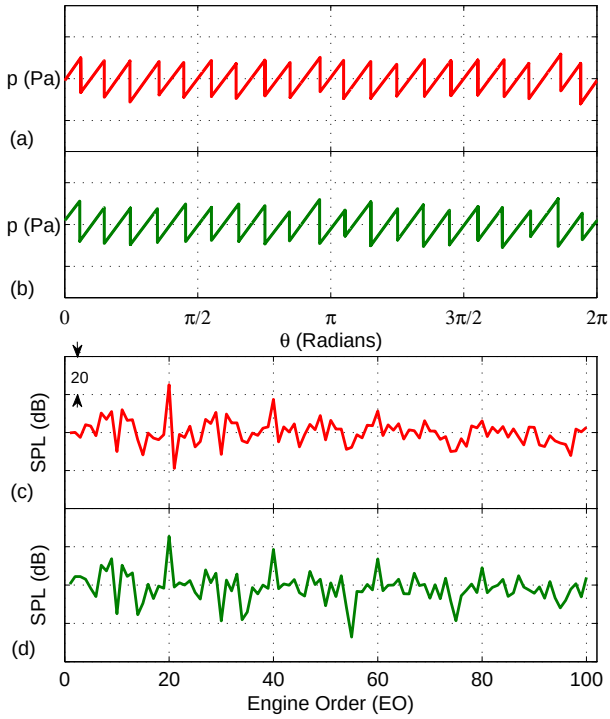

Figure 11.36: Simulation for rigid wall STG: station I waveform (a) IR1 (b) IR2 and spectrum (c) IR1 (d) IR2

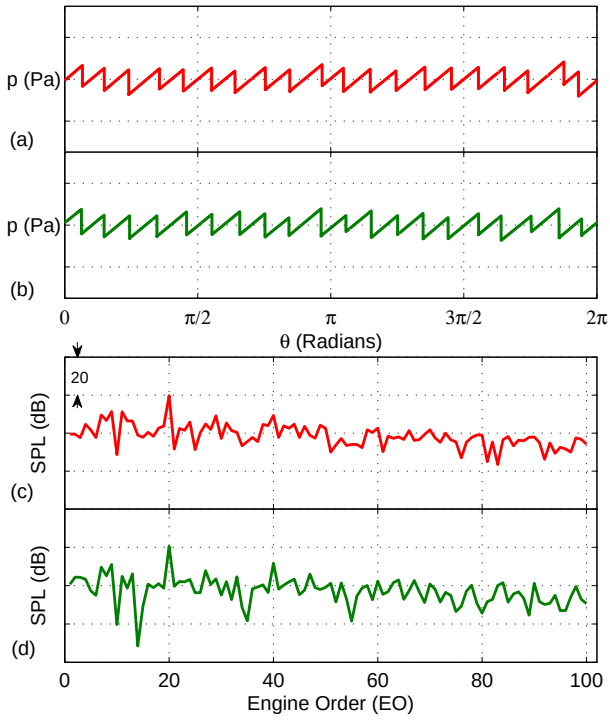

Figure 11.37: Simulation for rigid wall STG: station II waveform (a) IR1 (b) IR2 and spectrum (c) IR1 (d) IR2

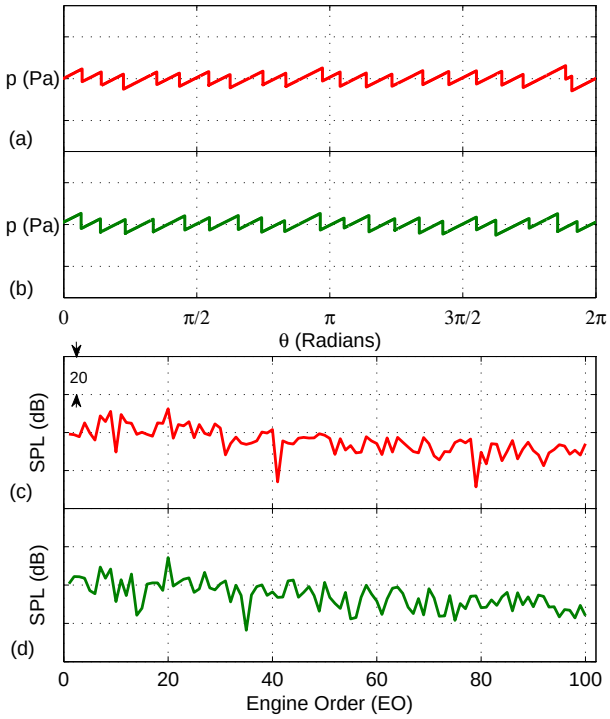

Figure 11.38: Simulation for rigid wall STG: station III waveform (a) IR1 (b) IR2 and spectrum (c) IR1 (d) IR2

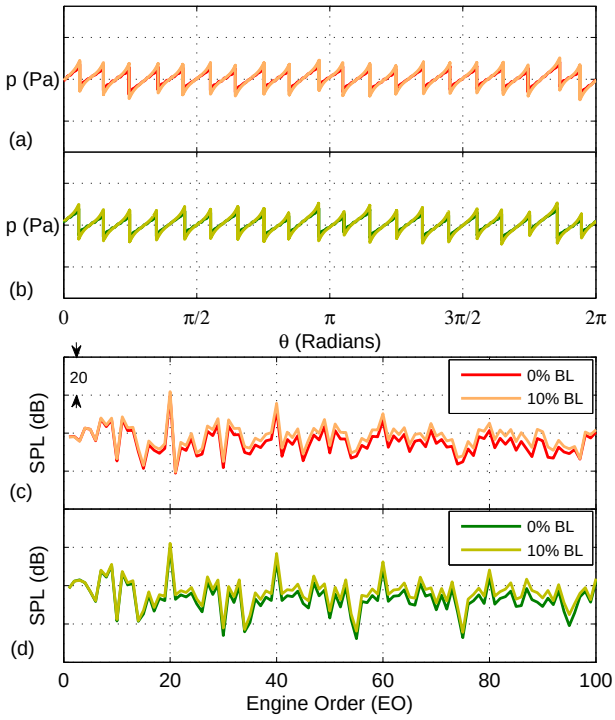

Figure 11.39: Simulation for lined wall STG: station I waveform (a) IR1 (b) IR2 and spectrum (c) IR1 (d) IR2

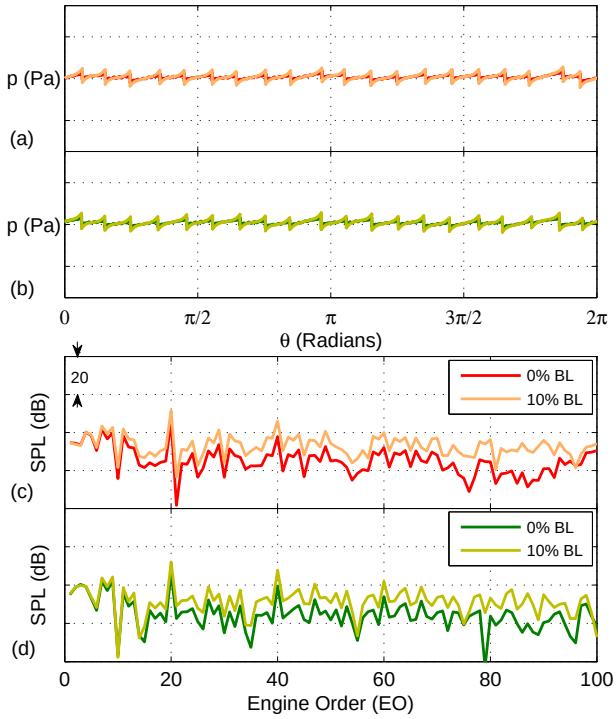

Figure 11.40: Simulation for lined wall STG: station II waveform (a) IR1 (b) IR2 and spectrum (c) IR1 (d) IR2

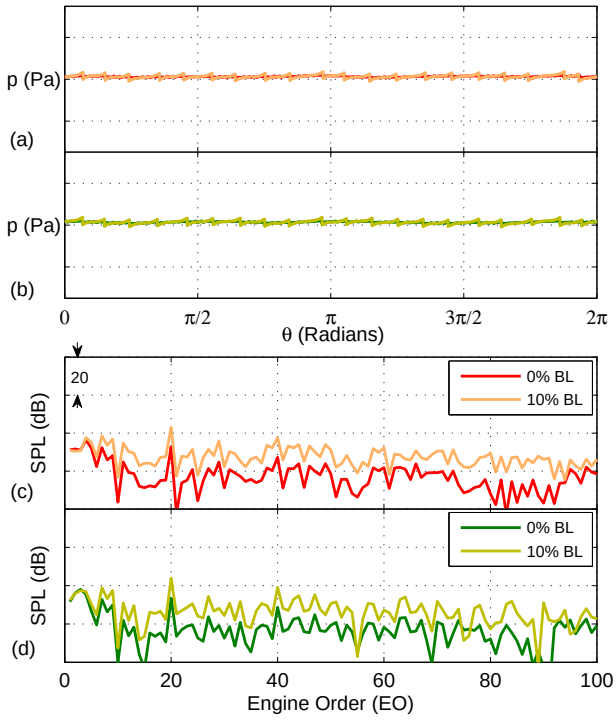

Figure 11.41: Simulation for lined wall STG: station III waveform (a) IR1 (b) IR2 and spectrum (c) IR1 (d) IR2

The results for propagation of IR1 and IR2 in the Rigid STG is presented in figure 11.42. It is observed for simulation in this duct that there is very little difference between the results for the two waveforms, except for the mid-duct where the duct contracts and flow speed-up region. In these regions, the BPF tone for the weakly irregular sawtooth suffers more attenuation. However, similar sound pressure levels are observed at the end of the simulation.

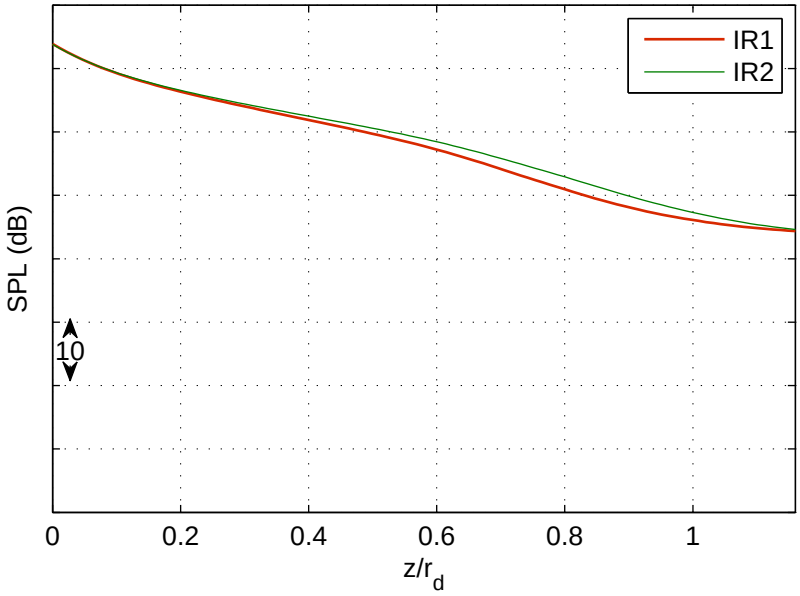

Figure 11.42: IR1 and IR2 BPF tone attenuation for rigid STG duct

Figures 11.43 and 11.44 are the plots of the SPL of the BPF tone (the dominant tone) over the length of the lined duct for boundary-layer thicknesses from 0% to 10% of the duct radius. For these two sawtooth waveforms very little differences is seen over the span of the propagation with sawtooth IR1 having a higher attenuation of about 1dB by the end of propagation. The almost negligible difference observed with the STG intake points to the dominance of the acoustic liner absorption over the nonlinear decay, especially for the BPF and neighbouring tones.

11.4.4 Results in the flow speed-up region

It is useful to see results of the progress of the waveform through the high speed flow region. The high flow speed values at the wall are expected to considerably impact on the nonlinear propagation and distribution of energy amongst the EO harmonics. Figures 11.45 and 11.46, show the waveforms and frequency spectra at the axial location of highest flow speed and at the duct lip for the FTG intake respectively. From figure 11.45(a) and (b), it is observed that the waveforms have been considerably more attenuated than at station III (see figure 11.32). The increase in flow speed has resulted in an increase in

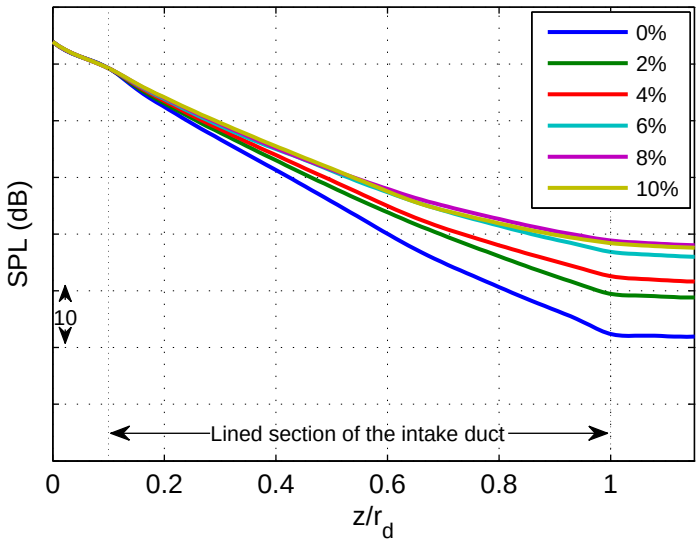

Figure 11.43: IR1 BPF tone attenuation for STG: Lined Duct: BL 0% to 10% of the radius

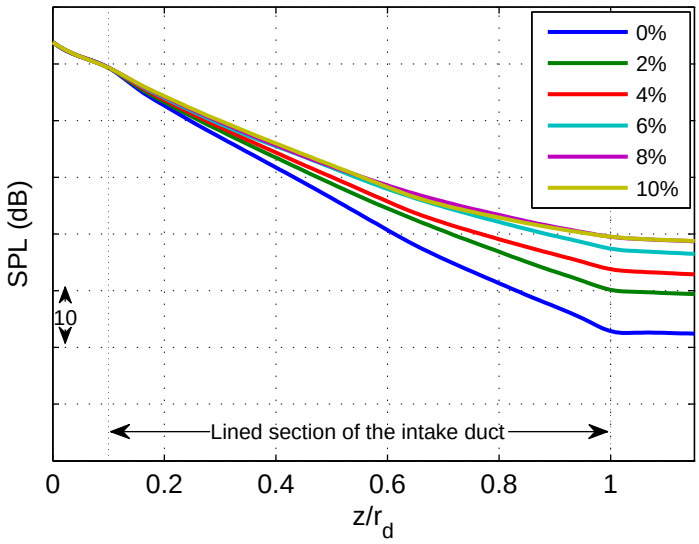

Figure 11.44: IR2 BPF tone attenuation for STG: Lined Duct: BL 0% to 10% of the radius

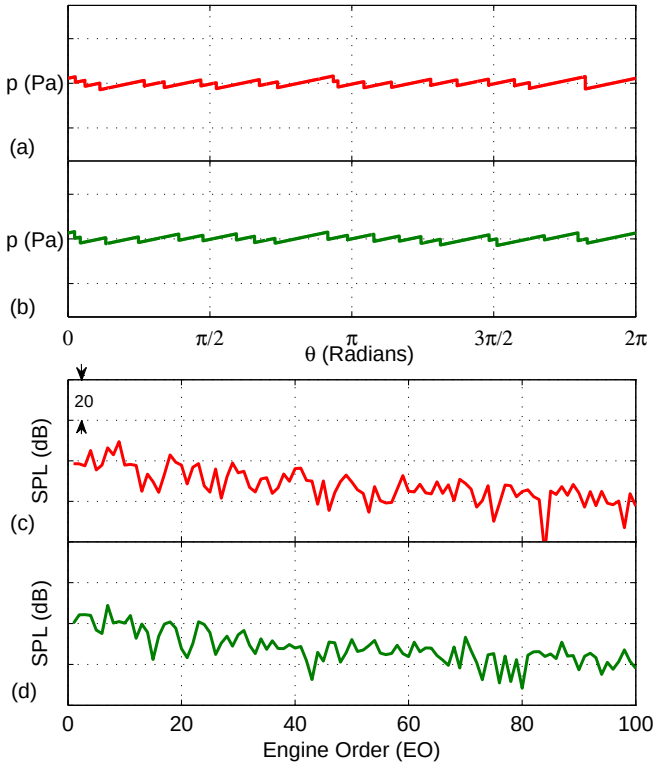

Figure 11.45: Simulation for rigid wall FTG at the point of highest flow speed: waveform (a) IR1 (b) IR2 and spectrum (c) IR1 (d) IR2

the time of flight, enabling more nonlinear attenuation per unit axial distance. At this point a few shocks, though now with low amplitudes, have merged (see figure 11.45(a)) and the spectrum has change drastically without any dominant BPF tone observable.

At the duct lip (figure 11.46), the waveform appears complete flat compared to the starting waveforms (see figure 11.29). The shocks have all being attenuated and the SPL-EO spectra look totally different with much lower levels at higher frequencies, and dominant low-frequency EO tones, which is the characteristic buzz-saw noise perceived after the pressure field is radiated from the duct. It is of note than the actual mechanism at the duct lip is complex and scattering to higher radial orders, evident in the radiation results (in chapter 8), may occur making the model results less valid in this region owing to the assumption of all energy being in the first radial order.

11.5 Axial variation of liner absorption

In order to shed more light of the predicted results for the lined wall simulation in the FTG and STG intakes, a closer look at the variation of liner absorption for the BPF tone is shown for the two geometries in figures 11.47 and 11.48. In figure 11.47, the differences

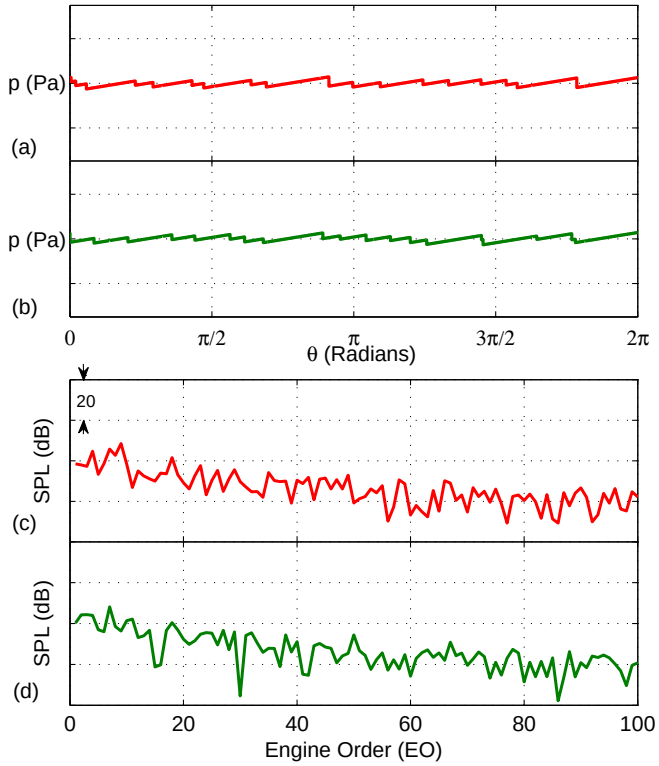

Figure 11.46: Simulation for rigid wall FTG at the duct lip: waveform (a) IR1 (b) IR2 and spectrum (c) IR1 (d) IR2

in the predicted liner absorption achieved for the different boundary-layer thicknesses ranges over several decibels. It is notable for the FTG that the absorption varies from the start to the end of the lined region over a large range due to the amount of change in flow speeds in the duct. The absorption rate first reduces as the duct slightly expands. It subsequently increases as the duct contracts and the flow speed rapidly increases. At the peak value of the flow speed, near the intake throat, liner absorption drops to almost zero making the liner similar to a rigid duct in this region. The observations in the STG duct are very different. Owing to the smaller gradients in the curvature of the inner geometry of the duct, the flow speed range is smaller. This is reflected in the modal decay rates which on average vary about 10dB/radius over the entire lined region for all the different boundary layer thicknesses. This explains why only small differences in the prediction are seen between this duct and a cylindrical duct: having in mind that modal decay rates for a cylindrical duct do not vary over the entire length of the lined region because there is no change in the radius.

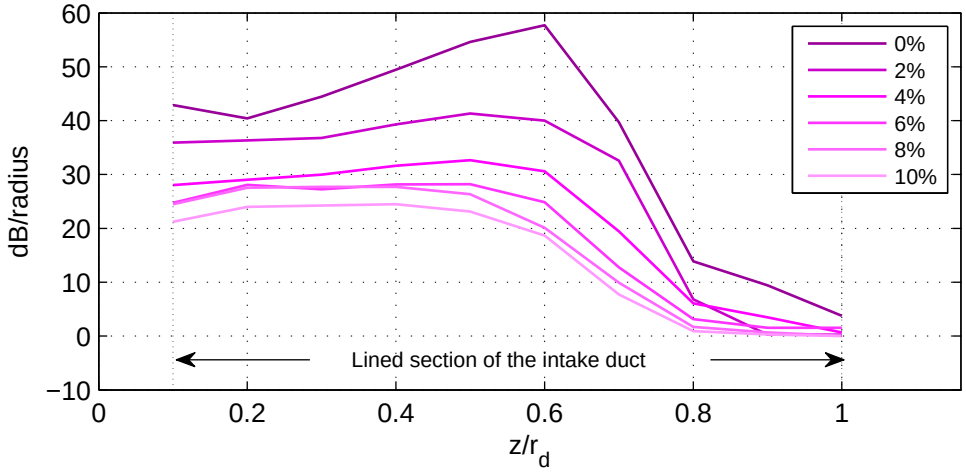

Figure 11.47: Acoustic liner decay rates in the FTG for different boundary-layer thicknesses, based on a SDOF cavity liner. Acoustic liner optimized for the BPF tone attenuation

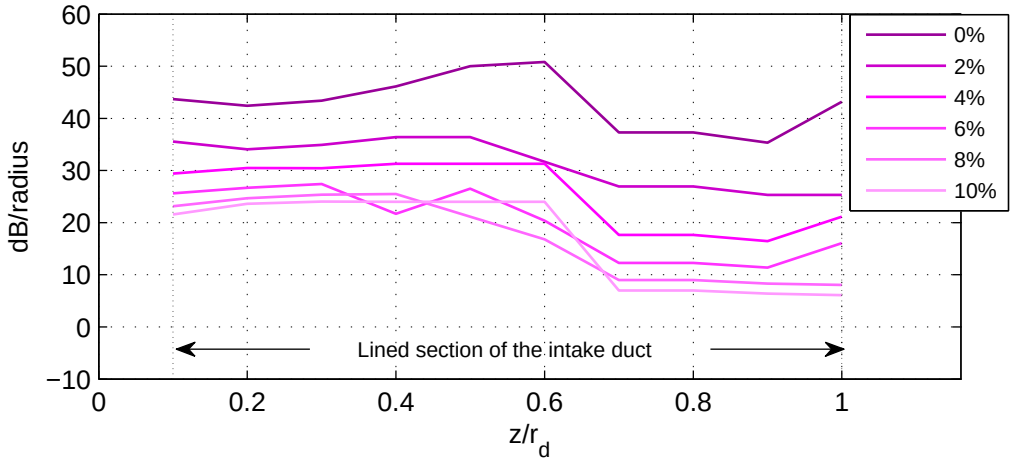

Figure 11.48: Acoustic liner decay rates in the STG for different boundary-layer thicknesses, based on a SDOF cavity liner. Acoustic liner optimized for the BPF tone attenuation

11.6 Comparison with measurements

The advanced propagation model was used to predict the supersonic fan noise levels for a model-scale rig intake (illustrated in figure 7.1) used by Rolls-Royce in an experimental test programme in the AneCom anechoic test facility in Germany. This measured data is the same as used in validation of the propagation models in previous chapters and in references [53, 106]. Results for an idealized cylindrical duct are presented in the comparisons.

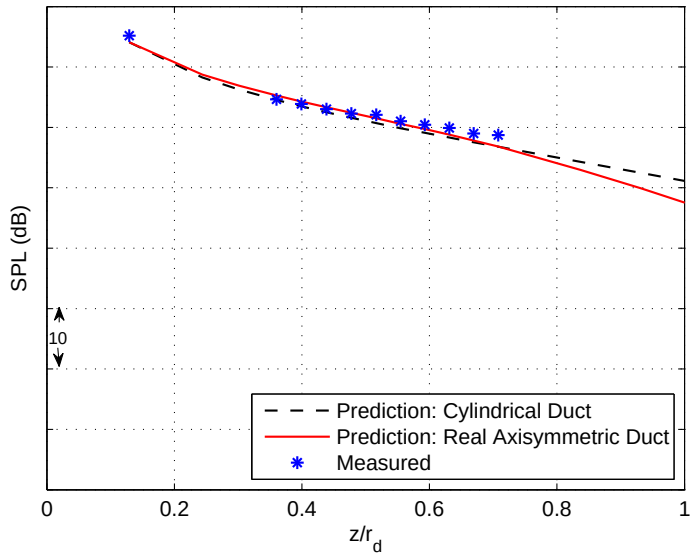

Figure 11.49: Rigid Duct: Measurements against prediction

11.6.1 Comparison against Rigid wall measurements

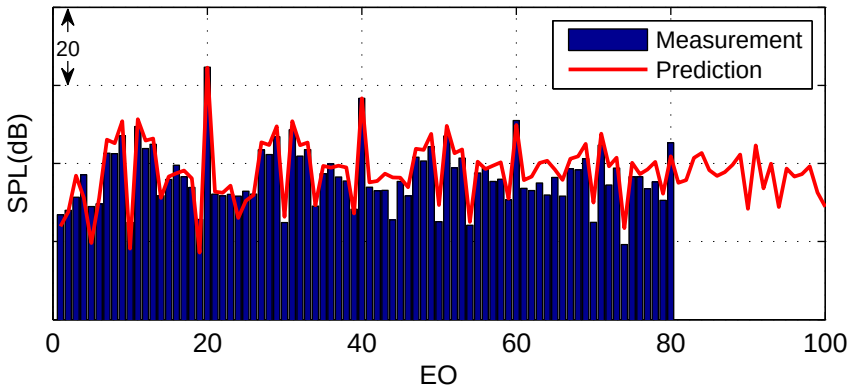

Figure 11.50: Rigid-wall duct: measurements against prediction at the first axial station

For the rigid wall test case, the predicted sound levels for the BPF tone using the actual model-scale geometry and for the idealized cylindrical duct are compared with measurements in figure 11.49. The effect of flow speed variation in the intake geometry can be observed from the predictions using the actual model-scale intake geometry. The initial increase in radius of the real geometry results in a reduction in attenuation, about 1dB higher than the cylindrical duct. As the radius then reduced and the flow speed increases, similar levels occur up to a distance equal to $z//r_d = 0.7$. The higher flow speeds near the duct lip lead to higher attenuation predicted for the real geometry, resulting in a 3dB difference at $z//r_d = 1$.

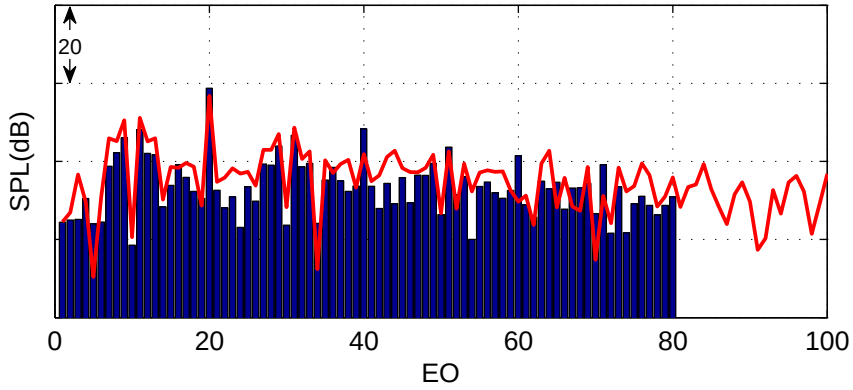

Figure 11.51: Rigid-wall duct: measured spectrum against prediction at the last axial station

11.6.2 Comparison against Lined wall measurements

The comparison of measured data and predicted sound levels for the BPF tone (EO 20) is shown in figure 11.52 for a range of boundary layer thicknesses for the propagation in the lined wall intake duct. Along the duct axis, the radius, flow speed and liner attenuation rates were permitted to vary in the simulations. For a particular result, the boundary-layer thickness is kept constant throughout the propagation distance. The difference between measurement and prediction ranges from an average of about 1.5 to 7dB from the first to the last (10th) axial measurement station. This is an improvement from the levels predicted in section 7.3 using the cylindrical duct model.

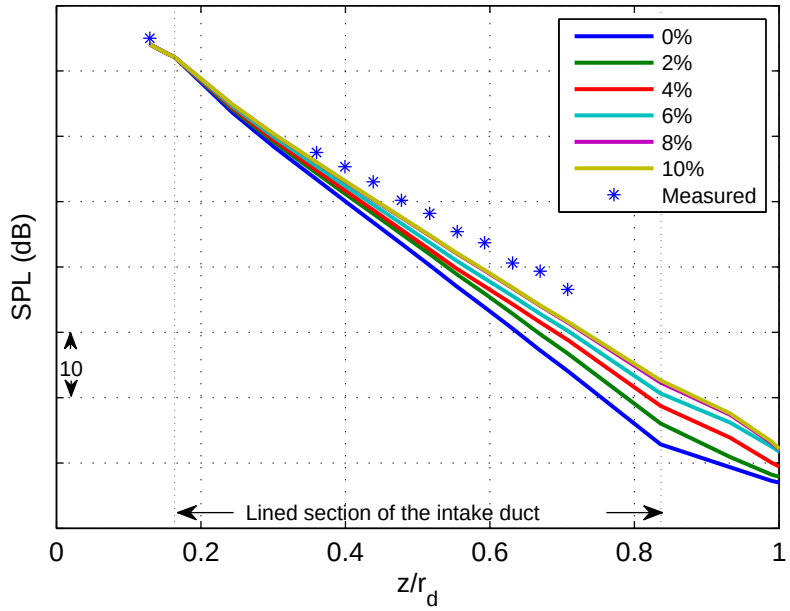

Figure 11.52: Lined-wall duct: measurements against prediction

Predicted levels for the rigid duct (see figure 11.49) showed very good agreement with measured data, hence, the difference between the measurements and prediction for the lined wall duct shows an overprediction of the attenuation by the liner. This may be traceable to the fact that a number of the real features, such as the actual variation of the boundary-layer along the duct wall, are unknown and, therefore, are only trialled in the model by examining a range of realistic values. Also, there are environmental and experimental equipment factors which can not be well represented such as background and equipment noise.

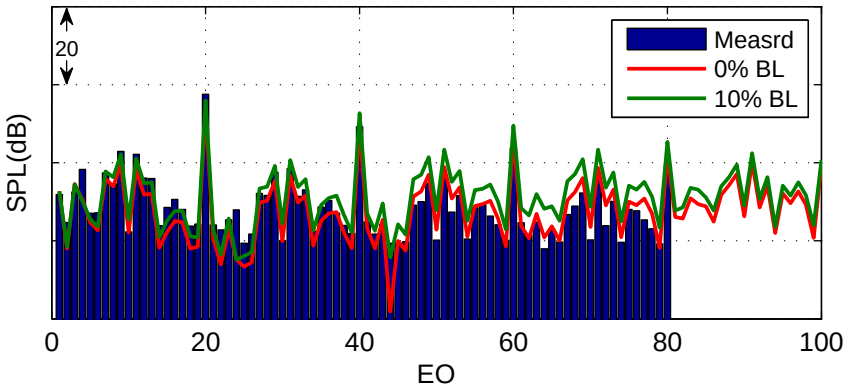

Figure 11.53: Lined-wall duct: measurements against prediction at the first axial station

A better insight into the performance of the prediction model for the lined wall duct can be seen from figures 11.53 and 11.54 which show the SPL-EO frequency spectra comparisons at the first and last axial stations respectively. Plots of the predictions are shown only for the lower and upper limits of the range of boundary-layer thicknesses, that is, thicknesses of the 0% or 10% of the duct radius at the fan. At the first axial station (figure 11.53), the prediction agrees more closely with measured spectrum. A closer look over the range of boundary-layer thicknesses trialled, shows that at higher frequencies the difference in the results with varying boundary-layer thickness is more obvious. The 0% boundary layer case better fits the trend of the measurements. At the last axial station, the prediction results suggest the presence of a boundary-layer thickness 10% which enables prediction to match the measurements more closely at most of the tones. The predicted results for 0% boundary-layer over-predict the attenuation of the tones.

Figure 11.55 shown the same comparison at the last axial station for an 8% boundary layer thickness. The agreement with measured data is seen to really improve but for the differences around BPF where the liner is optimized. It can be inferred from this observation that the boundary-layer thickness may vary significantly over the inner contour of the intake duct. Knowledge of the variation of the boundary-layer in the duct will be useful because the use of the appropriate absorption rates over the entire lined region may significantly improve the accuracy of the prediction capability.

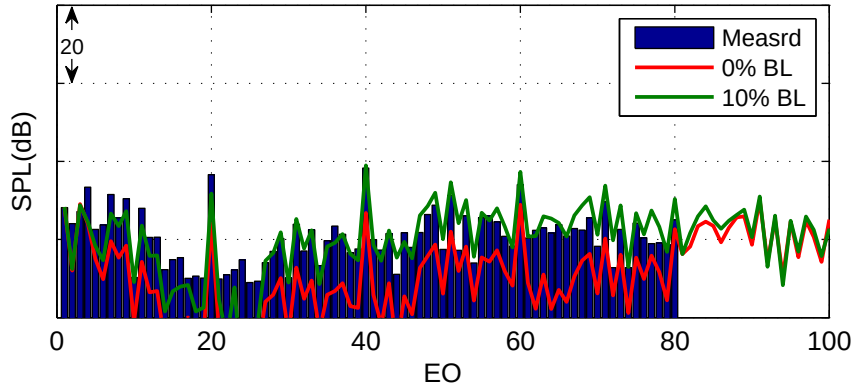

Figure 11.54: Lined-wall duct: measured spectrum against prediction at the last axial station

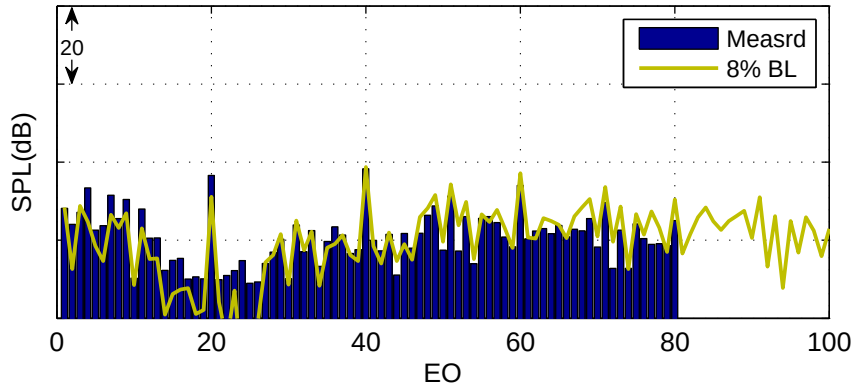

Figure 11.55: Lined-wall duct: measured spectrum against prediction with liner decay rates of 8% boundary-layer thickness at the last axial station

11.7 Summary

Extensive discussions of prediction results are presented for two different ducts: the static test STG and flight test FTG. Also predictions using two different sawtooth waveforms have been appraised. Results are shown and commented on for both rigid and lined wall ducts with varying radius, flow speeds and boundary-layer thicknesses. The effects of these variations are presented in the results for real ducts and comparisons with measured data are shown. The agreement of prediction and measurement most notably for the rigid wall intake duct are obvious. The evaluation of the level of agreement between prediction and measurement for the lined wall duct was carried out in order to demonstrate the ability and potential of the advanced nonlinear propagation model for reliable predictions for supersonic fan tones.

Chapter 12

Conclusions

The work presented in this thesis is focusses on the improvement of the prediction capabilities for supersonic fan noise generated by turbofan aircraft engines by the development of new prediction models. A comprehensive literature review has been undertaken on aircraft noise, and, specifically on buzz-saw noise. The chronological coverage of studies on supersonic fan noise gives an overview of the advancement in prediction capability, the challenges in the implementation and simplifications applied to reduce various complexities. The potential and usefulness, both for scientific studies and industrial application, of a reliable prediction model for supersonic fan noise, especially as an alternative to computationally expensive CFD models, was the key motivation that drove the relevance of the studies presented.

The key achievement/highlights of this thesis in the prediction of supersonic fan noise are summarised as

i New codes for shock tracking methods.

ii New Time-Frequency domain method for propagation in rigid and acoustically lined intakes.

iii Method to generation realistic source waveforms.

iv Radiation modelling of buzz-saw noise for far-field noise prediction.

v Advanced supersonic fan tone prediction method for an axisymmetric duct with axially-varying mean flow.

A chronological approach was employed in this thesis starting from earlier works, and then a gradual development up to present capabilities. Existing prediction models were initially discussed and key analogies and equations presented. These form a basis for comparison and benchmark testing. A time-domain model code was developed to match

the prediction capabilities for supersonic fan noise nonlinear propagation in rigid intake duct at the start of the project. The availability of this working time domain model, and the frequency domain model (FDNS) developed at the ISVR, allowed for continuous evaluation and improvement of the nonlinear propagation modelling.

The time-domain nonlinear propagation model (referred to as Sawtooth Propagation in Rigid Intake Ducts SPRID) is limited to investigations on the propagation of buzz-saw noise in rigid ducts. This baseline model was used for comparison for various test cases. It is developed to investigate supersonic fan tone levels in rigid wall intake ducts, and yielded very good agreement with measured data. Issues identified in the validation of the 1D nonlinear propagation model, especially that of the assignment of phases to measured data amplitude spectrum was investigated and this led to the approaches employed to the generation of realistic sawtooth waveform utilizing measured data.

The difficulty of including acoustic liner absorption in the time-domain model led to the development of a model called the Nonlinear Propagation of Sawtooth Waveforms in Intake ducts (NP-SWIND) using a combined time-frequency domain approach. This led to successful inclusion of the acoustic liner absorption in the prediction model. Both the time-domain and time-frequency-domain models were based on propagation in cylindrical ducts. The development of the time-frequency domain model brought capabilities to the same level as achieved by the FDNS model being able to predict nonlinear decay of shocks and the effects of liner absorption for supersonic fan noise in both rigid and lined wall intakes. Outputs of the time-frequency domain model agreed well with measured data in the rigid wall intakes, but not quite as well for the lined intake due to the overestimation of the liner attenuation, most especially for the BPF tone, albeit predictions were better at lower and higher frequencies. Further studies presented in the thesis highlight the developments of an advanced time-frequency domain model.

Prior to the development of the advanced time-frequency domain model for axisymmetric ducts, the propagation model was coupled to GX-Munt: a theoretical model for radiation from semi-infinite cylindrical or annular ducts or jets. This enabled the prediction of radiation of the propagated rotor-locked field for supersonic fan noise to the far-field, and comparisons were made with measured data. Results showed good agreement at polar angles where the rotor-locked field was dominant. At lower angles, where the multimodal field was dominant, the insignificant contribution of the rotor-locked field at these angles was confirmed. For higher angles, detailed studies presented show the presence higher radial orders of the rotor-locked field. The inclusion of these radial orders in the far-field prediction showed a significant improvement in agreement with measured far-field data.

The advanced model was developed for axisymmetric ducts with varying radius along the duct axis. Owing to the variation in radius, the model was also developed to incorporate more realistic in-duct mean flows. Comprehensive studies on the effects of inner geometry

variation and flow speed variation are presented. Commercial numerical and simulation softwares such as FORTRAN, MATLAB and COMSOL are used in the developement of the model codes and compressible mean flow simulations. Results of validation of the models are presented at each stage of development with various comparisons with model-scale fan rig test data acquired and provided by Rolls-Royce PLC, and benchmark FDNS results.

In addition to variation of radius and flow speeds, the nonlinear propagation model was improved to incorporate variation in acoustic liner modal decay rates as a function of axial position in the duct. This enabled the capability of taking inputs from a duct mode model for a range of boundary layer thicknesses. Results presented show that, in addition to the effect of varying radius and the mean flow, the thickness of the boundary layer can significantly affect the prediction results due to the influence of the boundary layer on the level of acoustic liner absorption achieved by the liner.

Novel studies have been presented on the nonlinear propagation of supersonic fan noise with the development of a combined time-frequency domain model for axisymmetric ducts for real mean flows and boundary layer effects. In accordance with the key aims set out for this project, improvement to the prediction capabilities of buzz-saw noise have been presented. Modelling nonlinear propagation in intakes has been brought closer to reality by the incorporation of real inner nacelle geometry and flow. In addition, boundary layer effects on liner absorption have also been added. Very good agreement is achieved for rigid wall intakes and reasonable agreement for various lined configurations when compared against experimental measurements. Far-field radiation of buzz-saw noise has also been extensively investigated.

Recommendations

Various items listed in the aims and goals for the project have been achieved. An improved nonlinear propagation model for the prediction of supersonic fan noise has been developed and tested. This model incorporates the nonlinear attenuation of shock waves, the absorption of sound by installed acoustic liners, the effect of variation in intake internal duct radius, the consequent changes in flow and variation in the liner modal decay rates. Also, an existing radiation model has been used to take the output of the propagation model and predict the sound levels in the far-field.

While all the project objectives have been completed, a number of features can be added to the propagation model to bring it even closer to what is observed in the reality. The use of the time-frequency domain approach opens up the possibilities of even improving this advanced model with more complex features. These features may help improve prediction or just allow for more insight into the generation of buzz-saw noise at the fan plane and propagation to an observer in the far field. Other features that may be included in the advanced model are

(a) Multi-level stream-tube propagation which can investigate the radial extent of the shock waves and how long this radial span is retained for various flow conditions and ducts. This would utilise the assumption of a radial stream-tube slices where there is no interaction across the streamlines. Also, the importance or effect of this on the propagation results can be investigated.

(b) The region close to the duct lip has a unique flow owing to the contraction of the streamlines of the inflow in this region which results in a flow speed up making the flow Mach numbers observed in this region considerably higher than elsewhere within the duct. Investigation on propagation of buzz-saw noise within this region may be very important to better predictions for the near and far-field. This region may cause significant scattering to higher radial orders.

(c) In this work, various boundary-layer thicknesses were considered but these were fixed over the entire length of the duct. An extension of this study will be to investigate the variation of boundary-layer thickness in real aircraft intake geometries, and use this as a foundation for the determination of boundary-layer thicknesses to be used during propagation in various regions of the duct.

The quest to better predict supersonic fan noise propagation and radiation continues as more features are added to the models for prediction and the number of assumptions made for simplification reduces. As computing capabilities increase over the coming years, numerical methods using high-performance computational fluid dynamics models and methods may become more feasible, ultimately resulting in the routine use of computational fluid dynamics CFD for the whole problem; that is, generation, propagation and radiation.

Appendix A

Flow chart: Combined Time-Frequency Domain Model

The flow chart shows the order of processes within the model. The chart has been separated into three parts for the ease of visualization. The three parts are named as; preparation, propagation and absorption phases. These are all linked in the model and have va number of interdependent processes. It should be noted that only the essential steps are shown in the flow chart. In the model code, there are various other counters, monitoring stations and result checking and figure plotting processes which are not included in the flow chart.

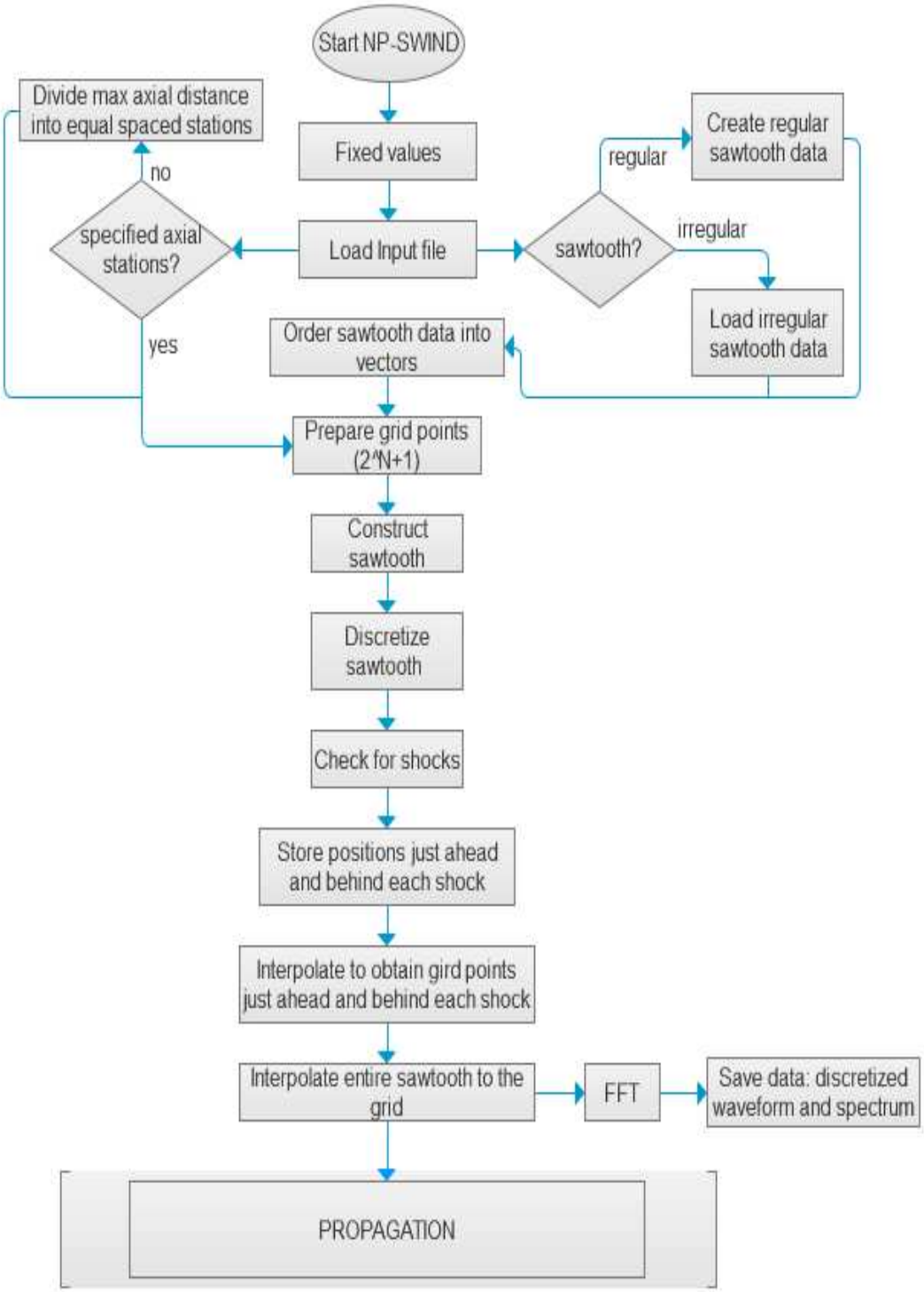
Start NP-SWIND
Fixed values
Load Input file
sawtooth?
regular
Create regular sawtooth data
irregular
Load irregular sawtooth data
specified axial stations?
no
Divide max axial distance into equal spaced stations
yes
Order sawtooth data into vectors
Prepare grid points (2^N+1)
Construct sawtooth
Discretize sawtooth
Check for shocks
Store positions just ahead and behind each shock
Interpolate to obtain gird points just ahead and behind each shock
Interpolate entire sawtooth to the grid
FFT
Save data: discretized waveform and spectrum
PROPAGATION

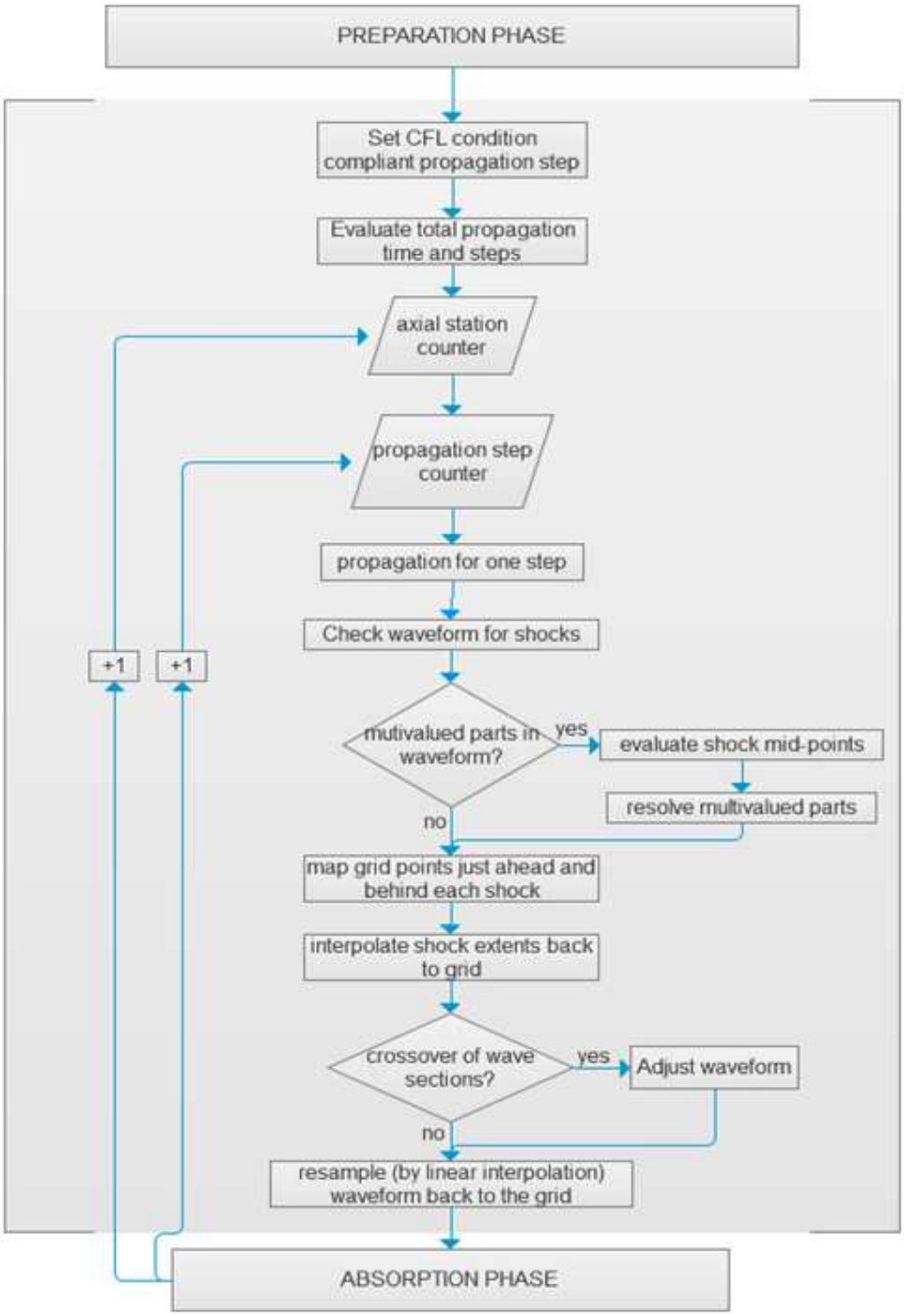
PREPARATION PHASE
Set CFL condition compliant propagation step
Evaluate total propagation time and steps
axial station counter
propagation step counter
propagation for one step
Check waveform for shocks
+1
+1
mutivalued parts in waveform?
yes
evaluate shock mid-points
resolve multivalued parts
no
map grid points just ahead and behind each shock
interpolate shock extents back to grid
crossover of wave sections?
yes
Adjust waveform
no
resample (by linear interpolation) waveform back to the grid
ABSORPTION PHASE

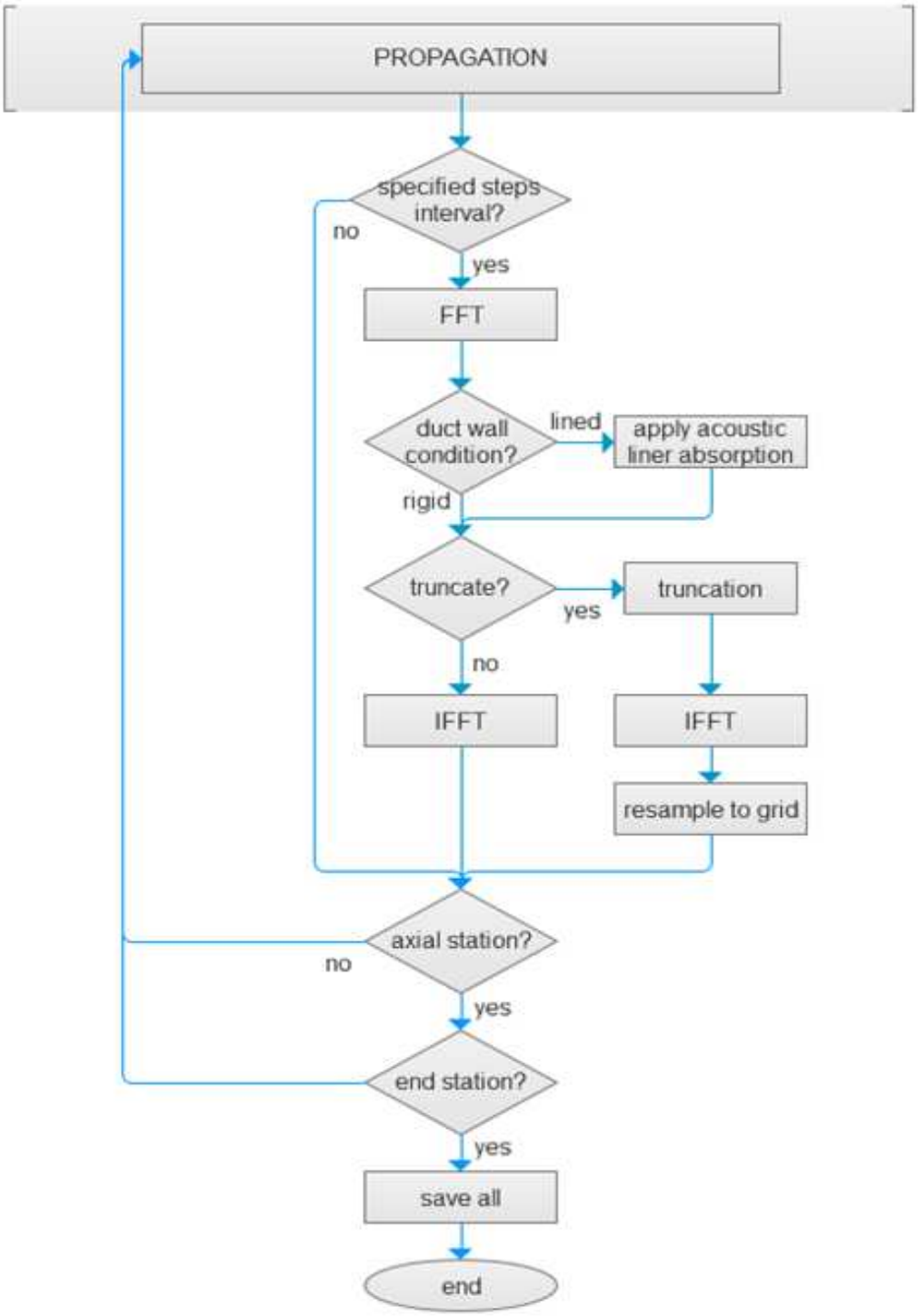
PROPAGATION
specified steps interval?
no
yes
FFT
duct wall condition?
lined
apply acoustic liner absorption
rigid
truncate?
yes
truncation
no
IFFT
IFFT
resample to grid
axial station?
no
yes
end station?
yes
save all
end

Appendix B

Experimental Measurements at axial stations

Measurements were acquired in the fan case close to the fan at ten different locations on the duct wall along the duct axis (illustration in figure 7.1). All pressure measurements are normalized with ambient pressure, P_M, measured for experiments.

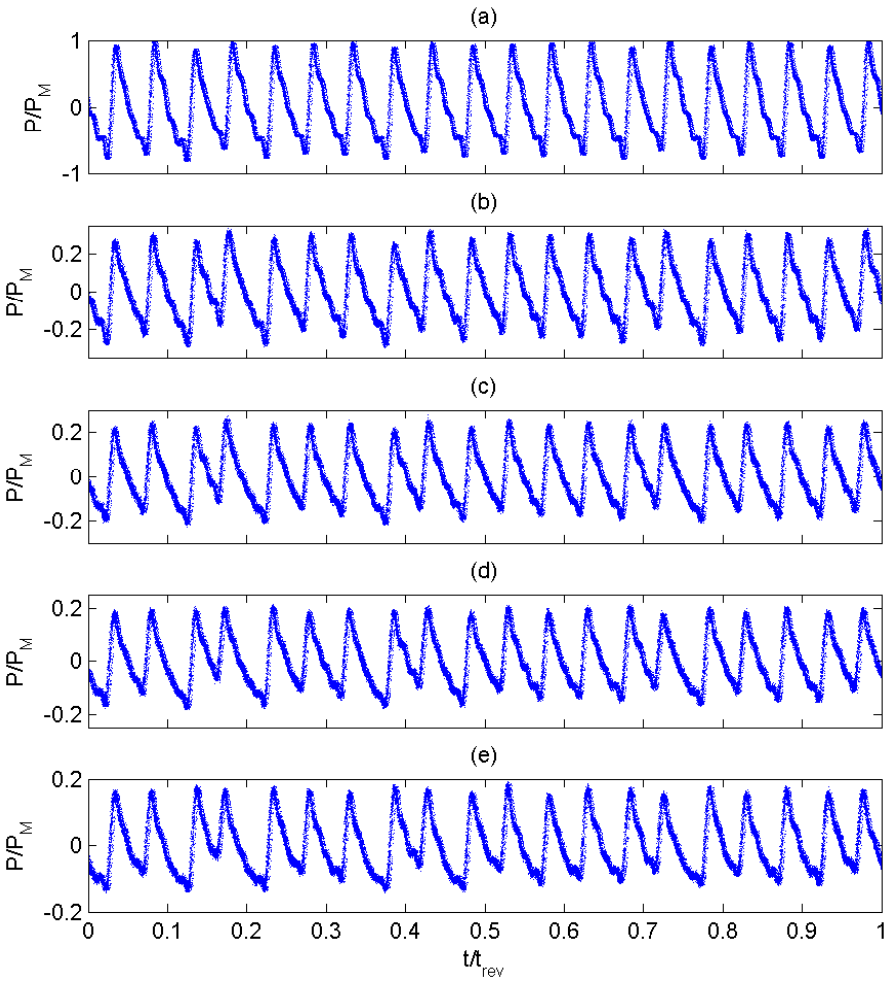

Figure B.1: Rigid-walled intake measurements: (a) near the fan (b) at $0.35r_d$ (c) at $0.483r_d$ (d) at $0.616r_d$ (e) at $0.75r_d$

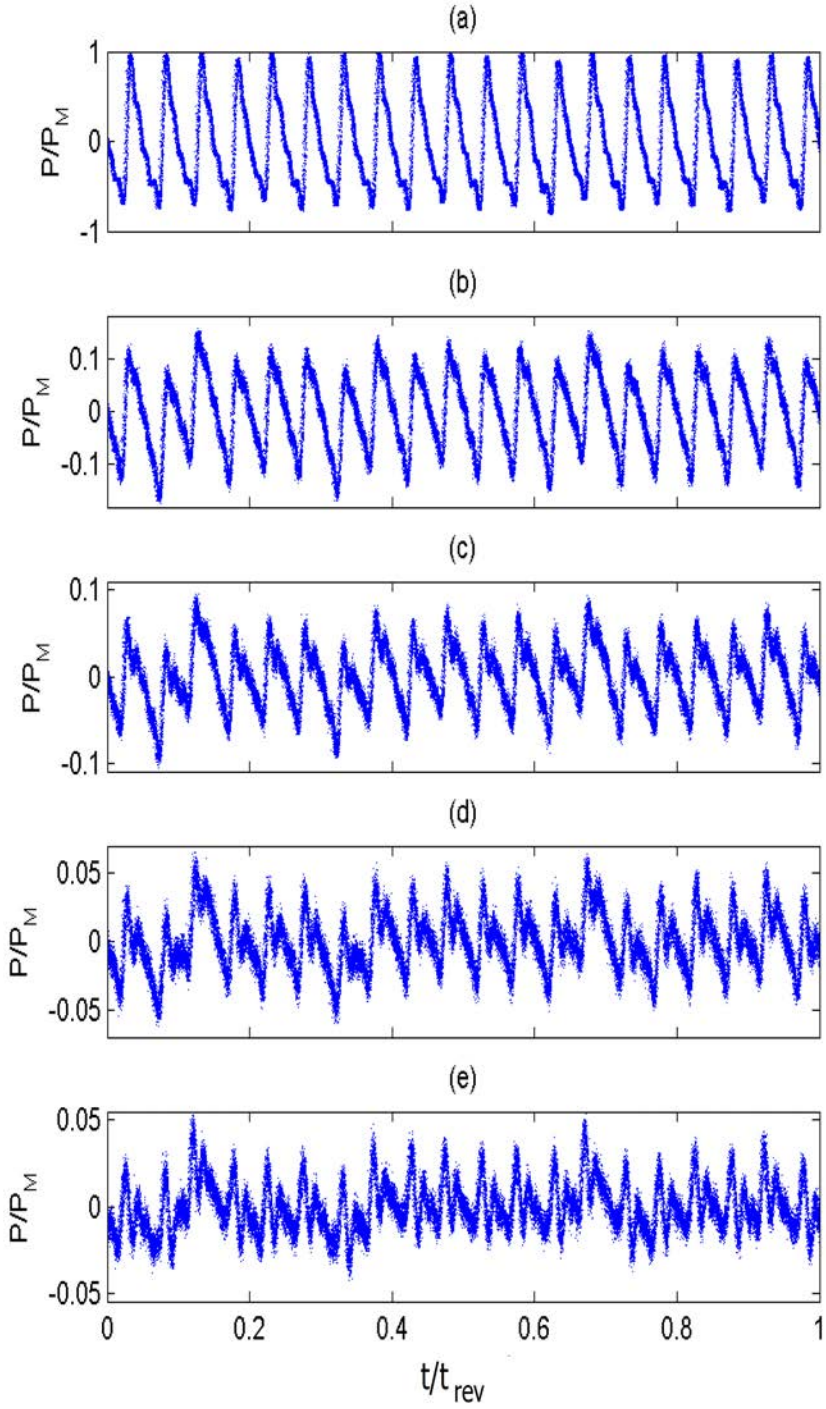

Figure B.2: Lined-walled intake measurements: (a) near the fan (b) at $0.35r_d$ (c) at $0.483r_d$ (d) at $0.616r_d$ (e) at $0.75r_d$

Appendix C

Duct wall pressure plots

The pressure distribution at wall for a cross-sectional slice at fan plane for a cylindrical duct of radius 0.5m is shown in figure C.1(a). Figure C.1(b) side view of this over a short length of propagation (similar to representations from numerical simulation results of CFD or CAA methods). The distribution along the entire wall of a cylindrical duct is over a short propagation distance can be seen in figure C.2.

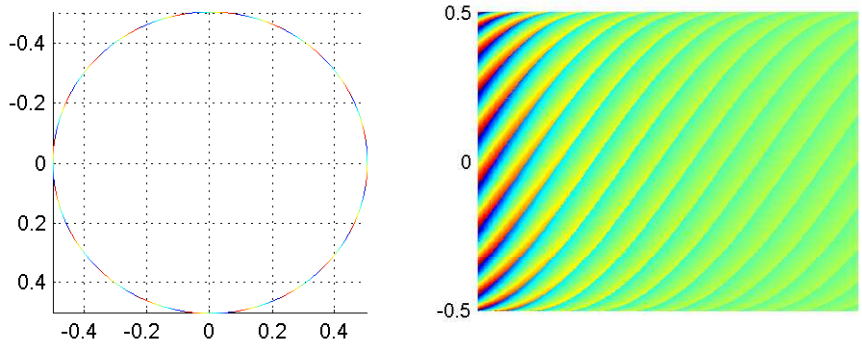

Figure C.1: Pressure field adjacent to the wall for regular sawtooth propagation in a cylindrical duct (a) side view (b) fan plane

Similar figures are shown for the propagation of an irregular sawtooth waveform in a rigid duct (Figures C.3 and C.4). Figure C.3 shows the pressure distribution adjacent to the wall for the propagation in a rigid cylindrical intake. In this figure the nonlinear attenuation of shocks are clearly visible and more interestingly in Figure C.4 and C.5, the changing shock spacing are also observed from the side view of the cylindrical duct and the 2D cascade. For the case where the wall of the cylindrical duct is lined, figures C.6 and C.7 shows an example pressure distribution adjacent to the wall, the side view (figure C.7) and the 2D cascade (figure C.8).

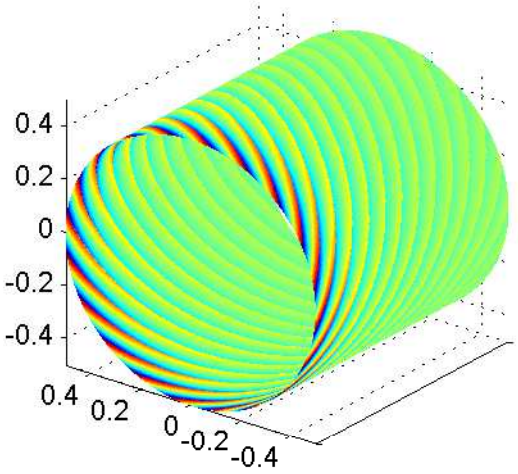

Figure C.2: Three-dimensional view of pressure field adjacent to the wall for regular sawtooth propagation in a cylindrical duct

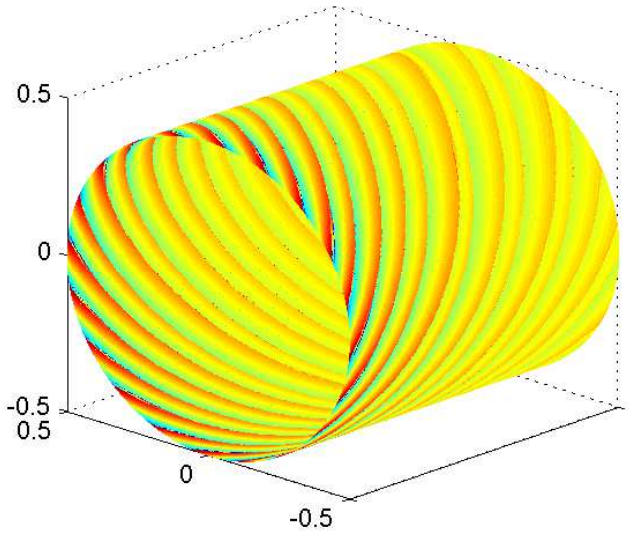

Figure C.3: Three-dimensional view of pressure field adjacent to the wall for irregular sawtooth propagation in a rigid cylindrical duct

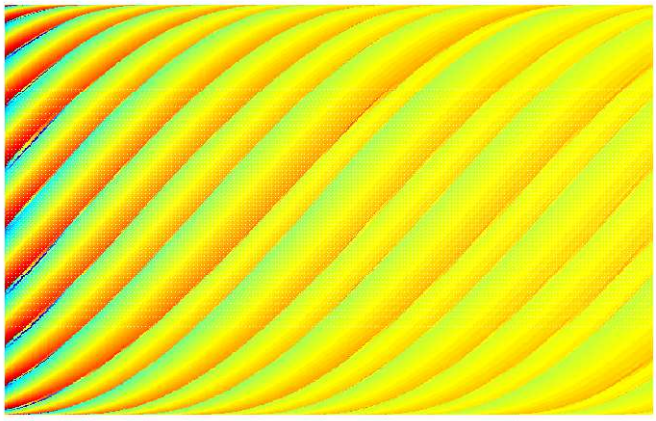

Figure C.4: Pressure field adjacent to the wall for irregular sawtooth propagation in a rigid cylindrical duct: side view

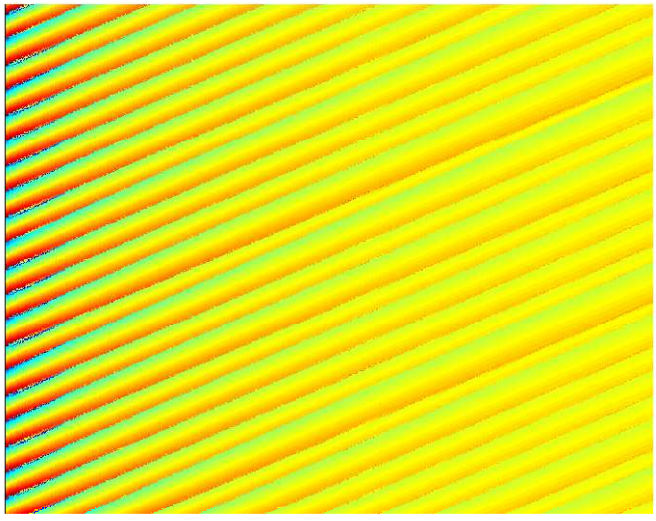

Figure C.5: Pressure field adjacent to the wall for irregular sawtooth propagation in a rigid cylindrical duct: fan 2D cascade

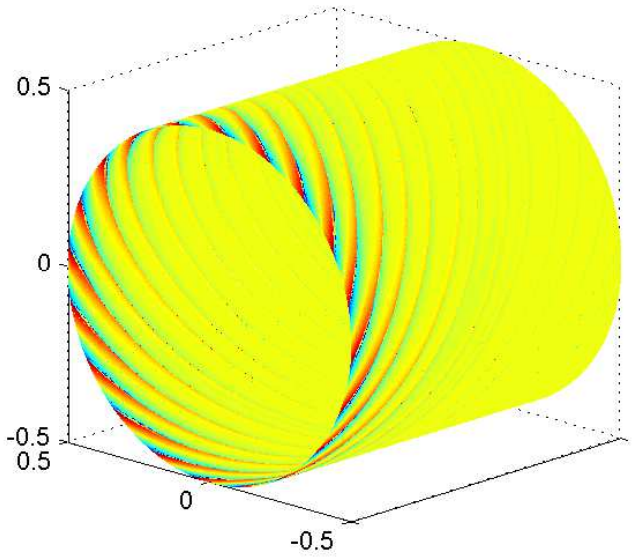

Figure C.6: Three-dimensional view of pressure field adjacent to the wall for irregular sawtooth propagation in a lined cylindrical duct

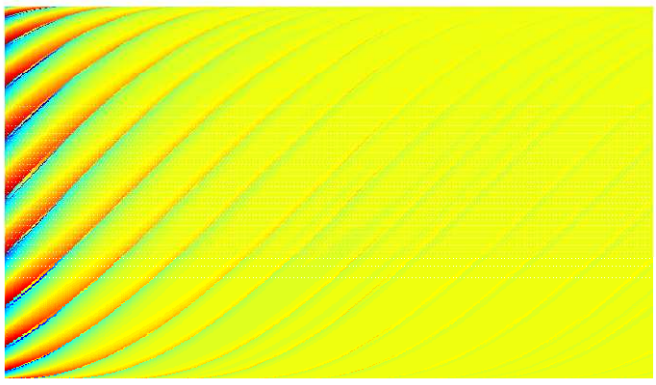

Figure C.7: Pressure field adjacent to the wall for irregular sawtooth propagation in a lined cylindrical duct: side view

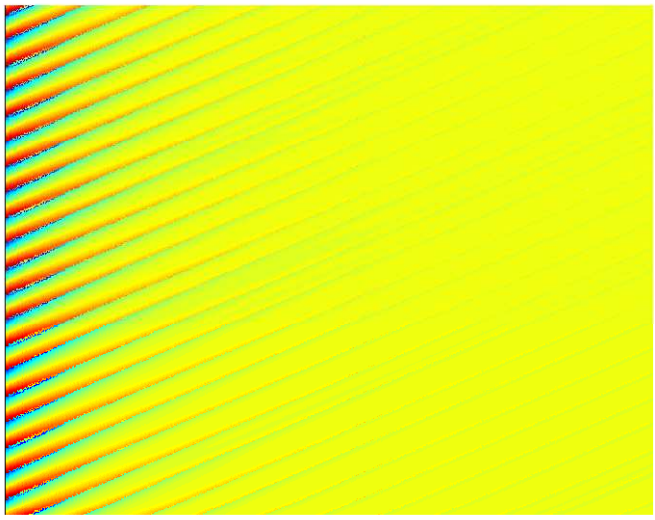

Figure C.8: Pressure field adjacent to the wall for irregular sawtooth propagation in a lined cylindrical duct: fan 2D cascade

References

[1] International Civil Aviation Organisation. *International Standards and Recommended Practices. Annex 16 to the Convention on International Civil Aviation. Environmental Protection: Volume 1 - Aircraft Noise*. International Civil Aviation Organisation, ICAO, sixth edition edition, 2011.

[2] International Civil Aviation Organisation. *Procedures for Air Navigation Services: Aircraft Operations Volume 1 Flight Procedures - Doc8168 OPS/611*. International Civil Aviation Organisation, ICAO, fifth edition edition, 2006.

[3] International Civil Aviation Organisation Committee on Aviation Environmental Protection. *Environmental Technical Manual. Volume 1 - Procedures for the Noise Certification of Aircraft*. International Civil Aviation Organisation, 2012.

[4] R. Sannino D. Casalino, F. Diozzi and A. Paonessa. Aircraft noise reduction technologies: A bibliographic review. *Aerospace Science and Technology*, 12(1):1–17, 2008.

[5] M.J.T. Smith. *Aircraft Noise*. Cambridge: University Press, 1989.

[6] H.H. Hubbard. *Aeroacoustics of Flight Vehicles: Theory and Practice. Volume 1 - Noise Sources*. Woodbury: Published for the Acoustical Society of America through the American Institute of Physics, 1995.

[7] M. J. Lighthill. On sound generated aerodynamically. i. general theory. *Proc. R. Soc. Lond.*, A211:564–587, 1952.

[8] Wilby J.F. Aircraft Interior Noise. *Journal of Sound and Vibration*, 190(3):545–564, 1996.

[9] M.G. Philpot. The buzz-saw noise generated by a high duty transonic compressor. *Journal of the American Society of Mechanical Engineers*, 70-GT-54, 1970.

[10] M.R. Fink. Shock wave behavior in transonic compressor noise generation. *Journal of the American Society of Mechanical Engineers*, 71-GT-7, 1971.

[11] D. Hawkings. Multiple tone generation by transonic compressors. *Journal of Sound and Vibration*, 17(2):241–250, July 1971.

[12] G.M. Lilley. Jet noise classical theory and experiments. *Aeroacoustics of flight vehicles: theory and practice*, 1:211–289, 1991.

[13] J. P. Raney. Research needs in aircraft noise prediction. *NASA TM X-72787 Third Interagency Symposium on University Research in Transportation Noise, Salt Lake City, Utah*, 1975.

[14] W.R. Graham, C.A. Hall, and M. Vera Morales. The potential of future aircraft technology for noise and pollutant emissions reduction. *Transport Policy*, 34:36–51, 2014.

[15] D. L. Huff. Noise reduction technologies for turbofan engines. *NASA TM*, 214495:2007, 2007.

[16] M. Lebrun L. Leylekian and P. Lempereur. An overview of aircraft noise reduction technologies. *Journal of AerospaceLab*, Issue 7(AL07-01):1 – 15, June 2014 2014.

[17] A. McAlpine and M.J. Fisher. On the prediction of buzz-saw noise in aero-engine inlet ducts. *Journal of Sound and Vibration*, 248(1):123 – 149, 2001.

[18] A. McAlpine and M.J. Fisher. On the Prediction of 'Buzz-saw' Noise in Acoustically Lined Aero-engine Inlet Ducts. *Journal of Sound and Vibration*, 265:175 – 200, 2003.

[19] C.L. Morfey and M.J. Fisher. Shock-wave radiation from a supersonic ducted rotor. *The Aeronautical Journal of the Royal Aeronautical Society*, 74:579–585, 1970.

[20] C.L. Morfey. Rotating blades and aerodynamic sound. *Journal of Sound and Vibration*, 28(3):587–617, 1973.

[21] A. McAlpine, M.J. Fisher, and B.J. Tester. 'Buzz-saw' noise: A Comparison of Measurement with Prediction. *Journal of Sound and Vibration*, 290:1202 – 1233, 2006.

[22] Gwenael Gabard and R.J. Astley. Theoretical model for sound radiation from annular jet pipes: far-and near-field solutions. *Journal of Fluid Mechanics*, 549:315–341, 2006.

[23] D. Mathews and R. Nagel. Inlet geometry and axial mach number effects on fan noise propagation. In *Aero-Acoustics Conference, Seattle, WA, October*, pages 15–19, 1973.

[24] R.A. Kantola and M. Kurosaka. The theoretical and experimental investigations on multiple pure tone noise - part 1. *National Aeronautics and Space Administration*, NASA CR-1831, November 1971.

[25] G.F. Pickett. Prediction of the spectral content of combination tone noise. *Journal of Aircraft*, 9(9):658–663, 1972.

[26] M. Kurosaka. A note on multiple pure tone noise. *Journal of Sound and Vibration*, 19(4):453–462, 1971.

[27] T.G. Sofrin and G.F. Pickett. Multiple pure tone noise generated by fans at supersonic tip speeds. *International Symposium on the Fluid Mechanics and Design of Turbomachinery, Pennsylvania State University*, 2:435–459, 1970.

[28] R.A. Kantola and M. Kurosaka. Theoretical and experimental investigations on multiple pure tone noise. *Journal of Aircraft*, 9(11):784–790, 1972.

[29] N.A. Cumpsty. Sum and difference tones from turbomachines. *Journal of Sound and Vibration*, 32(3):383–386, 1974.

[30] D.L. Hawkings. The effect of inlet conditions on supersonic cascade noise. *Journal of Sound and Vibration*, 33(4):353–368, 1974.

[31] M.S. Tsai. Propagation of buzz-saw noise in a nonuniform medium. *American Institute of Aeronautics and Astronautics AIAA 5th Aeroacoustics Conference*, AIAA79-0639, March 12-14 1979.

[32] B.S. Stratford and D.R. Newby. A new look at the generation of buzz-saw noise. *American Institute of Aeronautics and Astronautics AIAA 4th Aeroacoustics Conference*, AIAA77-1343, October 3-5 1977.

[33] D. Hawkings. Transonic fan noise. *Ministry of Defence(Procurement Executive), Aeronautical Research Council*, CP No. 1226:1–11, March 1972.

[34] P.G. Vaidya and K.S. Wang. Nonlinear resonance as the cause of multiple pure tones. *Journal of Aircraft*, 15(8):526–533, 1978.

[35] P.G. Vaidya. Multiple pure tone generation in aeroengine fans at subsonic and supersonic relative tip speeds. *American Institute of Aeronautics and Astronautics AIAA Journal*, 22(10):1366–1374, 1984.

[36] B.J. Tester M.J. Fisher and P.J.G. Schwaller. Supersonic fan tone noise prediction. *American Institute of Aeronautics and Astronautics AIAA 34th Aeroacoustics Conference*, AIAA-98-2249:290–300, 1998.

[37] Dilip Prasad and Jinzhang Feng. Propagation and decay of shock waves in turbofan engine inlets. In *ASME Turbo Expo 2004: Power for Land, Sea, and Air*, pages 1733–1745. American Society of Mechanical Engineers, 2004.

[38] J. Coupland, A. Wilson, N. Pollard, S. Uellenberg, C. Breard, and J. Diamond. Demonstration of a CFD-CAA methodology to predict buzz-saw noise propagation to the aircraft. In *13th AIAA/CEAS Aeroacoustics Conference (28th AIAA Aeroacoustics Conference)*, volume AIAA-2007-3517, Rome, Italy, 2007.

[39] Dilip Prasad, Ding Li, and David A Topol. Dispersion, dissipation and refraction of shock waves in acoustically treated turbofan inlets. *Journal of Sound and Vibration*, 2015.

[40] Braulio G. Pimenta and Roberto F. Bobenrieth Miserda. Validation of a moving-body high-order immersed boundary method for the multiple pure tone noise generated by supersonic rotor cascades (aiaa 2015-2518). In *21st AIAA/CEAS Aeroacoustics Conference,Dallas, Texas USA*, June 22 - 26 2015.

[41] S. Uellenberg. Buzzsaw Noise Prediction for Modern Turbofans. *10th AIAA/CEAS Aeroacoustics Conference*, AIAA 2004-3000, 2004.

[42] A. McAlpine, M.J. Fisher, and B.J. Tester. 'Buzz-saw' noise: A Comparison of Modal Measurements with an Improved Prediction Method. *Journal of Sound and Vibration*, 290:1202 – 1233, 2006.

[43] W. Eversman. Theoretical models for duct acoustic propagation and radiation. *Aeroacoustics of Flight Vehicles: Theory and Practice*, 2, 1991.

[44] S.W. Rienstra and A. Hirschberg. *An Introduction to Acoustics.* Instituut Wiskundige Dienstverlening Eindhoven Report IWDE 99-02, revised edition, 1999.

[45] M.L. Munjal. On the cut-on frequencies of a large round duct with azimuthal as well as radial partitions. *Journal of the Acoustical Society of America*, 84:1936-1939, 1988.

[46] Sung-Hwan Ko. Theoretical prediction of sound attenuation in acoustically lined annular duct in the presence of uniform flow and shear flow. *Journal of the Acoustical Society of America*, 54 (6):1592–1606, 1973.

[47] R. Fernando, R. Marchiano, F. Coulouvrat, and Y. Druon. Buzz-saw noise: Propagation of Shock Waves in Aero-engine Inlet Ducts. *Nonlinear Acoustics Fundamentals and Applications (American Institute of Physics AIP Conference Proceedings)*, 1022:99 – 102, 2008.

[48] R. Fernando, Y. Druon, R. Marchiano, and F. Coulouvrat. A Nonlinear Computational Method for the Propagation of Shock Waves in Aero-engine Inlets towards a new model for Buzz-saw Noise Prediction. *15th AIAA/CEAS Aeroacoustics Conference (30th Aeroacoustics Conference)*, AIAA 2009-3238, 2009.

[49] M. Kassem and A. Bennani. A three-dimensional cylindrical model for non-linear propagation prediction in lined intake ducts with uniform flow. In *20th AIAA/CEAS Aeroacoustics Conference, Atlanta, USA*, volume AIAA 2014-3114, June 16–20 2014.

[50] T. Oishi, S. Kusuda, H. Kodama, and M. Namba. Buzz-saw noise behavior due to influence of potential perturbation. *18th AIAA/CEAS Aeroacoustics Conference (33rd Aeroacoustics Conference)*, AIAA 2012-2266, 2012.

[51] A. McAlpine, P.J.G.Schwaller, M.J.Fisher, and B.J.Tester. 'Buzz-saw' noise: Prediction of the Rotor-alone Pressure Field. *Journal of Sound and Vibration*, 331:4901 – 4918, 2012.

[52] M. Kassem. Validation of a one dimensional model for nonlinear propagation in air intake ducts. In *19th AIAA/CEAS Aeroacoustics Conference, Berlin Germany*, volume AIAA 2013-2173, 2013.

[53] O.E. Adetifa, A. McAlpine, and G. Gabard. Modelling the nonlinear sound propagation and radiation of supersonic fan tones. *20th AIAA/CEAS Aeroacoustics Conference, Atlanta, Georgia, USA*, AIAA 2014-2945, 16 - 20 June 2014.

[54] Johan Thisse, C. Polacsek, Serge Lewy, and Anthony Lafitte. On the generation and propagation of multiple pure tones inside turbofans at transonic regime. *20th AIAA/CEAS Aeroacoustics Conference*, AIAA 2014-3104, June 16-20, Atlanta Georgia 2014.

[55] Alan McAlpine. 'AMcode'. Institute of Sound and Vibration Research, University of Southampton, United Kingdom.

[56] Alan McAlpine. Frequency domain numerical simulation FDNS code and results. Institute of Sound and Vibration Research, University of Southampton, United Kingdom.

[57] M.F. Hamilton and D.T. Blackstock, editors. *Nonlinear Acoustics*. Academic Press, 1998.

[58] F.M. Pestorius. Propagation of plane acoustic noise of finite amplitude. Technical Report ARL-TR-73-23 Applied Laboratories, The University of Texas at Austin AD778868, The University of Texas at Austin, 1973.

[59] R.O. Cleveland, M.F. Hamilton, and D.T. Blackstock. Time-domain modeling of finite-amplitude sound in relaxing fluids. *Journal of the Acoustical Society of America*, 99(6):3312 – 3318, 1996.

[60] W.F. Ames. *Numerical Methods for Partial Differential Equations*. Academic Press, 1992.

[61] F.M. Pestorius and D.T. Blackstock. *In Finite-Amplitude Wave Effects in Fluids*, chapter Propagation of Finite Amplitude Noise, pages 24–29. University of Texas at Austin, 1974.

[62] Alan McAlpine. 'Duct-mode code'. Institute of Sound and Vibration Research, University of Southampton, United Kingdom.

[63] Mathworks. *MATLAB Documentation for Matlab R2013b*. The Mathworks Inc., 2013.

[64] F.M. Pestorius, S.W. Williams, and D.T. Blackstock. Effect of nonlinearity on noise propagation. *Interagency Symposium on University Research on Transportation Noise*, June 1974.

[65] A. Korpel. Frequency approach to nonlinear dispersive waves. *Journal of Acoustic Society of America*, 67:1954 – 1958, 1980.

[66] I. Fatkullin and J. S. Hesthaven. Adaptive high-order finite-difference method for nonlinear wave problems. *Journal of Scientific Computing*, 16(1):47–67, March 2001.

[67] I.B. Shim, J.W. Kim, and D.J. Lee. Numerical study of n-wave propagation using optimized compact finite difference schemes. *AIAA Journal*, 41(2):316–319, 2003.

[68] Edward J Rice, Marcus F Heidmann, and Thomas G Sofrin. Modal propagation angles in a cylindrical duct with flow and their relation to sound radiation. In *NASA Technical Memorandum 79030*, January 15-17 1979.

[69] Edward J Rice, Marcus F Heidmann, and Thomas G Sofrin. Modal propagation angles in a cylindrical duct with flow and their relation to sound radiation. In *AIAA, 17th Aerospace Sciences Meeting, New Orleans, januaryy 15-17, 1979*, volume 1, 1979.

[70] Edward J Rice. Multimodal far-field acoustic radiation pattern using mode cutoff ratio. *AIAA Journal*, 16(9):906–911, 1977.

[71] Edward J Rice. Spinning mode sound propagation in ducts with acoustic treatment. *NASA Technical Note*, NASA TN D-7913, May 1975.

[72] A. Cargill B.J. Tester and B. Barry. Fan-noise duct-mode detection in the far-field: Simulation, measurement and analysis. *5th AIAA/CEAS Aeroacoustics Conference, March 12- 14, 1979, Seattle, Washington*, AIAA 79-0580, 1979.

[73] Alan McAlpine, Alex P Daymond-King, and Andrew J Kempton. Sound radiation from a flanged inclined duct. *The Journal of the Acoustical Society of America*, 132(6):3637–3646, 2012.

[74] Harold Levine and Julian Schwinger. On the radiation of sound from an unflanged circular pipe. *Physical review*, 73(4):383, 1948.

[75] S.D. Savkar. Radiation of cylindrical duct acoustic modes with flow mismatch. *Journal of Sound and Vibration*, 42(3):363–386, 1975.

[76] Y.C. Cho. Rigorous solutions for sound radiation from circular ducts with hyperbolic horns or infinite plane baffle. *Journal of Sound and Vibration*, 69(3):405–425, 1980.

[77] Y.C. Cho and K.U. Ingard. Exact solutions for sound radiation from a circular duct. Technical report, NASA Technical Memorandum 112200, June 1997.

[78] S.W. Rienstra. Acoustic radiation from a semi-infinite annular duct in a uniform subsonic mean flow. *Journal of Sound and Vibration*, 94(2):267–288, 1984.

[79] Xin Zhang, Xiaoxian Chen, CL Morfey, and PA Nelson. Computation of spinning modal radiation from an unflanged duct. *AIAA journal*, 42(9):1795–1801, 2004.

[80] M. Nallasamy. Computation of noise radiation from fan inlet and aft ducts. *Journal of aircraft*, 34(3):387–393, 1997.

[81] W. Eversman and I.D. Roy. Ducted fan acoustic radiation including the effects of nonuniform mean flow and acoustic treatment. *Final Technical Report, 31 Aug. 1981-30 Jun. 1993 Missouri Univ., Rolla, MO. Dept. of Mechanical and Aerospace Engineering and Engineering Mechanics.*, 1, 1993.

[82] G.F. Homicz and J.A. Lordi. A note on the radiative directivity patterns of ducts acoustic modes. *Journal of Sound and Vibration*, 41:283 – 290, 1975.

[83] X.D. Li, N. Schnoenwald, and F. Thiele. Numerical computation of sound propagation and radiation in a duct. In *7th AIAA/CEAS Aeroacoustics Conference, 28-30 May, 2001, Maastricht, The Netherlands*, volume AIAA 2001-2179, 2001.

[84] Yusuf Ozyoruk, Vineet Ahuja, Lyle N Long, and Frederic Souliez. Time domain simulations of radiation from ducted fans with liners. *7th AIAA/CEAS Aeroacoustics Conference, 28-30 May, 2001, Maastricht, The Netherlands*, AIAA 2001-2171, 2001.

[85] Alan McAlpine R. Sugimoto, Paul Murray and R.J. Astley. Prediction of in-duct and near-field noise for a fan rig intake. In *19th AIAA/CEAS Aeroacoustics Conference, May 27-29, 2013, Berlin, Germany*, 2013.

[86] E. Envia C.K.W. Tam, S.A. Parish and E.W. Chen. Physics of acoustic radiation from jet engine inlets. *18th AIAA/CEAS Aeroacoustics Conference, 4-6 June 2012, Colorado Springs, Colorado*, AIAA 2012-2242, 2012.

[87] F. Farassat and M.K. Myers. Extension of kirchhoff's formula to radiation from moving surfaces. *Journal of Sound and Vibration*, 123(3):451–460, 1988.

[88] F. Farassat. Linear acoustic formulas for calculation of rotating blade noise. *AIAA journal*, 19(9):1122–1130, 1981.

[89] R.J. Astley, R. Sugimoto, and P. Mustafi. Computational aero-acoustics for fan duct propagation and radiation. current status and application to turbofan liner optimisation. *Journal of Sound and Vibration*, 330(16):3832–3845, 2011.

[90] B. Noble. *Methods based on the Wiener-Hopf Technique for the Solution of Partial Differential Equations*, volume 69. Pergamon Press New York, 1958.

[91] D.G. Crighton and F.G. Leppington. Radiation properties of the semi-infinite vortex sheet: the initial-value problem. *Journal of Fluid Mechanics*, 64(02):393–414, 1974.

[92] G. Gabard. Gxmunt: User manual. Institute of Sound and Vibration Research, University of Southampton, SO17 1BJ, 26 November 2007.

[93] R Ramakrishnan. A note on the calculation of wiener-hopf split functions. *Journal of Sound and Vibration*, 81(4):592–595, 1982.

[94] R.M. Munt. The interaction of sound with a subsonic jet issuing from a semi-infinite cylindrical pipe. *Journal of Fluid Mechanics*, 83(04):609–640, 1977.

[95] Dilip Prasad and Jinzhang Feng. Propagation and decay of shock waves in turbofan engine inlets. *Journal of Turbomachinery*, pages 118–127, 2005.

[96] W. Roger Briley. Numerical method for predicting three-dimensional steady viscous flow in ducts. *Journal of Computational Physics*, 14(1):8–28, 1974.

[97] Jeffrey J. Defoe and Z. Spakovszky. Effects of boundary-layer ingestion on the aero-acoustics of transonic fan rotors. *Journal of Turbomachinery*, 135(5):051013, 2013.

[98] Dilip Prasad. Weakly nonlinear shock propagation in slowly varying one-dimensional flows. *Physics of Fluids (1994-present)*, 18(3):036101, 2006.

[99] Ed Obert. *Aerodynamic design of transport aircraft*. Ios Press, 2009.

[100] Jeffrey J. Defoe and Z. Spakovszky. Shock propagation and mpt noise from a transonic rotor in nonuniform flow. *Journal of Turbomachinery*, 135(1):011016, 2013.

[101] S. W. Rienstra and M. Darau. Boundary-layer thickness effects of the hydrodynamic instability along an impedance wall. *Journal of Fluid Mechanics*, 671:559–573, 2011.

[102] R Jeremy Astley, Rie Sugimoto, Prateek Mustafi, Matthew Kewin, and Iansteel Achunche. Liner optimisation for turbofan ducts-towards a fully automated approach. In *16th AIAA/CEAS Aeroacoustics Conference, AIAA-2010-3826, Stockholm, Sweden*, pages 7–9, 2010.

[103] S.W. Rienstra. Sound transmission in slowly varying circular and annular lined ducts with flow. *Journal of Fluid Mechanics*, 380:279–296, 1999.

[104] N. C. Ovenden and S. W. Rienstra. Mode-matching strategies in slowly varying engine ducts. *AIAA journal*, 42(9):1832–1840, 2004.

[105] B.K. Hodder. An investigation of engine influence on inlet performance. *NASA CR-166136*, 1981.

[106] Rie Sugimoto, Paul Murray, Alan McAlpine, and R Jeremy Astley. Prediction of in-duct and near-field noise for a fan rig intake. *19th AIAA/CEAS Aeroacoustics Conference, Berlin, Germany*, AIAA 2013-2022, 2013.

[107] COMSOL Multiphysics. *Introduction to COMSOL Multiphysics*. V5.1. COMSOL, 1998 – 2005.

[108] P. B. Murray and R. J. Astley. Development of a single degree of freedom perforate impedance model under grazing flow and high spl. In *18th AIAA/CEAS Aeroacoustics Conference (33rd AIAA Aeroacoustics Conference)*, page 2294, 2012.

[109] Edward J Rice. Model for the acoustic impedance of a perforated plate liner with multiple frequency excitation. *The Journal of the Acoustical Society of America*, 51(1A):94–95, 1972.

[110] Edward J Rice. A model for the pressure excitation spectrum and acoustic impedance of sound absorbers in the presence of grazing flow. In *American Institute of Aeronautics and Astronautics, Aero-Acoustics Conference, Seattle, Wash*, page 1973, 1973.

[111] I.J. Hughes and A.P. Dowling. The absorption of sound by perforated linings. *Journal of Fluid Mechanics*, 218:299–335, 1990.

[112] Xiaodong Jing and Xiaofeng Sun. Experimental investigations of perforated liners with bias flow. *The Journal of the Acoustical Society of America*, 106(5):2436–2441, 1999.

[113] Jean-Michel Roche, Laurent Leylekian, Grégory Delattre, and François Vuillot. Aircraft fan noise absorption: Dns of the acoustic dissipation of resonant liners. In *15th AIAA/CEAS Aeroacoustics Conference (30th AIAA Aeroacoustics Conference), AIAA Paper*, volume 3146, 2009.

[114] Jean-Michel Roche, François Vuillot, Laurent Leylekian, Grégory Delattre, E Piot, and F Simon. Numerical and experimental study of resonant liners aeroacoustic absorption under grazing flow. In *Proceedings of the 16th AIAA/CEAS Aeroacoustics Conference*, volume AIAA 2010-3767, 2010.

[115] A.W. Guess. Calculation of perforated plate liner parameters from specified acoustic resistance and reactance. *Journal of Sound and Vibration*, 40(1):119–137, 1975.